Microfluidic Devices for Electrical Interrogation of Gap Junction Connectivity

A dissertation submitted by

Joel H. Dungan

in partial fulfillment of the requirements for the degree of

Doctor of Philosophy

in

Electrical Engineering

Tufts University

February 2025

© 2025, Joel H. Dungan

Adviser: Valencia Koomson

ABSTRACT

Gap junctions are the cytosolic couplings between adjacent cells that mediate intercellular communication in non-neural cells. Numerous studies have shown that network connectivity though gap junctions is an essential element of growth, regrowth, and development. Meanwhile abnormal gap junction expression has been associated with various disease states including cancers.

Existing technologies to measure gap junction connectivity cannot offer non-invasive, repeatable, real-time measurement of connectivity in developing cell cultures. Benchtop dye diffusion assays are invasive and minimally repeatable. Whole-cell patch clamping techniques puncture cell membranes to offer high fidelity electrical measurement of gap junction conductivity. However, the technique is expensive and technically difficult to perform, and it is not well suited to measure connectivity in larger cell networks as they develop.

Microfluidic technologies offer an opportunity to create test conditions that could enable direct electrical measurement of gap junction connectivity in monolayer cell cultures. Two approaches enabled by microfabrication are explored. Laminar flow of sucrose solution is used to provide electrical isolation with the aim of forcing conduction through gap junction connected cell network. Alternatively, a micromechanical electrical isolation approach is employed wherein a thin elastomeric membrane is compressed tightly to the cell layer. Finally, the two approaches are evaluated in conjunction, creating a microfluidic analog of benchtop sucrose gap techniques.

In order to facilitate experimentation, a "lab-on-scope" platform is developed to closely integrate all of the peripherals required for a microfluidic lab. Magnetically latched valves, temperature regulation, flow sensing, fluorescent imaging, and electrical impedance spectroscopy are all enabled in a compact, cost-effective, and automated system. This modular platform fills a gap between scientists looking to leverage microfluidic technologies and the large and costly array of peripheral lab systems needed to operate microfluidic devices.

Using the lab-on-scope platform, seven microfluidic device designs are evaluated for their potential to characterize gap junction connectivity of normal rat kidney fibroblast cells (NRK-49F). While trilaminar flow devices show mixed results, devices using elastomeric valves show promise in terms of scalability and biologically relevant measurement conditions. Microfluidic sucrose gap devices are shown to measure an average of 6.5 kΩ increase in cell network impedance at 410 Hz in response to treatment with the chemical gap junction blocker, 2-APB.

ACKNOWLEDGEMENTS

I am extremely grateful to everyone who has helped me on my academic journey to this point. Over the past 8 years, I have had the pleasure of working closely with two distinguished labs at Tufts University. I would like to thank Prof. Koomson for all of her mentorship and guidance throughout this project. I could not have navigated through the challenges of academia without her insights and encouragement. Thank you to the graduate students of the Koomson lab, Alper, Ravi and Yun, for their companionship and consultation. I am grateful for the dedication of undergraduate students, Hannah Shafferman and Myles Lopes, who helped push experimentation forward. Thank you to Prof. Levin and all the members of his lab, who graciously hosted me as a visitor in their lab space. The Levin Lab became my second home in Boston, and I would like to thank Prof. Levin for fostering a positive environment of curiosity and exploration.

In particular, I wish to thank Dr. Juanita Mathews. She has been a steadfast research partner, advisor, and friend from the very beginning of this project.

Thank you to Prof. Guasto and Dr. Waisbord for sharing their wealth of microfluidic and fabrication knowledge. I am honored as well to have Prof. Sonkusale and Dr. Borenstein on my committee. Their guidance has been invaluable throughout this process. I would like to Dr. Vlahakis, the Tufts microfab manager, for encouraging and accommodating my experimental and less conventional work in the clean room.

Finally, a sincere thank you to all of my friends and family who have supported, encouraged, and occasionally consoled me along this journey. I can never express sufficient gratitude to my parents, Tom and Helen, who have always loved and supported me. Thank you to my loving wife, Mia, for bringing balance, warmth, and joy to my life daily.

PUBLISHED CONTENT AND CONTRIBUTIONS

Dungan, Joel, Juanita Mathews, Michael Levin, and Valencia Koomson (Sept. 2023). "Optimization of Oligomer Stamping Technique for Normally Closed Elastomeric Valves on Glass Substrate". In: *Micromachines* 14.9 (9), p. 1659. ISSN: 2072-666X. DOI: 10.3390/mi14091659. URL: https://www.mdpi.com/2072-666X/14/9/1659 (visited on 08/28/2023).

J.D. was the primary author of the manuscript and participated in conceptualization, development of methodology, fabrication of the devices, and development of software. J.D. was responsible for execution of investigation and analysis of the data.

– (Oct. 30, 2019). "Microfluidic Device for Electrical Measurement of Gap Junction Mediated Intercellular Communication with Integrated Calibration". In: microTAS 2019. Basel, Switzerland: 23rd Internation Conference on Miniaturized Systems for Chemistry and Life Sciences.

J.D. was the primary author and presenter and participated in conceptualization, development of methodology, fabrication of the devices, and development of software. J.D. was responsible for execution of investigation and analysis of the data.

– (6–Aug. 9, 2017). "Microfluidic Platform to Study Intercellular Connectivity through On-Chip Electrical Impedance Measurement". In: Circuits and Systems (MWSCAS), 2017 IEEE 60th International Midwest Symposium On. Boston, MA: IEEE, pp. 56–59. DOI: 10.1109/MWSCAS.2017.8052859. URL: http://ieeexplore.ieee.org/document/8052859/.

J.D. was the primary author and presenter and participated in conceptualization, development of methodology, fabrication of the devices, and development of software. J.D. was responsible for execution of investigation and analysis of the data.

TABLE OF CONTENTS

Abstract ii
Acknowledgements iii
Published Content and Contributions iv
Table of Contents iv
List of Illustrations vii
List of Tables ix
Nomenclature x
Chapter I: Introduction: Microfluidics as an Opportunity to Interface with Bioelectric Signaling 1
1.1 Microfluidics as an Opportunity in Bioengineering 1
1.2 Microfluidics to Characterize Cellular Interactions 2
1.3 Intercellular Communication in Developmental Biology 3
1.4 Gap Junction Measurement Technologies 4
1.5 Considerations for Electrical Measurement of Gap Junction Connectivity 5
1.6 Vision for a Closed-loop Training Platform 10
1.7 Organization 11
Chapter II: Fabrication of Microfluidic Devices for Cell Culture and Electrical Impedance Measurement 13
2.1 Introduction 13
2.2 Materials and Methods 15
2.3 Process Optimization 19
2.4 Process Validation and Characterization 23
2.5 Discussion 29
2.6 Conclusions 33
Chapter III: A Lab-on-Microscope Environment for Automated Biomicrofluidic Experimentation 35
3.1 Introduction 35
3.2 "Lab-on-Scope" - A Compact System for Microfluidics Peripherals 36
3.3 Cell Culture in Microfluidic Devices 42
3.4 Results 45
3.5 Conclusions 47
Chapter IV: Laminar Flow Based Microfluidic Devices to Interrogate Gap Junction Connectivity 48
4.1 Introduction 48
4.2 Methods and Design 50
4.3 Results 54
4.4 Discussion 62
4.5 Conclusions 68
Chapter V: Elastomeric Valve Based Devices to Interrogate Gap Junction Connectivity . . . 69
5.1 Introduction 69
5.2 Materials and Methods 72

5.3 Single Valve Devices . . . 74
5.4 Valved Sucrose Gap Devices . . . 83
5.5 Conclusions . . . 91
Chapter VI: Conclusions: Toward Microfluidic Gap Junction Measurement . . . 93
6.1 Comparison of Microfluidic Designs for Gap Junction Interrogation . . . 93
6.2 Future Work . . . 96
6.3 Contributions to the State of the Art . . . 100
6.4 Final Thoughts . . . 101
Bibliography . . . 102
Appendix A: Detailed Fabrication Recipes . . . 116
A.1 Electrode Fabrication . . . 116
A.2 SU8 Master Mold Fabrication . . . 119
A.3 PDMS Molding . . . 122
A.4 PDMS-PDMS Bonding . . . 124
A.5 PDMS-Glass Bonding (Oligomer Stamping Method) . . . 127
Appendix B: Cell Culture and Seeding Protocols . . . 130
B.1 General Approach . . . 130
B.2 Detailed Protocol . . . 130
Appendix C: Electrical Impedance Correlated to Flow Rate in Elastomeric Valves: An Analog Material Memory . . . 135
C.1 Introduction . . . 135
C.2 Methods . . . 136
C.3 Results . . . 138
C.4 Discussion . . . 147
C.5 Conclusion . . . 149
Appendix D: Trilaminar Flow Theory . . . 153

LIST OF ILLUSTRATIONS

Number *Page*

1.1 Scale of biological specimens for microfluidic study . . . 3
1.2 Electrical models pertinent to impedance measurements on biological cells . . . 6
1.3 Gap junction connections in a cell monolayer modeled as a resistive lattice . . . 9
1.4 Lock-in architecture and noise bandwidth reduction scheme. . . . 9
1.5 Vision for a closed-loop microfluidic training platform for exogenous control of cell differentiation . . . 11
2.1 Fabrication process diagram . . . 16
2.2 Elastomeric valve construction . . . 17
2.3 Alignment rig for PDMS bonding . . . 17
2.4 Bond strength estimation and measurement techniques . . . 19
2.5 Bond strength analysis characterized by contact angle and blister testing . . . 21
2.6 Profilometry measurements . . . 24
2.7 Bonding resolution analysis . . . 25
2.8 Impedance characterization of valve sealing, actuation time, and hysteresis . . . 26
2.9 Electrical characterization of valve resilience to back pressure . . . 28
2.10 A proof-of-concept 4×4 valved array chip integrating 24 valves . . . 29
2.11 Alternative fabrication methods. . . . 30
2.12 Optics and stamping pressure limit bonding resolution. . . . 33
3.1 Design of the lab-on-scope platform . . . 37
3.2 PDMS manifold produced from 3D printed cast . . . 38
3.3 Temperature stability of the lab-on-scope platform . . . 38
3.4 Complex impedance spectroscopy systems. . . . 39
3.5 Graphical user interface for lab-on-scope system . . . 41
3.6 Time course of NRK-49F cells seeded into a microfluidic device as monitored by GFP marked Cx43 protein imaging. . . . 45
3.7 Demonstration of pneumatic valve control and electrical measurement facilitated by the Lab-on-Scope platform in an arrayed microfluidic chip. . . . 45
3.8 Electrical monitoring of long-term cell culture in a microfluidic device. . . . 46
4.1 Trilaminar flow sucrose gap device design . . . 51
4.2 Impedance dependence on stream width in trilaminar flow . . . 55
4.3 Test solution impedance spectroscopy for trilaminar flow devices . . . 56

4.4 Calibration scheme to correct for stream width variation 57
4.5 A representative verification test using the chemical gap junction blocker, 2-APB . . 60
4.6 Results of trilaminar device testing with 2-APB on NRK-49F cultures 61
4.7 Poor cell health in NRK cultures exposed to long-term trilaminar sucrose flow . . . 62
4.8 Electrical modeling of cells under sucrose flow 64
4.9 Design of a bilaminar flow device with on-chip control site 67
5.1 Conceptual approaches to gap junction measurement 71
5.2 Device design using a single elastomeric valve to electrically isolate gap junctions . 75
5.3 Settling characteristic of the elastomeric valves 76
5.4 Cell and no-cell controls for the single valve device 78
5.5 Promising results in single valve devices showing increased impedance for NRK cells measured in the presence of 2-APB 80
5.6 Memory effect in single valve devices. Flow rate through PDMS valves is correlated to the subsequent impedance measured across them in the closed state. 82
5.7 Design of a microfluidic sucrose gap device 84
5.8 Microfluidic sucrose gap device designed for external sucrose perfusion switching . 86
5.9 Cell viability testing under compressive strain from valves in the microfluidic device 87
5.10 Polarity of the 2-APB molecule results in an altered frequency response 88
5.11 Control experiments in the sucrose gap microfluidic device 89
5.12 Gap junction blocker verification of device operation 91
5.13 Test results for the proof-of-concept microfluidic gap junction device 92
6.1 Pictorial summary of all microfluidic device designs intended for gap junction connectivity measurement on the Lab-on-Scope system 93
A.1 Electrode fabrication details. 119
B.1 Cell seeding process. 130
C.1 Device design for evaluation of normally closed elastomeric valves. 137
C.2 Correlation between the flow rate through PDMS valves and the subsequent impedance measured across them in the closed state 139
C.3 Demonstration of the longevity of the memory effect 140
C.4 Impedance response to different flow interval duration 142
C.5 A demonstration of the mechanical stability of the memory effect 142
C.6 Impedance response to different vacuum levels on the elastomeric valves during the flow phase 143
C.7 Test of overwrite time for a fixed flow rate 144
C.8 Investigation of an anesthesia technique 145
D.1 Theoretical model of electrical resistance resulting from trilaminar flow 154

LIST OF TABLES

Number *Page*

1.1 Reported values for resistive coupling between adjacent cells. 8

5.1 Comparison of gap junction measurement to reported literature 90

6.1 Comparison of the microfluidic device designs for electrical measurement of gap junction connectivity 94

C.1 Testing results for additional characterization of PDMS memory 146

NOMENCLATURE

2-APB. 2-Aminoethoxydiphenyl borate, a chemical gap junction blocker.

AFE. Analog front end, analog conditioning circuitry that receives an input signal and converts it (often through amplification and filtering) to a reliable signal for further processing.

CDA. Compressed Dry Air, clean pressurized air used in microfabrication.

CMOS. Complementary Metal-Oxide Semiconductor, a semiconductor fabrication strategy for dense integration of field-effect transistors.

DC. Direct Current, current which flows in only one direction as opposed to alternating (0 Hz frequency).

DMEM. Dulbecco's Modified Eagle Medium, a basal medium for mammalian cell culture.

DPBS. Dulbecco's Phosphate Buffered Saline, a balanced salt solution for mammalian cell culture. Unless otherwise specified, a formulation without calcium chloride and magnesium chloride is used.

ECM. Extracellular matrix, an extracellular protein structure that provides support to cells and improves substrate adhesion.

FBS. Fetal Bovine Serum, a nutrient serum derived from fetal calves that facilitates cell culture.

GFP. Green Fluorescent Protein, a protein used in fluorescent labeling that emits green light when excited in the blue to ultraviolet range. In the context of fluorescence imaging, GFP can also refer to dichroic filtration optimized for use with this fluorophore.

IC. Integrated Circuit, a circuit integrated at the transistor level into a semiconductor material.

NRK. The normal rat kidney fibroblast cell line (NRK-49F) used in most experiments.

PCB. Printed circuit board.

PDMS. Polydimethylsiloxane, an optically transparent silicone polymer. Unless otherwise specified, the Sylgard 184 formulation is used.

PPE. Personal Protective Equipment, equipment intended to prevent personal harm or injury.

RFP. Red Fluorescent Protein, a protein used in fluorescent labeling that emits red-orange light when excited in the blue-green range. In the context of fluorescence imaging, RFP can also refer to dichroic filtration optimized for use with this fluorophore.

RIE. Reactive Ion Etcher, an dry etching system that delivers plasma at low pressures.

TEER. Transepithelial electrical resistance, a related technology that quantifies the integrity of a cell layer as an electrical barrier measuring tightness rather than connectivity.

UV. Ultraviolet (light), electromagnetic radiation with wavelength between 10 and 400 nm.

Chapter 1

INTRODUCTION: MICROFLUIDICS AS AN OPPORTUNITY TO INTERFACE WITH BIOELECTRIC SIGNALING

Microfluidic technologies are rapidly emerging as a staging point for intersectional research and interdisciplinary engineering solutions. Devices designed to study adherent monolayer cell cultures are uniquely suited to cell-to-cell interactions and communication. Intercellular communication through gap junctions is critical to healthy development and electrical measurement of this interaction could have profound impacts on many crucial applications in bioengineering. To this end, this dissertation will explore microfluidic approaches to electrically measure gap junction communication in developing cells. This chapter will provide background information and motivation for pursuing novel engineering approaches to gap junction measurement.

1.1 Microfluidics as an Opportunity in Bioengineering

Although early microfluidic advances focused primarily on chemistry and parallelizing/miniaturizing analytical assays, these devices are also ideal to culture biological cells and to manipulate their aqueous environments. Microfluidic devices that manipulate fluids and flows in channels and chambers less that one millimeter in dimension offer distinct advantages over conventional cell culture approaches. Cell culture media, as well as chemicals and reagents, can be significantly costly and microfluidic devices can more efficiently deliver nutrients and biological factors (and remove waste) than traditional static culture due to their favorable surface area to volume ratio. Additionally, the precise fabrication and fluid control of microfluidic devices lends them well to automation and parallelization of cell culture (Vollertsen et al., 2020; Hung et al., 2005). With the integration of heating and other environmental sensors, microfluidics can be used to create microbioreactors that more closely replicate the in vivo environment (Pasirayi et al., 2022).

Automation and small volumes offer the opportunity to rapidly change the cell culture environment to set experimental conditions or to react to changes in biological signals. Further, on-chip mixers and gradient generators can be used to generate highly controlled reagent assays (S.-J. Lin et al., 2022). Microscale fluid dynamics can also be exploited to create unique test environments. Precise fluid control in many cases is made possible by the microscale fluid dynamics principle of laminar flow. Hydrodynamic focusing due to laminar flow is essential for many systems that process cells or cellular components in a single file flow, but can be used for many other effects such as cell patterning (Takayama et al., 1999), reagent treatment (Tarn, Lopez-Martinez, and Pamme, 2014), and the devices discussed the following chapters.

Fluid and environmental control on the same scale as biological samples offers additional unique opportunities to collect more accurate data and examine cellular interactions. Microfluidic devices can more readily integrate sensors and sources closer to the desired interrogation points. Optical detectors and sources can be coupled in via optical fibers or directly integrated under microfluidic channels (Măriuţa et al., 2020). Similarly planar electrodes for electrical stimulation and detection can easily be patterned on glass substrates, while direct integration over silicon microelectrode arrays is also possible. A plethora of other integrated sensors and actuators for microfluidic devices are still being explored including spatiotemporal chemical release (Selberg et al., 2020), acoustophoretic sorting (Lenshof, Magnusson, and Laurell, 2012), magnetic biosensors (Giouroudi and Kokkinis, 2017; Abu-Nimeh and Fathi, 2010), and more.

Given the potential for efficient cell culture and dense sensor integration, microfluidic devices offer an unparalleled opportunity for bioengineering innovation. Highly integrated sensors and multiplexed culture conditions promise a generation of new low-cost point-of-care diagnostic devices, while the further integration of sources and stimuli continues to advance research through complete lab-on-a-chip systems.

1.2 Microfluidics to Characterize Cellular Interactions

The diversity in microfluidic device design for biological investigation matches the scope of cell types and applications in microbiology, as depicted in Figure 1.1. Devices for biological interrogation can be grouped roughly by the cell culture paradigms they employ, and each type of device is best suited to study specific interactions. Nanofluidic devices are usually specialized for the study of DNA, proteins, or viruses and characterize or exploit specific binding or electrochemical interactions. The majority of microfluidic devices circulate single cells for the purposes of high throughput sensing or diagnostic analysis. So called flow cytometry can be used to characterize and sort flowing cells, especially bacterial and blood samples. In some cases, more detailed information can be attained by temporarily trapping individual cells through specialized flow regimes or vacuum. Single cells analyzed in isolation can yield insights into their composition and structure but often provide little functional information.

At the opposite end of the spectrum, organ-on-chip devices and complex heterocultures aim to create fully functioning in vitro models of systems in living organisms. These devices can study metabolic processes, tissue interfaces, and long range interactions. They are becoming an invaluable tool to evaluate drug efficacy and side effects relatively complex models. However, the biological complexity of these multi-tissue systems can mean that they are better suited as “black box” tools for drug assays than experimental devices to study specific interactions between cells.

Microfluidic devices facilitating adherent culture of cell monolayers then are ideal for investigating

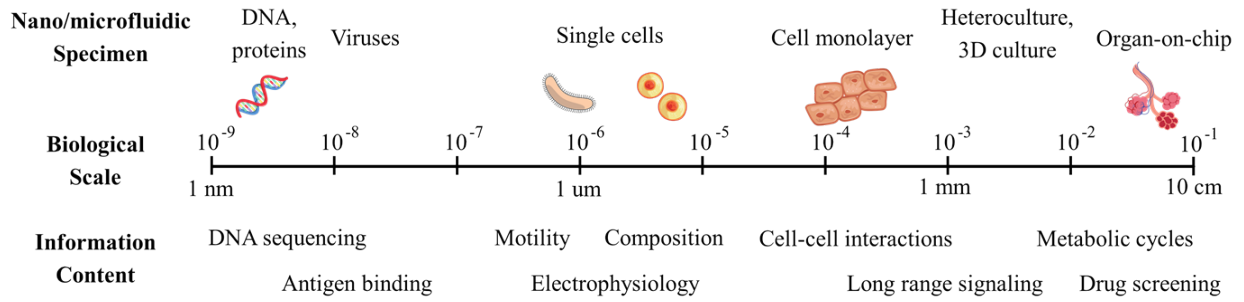

Figure 1.1: The scale of biological specimens for microfluidic study. Microfluidic devices can be scaled to match the appropriate size to study specific biological interactions and characteristics.

cell-to-cell interactions. A cell monolayer is the smallest unit block suitable for studying intercellular signaling at the most fundamental level. Because these microfluidic devices can be designed such that their scale matches the cell networks under examination, they present an unparalleled opportunity to study intercellular communication.

1.3 Intercellular Communication in Developmental Biology

Though it has long been known that neural cells send and receive electrical signals, the importance of non-neural electrical communication is recently being realized (Levin, 2021a; Bates, 2015; Oviedo, Morokuma, et al., 2010). Non-neural cells are known to communicate through gap junctions as part of embryogenesis, regeneration, and cancer suppression (Mathews and Levin, 2016; Nicolas Palacios-Prado and Bukauskas, 2009). While ion channels and ion pumps allow a cell to exchange ions with the extracellular fluid, gap junctions are cytoplasmic couplings between cells that permit the exchange of ions and small signaling molecules between neighboring cells. Gap junctions themselves are formed (in vertebrates) by clusters of highly specific hemichannel proteins called connexins. Some gap junctions are additionally capable of unidirectional transfer, causing diode-like rectifying pathways (Nicolás Palacios-Prado, Huetteroth, and Pereda, 2014). Gap junction transport can be regulated through a variety of means including chemical blockers, phosphorylation, voltage, and pH (Mathews and Levin, 2016). Since gap junctions offer the most direct means of intercellular communication and signaling molecule exchange, they are of particular importance in determining cell network dynamics.

A preliminary indicator of the importance of gap junctions to developmental processes was the observation that gap junctions help to form isopotential domains during embryogenesis of many organisms, which eventually develop into specific organs or features (Mathews and Levin, 2016). Electrical potential compartmentalization in embryos suggests that bioelectricity, and gap junction connectivity in particular, is extremely important in guiding the morphology of stems cells and pluripotent cells in general. For instance, the expression of gap junction channels is necessary to

mediate the calcium signaling that leads to the differentiation of dental pulp stem cells (S. Li et al., 2015). Similarly, gap junction expression has proved essential to the differentiation of lens cells in chicks (Gu et al., 2003), the establishment of left-right axis (Oviedo and Levin, 2007), and the patterning of the limb (Allen, Tickle, and Warner, 1990).

Cancer, in a sense, is the departure of developing cells from their anatomically intended morphology (Rubin, 1985; Levin, 2021b). Specifically, metastatic cell behavior has been modeled as a physiological (and informational) isolation of cells from a larger network that helps coordinate morphogenesis and suppress ancient unicellular behaviors (Moore, Walker, and Levin, 2017; Levin, 2019). Thus, gap junctions have been central to several emergent cancer studies. Tumor tissue itself is known to express fewer gap junctions compared to normal tissue, and many studies have observed a correlation between lowered gap junction connectivity and tumorgenesis (Aasen et al., 2016; Borek, Higashino, and Loewenstein, 1969; McEvoy et al., 2020; Mathews and Levin, 2016). In addition, cancer cells tend to maintain a depolarized membrane potential and this depolarization seems to be necessary for tumor proliferation (Yang and Brackenbury, 2013).

Gap junctional connectivity is important not only to normal and abnormal growth, but also to regrowth or regeneration. Planarian flatworms show remarkable capabilities to regenerate completely from body fragments. Studies on this model animal have shown that blocking gap junctional communication during regeneration results in permanent respecification of their natural target morphology, including the formation of double-headed planarian lines and even regeneration of heads of different planarian species (Emmons-Bell et al., 2015; Oviedo, Morokuma, et al., 2010).

As more fundamental knowledge is gained into the specific mechanisms through which intercellular communication affects cell development and end morphology, biomedical engineering solutions will be enabled for artificial tissue and organ growth, as well as the treatment of abnormal growth, including birth defects, degenerative diseases, aging, and cancer. Thus, we seek to develop a new lab-on-chip microfluidic device that would enable the experimenter to measure and modulate gap junction connectivity.

1.4 Gap Junction Measurement Technologies

An electrical measurement of gap junction connectivity is desired to enable real-time monitoring and repeatable assays. Electrical interrogation of biological cells is a natural approach because all cells manipulate their electrical potential through the regulation of ionic species and bioelectricity plays a key role in cell communication and development. As long as induced electrical currents are sufficiently low (typically less than 1 μA), electrical measurement is non-destructive and fundamentally non-invasive and repeatable (Meng, Rouabhia, and Z. Zhang, 2021). Electrical measurement systems can provide near instantaneous quantitative results which are ideal as feedback parameters

into a closed loop system. Further, electrical impedance measurements are an ideal starting point for microfluidic devices examining intercellular connectivity as they can be directly compared to trusted benchtop electrophysiological recordings.

Gap junction connectivity can be measured electrically through dual whole-cell patch clamping (Adermark and Lovinger, 2008; Rash et al., 2013). A portion of the cell membrane is captured tightly (often punctured) and sealed by vacuum in a glass micropipette. The tight seal allows stable electrical recording from the interior of the cell. The risk of cell damage and the complexity of operation in further increased in the case of measuring intercellular connectivity, as a second patch clamp must be performed on a neighboring cell. This technique produces high fidelity measurements of the conductance between isolated cell pairs (Veenstra, 2001). However, the process is expensive, invasive (compromising the cell membrane to introduce patch pipettes), and technically difficult to perform (Veenstra, 2016). Further, dual cell patch clamping measurements characterize only two cells, failing to capture larger network dynamics. While analysis of capacitive transients in single cell patch clamping has been shown to reflect a cell's connectivity to its network (Roos, Zoelen, and Theuvenet, 1996; E. G. A. Harks et al., 2003), throughput for patch clamping is extremely low, sampling only a few individual cells while requiring expensive equipment and specialized labor.

The diffusion of membrane impermeable fluorescent dyes can also be optically traced to measure gap junction connectivity (Abbaci et al., 2008). Dye can be introduced to a tissue sample through invasive means including microinjection (Meda, 2000) and scrape loading (Babica, Sovadinová, and Upham, 2016). Alternately, dye can be pre-loaded into a cell population and then co-cultured with non-dyed cells (Warawdekar, 2019). New microfluidic approaches have also sought to use laminar flow to spatially confine membrane permeable dye and to monitor its intercellular diffusion beyond the laminar boundary (Cédric Bathany et al., 2011; S. Chen and L. P. Lee, 2010). Dye methods reliably test for the formation of gap junctions, but struggle to provide real-time quantitative measurement of intercellular connectivity, as optical analysis is computationally intensive. Further, many dye techniques lack repeatability due to the difficulty of dye washout.

1.5 Considerations for Electrical Measurement of Gap Junction Connectivity

1.5.1 Electrode interactions

A working electrical equivalent model is necessary to effectively design microfluidic devices to measure complex electrical impedance. Such a model should include characterization of both the electrode-fluid interface and a model of the biological sample under test.

The most basic model of the electrode-electrolyte interface, known as the Randles model (Figure 1.2a), consists of a charge transfer resistance (R_{ct}) in parallel with the capacitance that arises

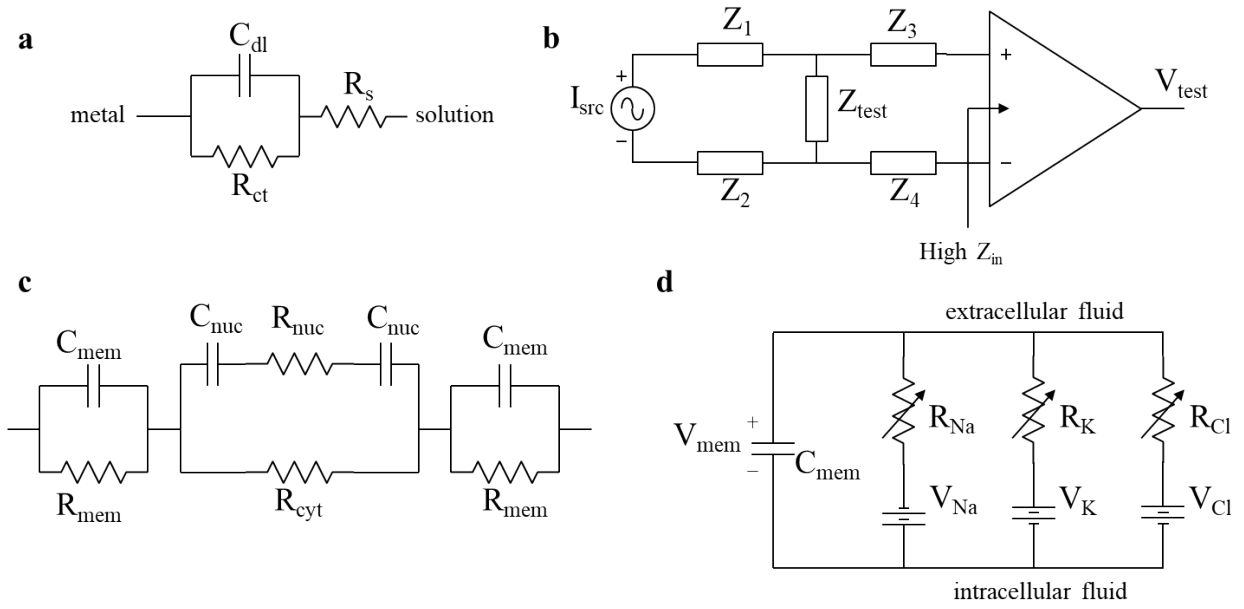

Figure 1.2: Electrical models pertinent to impedance measurements on biological cells. (**a**) The Randles model describes physics at the electrode interface. (**b**) The impact of electrode impedances Z1-Z4 can be minimized through a four point measurement. Though a current source and voltage amplifier are displayed, current sensing and a voltage source also result in a signal proportional to Z_{test}. Cell impedance can be described by (**c**) the two shell model , but ion transport through the membrane is better described at dynamic equilibrium by (**d**) the Hogkin and Huxley model .

from the electric double layer formed by mobile charge carriers at the boundary. The interface components are in series with a spreading resistance through the electrolyte solution, which is a function only of the electrode geometry and the solution's electrical resistivity.

R_{ct} models redox reactions that can occur between the metal and solution under thermodynamically and kinetically favorable conditions. The resulting faradaic current is often considered undesirable for biological applications because it can introduce harmful byproducts (Simon et al., 2016). R_{ct} is a function of the electrode metal, electrolyte ionic species, surface area, and temperature and can be quite large (hundreds of kiloOhms) for noble metals such as golds and platinum (Franks et al., 2005; Pradhan, Mitra, and Das, 2012).

The second important element of the Randles model is the electric double layer capacitance (C_{dl}). Charge induced on the surface of the metal electrode causes mobile ions in the solution to migrate toward the interface forming a layer of opposite charge near the surface (charge in solution actually distributed – see the more precise Chapman-Guoy-Stern model). C_{dl} is proportional to surface area and is dependent on applied voltage, ion concentration and the permittivity of the solution. C_{dl} can be quite significant as well, measuring roughly 10 $\mu F/cm^2$ for the sputtered gold electrodes used in

this work.

A few important device design considerations follow immediately from the first order electrode model. First, at frequencies near DC, the charge transfer resistance can contribute significant offset impedance to a direct measurement through fluid. Further, R_{ct} values are very difficult to match precisely from electrode to electrode. The effects of R_{ct} on the measurement can be minimized by taking a four-point measurement or through careful design of control experiments. At high frequencies, C_{dl} shorts out the charge transfer resistance and the sample under test can be measured more directly. However, sufficiently high frequencies often lie outside of the biologically relevant frequency band for sensing the aqueous transport of ionic species. Thus, alternate means must be devised to either mitigate or compensate for electrode impedance. In practice, the interface impedance is often modeled at a constant phase element (i.e. $Z_{dl} = 1/(j\omega C_{dl})^n$), though the order ($n$) usually ends up being near unity.

The four-point measurement technique (Figure 1.2b) is an effective method to reduce the effects of electrode polarization for impedance spectroscopy systems (Koklu, Sabuncu, and Beskok, 2016; Mazzeo and Flewitt, 2007). In theory, so long as the input impedance at the measurement electrodes is very large, the sample impedance can be directly recovered regardless of electrode impedances. However, Schwan (1966) warns that due to non-uniformity in the electrode surface, the sensing electrode can drift to a higher potential, causing measurement error. Additionally, parasitic capacitance on the sensing electrodes from interconnect and the amplifier's input capacitance can cause significant phase error (Mazzeo, 2009).

1.5.2 Modeling biological cells

Cells typically present a very large barrier to electrical access and thus are often modeled as pure insulators. For applications where detection of cells is based solely on their obstruction of a microchannel or the surface area of an electrode, cells are often modeled simply as the absence of conductive media(Yufera et al., 2011; Huang et al., 2003). Alternately, cells can be described as spherical membranes binding aqueous dielectric fluid. In this model, cells are presented as a capacitance or two capacitors in series at either side of a resistive element, representing enclosed cytoplasm. The two shell model, as shown in Figure 1.2c goes one step further in modeling the nucleus of (eukaryotic) cells as an additional membrane(Ellappan and Sundararajan, 2005). These models are reasonable for dielectric spectroscopy of simple suspended cells, but do not account for the active transmembrane ion exchange processes occurring in living cells.

Ion transport through the cell membrane was prominently modeled by Hogkin and Huxley as shown in Figure 1.2d (Hodgkin and Huxley, 1952). In the so called Hogkin and Huxley model, the lipid bilayer of the cell membrane is again modeled by a capacitance, Cmem. Sodium, potassium, and

Table 1.1: Reported values for resistive coupling between adjacent cells.

Source	Cell Line	Method	Cell-cell R_j Estimate
Beyer et al. (2000)	NRK-49F	Dual whole cell patch clamp	10 GΩ (Cx40)
Harris (2001)	various	Review, patch clamp	13 kΩ – 2 GΩ (25 plaques/cell, 1000 channels/plaque)
Valiunas et al. (2005)	NRK-49F	Dual whole cell patch clamp	100 GΩ (high end estimate)
E. G. A. Harks et al. (2003)	NRK-49F, HEK	Single patch clamp	6.6 MΩ (coupled), 2.4 GΩ (2-APB blocked)
Veenstra (2001)	N2A	Dual whole cell patch clamp	50 MΩ – 50 GΩ
Cedric Bathany et al. (2012)	NRK-49F	Estimation based on connexin studies	91 kΩ – 1.3 MΩ (25 plaques/cell, 1000 channels/plaque
Veenstra (2016)	N2A, HeLa	Dual whole cell patch clamp	50 GΩ (poorly coupled, fewer than 6 channels)

chlorine pumps are represented by voltage sources in parallel with time varying species-specific resistances. Though the Hogkin and Huxley model and its variants describe transmembrane transport well within a single cell, they do not describe the interactions between coupled cells. These types of models also do not generally hold much predictive value in terms of how a cell network will respond to changes in the extracellular conditions, as the variable transmembrane resistance values need to be measured and verified experimentally.

Adjacent cells can form gap junction channels that allow the flow of ions and other signaling molecules between cells. Most gap junctions are passive, and their only selection mechanism is by size. These passive junctions can be modelled as resistive connections between cells. Table 1.1 shows the reported values for resistive coupling span a significant range. Additionally, some cell lines may contain gated gap junctions that are voltage dependent (transistor) or unidirectional (diode), but these channels rarely dominate total charge transfer.

As a first order model, a cell monolayer can be considered as a repeating lattice where nodes represent cells and the edges are resistive gap junctions (Figure 1.3b). Resistance between two points in an infinite resistive lattice are explored in (Atkinson and Steenwijk, 1999). The results, plotted in Figure 6c, show both the importance of growing a densely connected confluent cell layer and that expected network impedance is not likely to exceed the cell-cell gap junction impedance by more than an order of magnitude.

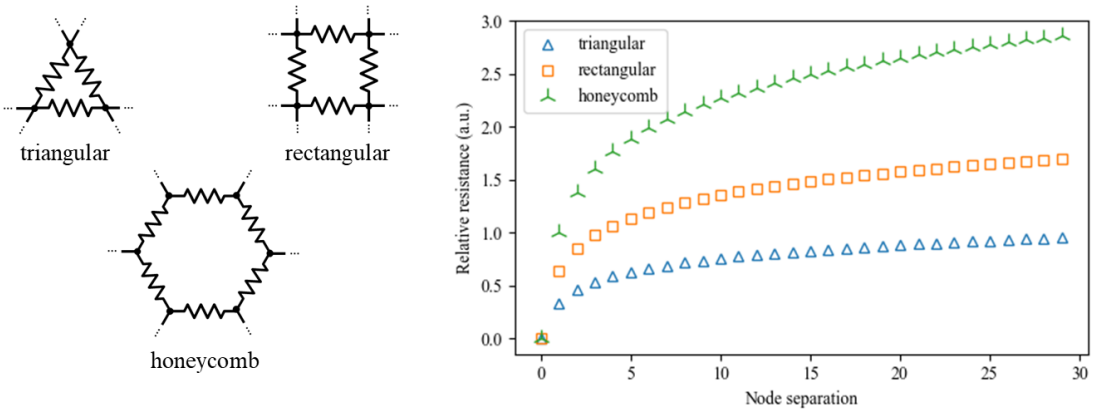

Figure 1.3: Gap junction connections in a cell monolayer modeled as a resistive lattice. Simulations show that for triangular, rectangular, and honeycomb infinite resistive lattices, the net impedance between any two points does not exceed the unit resistance by more than an order of magnitude.

1.5.3 Complex impedance theory

Often only simple resistance is considered when attempting to electrically measure gap junction connectivity; however, frequency and phase content provide a wealth of additional information that could be used to fully characterize gap junction activity. If gap junctions are blocked, charged ions become isolated in single cell, while open junctions allow ions to traverse a cell network freely. This charge isolation should result in capacitive differences and the effect has already been observed using patch clamping at the benchtop level (Roos, Zoelen, and Theuvenet, 1996).

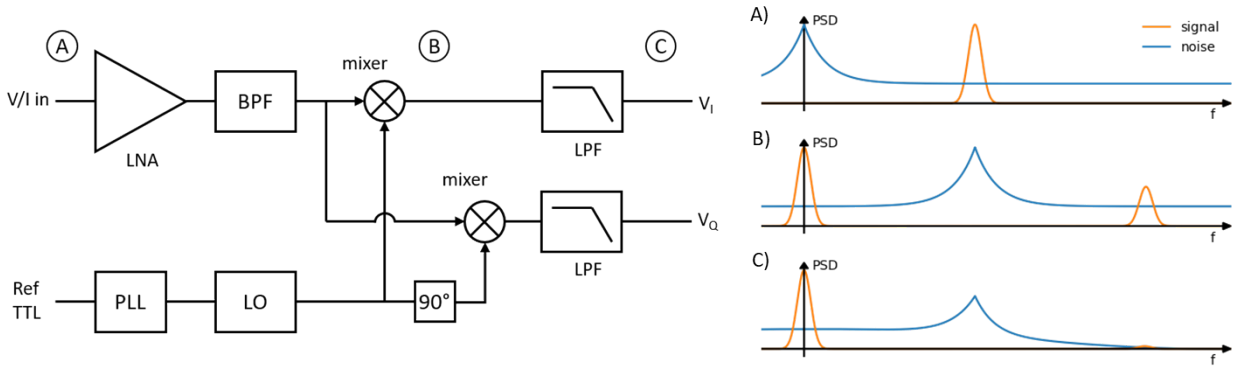

Figure 1.4: Lock-in architecture and noise bandwidth reduction scheme. The power spectral density of a signal in the presence of noise and interference are plotted on the right for three points in the signal path. The input signal is amplified by a low noise amplifier (LNA) and bandpass filtered (BPF) before being multiplied in the mixer by the synchronous signal generated by the local oscillator (LO) and phase locked loop (PLL). The measured value can then be read as the result of a low-pass filter. The quadrature or out of phase component is generated by mixing with a signal 90 degrees out of phase with the reference.

The lock-in architecture is a very popular means of recovering a signal in the presence of high noise through use of a quadrature modulator. As diagrammed in Figure 1.4, a sinusoidal source is applied to the impedance under test. The resulting current or voltage is then recovered by a low noise amplifier and in some designs passes through a power line notch filter or a bandpass filter at the synchronous frequency before reaching the synchronous detector. The detector multiplies the observed signal by a sine and cosine at the reference frequency, converting the frequency domain signal down to 0 Hz, where the in phase and quadrature components can be recovered by a low-pass filter.

The source of the lock-in architecture's popularity is its simplicity of design and favorable noise performance. The lock-in detector is extremely effective because it reduces the noise bandwidth to a very narrow portion of the frequency spectrum around the reference frequency. The reference frequency then should be selected in a portion of the spectrum with limited noise and interference. In this manner, lock-in detection is effective in avoiding 1/f noise at low frequencies as well as power line interference. The frequency spectra in Figure 1.4 illustrates this effect. The input signal is depicted in the presence of significant low frequency noise at the input to the detector (point A). Mixing with the coherent signal from the local oscillator (LO) shifts the signal to zero frequency and moves the noise to higher portion of the spectrum (point B), where it can be effectively filtered out of the final signal (point C).

1.6 Vision for a Closed-loop Training Platform

We have established a need to read intercellular communication and have proposed a potential means of doing so by leveraging microfluidic and electrical impedance spectroscopy technologies Thus, we aim to design a non-invasive lab-on-chip microfluidic platform to electrically interrogate gap junction connectivity. Such a platform, providing repeatable quantitative measurement of gap junction connectivity in networks, could elucidate fundamental processes in developmental and regenerative biology. However, even greater potential lies in an opportunity to not only read but write intercellular communication.

By additionally integrating a feedback signal (be it electrical, optical, thermal, or other), gap junctional networks may be able to be trained in a manner similar to firing in neural networks (Shahaf and Marom, 2001; Bakkum, Chao, and Potter, 2008). In this way, a closed-loop system could be developed to write intercellular connectivity. Figure 1.5a envisions such a system for the paramount case of pluripotent cells. Given the proven importance on gap junction connectivity in the developmental biology, it is not unreasonable to assume that a closed-loop system could advance towards exogenous control of the fates of differentiating cells. Such an achievement would have significant impact on synthetic morphology, tissue engineering, and research into cancers and

other developmental disorders.

To enable this vision, the ideal system should provide real-time quantitative measurement of gap junction resistance. Additionally, the platform should allow repeatable assays and be suitable for long term operation. We envision a custom integrated circuit (Figure 1.5b) could be designed to support a closed-loop microfluidic training platform for intercellular connectivity. Such a platform could have a major impact on how we develop, grow, and heal.

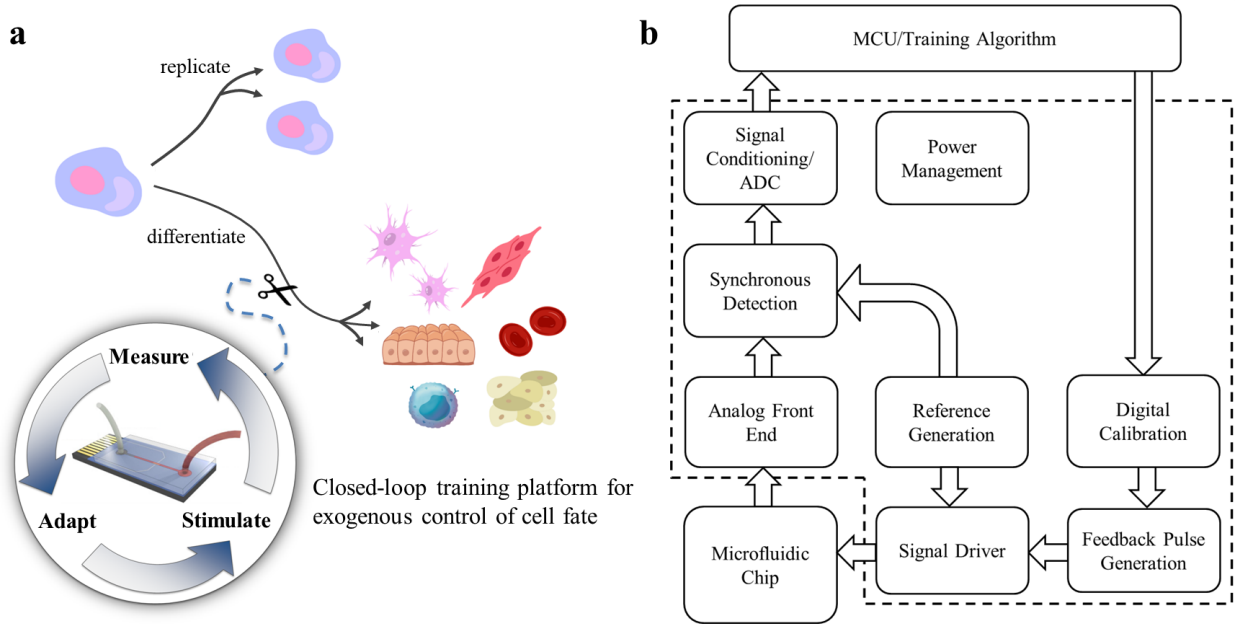

Figure 1.5: (**a**) Vision for a closed-loop microfluidic training platform for exogenous control of cell differentiation. (**b**) Block diagram of the an integrated circuit facilitation closed-loop gap junction measurement and training.

1.7 Organization

This thesis is organized into 6 distinct chapters. This chapter provides the necessary background and motivation to appreciate all following chapters. Chapter 2 details the fabrication approach used to create microfluidic devices studied in Chapters 4-6. The chapter introduces a novel method for selective bonding of PDMS valves onto glass. The process is fully optimized and thoroughly characterized. Chapter 3 presents the “lab-on-scope" platform that facilitates all microfluidic experiments described thereafter. The platform integrates all of the peripherals necessary for a microfluidic lab onto a microscope mounted printed circuit board. The chapter concludes by demonstrating the platform’s ability to facilitate monolayer cell culture in a microfluidic environment. Chapter 4 introduces microfluidic devices based on the principle of laminar flow which aim to study gap junction connectivity. Chapter 5 details 3 device designs based on normally closed elastomeric

valves as a means of electrical isolation of gap junction connectivity. Additionally, a material-based memory phenomenon is discovered in these devices which serves to complicate gap junction measurement. Finally, Chapter 6 provides concluding remarks, comparing all of the proposed devices in Chapters 4 and 5 and suggesting improvements for future work.

Chapter 2

FABRICATION OF MICROFLUIDIC DEVICES FOR CELL CULTURE AND ELECTRICAL IMPEDANCE MEASUREMENT

2.1 Introduction

Microfluidic devices have become indispensable research and diagnostic tools across a wide variety of applications. In research settings especially, the elastomer polydimethylsiloxane (PDMS) is a very popular material for microfluidic fabrication and rapid prototype development. PDMS has favorable mechanical and optical properties for many applications, and the fabrication process used to produce such devices is both low temperature and low cost. This "soft lithography" approach uses standard lithographic techniques to produce master molds from which many PDMS devices can be replicated by casting. A crucial quality of PDMS is the relative ease with which devices can then be bonded to a substrate thereby sealing off microfluidic channels.

PDMS can be permanently bonded to many substrates including glass and PDMS itself. Irreversible covalent bonding occurs when sufficient energy is applied to the PDMS to activate silanol groups on the surface. Often this energy is applied in the form of exposure to an air or oxygen plasma created in the proximity of a high frequency electrode, though surface modification through chemical treatment is also possible. Under the right conditions, these surface chains can covalently bond with other silanol groups on the substrate, releasing water. The surface activation also results in reduced hydrophobicity (Borók, Laboda, and Bonyár, 2021; Bhattacharya et al., 2005). Alternate PDMS bonding methods include partial curing, cross-linker diffusion, and chemical adhesive techniques in the case of PDMS-PDMS bonding (Eddings, Johnson, and Gale, 2008) and UV/ozone treatment (Yousuff et al., 2017) for PDMS-glass bonding. However, no bonding approach inherently enables selective bonding with microscale resolution.

Since their introduction, elastomeric valves have enabled a new generation of lab-on-a-chip microfluidic devices. The Quake group first presented pneumatically actuated positive pressure microfluidic valves for PDMS devices that are normally open, demonstrating that they could be used for effective fluid control and peristaltic pumping (Unger et al., 2000). Many other microvalve designs have since been proposed that rely on positive and negative pressure (Au et al., 2011), including doormat (N. Li, Hsu, and Folch, 2005), curtain (Mohan et al., 2011; Irimia and Toner, 2006), and plunger styles (Baek et al., 2005). Each valve type has particular strengths and weaknesses in terms of leakage, actuation pressure, and fabrication complexity and should be selected to fit the particular application. Normally closed vacuum actuated valves are particularly appealing

for portable applications. The primary drawbacks of such valves are that some positive pressure may be required to maintain the valve seal under heavy fluid pressure, and that their fabrication technique is more complicated than their normally open counterparts as it requires selective PDMS bonding.

Previous approaches to normally closed valve fabrication have required vacuum to be applied to pull the surface in the valve area away from the substrate and prevent bonding (Mohan et al., 2011). These approaches do not scale well to lab-on-chip devices with many valves, as managing vacuum lines can be cumbersome and their weight can pull and stretch the PDMS device during bonding. Further, thermal expansion of trapped gasses in the bonding process can make vacuum levels fluctuate problematically. Proposed solutions include the use of passivation layers (Estlack and Jungkyu Kim, 2022), soluble masks (Baek et al., 2005), and metal masking (Irimia and Toner, 2006). These approaches have shortcomings in terms of scalability and added fabrication complexity. Takayama(Mosadegh et al., 2011) presented a compelling approach based on an oligomer stamping intended method for PDMS-PDMS devices. The technique requires no additional chemicals or tools, rather a PMDS stamp is applied to the plasma treated bonding surface. Oligomer chains on the inactivated PDMS stamp remove the activated surface groups on the device to be bonded, leading to highly localized regions of reduced bond strength.

Takayama's approach allows the scalable fabrication of high density valved devices suitable for lab-on-chip applications. Here, we further investigate this technique, characterizing the oligomer stamping process quantitatively over a large parameter space through contact angle and blister burst testing for the first time. Further, we expand the previous approach to seek treatment and stamping conditions optimal for use with a rigid glass substrate. Such substrates easily facilitate the integration of electrodes into devices, which is essential for applications such as electrophoresis, electrical impedance tomography, and impedance flow cytometry. Additionally, glass substrates are often ideal or necessary for optical imaging. For biomicrofluidic devices, cell culture protocols are often optimized for use on rigid substrates. Integrated electrodes enable characterization of valve performance over a broad frequency range as well as leakage current monitoring. Valves fabricated using the optimized oligomer stamping technique are demonstrated to form strong seals withstanding fluid pressures greater than 200 mbar without any leakage current.

In particular, normally closed valves are of interested for biomicrofluidics as they offer the tightest seal to the substrate at the lowest activation pressures. This quality is important for complete isolation of chemical reagents, but it is also ideal for cell culture applications that require spatial isolation or compartmentalization of a continuous culture. To this end, we demonstrate a proof-of-concept device integrating 24 elastomeric valves to former a 4×4 array of interconnected cell culture chambers. We demonstrate that the process is suitable for microfluidic cell culture, fluid control,

and electrical isolation and measurement across a wide range of biomicrofluidic applications.

2.2 Materials and Methods

A basic description of the microfabrication process to create sealed PDMS devices with integrated elastomeric valves from (Dungan et al., 2023) follows below. For detailed recipes and instructions specific to the Tufts Micro/Nanofab, see Appendix A.

2.2.1 Fabrication Techniques

All device fabrication was performed in the Tufts Micro/Nanofab. Devices were constructed from polymethylsiloxane (PDMS, Dow Chemical Sylgard 184) at a 10:1 ratio of base to curing agent. All PDMS was degassed for approximately 30 minutes prior to molding and was fully cured in an oven at 60°C for approximately 1.5 hours. All PDMS surfaces intended for bonding experiments (including those without channels) were molded against silicon wafers to ensure maximum surface flatness and uniformity. Master molds were fabricated using standard lithography techniques using SU8-3050 (Microchem). All 65 µm thickness molds were spincoated on glass substrates at 2200 rpm for 30 s, soft baked at 95°C for greater than 15 minutes, and exposed to UV radiation (20 mW/cm^2 at I-line) for 15 s (or 10 s for silicon substrates), before post-exposure baking (4 minutes at 95°C) and agitated development for more than 10 minutes. 100 µm stamp molds were spun at 1000 rpm for 60 s, soft baked for greater than 30 minutes, UV exposed for 18s, post-exposure baked for 5 minutes, and developed for more than 15 minutes in agitated SU8 developer. To ensure easy mold release, masters were silanized by exposure to tridecafluoro-1,1,2,2-tetrahydrooctyl trichlorosilane (Gelest Inc.) for one hour in a desiccator. Glass substrates were cleaned in a 3:1 solution of sulfuric acid and hydrogen peroxide for 10 minutes prior to being thoroughly rinsed in deionized water and dried with compressed dry air.

Oxygen plasma treatments were performed using a reactive ion etching tool (Nordson March CS-1701). The tool allows for precise experimental control of treatment power and exposure time. All experiments used the tool's independent pressure control mode to regulate the oxygen gas pressure in the chamber to 500 mT during treatment.

2.2.2 Microvalve Fabrication

Negative pressure elastomeric valves with active areas of 400 x 500 µm (Figure 2.2b) were fabricated using a PDMS molding process and standard photolithographic techniques. SU8 was deposited to a depth of 65 µm for both the flow and pneumatic control layer master molds(Figure 2.1-2,3). The valve stamping mold was fabricated to with a feature depth of roughly 100 µm to accommodate levelling errors in alignment (Figure 2.1-1). The pneumatic layer was cast molded in an acrylic/glass fixture (Figure 2.1-5c), which ensured a uniform thickness of 5 mm and sufficient flatness of the

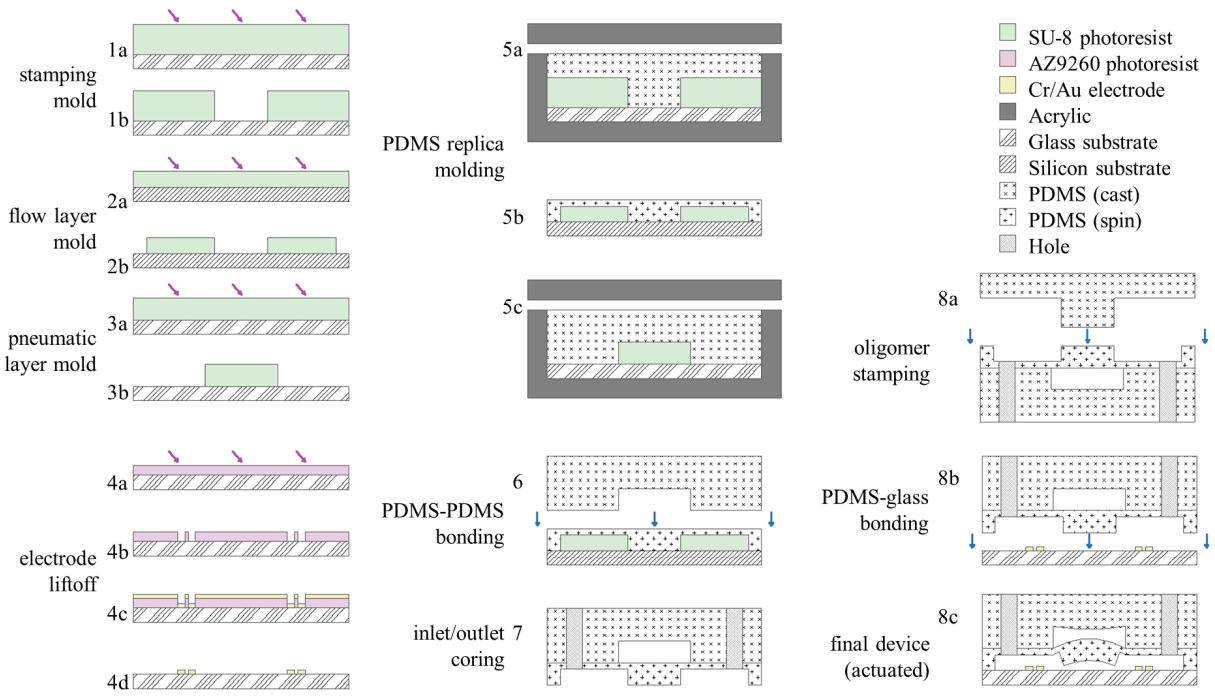

Figure 2.1: Device fabrication. The (**1a-b**) stamp mold, (**2a-b**) flow layer mold, and (**3a-b**) pneumatic layer mold are fabricated in standard photolithography using SU8. (**4a-d**) Electrodes are patterned on a glass substrate by liftoff photolithography and Cr/Au sputter deposition. (**5a, 5c**) PDMS is cast molded for the stamp and pneumatic layers and (**5b**) spincoated to form a thin membrane on the flow layer. (**6**) Flow and pneumatic layers are aligned and bonded by oxygen plasma treatment. (**7-8c**) The final device is plasma treated, stamped, and aligned and bonded over the electrodes.

top surface for subsequent alignment steps. A relatively thick device depth of 5mm was found to be favorable in handling the pneumatic layer with minimal stretching or warping. Special care is taken to avoid deforming the treated PDMS to avoid mechanical stress which can accelerate recovery of the surface treatment (Borók, Laboda, and Bonyár, 2021) and to improve alignment.

The flow layer mold was spin coated with uncross-linked PDMS at 2000 rpm for 60 s, forming thin (approximately 40 µm) membranes at the valve sites (Figure 2.1-5b). After curing, the cast pneumatic layer was released from the mold, while the flow layer remained on the wafer. Both layers were oxygen plasma treated simultaneously at 20 W for 30 s. A glass backing was applied to the pneumatic layer PDMS before the layers were quickly (less than 5 minutes) aligned and brought into light contact (Figure 2.1-6). The alignment rig (Figure 2.3a) was designed to quickly release the glass backing, so that the device could be transferred to a hotplate, completing the bonding with a 10 minute bake at 80°C. Once the bond was completed, the device was released from the wafer mold, trimmed to size, and cored with a 1.5 mm biopsy punch to create inlet ports (Figure 2.1-7).

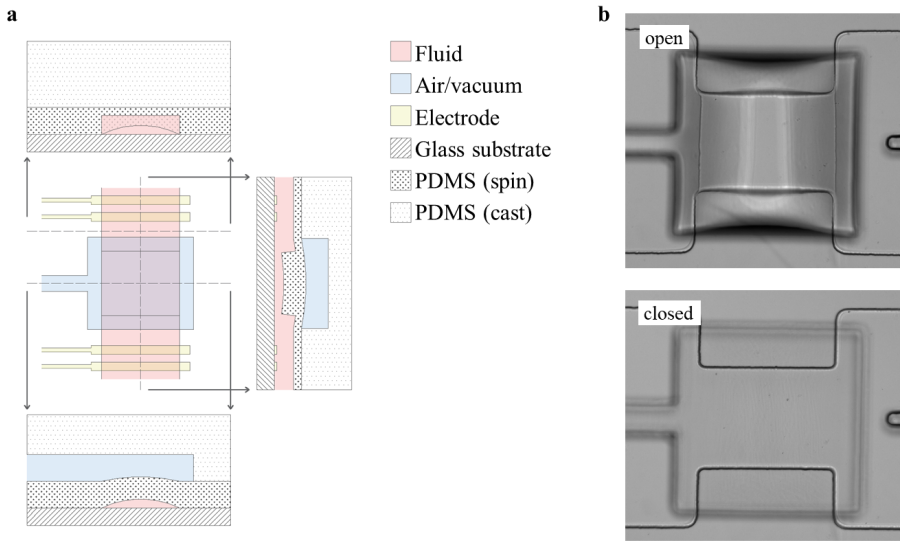

Figure 2.2: (**a**) Diagram of the valve construction showing three cross-sections of the valve operation shown in the open/vacuum state and (**b**) brightfield microscopy images (10x) of a valve in the open and closed positions with rhodamine dye flowing in the channel.

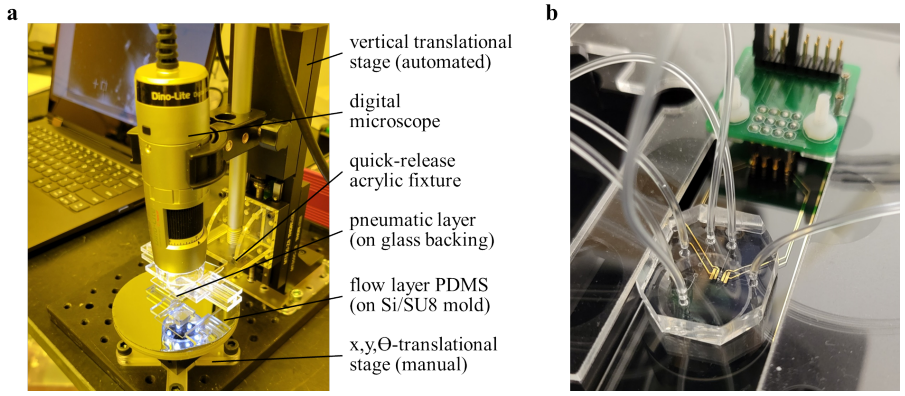

Figure 2.3: (**a**) Alignment rig for PDMS-PDMS bonding, oligomer stamping, and PDMS-glass bonding. (**b**) Completed microfluidic device featuring three normally closed valves mounted on an inverted microscope and electrically contacted.

Finally, the devices were treated, stamped, aligned, and bonded to glass slides patterned with gold electrodes (Figure 2.1-8). The untreated elastomeric stamp was mounted on a glass backing and pre-aligned with the device to be bonded to reduce the total plasma treatment recovery time. The PDMS device and glass substrate were simultaneously treated with oxygen plasma at 20 W for 30 s. Treated PDMS was brought into alignment with the valve stamp and contacted 3 times for 3 s using the automated mechanized stage. The device itself was then attached to a glass backing, aligned to fiducial markings on the glass substrate, and baked on a hotplate at 80°C for more than 10 minutes.

After cooling to room temperature, vacuum was pulled to release stamped areas, completing the valve fabrication.

The electrodes were fabricated on glass microscope slide substrates using a standard liftoff process (Figure 2.1-4) The electrodes were patterned lithographically using AZ9260 photoresist (AZ Electronic Materials) at a thickness of 6.5 µm. An adhesion layer was formed by first sputtering Chromium to a depth of 15 nm before further sputtering of gold electrodes to a depth of 210 nm. Liftoff was performed in heated Microposit Remover 1165 (Dow Chemical) overnight.

2.2.3 Valve Characterization

Four-point electrical impedance measurement was performed using a Keithley 6221 (Tektronix) alternating current source in conjunction with a digital lock-in amplifier (Stanford Research Systems SR830). The injected current amplitude was adjusted to match the dynamic range of the amplifier in each experiment, ranging from 10 nA to 1 µA. Complex impedance was recorded over a frequency spectra from 100 Hz to 10 kHz. Source frequency was swept in 30 logscaled values over a total of approximately 180 s, allowing settling time inversely proportional to source frequency and averaging 10 data points per frequency set point. Both instruments were controlled over serial interface and programmed via LabVIEW software (National Instruments). A four point measurement scheme serves to negate impact of lead and electrode contact resistances on the impedance measurement. Figure 2.3b shows the electrical interface to a microfluidic test device. Contact pads on the devices were probed using spring loaded contact pins (Millimax Series 825) which were routed to BNC connections through a printed circuit board. All electrical characterization of valve performance was conducted using Dulbecco's phosphate buffered saline solution (DPBS, Thermo Fischer Scientific) as the only media.

Dynamic pressure control for valve characterization was provided by an OB1 Mk3 regulator (Elveflow) with pressure stability and resolution below 0.1 mbar. This multichannel regulator was used to drive both fluid flow and positive pressure pneumatic actuation of the elastomeric valves. Vacuum pressure was generated by a portable 75 Torr vacuum pump (N810FTP, Ideal Vacuum Products). The flow of gas (biological atmosphere mixture, Airgas) was directed by solenoid valves controlled by a MUXW manifold (Elveflow). Coordination of all pressure controls systems was programmed in LabVIEW.

Microscopy images of the final normally closed valves were captured using an inverted fluorescence microscope (EVOS FL Auto 2) in phase contrast mode.

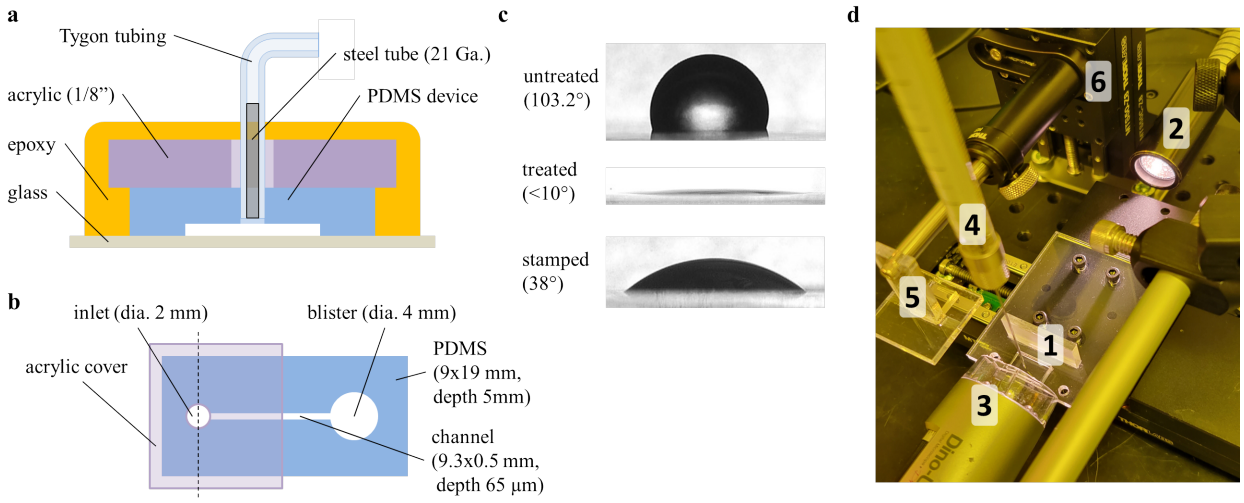

Figure 2.4: Bond strength estimation and measurement approaches. (**a**) A cross-section showing epoxy and acrylic scheme designed to provide structural support during high pressure burst testing, (**b**) the footprint for blister burst testing devices, and (**c**) representative images of a 20 W, 3 s oxygen plasma treatment on the contact angle of PDMS and recovery after oligomer stamping. The contact angle measurement and stamping rig (**d**) positions a sample (1) between dispersed incandescent background lighting (2) and a digital microscope (3). Liquid samples are dispensed from a mounted syringe (4). The automated translation stages (6) provide uniform and precise stamping (5).

2.3 Process Optimization

2.3.1 Contact Angle Measurement

Because the effectiveness of oxygen plasma surface treatment degrades over time (Borók, Laboda, and Bonyár, 2021), the contact angle measurement setup (Figure 2.4d) was located physically close to the plasma etching tool. Immediately following plasma treatment, 8 mm x 12 mm x 3 mm PDMS slabs were transferred to a fixture and secured for stamping or measurement. To ensure uniformity of stamping pressure and time, a programmable motorized translation stage (Thorlabs MTS50-Z8) was used to position and stamp the samples. Sessile drops of less than 2 µL of deionized water were deposited on the surface manually via a 23 gauge syringe (Trajan 000800). High resolution videos of the droplet placements were captured by a horizontally mounted digital microscope (Dino-Lite AF3113T) under approximately 20x magnification. Videos were trimmed to capture only the frames where the droplet was determined to be dynamically spreading, thus capturing only the advancing contact angle and more accurately reflecting the surface energy after treatment (Kwok and Neumann, 1999; Yuan and T. R. Lee, 2013). A subpixel edge detection algorithm was used to fit the droplet edge to a 2rd order polynomial and subsequently extract left and right contact angles for each frame of the trimmed video (Gorcum, 2023). Reported measurements reflect the average extracted angle over the valid frames of each droplet spreading. For untreated PDMS, the spreading

contact angle for deionized water was found to be 108.3°(versus 103.2°for static measurement).

Contact angle measurements serve as useful proxy for eventual bond strength. Plasma treatment of the surface renders it hydrophilic, so lower deionized water contact angle correlates with more effective surface treatment. Likewise, contact angle is inversely proportional to bond strength. However, for stamped samples, increased contact angle is ideal as it indicates reduced bonding in the valve area.

The effects of oxygen plasma treatment for bonding on non-stamped PDMS have been previously investigated (Bhattacharya et al., 2005). It was shown that contact angle reaches a minimum near a plasma treatment power of 20 W over a total exposure time of 30 s. However, the accuracy of telescopic contact angle goniometers in general decreases significantly at lower contact angles (Yuan and T. R. Lee, 2013), and our setup was unable to detect any statistically significant difference in angles resulting from the reasonable range of treatment conditions on unstamped samples. Droplets deposited on treated surfaces exhibited strong wetting, with near zero contact angles. These results were significantly lower than the previous study (Bhattacharya et al., 2005), though others have also assessed the contact angle under plasma treatment to be too near zero to report any other result (Mosadegh et al., 2011).

Figure 2.5 shows the results of oligomer stamping on the PDMS bond strength via treatment with oxygen plasma. The effectiveness of the stamping approach is clearly demonstrated with the contact angle recovering nearly 40° for most treatment conditions. As shown in Figure 2.5a, for 30 s treatments at 500 mT, the measured contact angle shows little dependence on the treatment power. While the average values generally show a constant contact angle recovery compared to the previously published unstamped results (i.e. a similar shape with a minimum near 20 W), the standard deviations of the measurements ($N \geq 3$ drops, 6 angles) are quite large. Though attempts have been made to control as many variables in the stamping process as possible (i.e. duration, pressure, angle) through automation, the effect on the surface treatment still seems to be quite variable. One difference that was observed between samples which is particularly difficult control is the manner in which the stamp and surface under test separate. For the large surfaces necessary for droplet spreading, the PDMS samples tended to peel apart in a wavefront which originated at inconsistent locations throughout these experiments. As a result, some areas of the samples may have experienced more mechanical perturbance as the final region of contact often sprang apart elastically.

Contact angle results examining the effect of plasma treatment time at source power of 20 W (Figure 2.5b) showed a much stronger dependency. Again, the minimum contact angle matches the previously reported minimum for unstamped PDMS near 30 s. This minimum is expected for unstamped PDMS as insufficient exposure produces fewer of the silanol chains needed for bonding

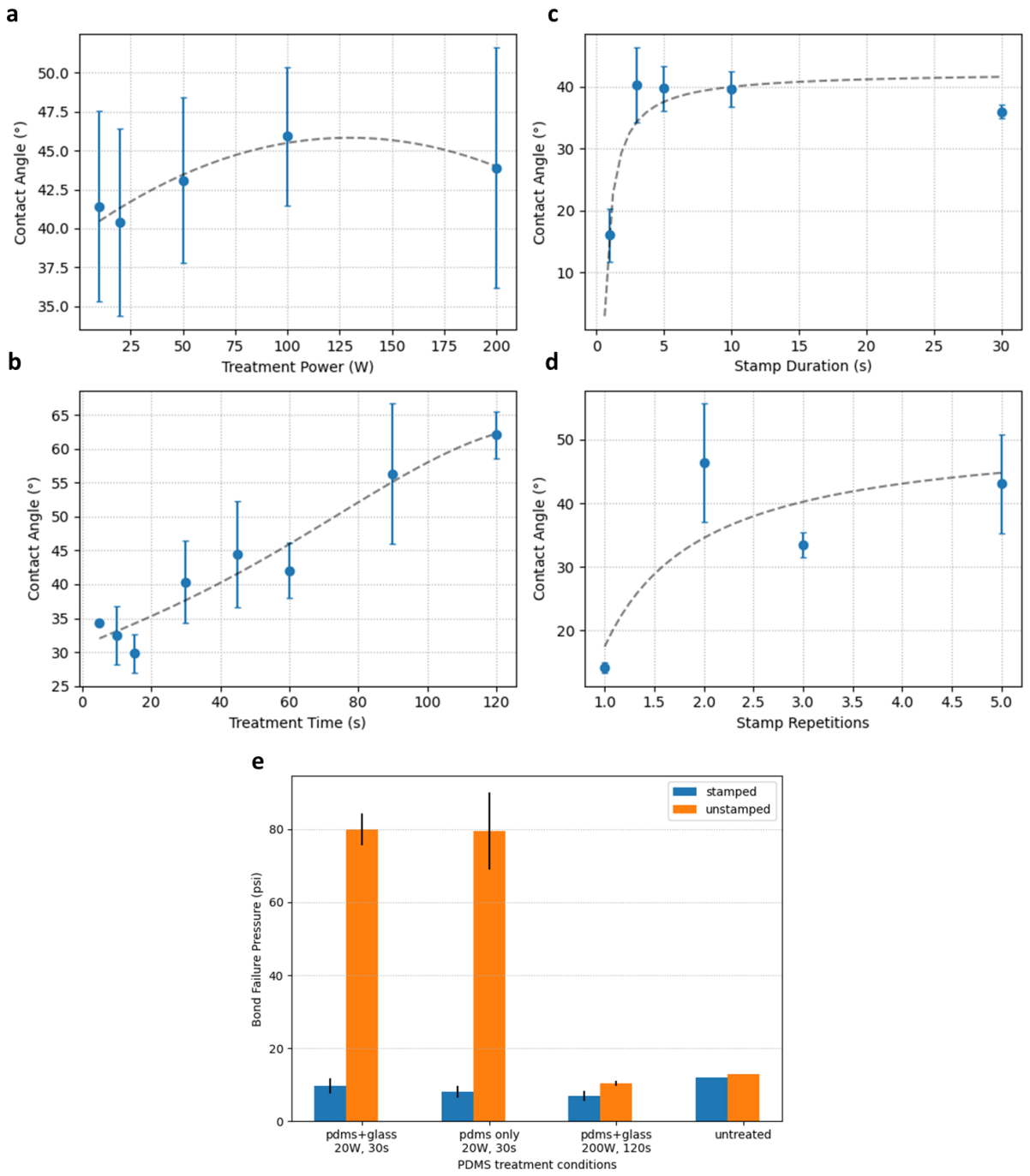

Figure 2.5: (**a-d**) Spreading contact angle measurement results for deionized water on PDMS samples treated by oxygen plasma and subsequently stamped with untreated PDMS. (**a**) Plasma treatment power was investigated at a fixed treatment time of 30 s and 3 s stamp duration and (**b**) treatment duration was swept at 20 W treatment power and 3 s stamp duration. Similarly, experiments investigating the (**c**) stamping duration and (**d**) number of stamping repetitions used treatment conditions of 20 W for 30 s exposure. (**e**) Additionally, blister bursting tests were conducted to evaluate the pressure at which bonded devices failed.

and increased overexposure results in the formation of a brittle silica-like layer (Owen and Smith, 1994; Jongsoo Kim, Chaudhury, and Owen, 2000). Oligomer stamping likely acts by removing or reorienting the activated surface groups and should not be able to reverse the formation of the silica layer. Rather, its action seems to be proportional to the concentration of activated surface groups, resulting in similar contact angle curve shapes.

The stamp contact duration was shown to play a significant part in the effectiveness of the oligomer stamping approach in selectively removing the PDMS surface treatment. Figure 2.5c shows that under test conditions of 20 W treatment time for 30 s, the optimal stamping time should exceed 1 s, but that contact lasting longer than 3 s offers no further benefit. While the mechanism of oligomer stamping does not seem to occur instantaneously, contact angle testing in Figure 2.5d shows that the action can be repeated. Making stamp contact with the treated surface multiple times further decreased contact angle in the contacted area. However, this approach showed diminishing returns after 3 repeated stamps. So long as alignment can be retained between successive contacts (requiring both the stamp and the device to be well fixed on their backings), multistamping is an effective way to increase the bond strength margin between the treated and stamped areas without compromising spatial resolution.

Oligomer stamping is clearly an effective means of spatial patterning of plasma surface treatment on PDMS. For optimal recovery of non-bonding areas, stamps should contact the surface for more than one second and contact should be repeated at least three times. Following these recommendations, sufficient removal of the surface treatment to prevent bonding can be achieved for any treatment conditions. Thus, for normally closed PDMS valves the surfaces should be treated to optimize the performance of the bonding surfaces, rather than ensure valve release.

2.3.2 Blister Testing

To directly measure PDMS-glass bond strength, a pressurized blister burst testing method was developed. PDMS devices (5 mm thickness) with simple closed channels were bonded to glass substrates. A girdle of acrylic plastic and epoxy (3M DP100) was constructed to secure the inlet tubing at pressures exceeding 100 psi (Figure 2.4a). The 4 mm diameter termination port on each device was not reinforced, causing inflation of nitrogen gas to exert force on the blister edge, eventually leading to breakdown in bond integrity at high pressures. Figure 2.4b indicates the complete device specifications, since burst testing is known to be dependent on the blister geometry (Lu, P.-T. Lin, and Pai, 2007). Video feeds from a digital microscope (Dino-Lite AF3113T) and a webcam directed at the pressure gauge were synchronized and analyzed to detect the critical pressure at which bond breakdown first occurred. For elastomer stamping experiments, the mechanized rig used for contact angle measurements (Figure 2.4d) was used to stamp the blister portion of the

sample, ensuring uniform stamping pressure and duration.

Blister bursting tests assessing bonding strength (Figure 2.5e) confirm contact angle results, showing an 8x decrease in bond strength between treated and stamped samples for the optimal bonding conditions of 20 W and 30 s. Interestingly, treatment of the glass substrate seems to have little effect on the final bond strength. This investigation found that plasma treating the substrate seems primarily to decrease the variability in the bonding process. This advantage could likely be attributed to removal of any possible surface contamination by plasma treatment, rather than to surface activation. Burst testing further demonstrated that the conditions at which the stamped contact angles were greatest (high treatment power and long exposure) are unsuitable for device bonding. In fact, both stamped and unstamped samples exposed to 200 W oxygen plasma for 2 minutes exhibited poorer substrate adhesion than untreated PDMS.

2.4 Process Validation and Characterization

2.4.1 Profilometry

Profilometry measurements confirm master mold fabrication accuracy. Figure 2.6 shows profilometry results for a trilaminar chip design fabricated in SU8-3050 on a silicon wafer. The Dektak XT profilometer provided surface measurements by dragging a fine stylus time across a sample. The stylus is affixed to a cantilever allowing the precise detection of vertical deflections. The minimum horizontal resolution for the measurements provided was 0.33 μm with a maximum vertical range of 524 μm. Such profilometry measurements are useful both to assess the accuracy of the lithography progress and to establish an estimate for margin of error calculations relying on constant film thickness.

In the measured region near the center of the wafer, the layer depth varied roughly linearly along the direction of flow in the molded device. The total measured deviation in height was approximately 3μm (3.9%) over a horizontal distance of approximately 8 mm. However, the input channels were matched in height to 0.24%. The average channel height measured (76.6 μm) was in good agreement with the target process height of 75 μm.

The profilometry results can also be used to assess the accuracy of the photolithography process in transferring the lateral mask geometries. However, the precision of the measurement is limited by the geometry of the profilometer stylus. The angled vertical transitions of the sample profiles in Figure 2.6b are an artifact of the sharpness of 2.0 μm profilometer stylus used in these measurements. Additionally, any error in performing the trace perfectly perpendicular to the channel wall results in a lengthening of the measurement. Even so, the average width error versus the mask dimensions was 5.0%. Given the positively skewed inaccuracy of measurements and the lower dependency of flow rates on channel width (as compared to height), this accuracy should be acceptable for nearly

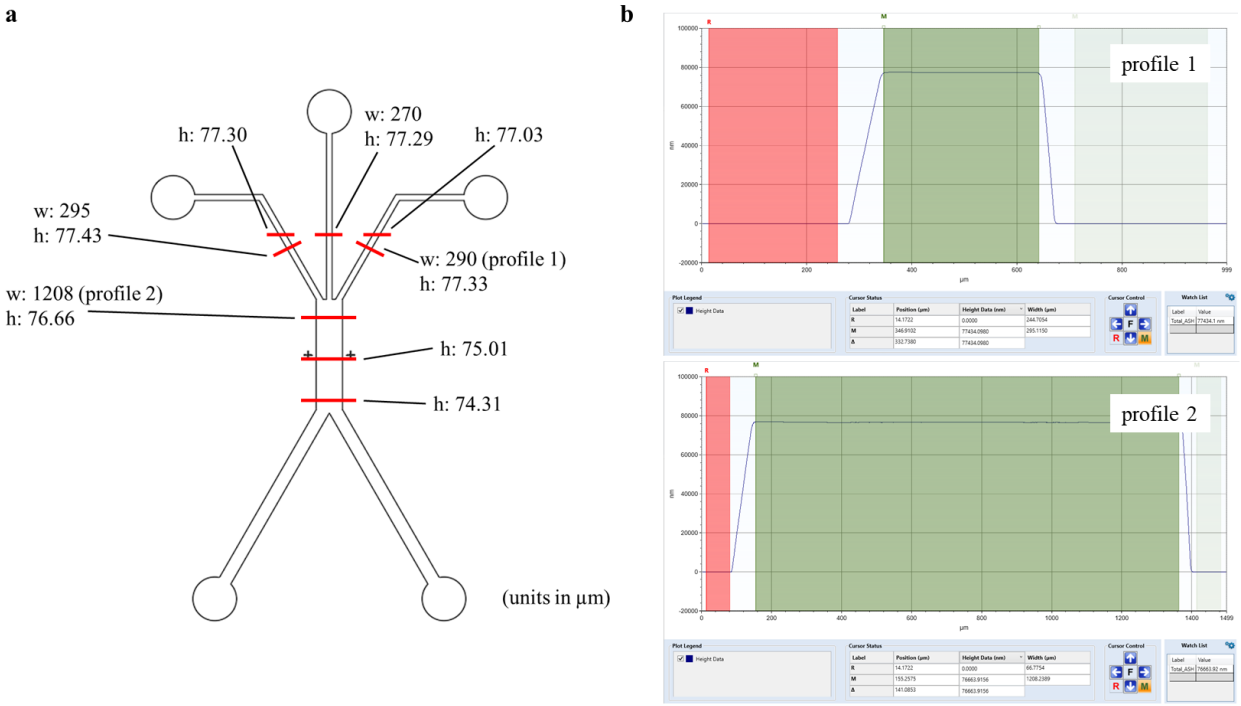

Figure 2.6: Profilometry measurements for a trilaminar chip fabricated in this process validate SU-8 lithography accuracy. (**a**) Profilometry scans were made across various points on the device (marked by red lines). (**b**) Profile readouts were used to extract height and width measurements.

all applications.

2.4.2 Bonding Edge Analysis

High resolution imaging was used to characterize the possible resolution of bonding edges using the oligomer stamping process in order to estimate scalability. Seven intended straight bond edges encompassing 2309 µm were imaged using phase contrast microscopy at 20× magnification (Figure 2.7). The edge location was extracted and the standard deviation from the average edge position was calculated for each image to estimate the uncertainty in edge position. Over all seven samples, the average standard deviation was 3.79 µm, suggesting that the current process should be able to reliably integrate valves with a node spacing of tens of microns. The bond edge variation seems to be primarily limited by surface strain due to stamping (see Figure 2.12).

Note that these measurements are meant to represent the future scaling capabilities of the process and were charitably sampled from devices in later fabrication runs, where the stamping technique was significantly improved compared to previous work (Dungan et al., 2023).

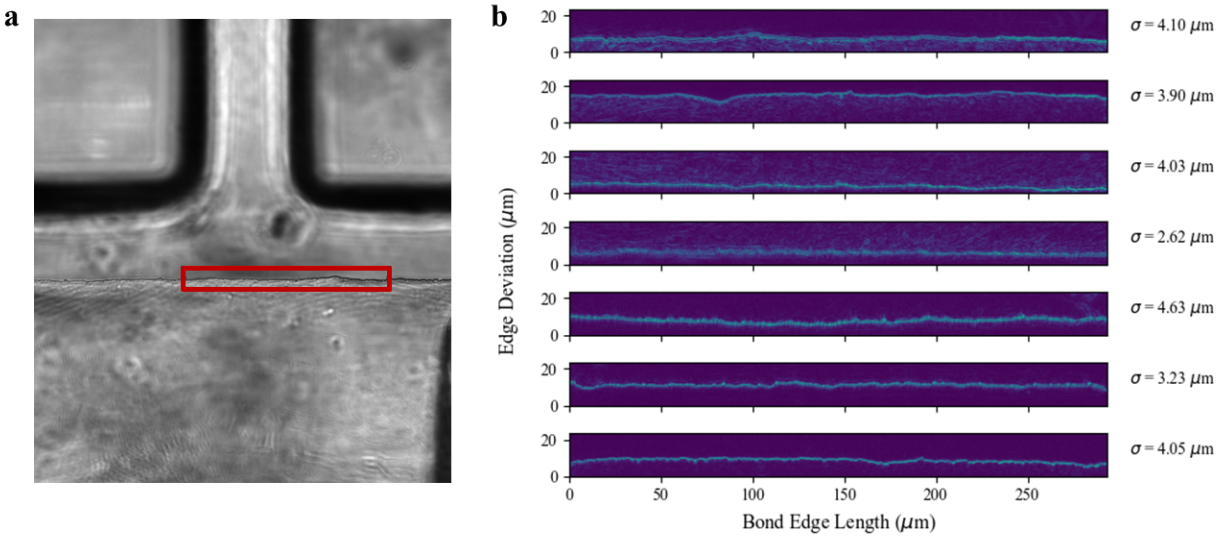

Figure 2.7: Bonding resolution analysis was performed by (**a**) imaging intended straight bond edges in phase contrast at 20× magnification. (**b**) An edge detection algorithm was used to extract bond edges and the standard deviation from the mean was extracted from 7 samples, resulting in an average standard deviation of 3.79 µm.

2.4.3 Electrical Characterization of Valve Performance

Fabrication on glass is ideally suited to integrate planar microelectrodes into valved microfluidic devices. In the presence of a highly conductive media, such as DPBS, the electrical impedance seen across the valve site serves to characterize the effectiveness of the valve sealing (H. Chen et al., 2008) and the impedance ratio between the open and closed states of the valve signifies the electrical isolation it provides at each frequency. Figures 2.8a and 2.8b show the characteristic complex impedance spectra for a representative valve at various actuation pressures. At low frequencies, the valve impedance magnitude exceeds 8 MΩ for positive actuation pressures greater than 10 mbar when the valve is sealed. In contrast, the measured impedance magnitude for the valve in the open state (vacuum) is only 190.0 kΩ at 10 Hz, a 35 fold difference. At 30 mbar actuation pressure, the valve in the closed state exhibits a maximum of 55.6 times greater impedance magnitude over the open state, showing that such normally open valves are suitable to provide reversible electrical isolation of different microfluidic compartments.

In the closed state, the valve impedance curves are bandwidth limited by the cabling (BNC) connecting benchtop instruments to the device under test. The closed valve impedance closely matches a single pole model with a cutoff frequency of 31 Hz. At 30 mbar, it can be modeled by a resistor and capacitor in parallel with equivalent values of 8.2 MΩ and 0.62 nF. Resistive load tests have verified that this parasitic capacitance is introduced in the cabling rather than the device or

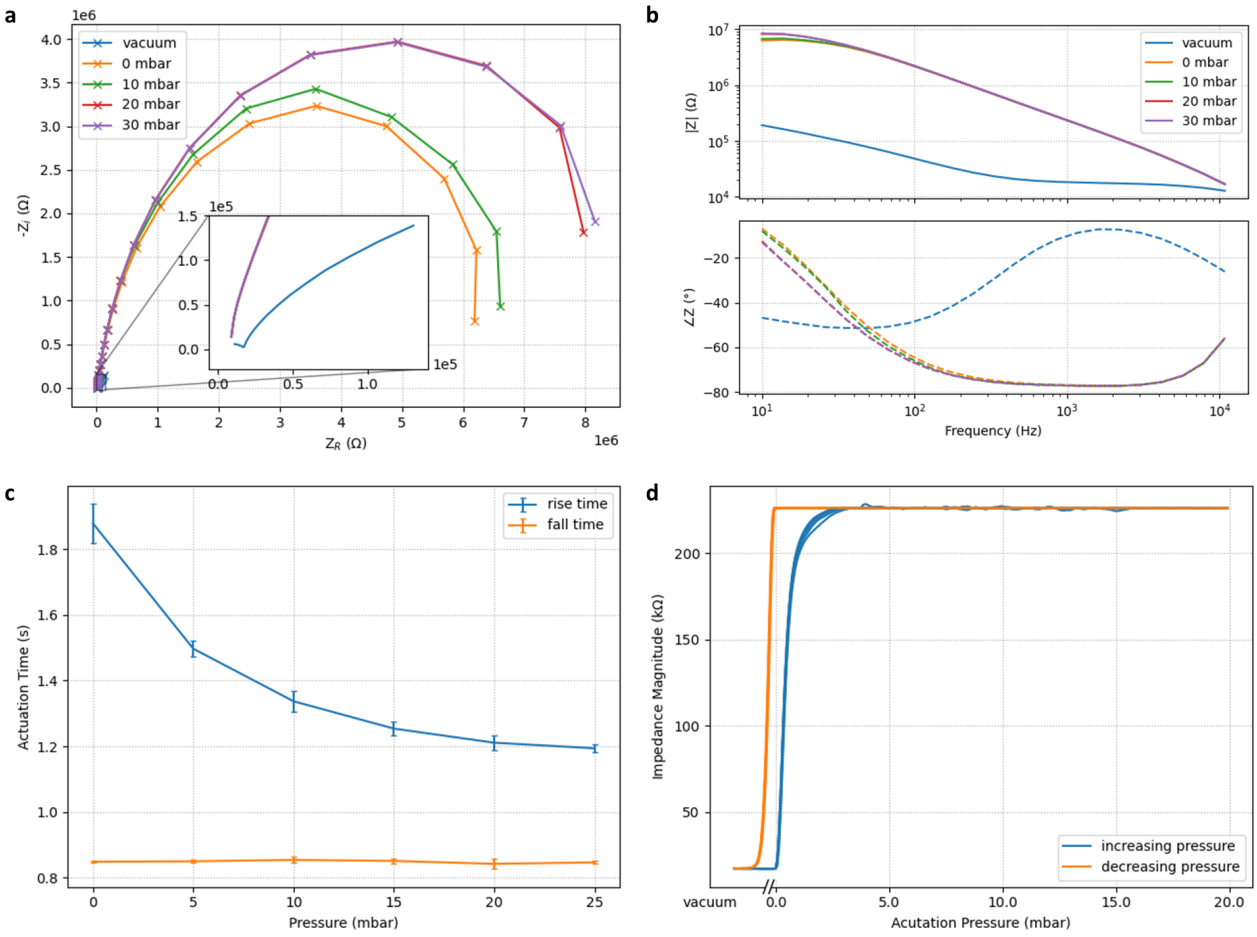

Figure 2.8: Impedance spectra for a valve in DPBS at various actuation pressures in both (**a**) Nyquist (**b**) and Bode plots. The current source (1 µA for vacuum, 10 nA for all other sweeps) was swept through evenly logspaced frequency points from 10 Hz to 10 kHz. (**c**) Valve actuation time was measured between 10% and 90% of the settled values of complex impedance magnitude after 60 s. A 1 kHz, 100 nA current stimulus was used to probe valve impedance. (**d**) Valve hysteresis was observed by step-wise increasing the actuation pressure from 0 to 20 mbar, then ramping the pressure back to 0 mbar, before returning to vacuum. The corresponding impedance through the valve was recorded for a 100 nA signal at 1 kHz, sampled continuous every 250 ms. Five complete cycles are overlapped in the plot.

interconnect. The valve barrier then represents a constant resistance over the biologically relevant spectrum. Even in its resting state (0 mbar) the valve represents an extracted resistance of 6.4 MΩ, making these devices useful for applications characterizing analytes across a broad frequency range (e.g. dielectric spectroscopy flow cytometry) or those using high frequency stimulation.

Ionic conduction in the open valve state also experiences significant degradation across the measured frequency range. The vacuum curve shape in Figure 2.8a is reminiscent of the characteristic the series connection of two parallel resistor-capacitor pairs. This model matches previously studied

electrical models for the electrode-fluid interface, where a large capacitance arises from the electric double layer formed by free ionic species at the interface and a resistance models redox reactions responsible for charge transfer (Stojek, 2002; Franks et al., 2005).

Valve actuation time is shown to be a function of the pneumatic actuating pressure in Figure 2.8c. The rise time corresponds to the impedance magnitude rise observed when positive pressure is applied to a valve's pneumatic chamber, and is calculated as the time difference between 10% and 90% of the total impedance rise after 60 s. As would be expected, driving the system at higher pressures causes more rapid deflection of the elastomer membrane, resulting in shorter rise times. However, diminishing returns in rise time are observed beyond 20 mbar and valves should be operated at the minimum acceptable pressure level to preserve longevity. Fall times (the time to drop from 90% of the sealed impedance to 10% once vacuum is applied) do not exhibit a dependency on the previous actuation pressure since all valves are well sealed after 60 s and an identical vacuum pressure is applied in all cases. Presumably, decreased vacuum strength would result in increased falling valve actuation times, but this response was not investigated. Figure 2.8b shows the valve hysteresis for a 1 kHz signal as a function of the actuation pressure. We posit that this hysteresis effect is primarily mechanical in nature. When vacuum is released on the valve, the elastic membrane begins sealing immediately, achieving a 10-fold impedance increase with less than 1 mbar of applied pressure. The valve impedance plateaus at less than 5 mbar of positive pressure, indicating that the membrane has completely sealed against the substrate. Once sealed, the elastomer is in a low energy state and electrical isolation is retained upon decreasing the actuation pressure back to zero. For low power solutions that rely on solenoid valves to apply pressure, this result implies that a scheme where the actuation pressure is briefly pulsed instead of held continuously is feasible.

The valve dynamics are explored in Figure 2.9 and such a pulsed actuation scheme is demonstrated. The ability of the valve to create and maintain a complete seal in the presence of positive pressure applied to the fluid channel was tested. A test valve was first closed for 10 s using varying actuation pressures (0, 10, 20, and 30 mbar) before the pneumatic pressure on the valve was released and positive pressure on the fluid channel flowing into the valve was increased linearly every 3 s. The electrical impedance was measured across the valve to monitor the seal quality and any leakage current. In Figure 2.9a, when zero positive pressure was applied to the valve, its elastomeric membrane slowly returned to its resting state against the substrate, resulting in a gradual increase in impedance. However, the force generated by the elastomer relaxation was likely insufficient to expel all of the conductive fluid under the valve area, resulting a poor seal and a small fluid leakage current under the valve. The leakage current expanded at higher driving pressures, resulting in declining electrical impedance. Valve impedance decreased to 90 percent of its maximum value at less than

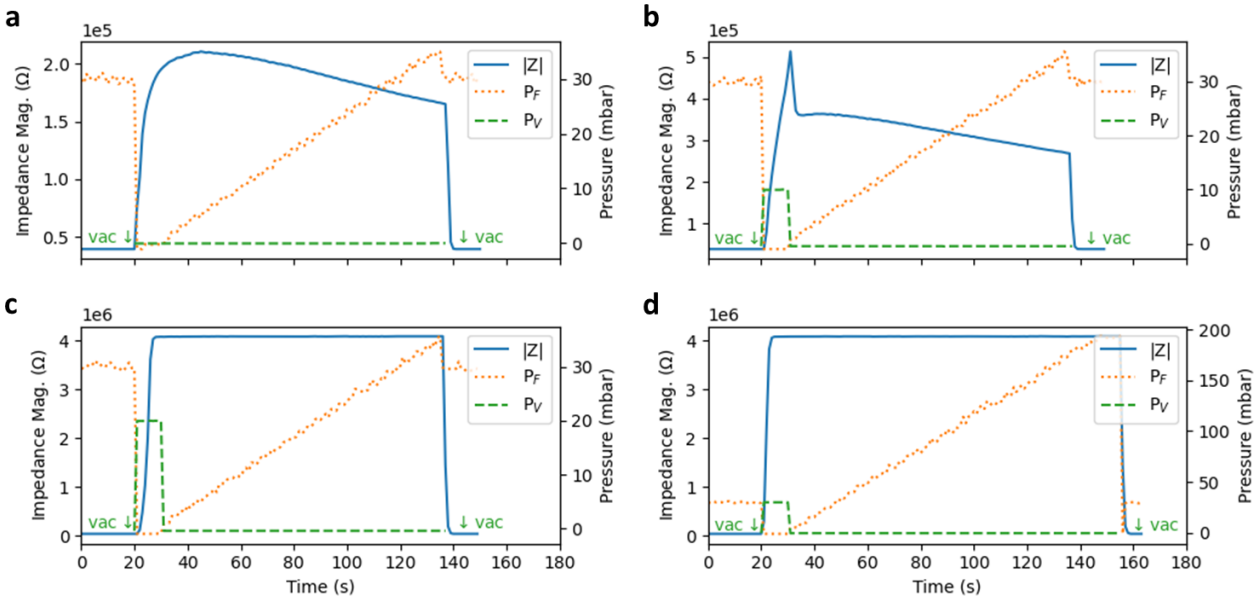

Figure 2.9: Valve resilience to fluid flow pressure (P_F) in the channel characterized by electrical impedance through the valve at 100 Hz. Valves were initially in an open state before the pneumatic valve pressure (P_V) was pulsed at (**a**) 0 mbar, (**b**) 10 mbar, (**c**) 20 mbar, and (**d**) 30 mbar for 10 s. As the back pressure on the valve was then ramped linearly, leakage current through the valve could be observed as a decay in valve impedance magnitude. Experiments began and ended with P_V pulled to vacuum (approximately -100 mbar, denoted by downward arrows).

24 mbar, suggesting that for operation without positive pressures some amount of fluid leakage must be acceptable (e.g. a peristaltic pump or control of flowing cells suspensions) or the device must operate at very low pressure. At 10 mbar actuation pressure (Figure 2.9b), the valve impedance rose quickly, but it was still insufficient to form a complete seal in the 10 s actuation window. A small leakage current was still present as evidenced by the similarity of the post-actuation curve shape with that of the 0 mbar case. Figure 2.9b indicates a trade-off between the actuation pressure and actuation window in order to form complete seals in this pulsed control scheme. For a 10 s actuation window, 20 mbar actuation pressure is sufficient to fully seal the channel as evidenced by Figure 2.9c. Further, Figure 2.9d demonstrates that for a 10 s pulse of pressure at 30 mbar, the valve forms a sufficient seal to the substrate to withstand a 200 mbar flow pressure (the full range of the experimental pressure controller) without any leakage current forming. Presumably, these valves can withstand even greater fluid pressure given sufficient actuation pressure and time to form a tight seal to the substrate.

2.4.4 Arrayed Device for Cell Culture

To demonstrate the potential for dense integration of microfluidic valves developed in this process, an arrayed microfluidic chip (Figure 2.10) was fabricated. The device uses 24 valves to control

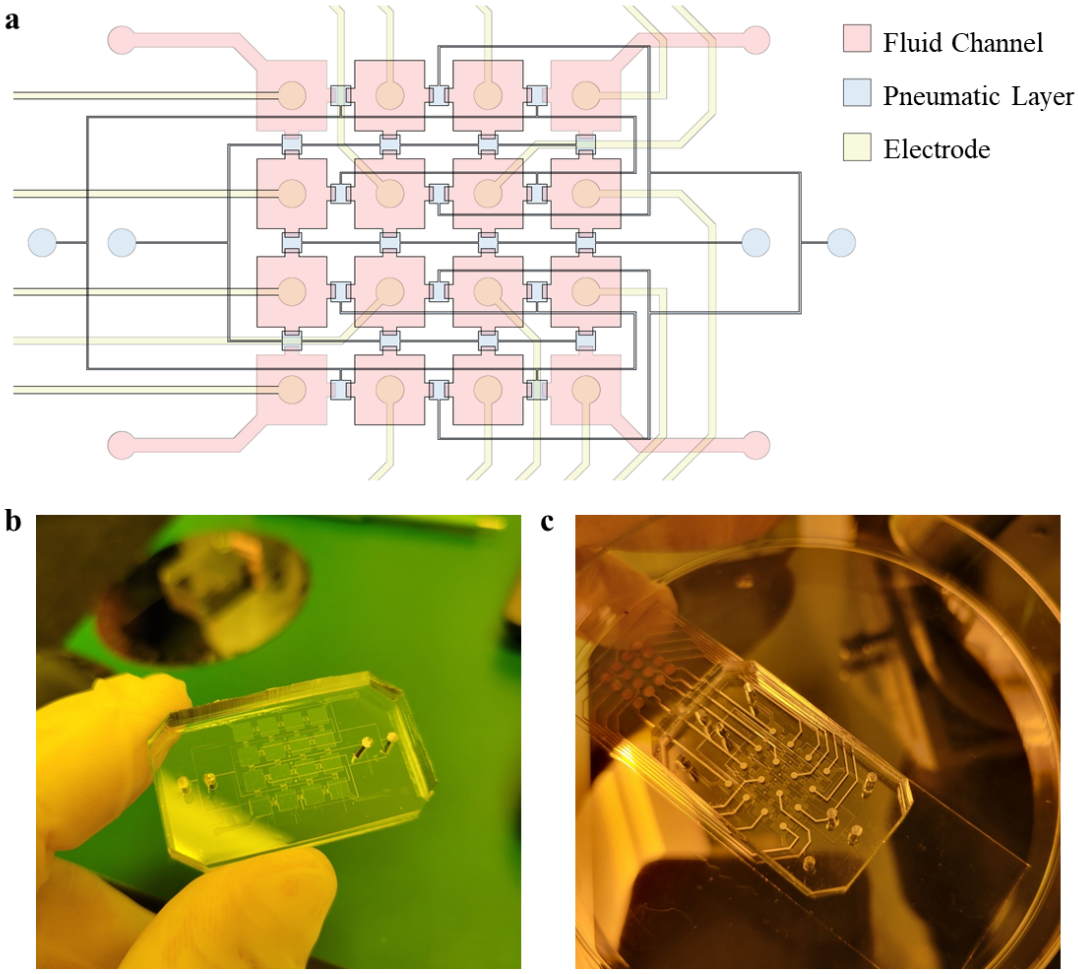

Figure 2.10: (**a**) Design of a proof of concept 4×4 valved array chip integrating 24 valves for cell culture isolation. The device is shown (**b**) before and (**c**) after successful substrate bonding.

isolation of 16 cell culture wells. Pneumatic control of the valves was designed in a row and column scheme such that any adjacent pair of wells can be isolated from the rest of the network using only 4 pneumatic inputs. All 24 valves on the devices were successfully aligned and bonded, demonstrating the potential of this process for large scale microfluidic integration (Section 3.4.2 shows additional impedance data demonstrating the successful operation of the device.).

2.5 Discussion

2.5.1 Alternative Approaches

Several alternative fabrication approaches were attempted but were deemed unsuitable for reliable and biocompatible microfluidic device manufacture. Figure 2.11 depicts three of these approaches: 3D printing, film lamination, and wafer-scale bonding.

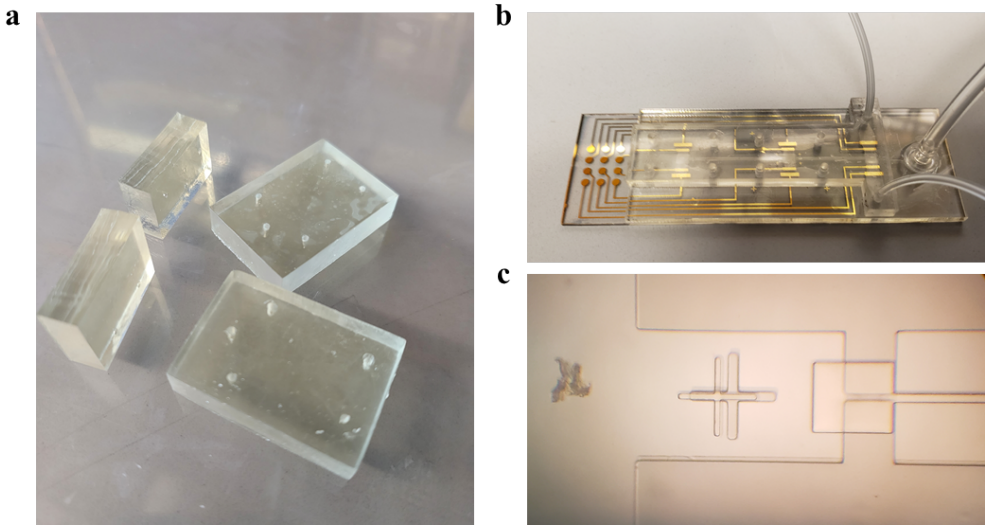

Figure 2.11: Alternative fabrication methods. (**a**) 3D printing with flexible resin, (**b**) positive pressure valve using polyurethane film, and (**c**) wafer-scale bonding were all unreliable for effective microvalve manufacturing.

3D printing technology is constantly improving, and resolutions of high-end 3D resin printers are well within the minimum specifications necessary to form microfluidic channels and valves. Additionally, clear and flexible resins with elastic molduli similar to that of PDMS are available. While valved microfluidics are easily and conveniently designed for direct 3D printing, practical limitations of the printing workflow make it unsuitable for producing valves. Though microscale channels can be cured into the resin, washout of uncured resin is exceptionally difficult or impossible in some cases. The high viscosity of uncured resin and microscale channel dimensions require massive pressures to force flow. Further, ethanol and isopropanol used to clean prints are not solvents for the uncured resin, so washout of closed channels (such as pneumatic lines), proves impossible.

Printing of resin molds in place of SU-8 photolithography may be achievable. However, partially cured monomers on the print surface interfere with subsequent PDMS molding and significant additional processing is required to remove the monomers completely (Tjong, Teixeira, and Frampton, 2020). This additional processing in many ways voids the appeal of 3D printing for rapid prototyping as compared to photolithography. 3D printing shows promise as a means of microfluidic fabrication, but will require several advances to meet the quality of soft lithography - namely, an effective solvent for uncured resin, a patternable and biocompatible epoxy for substrate bonding.

Fabrication using a film lamination approach was also explored. A 75 µm pressure sealing adhesive was laser cut to form channels and laminated onto a thin, flexible (50 µm, durometer 85A) polyurethane film. Pneumatic channels were cut into a rigid acrylic backing (Figure 2.11b). Though

more suitable for mass production, this fabrication approach is only capable of forming positive pressure valves. These valves allowed significant leakage currents at the nominal valve pressures, sealing to only 34.1 kΩ at 0 mbar and 96 kΩ at 30 mbar (versus 6.4 MΩ and 8.2M Ω for the normally closed PDMS valves). Normally closed valves are essential to provide maximal electrical isolation at low valve pressures.

Three alternative techniques for fabricating negative pressure valves in PDMS also merit discussion. Wafer-scale bonding, thin layer separation, and partial curing methods all met with limited success. The bonding process was originally attempted at wafer-scale, assembling many device replicates or variations on a single large mold. Attempting to bond PDMS across a 4 inch wafer exacerbated many of the issues discussed in the following section. Specifically, issues with drooping, stretching, and leveling of the soft material led to trapped gas and uneven contact pressure. Additionally, the thermal contraction of PDMS after mold release led to very poor alignment near the wafer edges (Figure 2.11c). An attempt to preemptively expand the pneumatic mold improved alignment but ultimately proved unreliable without additional iteration and tightening of curing times. In addition to the wafer-scale bonding approach, early devices used a “slightly open" approach, wherein a two layer flow mold formed a very thin separation (1.5 μm) in the valve seat area to allow normal glass bonding. However, the elasticity of PDMS meant that bonding still had to be performed while the valve was activated by vacuum pressure, which was ultimately too cumbersome to form reliable bonds. The slight openness also represents a compromise in the electrical isolation achievable by these types of devices. Finally, bonding through partial curing as recommended by Eddings, Johnson, and Gale (2008) and Mohan et al. (2011) was attempted, as constructing the PDMS layers using mismatched ratios of curing agent and allowing diffusion of cross-linker across the bond interface should lead to the strongest possible final bond. However, working with partially cured PDMS in the alignment apparatus proved to be a messy an unreliable endeavor.

2.5.2 Limitations and Future Work

Traditional lithographic alignment processes are not optimized for “soft" materials. PDMS alignment for bonding in particular presents a variety of challenges, namely (1) the possibility of layers stretching or drooping, (2) challenges related to leveling soft surfaces, and (3) more pronounced thermal contraction.

The elastic nature of PDMS permits stretching, warping, and drooping of thin layers if not rigidly backed during alignment. Ideally, layers should be cured against transparent backing and not released until alignment is complete. Care must be taken, however, to ensure that the backing itself is either sufficiently light or well balanced enough that it does not exert significant levering force on the device after alignment while the bond is developing.

Contrary to normal photoresist alignment processes, where cross-linked photoresist may be contacted to the mask in the stage leveling step prior to alignment, the treated PDMS surface must not contact its bond target prior final contact. Further, the compressibility of PDMS makes leveling procedurally difficult, as a freely rotating stage may compress the device rather than adjusting its angle of alignment.

PDMS experiences a small amount of thermal contraction when cured at an elevated temperature and then released from a mold. (Madsen et al., 2014) The scaling factor of this contraction is a function of the base to cross-linking agent ratio of the PDMS, the curing temperature and time, and in the presence of a backing material is further affected by layer thickness. Complications of thermal contraction limited this investigation to pursuing a single device production scheme, though wafer-scale alignment of multiple devices should be possible though continued iteration and pre-expansion of the pneumatic layer mask.

If the challenges of (1) and (2) are addressed and good alignment is achieved, further issues can arise due to the trapping of air. In a normal PDMS device bonding process (without alignment), devices are usually contacted at a single point and the contact propagates as a wavefront as the elastomer relaxes onto the surface. However, when both surfaces are leveled, contact can occur at multiple points across the device, causing air pockets to arise in the bonding interface. The gas permeability of PDMS can help evacuate some of these air pockets during the heated curing phase, but they often result in areas of decreased bond strength.

Finally, The compact digital microscope used in the alignment rig was suitable for the purposes of this work, but better optics would enable more uniform contact pressure. Figure 2.12 shows typical images captured by the alignment rig. In the current process, contact completion and pressure are estimated by eye. Because mechanical perturbation of the surface can lead to degraded surface treatment, excessive contact pressure as shown in Figure 2.12c is a main limiting factor to bonding resolution. Leveling errors can exacerbate this problem if a portions of the stamp contact asynchronously leading to uneven stamping pressure.

Many of these challenges could be addressed through the continued development of a customized alignment and plasma treatment rig. An ideal tool might operate similarly to a mask aligner where the UV lamp is replaced by a plasma source. The ability to align soft layers and fix their position during plasma treatment would alleviate many of the noted limitations of this approach. Practically, alignment challenges, rather than bond strength, are a stronger driver of low yield of valved devices. In theory, spatial resolution of the approach is limited only by lithographic resolution and alignment quality.

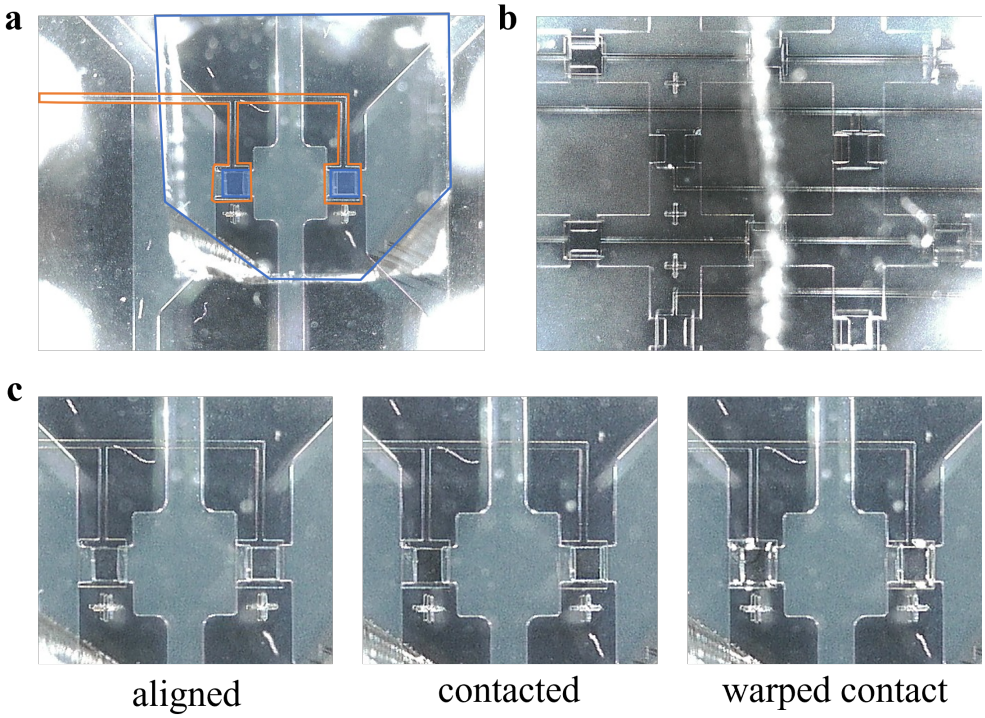

Figure 2.12: The resolution of the bonding process is primarily limited by the alignment instrumentation. (**a**) Multiple transparent layers are difficult to distinguish, especially in (**b**) densely integrated designs. (**c**) These poor optics make it difficult to identify when contact is establish and how much pressure has been applied.

2.6 Conclusions

A spatially selective bonding method has been demonstrated to fabricate normally closed microfluidic valves on glass substrates. This oligomer stamping technique had not previously been demonstrated on glass and prevents the need to actuate valves during bonding process, thereby increasing fabrication reliability and enabling large scale integration. The oligomer stamping process itself has been examined in detail using contact angle measurements to predict bonding strength. The stamping mechanism was found to produce a roughly constant recovery of the PDMS surface hydrophobicity over a wide range of exposure parameters. Further, the oligomer interaction with activated surface groups does not occur instantaneously, rather stamping to remove plasma surface treatment should maintain contact for greater than 3 s and may be repeated to ensure maximum recovery of hydrophobicity. Blister burst testing showed that in practice, this stamping technique is sufficient to prevent bonding under any surface treatment conditions, so oxygen plasma treatment should be optimized for efficient bonding of the device area rather than minimum bonding in the valve area, i.e. 20 W exposure for 30 s.

The elastomeric valves fabricated using this optimization require only two PDMS layers (and no

additional chemicals or fabrication tools) and permit convenient integration of electrodes into a microfluidic device. Integrated electrodes enable monitoring of valve behavior among a number of other useful applications. Here, electrical impedance measurements through the valves have demonstrated reversible electrical isolation beyond 8 MΩ at exceptionally low actuation pressures (less than 30 mbar). Further, a pulsed actuation scheme was explored in which positive pressure is applied briefly to seal the valve against the substrate before releasing pneumatic pressure to conserve operational energy. Electrical measurement verified that valves pulsed in this manner at 30 mbar for 10 s were able to withstand channel back pressures greater than 200 mbar without leaking. Dense integration was demonstrated for 24 valves isolating a proof-of-concept 4×4 cell culture well array. The presented microcontact method of valve fabrication is suitable for dense integration of many normally closed elastomeric valves on glass substrates, enabling applications where optical imaging or electrode integration are critical.

Chapter 3

A LAB-ON-MICROSCOPE ENVIRONMENT FOR AUTOMATED BIOMICROFLUIDIC EXPERIMENTATION

3.1 Introduction

Microfluidic devices are becoming ubiquitous as essential research tools in the fields of chemical synthesis (Nunes and Stone, 2022), environmental engineering (T. Wang, Yu, and Xie, 2022), pharmaceutical development (Hamdallah et al., 2020), biosensor technology (Rivet et al., 2011), biomedical engineering (Natu et al., 2023), and more (Whitesides, 2006; Niculescu et al., 2021). As the scope of applications for microfluidics grows, so too escalates the demand for a universal support system to facilitate microfluidic experimentation.

Ironically, many microfluidic lab-on-a-chip devices often require a whole lab of support systems. The standard system requires fine control of either pressure or flow rate and some form of valve system for fluid handling. Additionally, many applications may call for gas/vacuum switches to operate on-chip pneumatic components, such as pumps and microvalves (Au et al., 2011). Biomicrofluidics, involving living cells or organisms, present additional requirements, including temperature regulation, live cell imaging, and sterility considerations (L. Kim et al., 2007). Further, many applications may require electrical interactions to probe (Bruno et al., 2020), manipulate (H. Zhang, Chang, and Neuzil, 2019), or stimulate samples (J. W. Kim et al., 2022) or even modulate flow (Shaffer et al., 2023). Other common electrical sensing modalities in microfluidic applications include electrical impedance spectroscopy (Fernandes et al., 2022), electrical flow cytometry (Gajasinghe et al., 2016), and transendothelial electrical resistance monitoring (F. Henry et al., 2017). Commercial options for microfluidic peripherals do exist, but most offer relatively expensive, modular benchtop equipment. Meanwhile, complete microfluidic solutions in research and development are often designed for application specific purposes (R. Wang et al., 2022; J. Wu et al., 2014; Y. Zhang, Tseng, and Schlichtmann, 2021; Herr et al., 2007).

To reduce costs and complexity of operating microfluidic experiment across a wide range of applications and to increase the accessibility of microfluidic technologies, we present a "lab-on-scope" platform. Here, we describe a unified solution for biomicrofluidic experimentation in which regulated heating, fluid control through magnetically latched solenoid valves, and modular electrical measurement are all integrated on a microscope mounted printed circuit board (PCB). The platform's capability to facilitate microfluidic cell culture is demonstrated through a real-time continuous electrical monitoring of NRK-49F cells in a monolayer culture. Further, the ability

to pragmatically manipulate liquid/gas flow is demonstrated through paired optical and electrical observation of an arrayed microfluidic device containing 24 elastomeric microvalves.

3.2 "Lab-on-Scope" - A Compact System for Microfluidics Peripherals

3.2.1 Design of a portable microfluidics lab

We propose a system that mounts directly onto a standard microscope stage, bringing all the peripheral microfluidic support services closer to the experiment. Figure 3.1a shows the high-level block diagram for the system. On board communication (except for the heater) is handled over I^2C protocol by a mounted microcontroller unit (Raspberry Pi 3B+). The microcontroller continuously runs a server which listens for commands sent over TCP/IP socket protocol from an application on a personal computer.

The platform provides an array of eight 2:1 magnetic latching solenoid valves with a small form factor (LHLA1231111H[1], Lee Co.). These valves save energy because the magnetic latch must only be temporarily overcome by the solenoid force in order to switch states. More importantly, because both rest states require no current, the valve does not heat based on switch position. This property is ideal for experimental control where solution temperature can significantly affect impedance measurements. H-bridge drivers (NCV7702B, ON Seminconductor) are used to drive the solenoid valves in both forward and reverse polarities. Because these drivers require both a state and enable signal for each valve, a GPIO (general purpose input/output) expander is necessary. Valves can be stoppered to operate in 1:1 mode.

Figure 3.1b shows the layout of the PCB. All electronic components are situated far from the microfluidic chip area to prevent accidental wetting. Additionally, nearly all components are mounted on the top side of the board to avoid contact with the objective of an inverted microscope. The exception is that the valve array is mounted (electrically) on the backside such that the valve ports fit through slots in the PCB and are accessible on the topside.

To couple the ported valves into the fluidic system, a PDMS manifold was molded from a resin 3D printed cast. The manifold allows tight push fit connections to 22 gauge steel tubing and is fastened in place by a 3D printed cover. Figure 3.2 shows the manifold and the mold used to produce it. The PDMS manifold achieved leakless coupling of the valves for gas pressures in excess of 200 mbar.

3.2.2 Temperature regulation

Joule heating of a transparent indium tin oxide (ITO) thin film (~100 Ω, Structure Probe, Inc.) is regulated through pulse width modulation (PWM) by the DRV103 power driver (Texas Instruments,

[1] While these valves are ideal for many applications, the armature directly contacts the experimental fluid, and they may not by suitable for use with "aggressive" fluids.

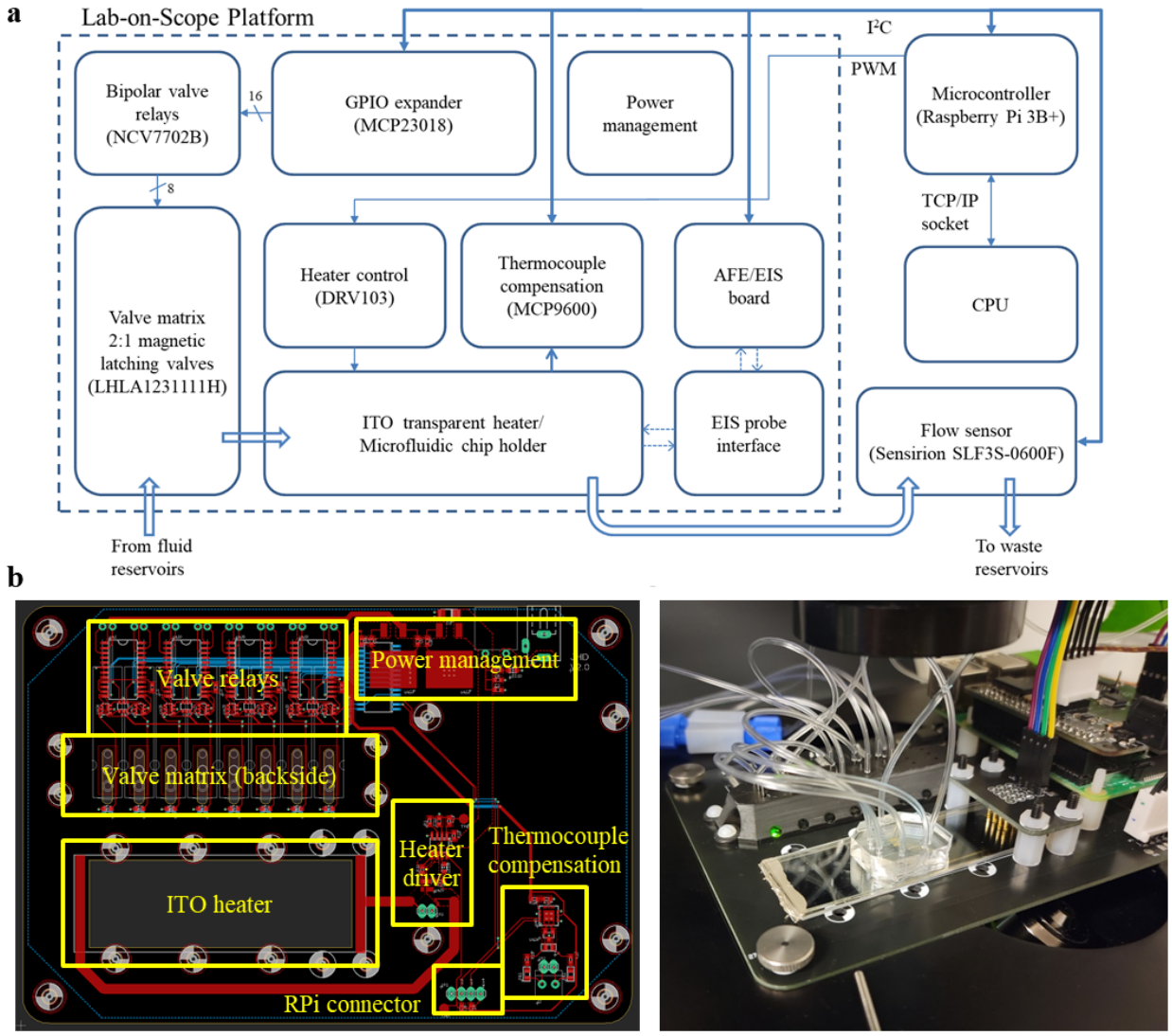

Figure 3.1: (**a**) A block diagram of the lab-on-scope system, (**b**) layout of the PCB, and (**c**) the realized system mounted on an inverted microscope.

Inc.). PWM allows finely tuneable average power to be dissipated through the heater. The ITO slide is bonded to the PCB with high conductivity silver epoxy (8331-14G, MG Chemicals). The total contact resistance of the epoxy joints is approximately 75 Ω, which fundamentally limits power dissipation in the heater film. Temperature at the heater is sensed by a K-type thermocouple. A compensation circuit (MCP9600, Microchip Technology, Inc.) is needed to convert the thermocouple measurements to absolute temperatures, which are transmitted over I^2C connection. A PID loop running on the microcontroller provides close regulation of the temperature by adjusting the power driver output based on the measured temperature value, integral over time, and rate of change. Figure 3.3 shows that for a set point of 35°C, the platform maintained the target temperature for

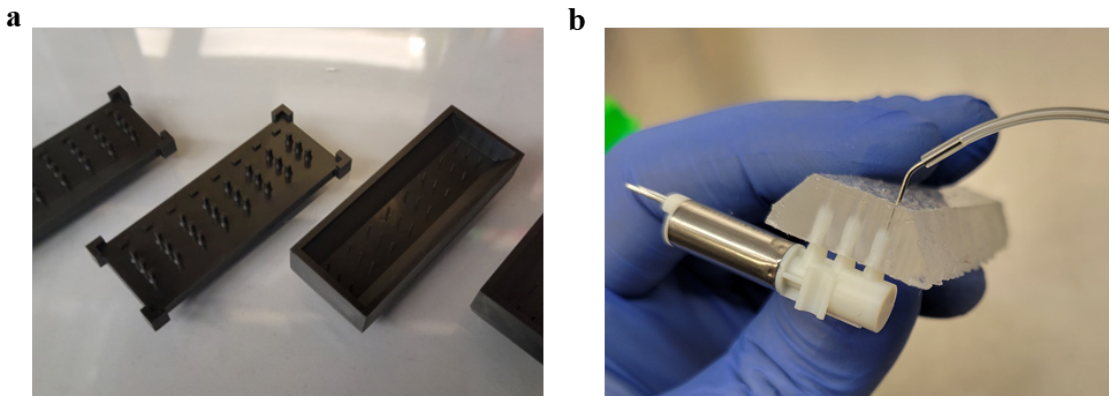

Figure 3.2: The (**a**) 3D printed mold and (**b**) PDMS cast of the manifold used to couple miniature solenoid valves to the microfluidic tubing.

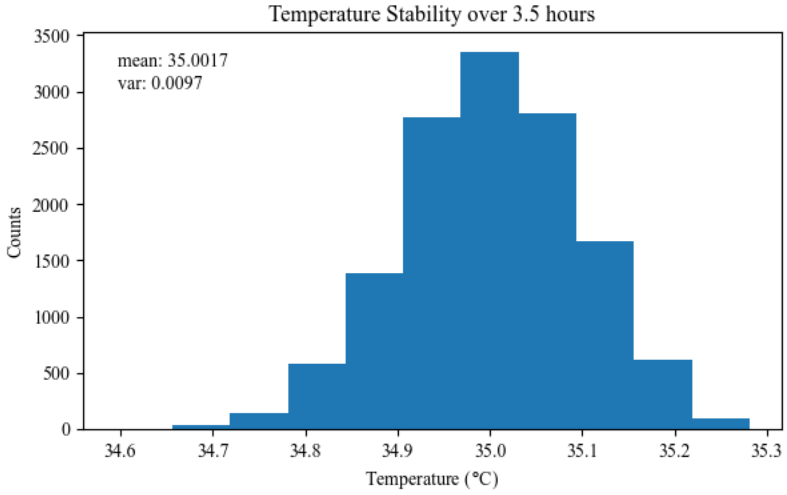

Figure 3.3: Temperature stability of the lab-on-scope platform, measured over 3.5 hours at 60 Hz sample rate.

3.5 hours with only 0.0087°C variance.

3.2.3 Electrical impedance measurement

Because of the breadth of electrical sensing and stimulating applications, we have opted for a modular design to integrate microelectronics. Electrical components are integrated on PCBs mounted directly onto the microcontroller headers (HATs in the Raspberry Pi nomenclature) to allow synchronization of data and control signals. Additionally, this approach helps to isolate sensitive analog circuits from the noisy power electronics on the main lab board. Figure 3.4d shows two of these HATs designed to measure complex impedance over the biologically relevant frequency spectrum.

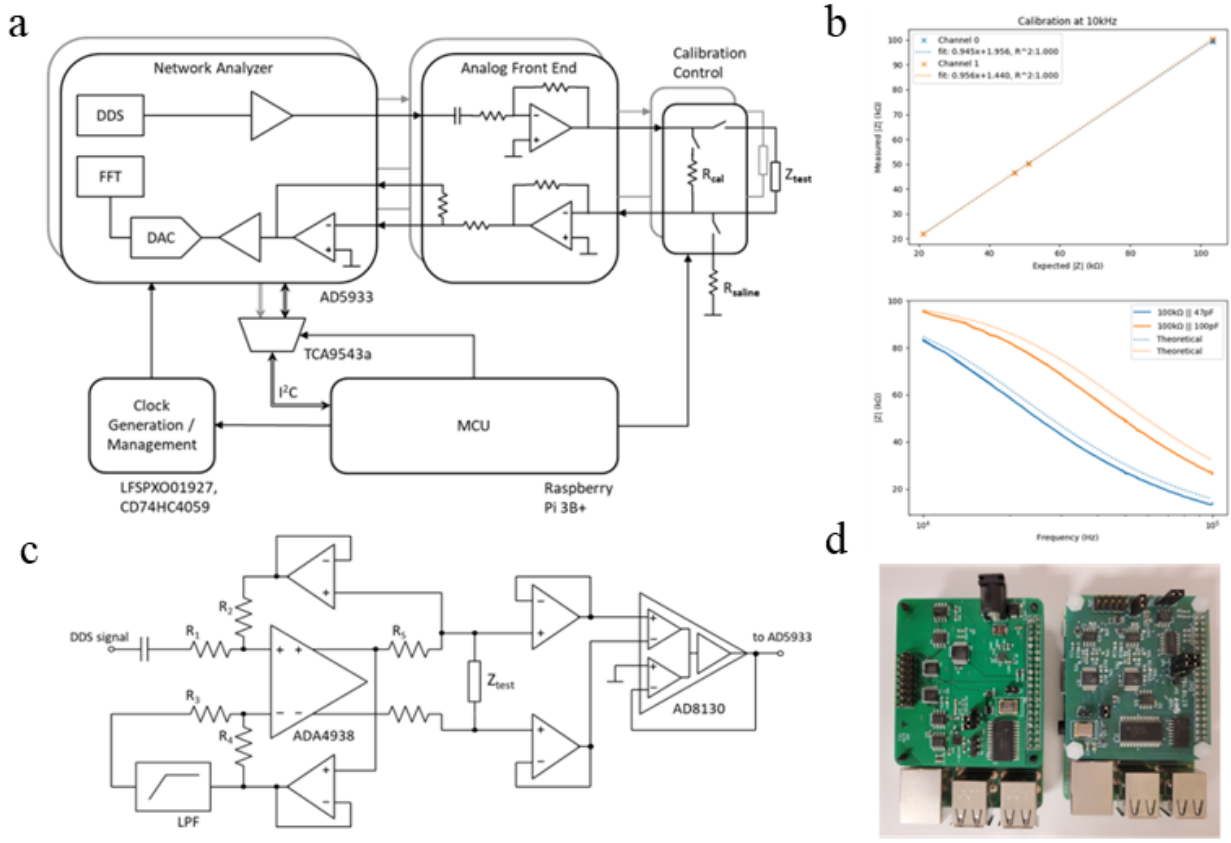

Figure 3.4: Complex impedance spectroscopy systems. (**a**) Block diagram for a compact complex impedance measurement system for programmatic frequency sweeps up to 100 kHz and (**b**) calibration testing results on lumped element standards. (**c**) An alternate driver circuit and AFE design that enables four terminal current driven bioimpedance sensing. (**d**) Four point (left) and two point (right) bioimpedance measurement systems are integrated on PCBs that mount directly onto a microcontroller.

Figure 3.4a presents a lock-in detection system capable of two-channel complex impedance spectroscopy up to 100 kHz. The design uses Analog Devices network analyzer, AD5933, to achieve magnitude error less than one percent on lumped circuit calibration models at 10kHz (Figure 3.4b). The AD5933 features a direct digital synthesis unit which serves as the signal source for the lock-in detection scheme. A low noise analog front end (AFE) has been devised to drive the signal as a voltage into a calibration impedance or the sample under test. Further, the AFE recovers the current signal and converts it back to a voltage which is then digitized in the AD5933. Synchronous detection is performed in the frequency domain on chip. The AD5933 interfaces with a Raspberry Pi microcontroller over I^2C protocol (using a custom made Python wrapper library), so the system is programmable and reconfigurable.

An alternate AFE for four point measurement using the AD5933 is shown in Figure 3.4c. The

approach, based on previous bioimpedance current source architectures (Pliquett et al., 2011; Mahnam, Yazdanian, and Mosayebi Samani, 2016; Cabrera-López et al., 2016), uses feedback to convert a single-ended voltage input into differential current that is driven in a balanced manner across the test impedance. The transconductance factor relating the input voltage to output current is given by:

$$G = \frac{R_2R_3 + R_2R_4}{(R_1 + R_2)R_3R_S} \rightarrow \frac{1}{R_S}, \text{ when } R_1R_4 = R_3R_2. \tag{3.1}$$

Similarly, the output impedance approaches infinity if the input and feedback resistors are well matched. The AFE additionally senses the differential voltage across the load impedance and level shifts it appropriately to supply to the AD5933 for completion of the lock-in detection. Both of the realized bioimpedance spectroscopy systems shown in Figure 3.4d are low-cost, compact, and ideally suited to interface lab-on-chip microfluidic devices.

3.2.4 Interfaces and integration

Many approaches have been proposed to interface between electrodes on a microfluidic device and external electronic amplifiers and signal processing electronics with no clear dominant solution. In fact, the electrode integration and interconnect is often not described in many publications. Probably the most common approach is to clamp leads to on-chip pads, a technique which is neither robust nor compact and does not scale well for more complex devices with multiple electrode pairs. Clamp contacts can twist, scrape contact pads, impede imaging, and often introduce significant parasitic capacitance due to having several uneven points of contact. Another option is to solder wire connections or wire bond directly to pads on the microfluidic chip. While more electrically stable, soldering to thinly deposited metal pads cause delamination and wire bonding requires proper encapsulation for mechanical robustness. Additionally, permanent wire connections can become inconvenient for handling and cleaning of the microfluidic device.

The most electrically ideal approach likely integrates microfluidic channels directly over the electronic sensing components, whether on PCB (Babikian, 2016) or directly on CMOS (A. Wu et al., 2010). While direct integration reduces parasitic capacitance and limits the chance of coupling between the signal lines, these solutions are not always practical for rapid prototyping. Additionally, the design of these integrated devices often requires well or via-like structures that may not be suitable for all flow regimes, such as those relying on complex patterns of laminar flow.

The authors find that spring loaded probe pins are an ideal compromise for most applications. Spring pin connectors (Mill-Max 821 series) provide milliOhm contact resistance. Further, they are suitable for fairly dense interconnect (100 contacts/in^2) and are simple to implement and reconfigure at the PCB level. These compressible probe pins can be used to connect directly to amplifiers on a PCB or connected to a larger processing circuit via a short shielded jumper

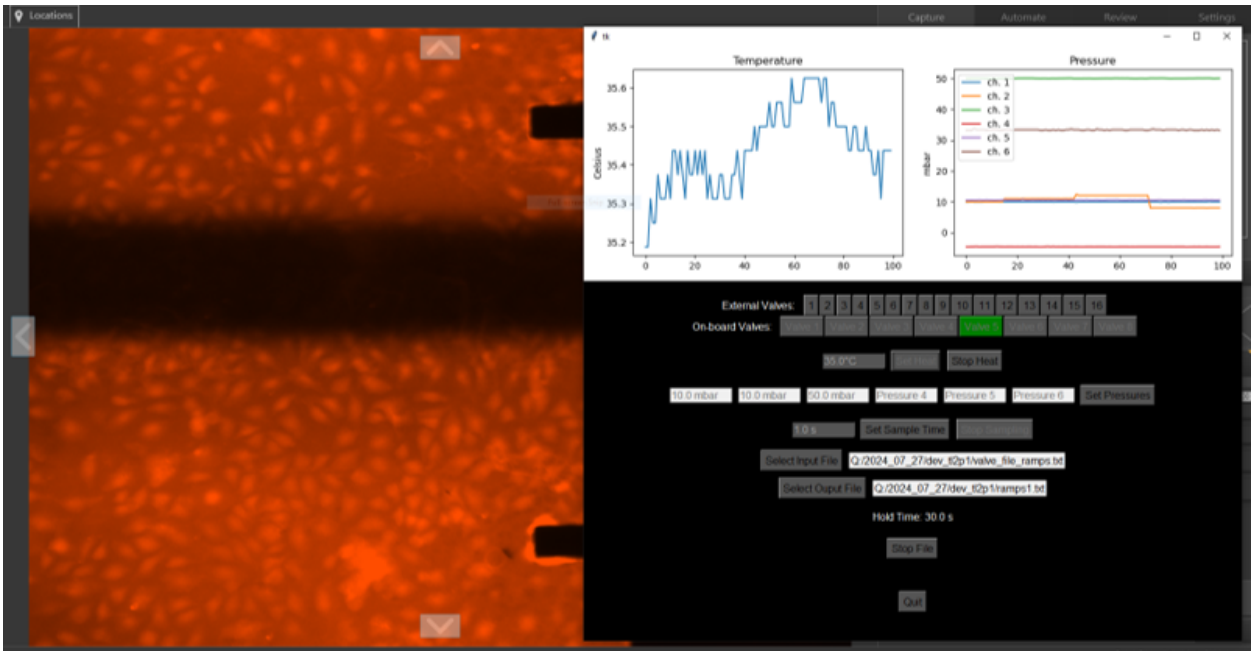

Figure 3.5: The graphical user interface for the lab-on-scope system displays the temperature and pressure history and allows manual or programmatic control of valve states, temperature setpoints, and pressure setpoints.

cable. This solution provided flexibility to support a wide range of electrical sensing or stimulation systems.

3.2.5 Software and user interface

A graphical user interface has been designed in Python to more easily facilitate sending commands from a client module to the lab-on-scope server. Figure 3.5 shows this prototype user interface, which displays temperature and pressure history and allows manual control of valve states and setpoints for pressure and temperature. (Pressure is regulated externally by an Elveflow OB1 Mk3+, but control is synchronized through a Python API in the application.) In addition, the user interface allows programmatic control of all elements of the platform through human-readable text configuration files. These automated run sequences allow intricate synchronization of valve switches and pressure waveforms, enabling complicated experimental protocols to execute reliably and repeatably.

3.2.6 Other considerations

For applications requiring flow rate monitoring, an external compact thermal transfer sensor (SLF3S-0600F, Sensirion AG), which also operates over I^2C protocols, is used. The flow sensor could be affixed to the board, but it is often more convenient to allow flexibility in the sensor

placement so that the path of the output tubing is streamlined.

The platform itself is not constrained to any particular perfusion system. Peristaltic, syringe pump, and pressure driven systems are all viable. In the experiments that follow, an Elveflow OB1 Mk3+ pressure controller is used. However, no hardware at all is necessary for fine control of microfluidic flow. Simple elevation of fluid reservoirs can provide reliable gravity driven flow (Gnyawali et al., 2017).

A number of other features could be helpful in many applications, but were considered outside the scope of this work. A pH monitoring system would be helpful for any biological culture application. Additionally, bubble traps are ideal for many microfluidic applications (but can be built into microfluidic devices) and may be incorporated into the system in future iterations.

3.3 Cell Culture in Microfluidic Devices

The lab-on-scope platform is intended to enable reliable biomicrofluidic experimentation. This section will provide general guidelines for successful seeding and microfluidic culture of cell monolayers using the platform.

Microfluidics dealing with adherent cell monolayers incur some inherent challenges that need to be managed or designed around. These challenges include seeding cells effectively and accurately, managing shear stress due to flow, providing sufficient gas and nutrient exchange, and designing for long term viability. The authors work primarily in a Normal Rat Kidney (NRK-49F, NRK) cell line, including some genetically altered variants. NRKs are a reasonably hearty line that forms strong Cx43 junctions (Cédric Bathany et al., 2011). While every cell line will have ideal parameters and protocols for proper culture, what follows are some general guidelines for seeding and culture of 2D adherent cells in the microfluidic environment. For a detailed protocol of NRK cell seeding into microfluidic devices, see Appendix B.

3.3.1 Considerations for Microfluidic Cell Culture

While the surface area to volume ratio of microfluidic devices is favorable over conventional dish culture for efficiency of nutrient and drug delivery, small volumes also mean that additional care must be taken to ensure that nutrients are not depleted and to limit the buildup of metabolic waste. This issue is particularly pertinent during seeding when flow must be stopped entirely to immobilize cells for adhesion. Where possible, and especially at large culture wells, channel heights greater than 50 µm are recommended to provide sufficient media volume to support several hours of static conditions.

Most cell lines are very sensitive the pH and CO_2 levels in their environment. To this end, when microfluidic devices are not contained in a CO_2 controlled incubator a pH buffer is recommended.

HEPES (4-(2-hydroxyethyl)-1-piperazineethanesulfonic acid) is a zwitterionic buffer that can be added to cell media at a 10mM concentration to prevent rapid fluctuations in pH level. Further, for pressure driven systems, media reservoirs should be regulated to the lowest reasonable operating pressure using a gas mixture of O_2, CO_2, and N_2 matching the ideal biological atmosphere.

In long term microfluidic culture, bacterial infection can quickly devastate cultured cells and muddle imaging and flow conditions. Thorough sterilization of all biologically facing components of the microfluidic system is a critical starting precaution. Some components such as off-chip valves or connectors may not be suitable for treatment by UV or autoclave. A pre-flush with alcoholic disinfectant such as ethanol, followed by thorough rinsing in DI water is usually sufficient to prevent infection. Media treatment with an antibiotic such as a low concentration of penicillin streptomycin may also prove useful. Finally, waste reservoirs at atmospheric pressure can be protected from outside contamination via a microbial syringe filter with less than one micron pore size.

Preventing the intrusion of gas bubbles can often be the unexpected crux of microfluidic integration. Bubbles may also form seemingly spontaneously in media inside the chip. Gases dissolved in solution can nucleate into bubbles in reaction to decreased pressure and increased temperature. This bubble formation can be mitigated through a few means. Careful mixing of solutions, so as not introduce excessive gases is a good start. Mixing through repeated pipetting is preferred to vortex mixing. Further, media used in microfluidic experimentation can submersed in an ultrasonic bath prior to use. Sonication in a heated bath for 30 minutes prior to experimentation has anecdotally reduced bubble formation. Further precautions can be taken to reduce temperature and pressure changes including ensuring that the media is constantly heated in the reservoir and delivery tubing. Care should be taken to reduce sudden pressure changes as well. Lowering pressure on the inlet reservoirs may be helpful or alternately the outlet reservoirs may be pressurized to reduce the overall gradient drop through the device. Polydimethylsiloxane (PDMS) is moderately air permeable, so the later approach may also help to force trapped gas out directly though the device walls. Finally, gas trapping in the initial wetting of the device should be taken into consideration during design. Rounding sharp corners, especially in low pressure areas such as large cell culture wells can prevent bubble formation during the initial wetting. Additionally, pre-filling the device with a surfactant, such as ethanol, helps to ensure a bubble free environment.

Perhaps the most unique challenge presented by microfluidic culture of adherent cells is the management of shear stress on the cells. Fluid flowing past adherent cells causes shearing force proportional to the flow rate (with the constant of proportionality being the fluid viscosity). Some cell lines may be better adapted to deal with shear stress than others. Epithelial cells, for instance, experience near constant shear stress in vivo; however, shearing may cause stress responses and even morphological changes in some cells. Complete cleaving from the substrate and delamination of the cell layer is

possible if flow rates are too extreme. Without changing fluid viscosity, shear stress can be reduced only by reducing the flow rate in the cell culture area. Typically, this is most directly achieved by increasing the height of cell culture chambers, however, if the application allows, the culture well can be designed so that barriers block direct flow and nutrients are supplied only through diffusion (Coluccio et al., 2019). Cells can also be conditioned to withstand more shear stress if seeding protocols are optimized for strong adhesion and early exposure to flow conditions.

3.3.2 Device Seeding Techniques

In ex vivo cell culture, an extracellular matrix (ECM) is often applied prior to seeding to create a favorable environment for cell adhesion. ECMs are typically comprised of fibrous non-cellular proteins that provide a structural framework for cell growth and may additionally contain and provide storage for growth factors and nutrients. In a microfluidic environment where shear stresses can be large and the channel walls often have a very low degree of surface roughness, a good ECM coating is a practical requirement to maintain cell adhesion. Laminin, fibronectin, and collagen are commonly applied as ECMs in microfluidic devices; however, the mouse derived hydrogel, Matrigel (Corning Inc.), is a highly effective surface coating for many applications. Matrigel includes additional growth factors that improve cell health while providing a structural framework for strong cell adhesion. Additionally, Matrigel coatings have contributed no noticeable effect on impedance measurements in cell culture media.

Once the ECM coating is applied, cells can be prepared for seeding. Cells can be cultured through standard protocols on Petri dishes and allowed to proliferate in an incubator until near confluence. Once a sufficient culture has been established cells can be cleaved from the dish using Accutase or trypsin and centrifuged. Dissociated cells can then be re-suspended in the desired concentration of media before seeding. For average epithelial cells, a very dense suspension of roughly 1500 cells/μL will require less culture time under microfluidic flow. The cell slurry can be injected into the device and will form a monolayer through sedimentation. To halt flow and immobilize cells for adhesion, all liquid ports should be joined in one liquid reservoir.

Seeding of the microfluidic chip is typically performed by hand and therefore poses one of the greatest risks to introduce unwanted bubbles to the setup. A few other precautions are recommended to prepare the chip for seeding. Pre-filling the chip with a surfactant, such as ethanol, is a good way to wet complex features with reduced risk of creating air pockets. The surfactant should be thoroughly washed out with deionized water prior to avoid any exposure to the cells. Thereafter convex droplets should be maintained on all liquid ports of the microfluidic chip until it is connected to the flow system. Droplets ensures that liquid to liquid contact can always be formed for seeding and media changes.

3.4 Results

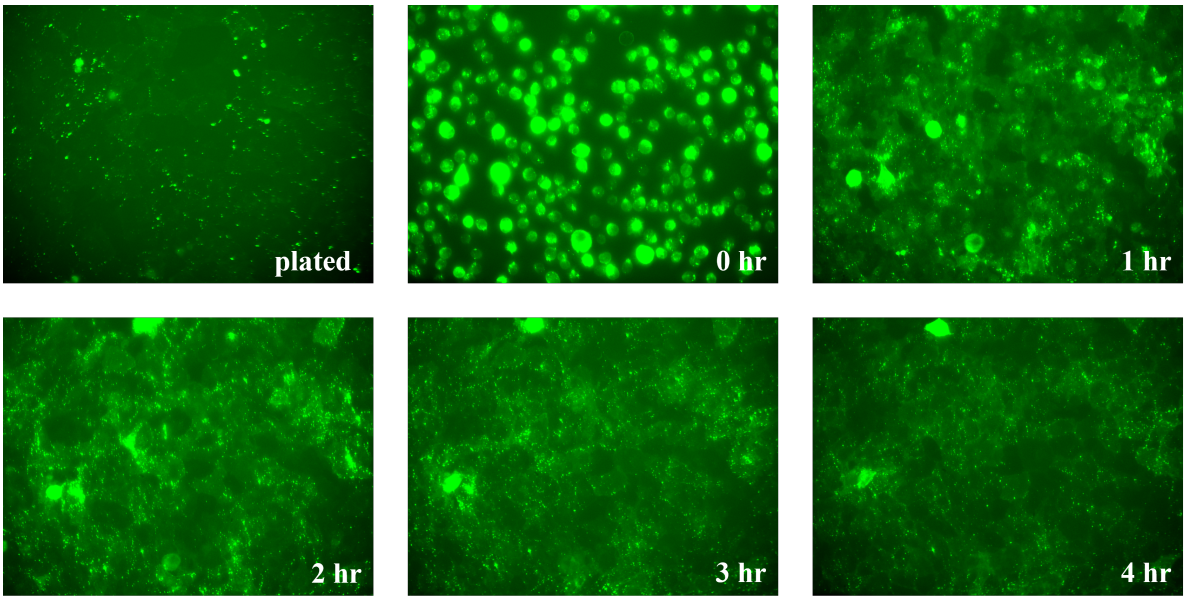

Figure 3.6: Time course of NRK-49F cells seeded into a microfluidic device. Cells have been genetically modified such that the Cx43 protein is marked with green fluorescent protein. After 4 hours, connexins have migrated to the cell boundaries, forming gap junctions (GFP false color, 20x).

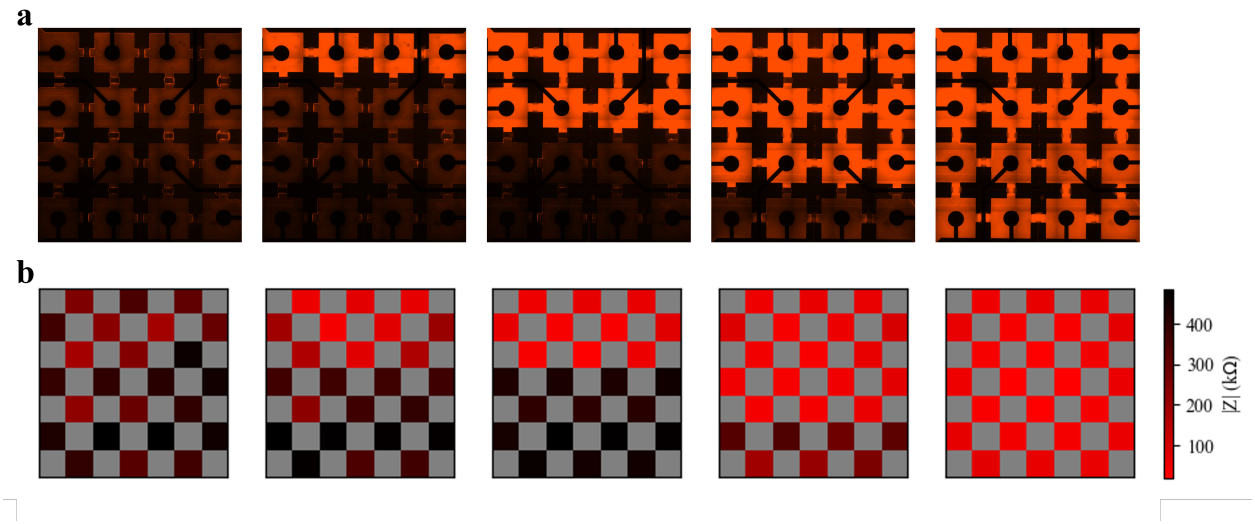

Figure 3.7: Demonstration of pneumatic valve control and electrical measurement facilitated by the Lab-on-Scope platform. A device containing 16 chambers separated by elastomeric microvalves was (**a**) programatically perfused with a conductive rhodamine-dyed solution (phase contrast/RFP fluorescence composite, 4x, false color), while (**b**) electrical resistance measurements between electrodes pairs in each adjacent well recorded.

3.4.1 Confluent Cell Culture and Fluorescence Monitoring

Through fine fluid control, integrated heating, and enabled fluorescent imaging, the lab-on-scope platform is able to capture the successful establishment of a well connected confluent cell monolayer in a microfluidic chip. Figure 3.6 shows a time course of NRK cells being seeded into a microfluidic device. Cx43 proteins in the cells are marked with green fluorescent protein. Immediately after seeding (0 hr), the cells are spherical and the connexins are conglomerated due to dissociation. As the cells sediment and adhere over 4 hours in the Lab-on-Scope, these proteins redistribute to the cell edges, forming gap junctions and a well connected network.

3.4.2 Fluid Control and Impedance Measurement in an Arrayed Device

As a demonstration of fluidic and pneumatic control paired with electrical measurement, an arrayed device was tested. The microfluidic device consists of 16 chambers, each containing an electrode and separated from its neighbors by a normally closed pneumatic microvalve. A conductive 1 M

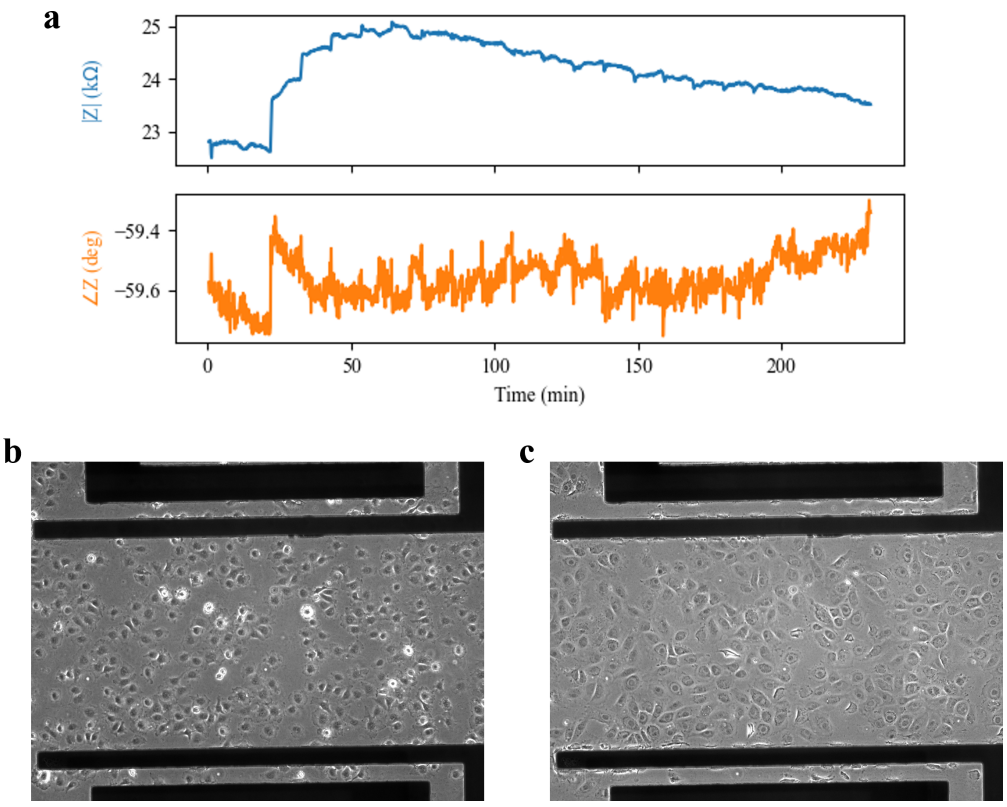

Figure 3.8: Electrical monitoring of cell development in a microfluidic device. (**a**) NRK-49F cells were continuously electrically monitored at 1 kHz and sampling period of 10 s. Phase contrast images (10×) show the culture (**b**) immediately after seeding and (**c**) after 3 hours. Flow in the channel was initiated after 20 min causing significant flattening of the cell structures and increased impedance.

NaCl solution with rhodamine dye was perfused into the device along with undyed deionized water in a programmatic sequence. Figure 3.7a shows the stitched fluorescence images of the device in each state of the control sequence. The corresponding impedance measurements at 1kHz are shown in Figure 3.7b. The similarity of the images and impedance measurements demonstrates the utility of the platform to synchronously monitor the device optically and electrically, while pneumatically controlling flow in the device.

3.4.3 Impedance Monitoring of Culture Confluence

As additional demonstration of the suitability of the platform to facilitate cell culture and impedance monitoring, confluence monitoring is performed during cell culture. The formation of a tight monolayer can be detected electrically in a manner similar to TEER (De Blasio et al., 2004; Gerasimenko et al., 2020). Figure 3.8 shows the results of this experiment. NRK-49F cells were seeded into a microfluidic device at 3750 cells/µL and allowed to grow into a confluent monolayer for more than 3 hours. Electrical impedance was recorded continuously with a sampling time of 10 s and a source stimulus of 1 µA at 1 kHz. 20 minutes after initial seeding, moderate flow was initiated in the channel which triggers distinct morphological change of the cells in response to shearing forces. Under flow these epithelial cells flatten to the substrate, reducing their profile and expanding laterally. This change is observed in the sharp increase in the impedance profile in Figure 3.8a.

3.5 Conclusions

A Lab-on-Scope system has been proposed to closely integrate the peripheral elements necessary to support modern biomicrofluidic experiments. The system brings transparent heating, liquid and pneumatic control, and electrical sensing/stimulation closer to the microfluidic chip for enhanced experimental control. Further, the system can integrate flow rate monitoring, pressure control, and external solenoid valves for complete programmatic control of experimental conditions. A graphical user interface has been developed to unify communication and timing between all the elements, and allow a convenient user experience. The system is suitable for use in a wide variety of microfluidic and biomicrofluidic experimentation. As a demonstration, 2D electrical resistance mapping was performed on a 16 well device containing 24 elastomeric microvalves. Further, NRK cells cultured using the platform developed tight junctions in a healthy monolayer, as reflected in continuous electrical impedance monitoring of the cell layer. Overall, the Lab-on-Scope system aims to unify all of the microfluidic peripherals into a compact and cost-effective form factor, expanding access to microfluidic technologies and enabling greater programmatic control of experimental conditions.

Chapter 4

LAMINAR FLOW BASED MICROFLUIDIC DEVICES TO INTERROGATE GAP JUNCTION CONNECTIVITY

4.1 Introduction

4.1.1 Importance of Gap Junction Connectivity to Developmental Biology

Intercellular communication is mediated by cytoplasmic couplings called gap junctions. In vertebrates, these intercellular channels are formed from clusters of hemichannel connexin proteins located on the cell membrane that allow direct diffusion of signaling molecules (Harris, 2001). As the most direct mediators of cell-to-cell communication, gap junctions play a crucial role in the network dynamics that appear to govern many important developmental processes, including embryogenesis, regeneration, and cancer suppression (Mathews and Levin, 2016).

In normal growth, gap junctions appear necessary to establish large scale patterns and to guide pluripotent cell fates toward the correct morphology. Gap junction expression has been shown to affect organ and limb patterning (Mathews and Levin, 2016; Allen, Tickle, and Warner, 1990), the establishment of left-right asymmetry (Oviedo and Levin, 2007), and the differentiation of many cell types, including lens cells (Gu et al., 2003), dental pulp stem cells (S. Li et al., 2015), and neuronal precursors (Bani-Yaghoub et al., 1999). Gap junctions also seem to serve a central role in regeneration (Lorraine, Wright, and Martin, 2015) and respecification. In planarian flatworms, disruption of gap junction communication during regeneration can lead to double-headed specimens or even worms with characteristics of different planarian species (Emmons-Bell et al., 2015; Oviedo, Morokuma, et al., 2010). The importance of gap junction connectivity to developmental biology suggests potent applications in synthetic morphology and tissue engineering.

Aberrant gap junction expression is associated with various disease states, including tumorgenesis and cancer. Metastatic cell behavior models primitive unicellular activity disconnected from a larger computational network which would direct its morphogenetic goals (Moore, Walker, and Levin, 2017; Levin, 2019). Thus, tumor tissue expresses less gap junctions and lowered gap junction connectivity is correlated with tumorgenesis (Aasen et al., 2016; Borek, Higashino, and Loewenstein, 1969; McEvoy et al., 2020). Restoring intercellular connectivity and normal bioelectric signaling is an emerging therapy approach for endogenous cancer suppression.

The importance of gap junction communication to so many fundamental processes in developmental biology motivates the development of a reliable and repeatable assay to quantitatively assess gap junction connectivity in cell networks. Further, to investigate functional roles, assays that can

manipulate junction dynamics with agents such as chemical gap junction blockers are needed.

4.1.2 Approaches to Gap Junction Measurement

Gap junction connectivity can be measured electrically through dual whole-cell patch clamping. This technique produces high fidelity measurements of the conductance between isolated cell pairs (Veenstra, 2001). However, the process is expensive, invasive (compromising the cell membrane to introduce patch pipettes), and technically difficult to perform (Veenstra, 2016). Further, dual cell patch clamping measurements characterize only two cells, failing to capture larger network dynamics. While analysis of capacitive transients in single cell patch clamping has been shown to reflect a cell's connectivity to its network (Roos, Zoelen, and Theuvenet, 1996; E. G. A. Harks et al., 2003), throughput for patch clamping is extremely low, sampling only a few individual cells while requiring expensive equipment and specialized labor.

The diffusion of membrane impermeable fluorescent dyes can also be optically traced to measure gap junction connectivity (Abbaci et al., 2008). Dye can be introduced to a tissue sample through invasive means, including microinjection (Meda, 2000) and scrape loading (Babica, Sovadinová, and Upham, 2016), or can be pre-loaded into a cell population and then co-cultured with non-dyed cells (Warawdekar, 2019). New microfluidic approaches have also sought to use laminar flow to spatially confine membrane permeable dye and to monitor its intercellular diffusion beyond the laminar boundary (Cédric Bathany et al., 2011; S. Chen and L. P. Lee, 2010). These methods struggle to provide continuous real-time quantitative measurement of intercellular connectivity due to the difficulty of dye washout and reinjection. Redistribution techniques, such as fluorescent recovery after photobleaching (FRAP) Wade, Trosko, and Schindler, 1986, can offer near real-time measurements. However, dye transfer in general may not fully capture bioelectric signaling as junctions that are electrically coupled may not effectively transfer dye due to molecular size or chemical properties Traub et al., 1994; Steinberg et al., 1994.

Cedric Bathany et al. (2012) proposed an electrical measurement of gap junction connectivity through a microfluidic sucrose gap platform. The device established trilaminar flow, wherein two conductive saline streams act like a sheath for a non-conductive sucrose solution. The sucrose region provides electrical isolation over a cell monolayer, forcing electrical current through the gap junctions and yielding a measure of gap junction conductance in the cell network. Here, we attempt to replicate and improve upon the findings of Cedric Bathany et al. (2012). Despite methodological improvements, we ultimately report that the approach may not be as reliable as once thought for electrical gap junction interrogation. However, important considerations for design of electrical sucrose gap platforms based on trilaminar flow are explored and potential sources of error based on updated bioelectrical modeling are presented.

4.2 Methods and Design

4.2.1 Trilaminar Device Design with Integrated Microvalves

Previous trilaminar sucrose gap devices used a compression design to seal rigid microfluidic channels against a glass backing at the time of experiment. We have created a design for closed devices to increase repeatability and experimental control.

Transitioning to a closed design permits the “soft lithography" manufacturing approach that is ubiquitous in microfluidic devices (Whitesides, 2006). Because soft lithography is a replica molding technique, many identical devices can be produced through relatively cheap, low temperature processes. Closed devices eliminate the risk of fluid leakage and reduce the risk of introducing bubbles or contaminants that compression devices can experience during assembly. Generally, closed devices should lead to better test-to-test repeatability as the channel geometry is fixed in place.

Most importantly, adopting a closed fabrication regime presents the opportunity to integrate elastomeric valves for on-chip fluid control. The sucrose solution is not a biologically relevant environment and prolonged exposure can lead to membrane potential depolarizaion and adverse cell health effects. Therefore, the sucrose gap conditions should be maintained for as short a time as possible between assays. If the perfusion switching junction for the sucrose solution is located off-chip, a macroscale dead volume of solution in the tubing must be flushed between each experimental condition. Flushing the dead volume either costs time (usually several minutes) or compromises cell health due to excessive shear stress if the flow is too rapid. Integrating pneumatic microvalves into the chip results in microsecond solution exchange, eliminating this trade off.

The primary disadvantage of the closed device approach is that it shifts burden from troublesome device assembly to cell culture in the microfluidic chip. Cells must be seeded into the device and cultured over the electrodes until they form a connected monolayer, which is a lengthy process that can practically limit testing throughput. Further, cells seeded in this manner distribute throughout the device, including in the upstream saline side channels, which can be a source of flow instability. Additionally, the closed devices are fabricated using the elastomer, PDMS, which is moderately gas permeable and has been shown to absorb small molecules (Meer et al., 2017). Finally, the closed device design *a priori* limits the number of different sucrose perfusions that can be used in the assay. In this work we have opted to switch between two solutions, but more channels could easily be added in a future design.

Figure 4.1a shows the design for a closed trilaminar sucrose gap device with integrated microvalve switches. Saline solution (with membrane non-permeable dye for stream width tracking) is perfused into fluidic ports 3 and 4. normally-closed elastomeric valves (pneumatic ports a and b) control perfusion of sucrose solutions into the central inlet channel from either fluid port 1 or 2. Three

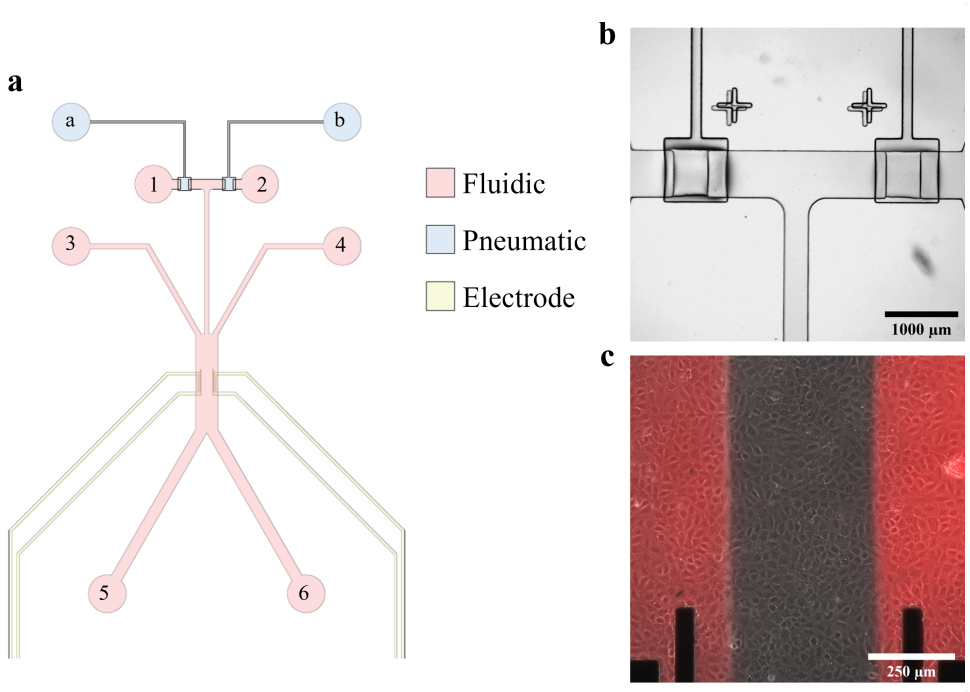

Figure 4.1: Trilaminar flow sucrose gap device design. (**a**) Saline is perfused into fluidic ports 3 and 4, while sucrose solution feeds into ports 1 and 2, creating a region of trilaminar flow over planar microelectrodes. (**b**) Flow into the middle sucrose channel is controlled pneumatically by normally-closed elastomeric valves, shown in the open position (4x, brightfield). (**c**) NRK cells are cultured in the device and measured under the trilaminar sucrose gap. To monitor the laminar flow boundaries, rhodamine dye is added to the saline channels (10x, composite phase contrast/RFP, false color).

fluidic inlet channels converge to form a sucrose gap region of trilaminar flow over the planar electrodes (Figure 4.1c). The central sucrose channel is approximately 250 µm by 7.5 mm and the side saline channels are 275 µm wide with a total length of 8.6 mm. These dimensions are designed such that the sucrose stream occupies 30% of the total 1200 µm width in the trilaminar flow region, where the inner electrode spacing is 600 µm. Sensing electrodes are 50 µm by 1350 µm, and source electrodes measure 100 µm by 900 µm. The effluent is divided into two channels to insure electrical isolation by splitting the sucrose stream. The fluidic layer is made as deep as reasonable in the fabrication process (75 µm), both to maximize the available nutrient volume during culture and to reduce the impact of the cell layer on the hydrodynamic resistance of the channels.

The switching valves associated with pneumatic ports a and b are left in their normally-closed state during cell seeding, ensuring that no cells are trapped under the valve seat. This approach guarantees that the valves seal tightly against the substrate, preventing leakage and ensuring consistent switching. Integrating elastomeric valves into the design allows the sucrose solution to be switched and completely re-perfused within hundreds of microseconds, drastically reducing the run time of

gap junction blocker assays.

4.2.2 Fabrication

Device fabrication, including selective bonding of the elastomeric valves by an oligomer stamping method, follows a protocol previously described.(Dungan et al., 2023)

Cr/Au electrodes were sputter coated onto glass microscope slides using a liftoff process. The substrates were cleaned by piranha etch and oxygen plasma treatment. Electrodes were photolithographically patterned using an Omnicoat (Kayaku) release layer (spin coated at 3000 rpm for 30 s) and positive photoresist AZ9260 at approximately 6.5 µm thickness. After oxygen plasma treatment (200 W, 30 s, 70 mT), Cr/Au electrodes were deposited by sputter coating to a depth of 30 nm and 210 nm depth, respectively. Liftoff was performed Microposit Remover 1165 at 55°C for more than 8 hours.

The microfluidic device is composed of two layers of replica molded PDMS (Sylgard 184) prepared at the standard 10:1 elastomeric base to curing agent ratio. Master molds for both layers were fabricated on silicon wafers using negative photoresist SU8-3050. The SU8 was deposited using standard lithographic techniques to a depth of 75 µm. Following silanization, the fluidic layer was spin coated with uncrosslinked PDMS for 60 s at 2000 rpm, while the pneumatic layer was cast molded to a depth of 5 mm.

The layers were bonded by oxygen plasma treatment (20 W, 30 s, 500 mT) and alignment was performed with a custom rig. First, the pneumatic layer was bonded over the thin membranes of the fluidic layer. The device was released from the wafer and cored to form inlet/outlet ports. After plasma treatment, valve seat areas were stamped with untreated PDMS to selectively remove the surface activation before bonding onto the glass substrate.

4.2.3 Experimental Setup

All experiments were driven by pressurized nitrogen gas (Airgas, Inc), which was programatically controlled by OB1 Mk3+ regulators (Elveflow). A portable laboratory pump provided vacuum at -75 Torr (N810FTP, Ideal Vacuum Products). Compact magnetically-latching solenoid valves (LHLA1231111H, Lee Co.) were used to switch between vacuum and positive pressure. Electrical measurements were recorded using a Keithley 6221 alternating current source (Tekronixs, Inc.) in conjunction with a SR830 digital lock-in amplifier (Stanford Research Systems). All stimulus signals used 100 nA amplitude. The lock-amplifier was used in floating configuration with a 300 ms time constant. High resolution images were captured by an EVOS M7000 inverted fluorescence microscope. Devices were imaged through a transparent indium tin oxide coated heater which was maintained at 37°C.

4.2.4 Cell Culture Protocols

NRK-49F is a fibroblast cell line that is derived from rat kidney and is known for dense expression of gap junctions (primarily Cx43) (E. Harks et al., 2003; Yan Xu et al., 2021). The line has been previously used to study gap junction connectivity (Cédric Bathany et al., 2011; Shao et al., 2005). NRK cultures were passaged a minimum of 2 times and a maximum of 5 times after being thawed from frozen stock and were maintained at 70-85% confluence. Cells were dissociated from plated cultures by application of Accutase for 6 min and seeded into the microfluidic devices at a density of 15,000 cells/μL. Prior to seeding, devices were treated with a 1:20 by volume dilution of Matrigel in DMEM and incubated for greater than 30 minutes. Media in the cultured devices was carefully exchanged every hour, and devices were connected to the perfusion system after more than 4 hours of static incubation at 37°C.

4.2.5 Chemicals and Reagents

The stock sucrose solution was prepared at 300 mM concentration in deionized water and passed through a 0.22 μm filter. In experimentation, sucrose solution was balanced with DMSO to match the volume fraction in the 2-aminoethoxydiphenyl borate solution (0.1%). 2-APB (Sigma-Aldrich) was dissolved to 100 mM in DMSO and stored in aliquots at -20°C. The saline solution consisted of 75 mM NaCl, 15 mM KCl, 2 mM $MgCl_2$, 1 mM $CaCl_2$, 94 mM mannitol, and 10 mM HEPES buffer. The solution was corrected to a pH of 7.4. Cell culture media consisted of Fluorobrite DMEM (Thermo Fisher Scientific, Inc.) with 10% by volume fetal bovine serum, 100 U/mL penicilin-streptomycin, and 1× GlutaMAX (Fisher Scientific, Inc.). Rhodamine B dye (Fisher Scientific, Inc.) was added to solutions at 1.5 μM concentration.

4.2.6 Molecular Biology and Generation of a Stable Cell Line

The CAG ArcLight construct was subcloned from the plasmid ArcLight Q239 using HindIII and HpaI and was a gift from Vincent Pieribone (Addgene plasmid #36856) Jin et al., 2012. The subcloned fragment was cloned into a pENTR1A plasmid with a CAG promoter and multiple cloning site (MCS) followed by an SV40 poly(A) using the same sites as were used in excising the fragment from the parent plasmid. The resulting pENTR1A CAG ArcLight plasmid was then Gateway LR clonased (11791020, ThermoFisher) into the hyperactive piggyBac transposase-based, helper-independent, and self-inactivating delivery system, pmhyGENIE-3, a gift from Stefan Moisyad Marh et al., 2012; Owens et al., 2013. The pmhyGENIE-3 had a neomycin resistance gene in the backbone. The resulting plasmid HypG3 NeoBB ArcLight was purified using a ZymoPURE Plasmid Miniprep Kit (D4210, Zymo Research) and used for subsequent transfection.

The NRK-49F ArcLight cell line was made by transfecting the cells at 30% confluence with 500 ng of the transfection grade plasmid, 1 μL of Lipofectamine 3000 (L3000008, Thermo Fisher Scientific),

and 1 µL of P3000 reagent in 50 µL of Opti-MEM I Reduced Serum Medium (31985062, Thermo Fisher Scientific) and then adding the complex to one well of a 24-well plate containing complete FluoroBrite DMEM media (Thermo Fisher Scientific). Fresh culture media was added after 24 hours and replaced the reagent media. Cells were under selection with 1.2 mg/mL G418 (10131035, Thermo Fisher Scientific) for 2 weeks before serial dilution into 96 well plates for clonal isolation. Only the clone showing robust growth and strong expression was chosen.

4.3 Results

4.3.1 Stream Width Instability Causes Measurement Error

Stream width stability and consistency is crucial to the operation of the laminar flow device. The width of the sucrose gap is sensitive to changes in cross-sectional area of the upstream channels such as debris or bubbles, as well as to pressure imbalance (including hydrostatic pressure), viscosity differences in solutions, and temperature differentials (affecting the viscosity). To maintain constant stream width all of these factors must be tightly controlled. (See Appendix D for an analytical characterization of stream width under trilaminar flow.)

To study the effect of stream width variation on electrical impedance in the trilaminar flow microfluidic device, we conducted a control experiment in which the middle stream width was varied via a ramp of the driving pressure applied to rhodamine-dyed sucrose in the middle stream. Figure 4.2 shows these results. At each driving pressure, the stream was captured through fluorescent microscopy and was spatially averaged to produce an intensity profile in the axis perpendicular to flow. The stream width was then extracted from each frame as the full width at half the maximum peak height (Figure 4.2c). Electrical impedance was simultaneously measured continuously and the average value corresponding to each pressure step was extracted (Figure 4.2b). The resulting plots of stream width versus measured impedance are shown for a 100 Hz electrical stimulus and a 1 kHz signal in Figures 4.2d and 4.2e. The resulting curves are fit to an error function which is used as a practical form here but may be a physically relevant model (see Appendix D).

At 100 Hz, the maximum magnitude sensitivity corresponds to 1.746 kΩ/µm, showing that small fluctuations in pressure or minuscule obstructions to flow that alter the stream width by only microns can have significant impact on the measurement. Perhaps more importantly, small differences in viscosity, hydrostatic pressure in the reservoirs, or hydraulic resistance in delivery (i.e. bubbles, tubing lengths, etc.) between the sucrose test solutions can produce significant impedance mismatches even when stream widths appear matched under visual inspection. These results suggest that tests should not run unsupervised without stream width tracking. However, corrective calibration of stream width differences may be possible when following a procedure similar to the experiment of Figure 4.2 (see Section 4.3.3).

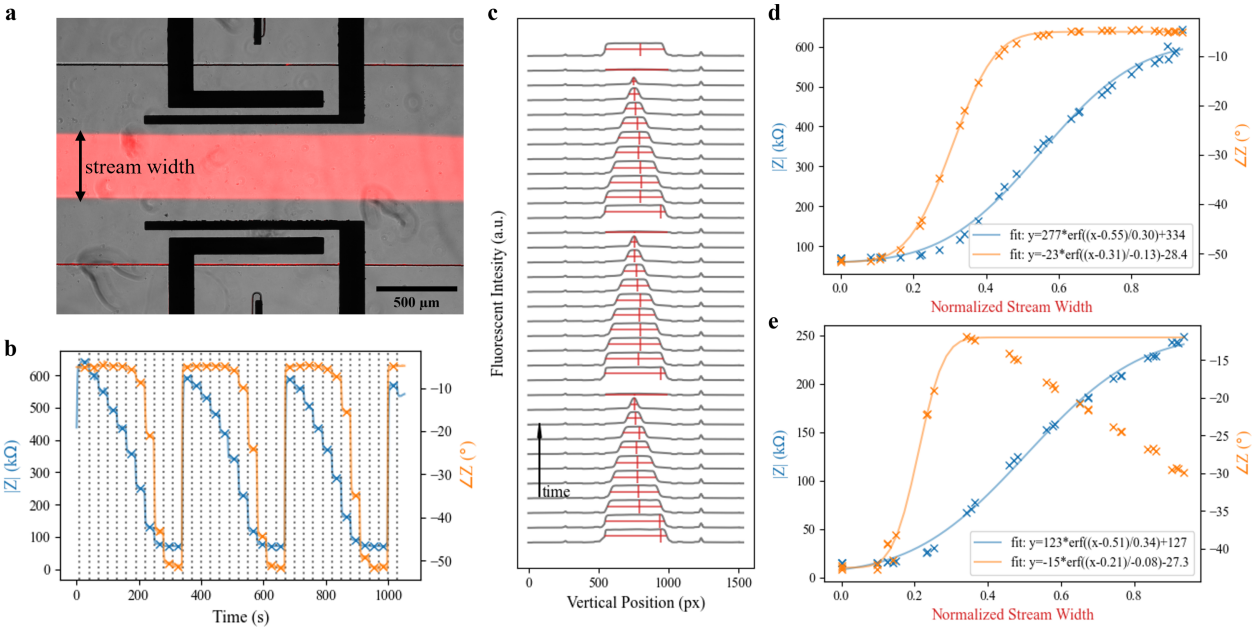

Figure 4.2: Impedance dependence on stream width. (**a**) The stream width in the trilaminar flow device was monitored via fluorescence microscopy and rhodamine dye. (**b**) The center stream width was varied by ramping the driving pressure, while the electrical impedance was continuously monitored at 100 Hz. (**c**) For each step, the stream widths are extracted from fluorescence images and (**d**) plotted against the average impedance over that interval. The results show good agreement with an error function fitting. Widths are normalized against the sensing electrode separation. (**e**) The experiment was repeated at 1 kHz, resulting in a degradation of the phase characteristic.

At low frequency (100 Hz) there exists an operating region above roughly one third of the available channel width where the phase is resilient to stream width variation. Using the trilaminar device in this operating region is a promising option for robust operation, though phase results lack the direct physical interpretation of resistance values. Additionally, At higher frequency (1 kHz), the same operating region shows linear decay, so the phase dependency may not be a reliable marker for all assays.

4.3.2 Need for Closely Balanced Control Solutions

As a gap junction blocker assay, this measurement is fundamentally differential. Any effect of a chemical gap junction blocker on cellular network conductivity must be judged against an appropriate control solution. The control solution must be biologically inert, viscosity matched, and osmotically balanced. But crucially, the control solution must also be carefully balanced against the test solution conductivity to provide a fair means of comparison.

Additionally, the large polar molecules, such as 2-APB (pK_a=9.6 (Bilmen et al., 2002)), can significantly impact the electric double layer formed at electrode interfaces, leading to an altered

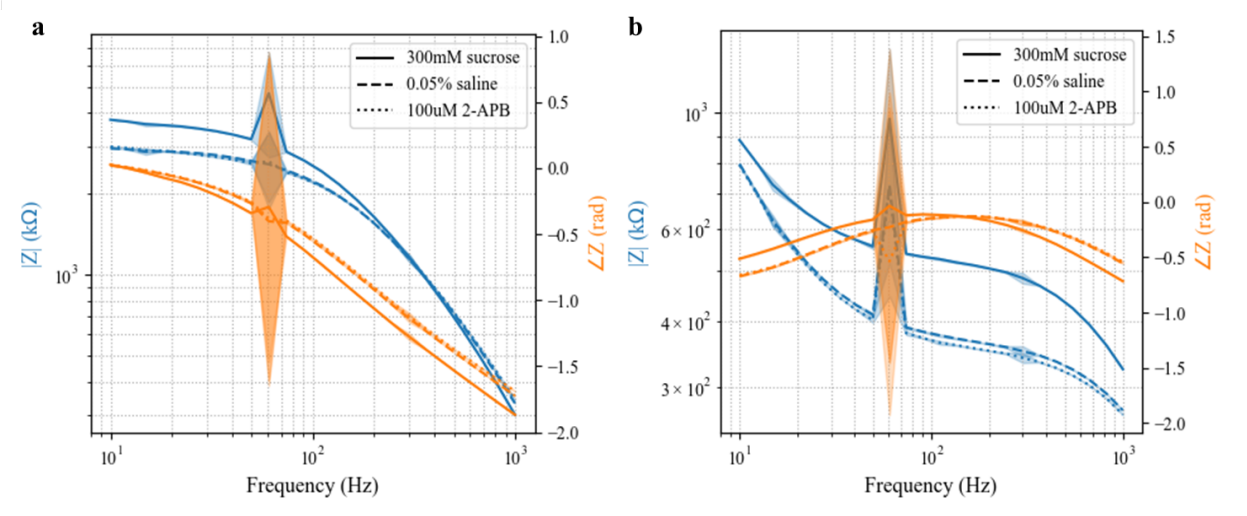

Figure 4.3: Test solutions must be carefully electrically balanced in the trilaminar device. (**a**) Impedance sweeps for sucrose solution and sucrose solution with 100 µM 2-APB filling the full channel (not trilaminar) allow electrode interactions that result in a magnitude crossover at 339 Hz. However, (**b**) impedance sweeps of the same solutions in trilaminar flow do not show the same frequency dependence. Adding 0.05% by volume saline to the sucrose solution results in a good impedance match, especially at low frequencies. Each sweep represents the aggregated data of 3 trials. Confidence intervals represent one standard deviation.

frequency response. Figure 4.3 demonstrates this issue for the case of 2-APB. When the solutions were allowed to fill the full channel of the device (including covering the electrodes), the impedance sweep (Figure 4.3a) for the 2-APB solution initially shows greater magnitude at low frequencies but crosses over the control solution at 339 Hz. However, under trilaminar flow, the same solutions have a consistent magnitude separation in the absence of electrode interactions (Figure 4.3b). Thus, each reagent in the assay requires a carefully balanced control formulation that is measured in stable trilaminar flow at the test frequency. Our testing found that the addition of 0.05% saline solution by volume to the sucrose control solution results in a good impedance magnitude match for a 100 µM 2-APB solution at low frequencies.

Because of electrode interactions, external conductivity meters are unlikely to be adequate to evaluate control solution formulations. These experiments should occur under trilaminar flow, which should be optically monitored for stable and repeatable flow as we have shown that micrometer deviations in stream width can result in kilohms of measurement error. Even when a balanced formulation is reached the repeatability of preparation and purity of stock solutions represent a significant source of error.

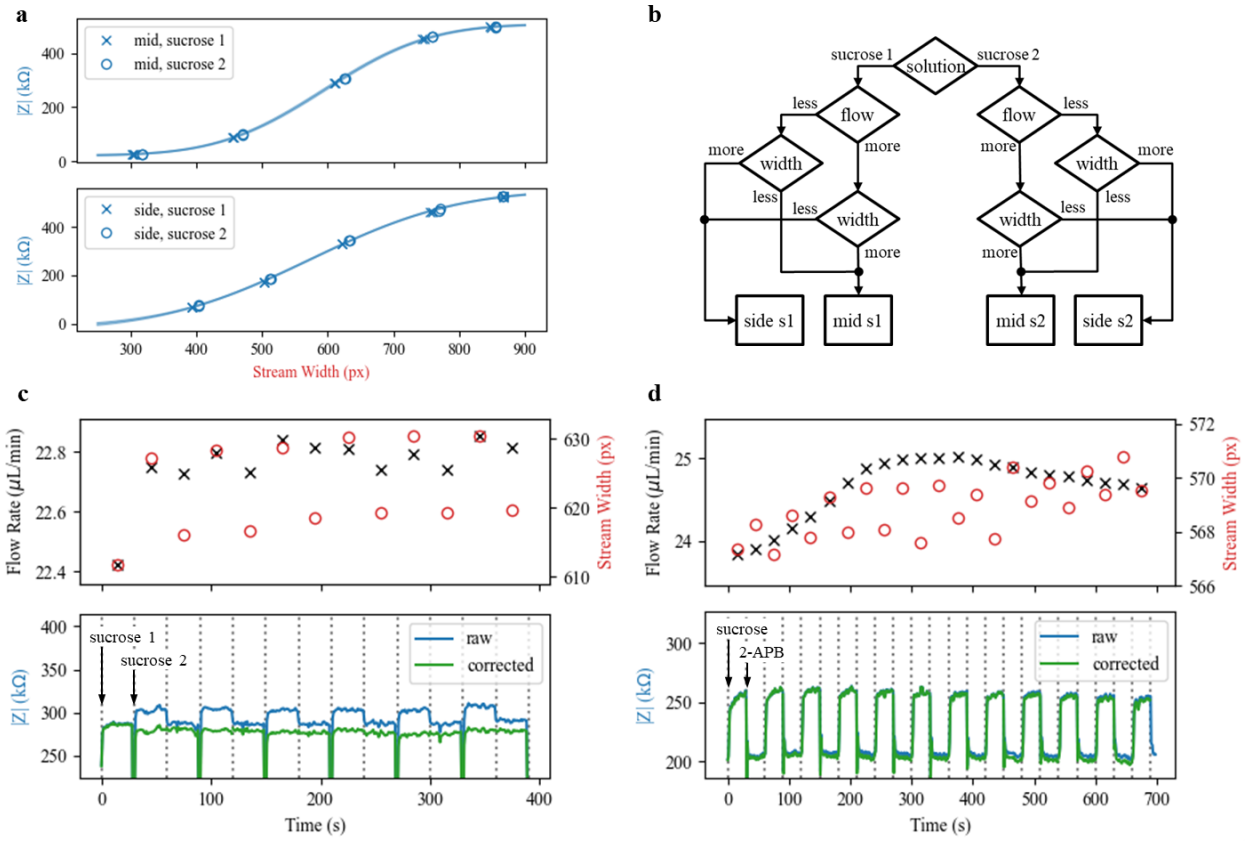

Figure 4.4: Calibration scheme to correct for stream width variation. (**a**) For both solutions, calibration sweeps were performed to find an error function fit for the impedance versus stream width. For the“mid" sweeps the middle sucrose solution pressure was varied to produce the width change, while pressure on the side saline channels was varied to produce the “side" curves. (**b**) A decision tree using the stream width and flow rate information was used to determine which of the four calibration curves should be applied to subsequent data. In switching experiments, the calibration approach was effective in correcting stream width differences in (**c**) a control experiment switching between two sucrose solutions, but did not affect (**d**) a switching experiment where the solutions' conductivity does not match (300 mM sucrose and 100 μM 2-APB at 410 Hz in this case).

4.3.3 Novel Calibration Approach Correct Stream Width Variation

We propose a calibration scheme to correct electrical measurement error due to stream width variation in trilaminar flow devices. To verify the approach, two matching sucrose solutions were alternately perfused into the device as a control experiment shown in Figure 4.4. In order to determine the dependency of measured impedance on stream width, two calibration experiments similar to that of Figure 4.2 were first carried out. For each solution, the driving pressure on the middle sucrose channel was linearly ramped around the intended operating pressure. The stream width was monitored by fluorescence microscopy and electrical impedance was continuously measured, creating the “mid" calibration curves (Figure 4.4a, top). These experiments were repeated, instead varying the pressure on the side saline channels, to create the “side" calibration curves (Figure 4.4a, bottom). Each dataset in Figure 4.4a represents the extracted impedance magnitudes and stream widths from three independent pressure ramps. All four calibration datasets were fit to an error function by a least squares method.

During experimentation, the total flow rate and stream width was continuous monitored to determine which of the calibration curves was most appropriate to use to adjust the measured impedance. The decision tree in Figure 4.4b shows how the proper calibration curve was selected. For each solution, when the average flow rate increased and the center stream width increased or when the flow rate decreased along with the stream width, the “mid" calibration associated with incident flow rate changes in the middle stream was used. Increase in total flow rate resulting in lowered middle stream width or decrease in flow rate corresponding to increased stream width indicated a variation associated with the “side" calibration. Calibration was applied additively, calculating via the fitted complementary error function the impedance change associated with the stream width deviation from the initial width.

Figure 4.4c shows the effect of the calibration scheme for the sucrose control experiment. Over the full experiment, the difference between the average values of the two sucrose solutions was 17.1 kΩ in the raw data, which was reduced to 0.21 kΩ in the calibrated result. The calibration scheme could, in theory, be run in real time and at higher optical sampling rates, after initial experiments to extract the correction curves. Additionally, a similar approach should prove effective in correcting phase measurements as well, so long as an appropriate fitting function can be determined.

Importantly, this calibration approach responded only to changes in the stream width. Because the test solutions were calibrated independently, impedance differences arising from gap junction connectivity or solution conductivity were not affected. Figure 4.4d demonstrates that for a case where the test solutions have mismatched conductivity (i.e. the two curves in each plot of Figure 4.4a would not overlap), the calibration algorithm was ineffective at equalizing impedance results. The measured impedance of 300 mM sucrose and 300 mM sucrose solution with 100 µM 2-APB

(see Figure 4.3a) were still significantly different after correction.

While this approach has proven effective mitigating the effect of width deviations, it may not be effective in all circumstances. The stream width is extracted only from fluorescent imaging of rhodamine dye. If conductive species were present with significantly different diffusion coefficent from the dye, potential error might arise if the charge concentration was not well correlated with the distribution of the dye. Additionally, cell experiments increased background fluorescence and uptake of the dye into damaged cells hamper width extractions. Further, for experiments involving sensitive or poorly adhered cell cultures, the flow rate range available for initial calibration sweeps may be significantly decreased.

4.3.4 Gap Junction Blocker Assay Results

2-APB dose dependently and reversibly blocks gap junctions in NRK cells, including prominent connexins Cx43 and Cx50 at concentrations over 51.6 µM (Bai et al., 2006; E. G. A. Harks et al., 2003). 2-APB has been employed previously as a gap junction blocker assay in trilaminar flow devices (Cedric Bathany et al., 2012).

Over a number of tests, our trilaminar platform has failed to measure significant gap junctional resistance changes in NRK-49F cultures in response to the chemical gap junction blocker, 2-APB. Figure 4.5 shows a representative test in which the osmotically balanced control solution (300 mM sucrose, 0.1% DMSO, 0.05%conductive solution) is alternately perfused with a solution containing gap junction blocker (300 mM sucrose, 0.1% DMSO, 100 µM 2-APB) over NRK-49F cells in 240 s increments. Images from the beginning and end of the sample show consistent flow conditions and acceptable cell health. While the raw data shows a minor increase in the measured impedance under flow of the 2-APB solution, applying correction technique described in Section 4.3.3 to account for stream width and flow rate variation results in a reversal of the results. That is, the increase in impedance in the raw data was due to stream width variation that is difficult to perceive by eye, and no significant change in the cell impedance was due to the presence of gap junction blocker.

Across multiple samples, no significant impact of treatment with gap junction blocker is observed. Figure 4.6 shows the results of multiple trilaminar flow assays using 2-APB where the electrical impedance across the sucrose gap was measured continuously at 10Hz. 2-APB tests switched every 240 s between the control sucrose solution and the 300 mM sucrose containing 100 µM 2-APB. Prior to each test calibration sweeps were performed to evaluate stream width dependence. The average value for both the control and test conditions in Figure 4.6a appears to depend primarily on the stream width, though some variability is present due to the tightness of the cell layer formed over the electrodes. Notably, the average measured impedances are not significantly reduced as compared to the no-cell control experiments, indicating an intracellular access issue. Figure 4.6b shows the

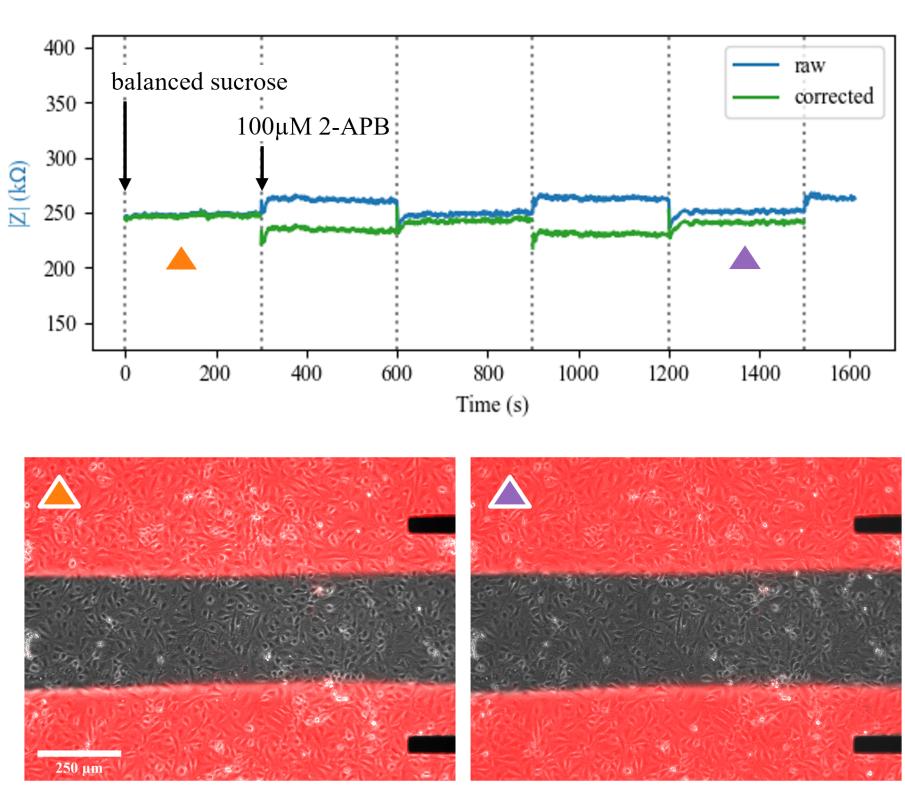

Figure 4.5: A representative system verification test using the chemical gap junction blocker, 2-APB. The blocker was alternately perfused with a balanced sucrose control solution every 240 s. Flow rate and stream width based calibration of the electrical resistance measurements shows that perceived impedance increases due to 2-APB are likely inaccurate. Composite fluorescence/phase contrast images (10x, phase contrast/RFP, false color) from the beginning and end of the sample show that cell integrity and flow control were consistent over the length of the test.

impedance magnitude difference between each successive pair of control and test conditions in the same switching experiments after calibration for stream width variation. (i.e. each data point is the result of an experimental condition measurement subtracted from a control condition measurement, so that a net increase due to the experiment conditions would yield a negatively biased distribution.) No dataset is significantly biased away from zero, meaning that exposure of the culture to 100 µM 2-APB had no meaningful effect on the measured impedances.

4.3.5 Cell Health Concerns

The trilaminar flow device poses several inherent challenges to cell health. Stable flow rates must be maintained continuously which exposes the cell layer to constant shear stress. Reducing flow rates presents a tradeoff with the electrical isolation provided by the sucrose stream as lower flow results in increased diffusion at the flow boundary (see Appendix D).

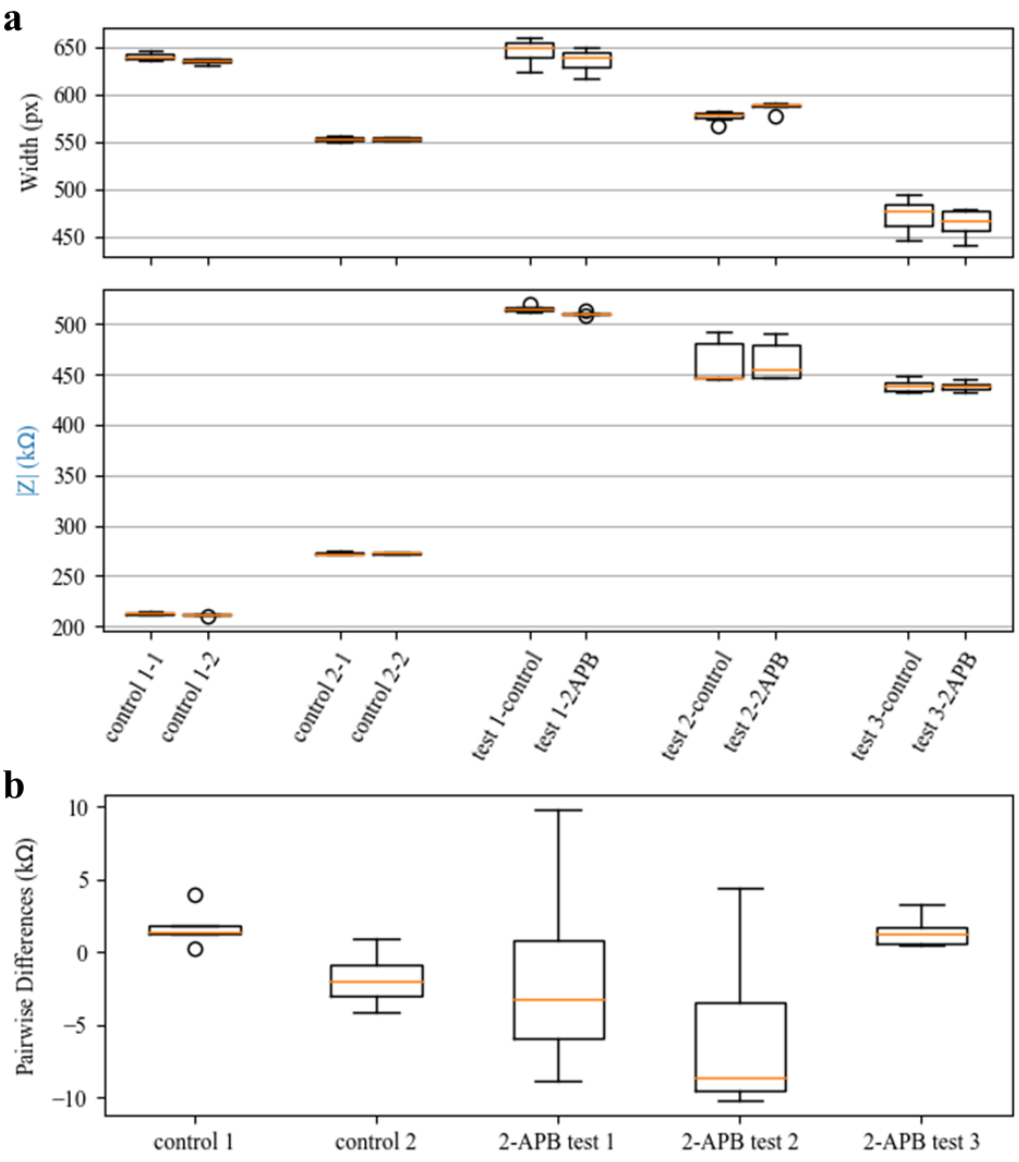

Figure 4.6: Results of trilaminar device testing with 2-APB on NRK-49F cultures. Confluent cell populations in the device were treated alternately with 100 uM 2-APB and the sucrose control for 4 minutes periods. (**a**) The average impedance values over these periods show no significant difference between the two conditions. (**b**) Results calibrated based on stream width additionally show no significant difference from control conditions. Box plots show standard quartiles.

Additionally, pure sucrose is an abiological extracellular condition and prolonged exposure to this environment is taxing on cell health. Figure 4.7 shows a culture that was exposed to sucrose gap conditions for greater than 80 minutes. Zeiosis (cell blebbing) is visible in cells in the central sucrose region. Further, unwanted cytoskeletal effects are visible, especially at the laminar flow boundaries. At the boundaries, cells retract and eventually become disaggregated from the rest

of the monolayer. The cause of this disaggregation along the laminar boundary is not clear. The solutions are osmotically balanced and pH matched. Cells in this region may experience uneven shear stress across their membranes if the solutions have significant viscosity differences. The most likely cause of these cytoskeletal effects is that cells in the boundary region may experience a large fluctuations or gradients in their in membrane potentials. Cell health concerns under sucrose flow make the system non-ideal for assays involving gap junction blockers with long uptake or washout times, such as meclofenamic acid, because interrogation times must be kept brief.

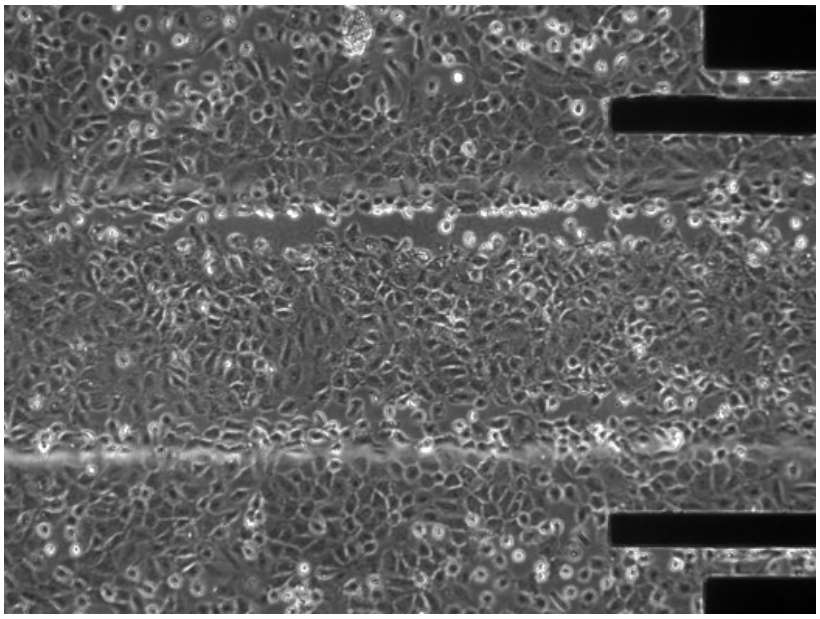

Figure 4.7: Poor cell health observed in NRK cultures exposed to trilaminar sucrose flow for greater than 80 mins. In response to stress, the monolayer disaggregates especially at the laminar flow boundaries. Zeiosis is observed in the cells that were maintained in the sucrose stream. (10x, phase contrast)

4.4 Discussion

The trilaminar flow sucrose gap approach is a promising means to isolate distinct regions of a cell layer in an attempt to force electrical signaling through the intercellular connections (gap junctions). However, the approach inherently incurs several sources of error and forces design trade-offs that make the signal through the gap junctions exceptionally difficult to recover. We review the sources of error previously described and discuss other fundamental issues with the approach, namely the lack of intracellular access and assumptions about the electrical modeling of cells living in a sucrose environment.

4.4.1 Sources of Error

We have already identified and characterized several inherent sources of error in the trilaminar sucrose gap approach. Stream width stability and repeatability is crucial to reliable operation. At 100 Hz potential error is as high at 1.746 kΩ/µm. Width variation can result from differences in flow conditions and fluid viscosity. Additionally, for gap junction blocker assays, a suitable sucrose control solution must be established for any chemical blocker that changes the conductivity of a sucrose solution. Finding reliable control solutions requires a titration search, using an equivalent electrode configuration and test frequency as the microfluidic device. The conductivity of gap junction blockers directly reduces the signal quality in an assay because the sucrose solution impedance is seen in parallel with the gap junctional network impedance. Finally, maintaining cell health in the presence of continuous sucrose flow is a concern. Poor cell health could lead to lowered connectivity in the cell layer and decreased signal. Further, cell health concerns limit the variety of gap junction blockers that are suitable for the assay to those with rapid activation and washout times.

4.4.2 Intracellular Access and Shunting Resistance

This trilaminar approach has no direct means of intracellular electrical access. Instead, electrical access into the cell layer has two primary pathways - through transmembrane protein structures or directly through the cell membrane. The former process relies on driving a drift flux of charged ions through ion channels, while the latter (in the absence of electroporation) must move charge through field effects. Neither pathway is well suited for low frequency conduction, resulting in large total membrane impedances. In whole cell patch clamp recordings, the membrane resistance is usually found to be several hundred megaOhms (Kodirov, 2023). In NRK cells specifically, the average total conductance of the ion channels in single cells was found to be 3.24 nS, corresponding to a membrane resistance of 309 MΩ, with a similar total of 2.01 nS for small cell clusters (E. Harks et al., 2003). The membrane resistance is so large that single and double shell cell models used in dielectric spectroscopy often model the membrane only as a capacitance (Youchun Xu et al., 2016). While the membrane can be capacitively bypassed at high frequencies ($\gtrsim$ 50kHz), at such frequencies the dominant charge transport mechanism is likely dipolar relaxation rather than ionic transport through the gap junctions. In the end, the intracellular access resistance, R_{access}, must be considered in parallel with the sucrose resistance (which is especially problematic if sucrose conductivity is modified by a drug or control balance). Any change in network resistance due to a gap junction blocker will be significantly degraded if the sucrose resistance does not exceed the intracellular access resistance.

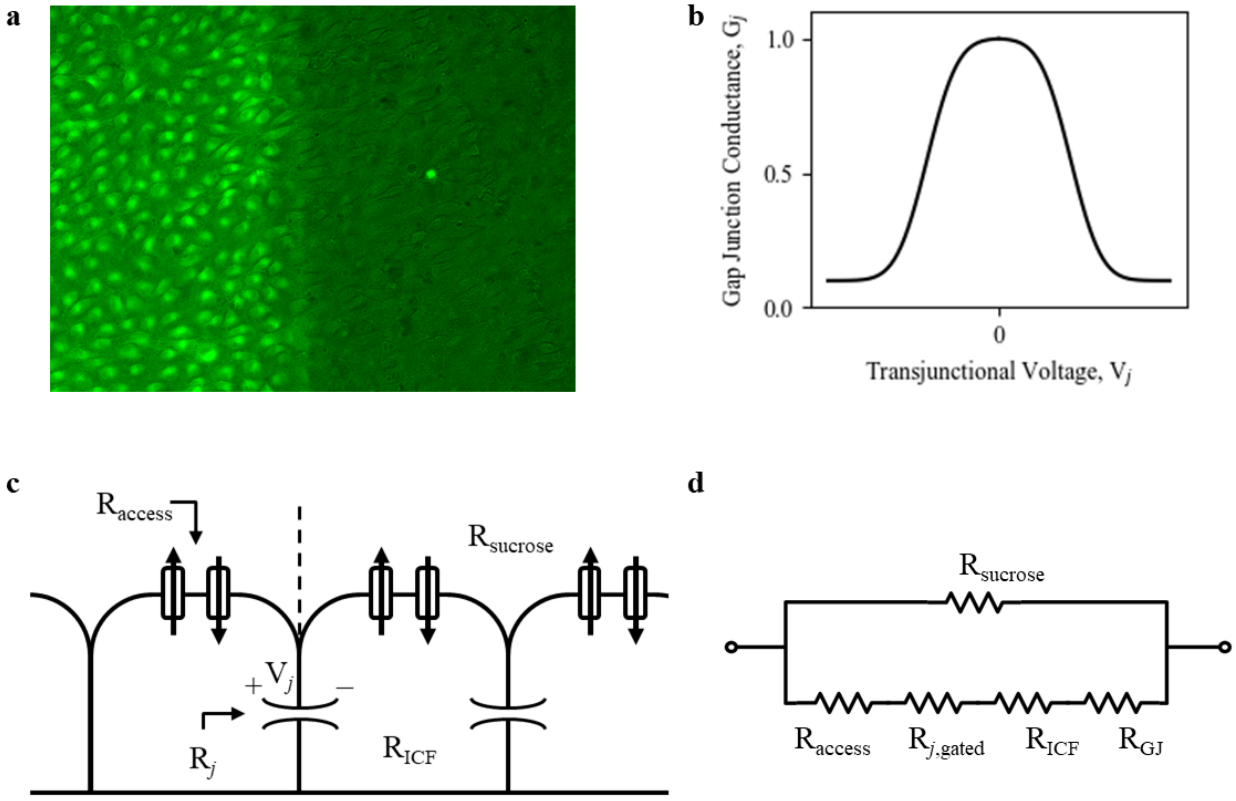

Figure 4.8: Electrical modeling of cells under sucrose flow. (**a**) Fluorescent imaging of NRK cells expressing Arclight membrane potential reporter under laminar flow (10x, GFP, false color). Cells at left are in saline solution, while cells at right appear heavily depolarized in the sucrose stream. (**b**) Typical response of gap junction conductance to transjunctional voltage, adapted from Harris (2001). (**c**) Diagram of electrophysiological mechanisms at the laminar flow boundary. (**d**) A simplified lumped circuit model showing the difficulty of recovering gap junction resistance values given the other significant impedances present.

4.4.3 Problems with the Electrical Model

Genetically expressed voltage sensors can lend some insight into the electrodynamics in the trilaminar device. Fluorescent imaging of ArcLight expressing NRK cells in Figure 4.8a shows that cells in sucrose are heavily depolarized (i.e. the net intracellular charge is positive relative to the normal resting membrane potential). This result poses a number of issues. Nearly all connexins are known to be voltage sensitive. Particularly, the junctional conductance in response to a potential difference between the adjoined cells (transjunctional voltage, V_j) has the characteristic shown in Figure 4.8b, where swings to hyperpolarized or depolarized states result in dramatic conduction loss (Harris, 2001; Bukauskas and Verselis, 2004). Large resistances due to voltage-gating effects at the sucrose border serve to exacerbate the intracellular access problem, presenting an additional large impedance in parallel with the sucrose isolation resistance that obscures gap junction changes

in the network.

Beyond membrane potential reporting, little information is available concerning the electrophysiology of NRK cells in a sucrose environment, making their behavior difficult to model electrically. For gap junction interrogation, the ideal cell response to extracellular sucrose would be the complete closing of all ion channels. Such a response would result in the membrane potential remaining at a resting level in the sucrose region and being maintained by saline contacted cells through gap junctional channels. However, Figure 4.8a shows that this is clearly not the case in the trilaminar device. Rather, transmembrane structures to the extracellular sucrose appear to be active, and vertical transport of the charge carriers in solution seems to dominate horizontal diffusion in the gap junctional network, resulting in clear depolarization. Active exchange with the sucrose solution produces a number of concerns including that the resistance of the sucrose may be further lowered by ion flux out of the cell layer. Additionally, conduction in the intracellular spaces (which is usually considered very high, with the fundamental Hodgkin and Huxley model assumes perfect conduction) may be significantly reduced. Because the charge carriers in solution are ionic species and these ions are subject to drift and diffusion out of the cell layer, we arrive at a challenge similar to attempting to transmit a longitudinal wave in a lossy medium. Benchtop sucrose gap systems are typically used to examine electrically active tissue transmitting transverse waves. The technique may be better suited to these applications where the sucrose isolation acts similarly to myelination, rather than for impedance measurements where the sucrose environment seems to have a significant attenuating factor.

In summary, Figure 4.8d provides a simplified lumped model of the significant impedances which obfuscate a measure of gap junction impedance in the trilaminar device. The device establishes a sucrose isolation impedance ($R_{sucrose}$), which should appear in parallel with the total resistance through gap junctions in the network (R_{GJ}). However, R_{GJ} appears in series with the intracellular access barrier into the cell layer (R_{access}), a significant impedance due to voltage gating of channels at the laminar flow barrier ($R_{j,gated}$), and increased resistance due to ionic depletion in the intracelluar fluid (R_{ICF}). In order to force a significant fraction of the current through gap junctions, $R_{sucrose}$ must be large comparable to the series resistances in the lower branch of Figure 4.8d. In control experiments in our devices, the sucrose impedance measured roughly 275 kΩ at 100 Hz in normal operating conditions. Each element in the series branch could reasonably be expected to be of similar or greater magnitude to the sucrose isolation impedance, resulting in poor signal quality that largely reflects only the sucrose stream width.

The problem of intracellular access can be overcome through engineering means. Three dimensional electrode surface structures in combination with electroporation have succeeded in bringing electrodes into the intracellular space, but the fabrication processes are highly non-trivial (Abbott,

Ye, Ham, et al., 2018; Ojovan et al., 2015). Improving intracellular access is likely the most important opportunity for advancement as placing electrodes in the intracellular space would cause the membrane impedance to work in favor of signal integrity (shifting R_{access} to the opposite side of the voltage divider in Figure 4.8d). The issues related to cell physiology in sucrose solution, namely cell health concerns, junctional voltage gating, and ion depleted intracellular fluid may require adjustments to the experimental approach. Rather than continuous flow, the full cell culture could be brought to normal resting equilibrium in media and then treated with chemical blockers (in media). Using integrated valves for rapid switching, a trilaminar sucrose bolus could be pulsed in and the electrodynamics of sucrose gap formation might be used to elucidate the gap junctional network connectivity. Finally, direct improvements to the control systems are still possible to further manage experimental variables. Improved flow stability through development of feedback system Fütterer et al., 2004 and improved time resolution of calibration though continuous electrical stream width monitoringMavrogiannis et al., 2017 might be achieved. Electrical measurement of gap junction connectivity in microfluidic devices should be achievable if these engineering challenges can be met.

4.4.4 Alternate Approaches

One significant system improvement would be the inclusion of an on-chip (no-cell) control site. Not only would a simultaneous control double the testing throughput, it would help alleviate the control solution issues discussed in Section 4.3.2. If test conditions can be well replicated between the two interrogation sites, on-chip controls would serve as a better basis of comparison than independent controls because they could eliminate minor variations in solution preparation or stream width fluctuation.

However, design of an integrated control site requires a number of changes stemming from the issue of electrical current shunting through the conductive saline solution between the two sites. Figure 4.9 shows a design solution based on a bilaminar flow approach. To prevent current flow through the saline, large ground plane electrodes are added upstream and downstream of each interrogation site. The electrical measurement scheme (Figure 4.9b) uses operational amplifiers in feedback to force virtual shorts between their inputs. Since the saline solution is then grounded at both the interrogation site and the ground plane electrodes, no current should flow through it. Thus, the two sites are effectively electrically isolated.

While the bilaminar design and electrical scheme is effective in theory, the design encounters several practical issues that would need to be rectified through further iteration. Selective cell culture in the channel is somewhat difficult and in this design required the device to be compressed to a substrate after culture rather than fully bonded and sealed. Compression devices are very

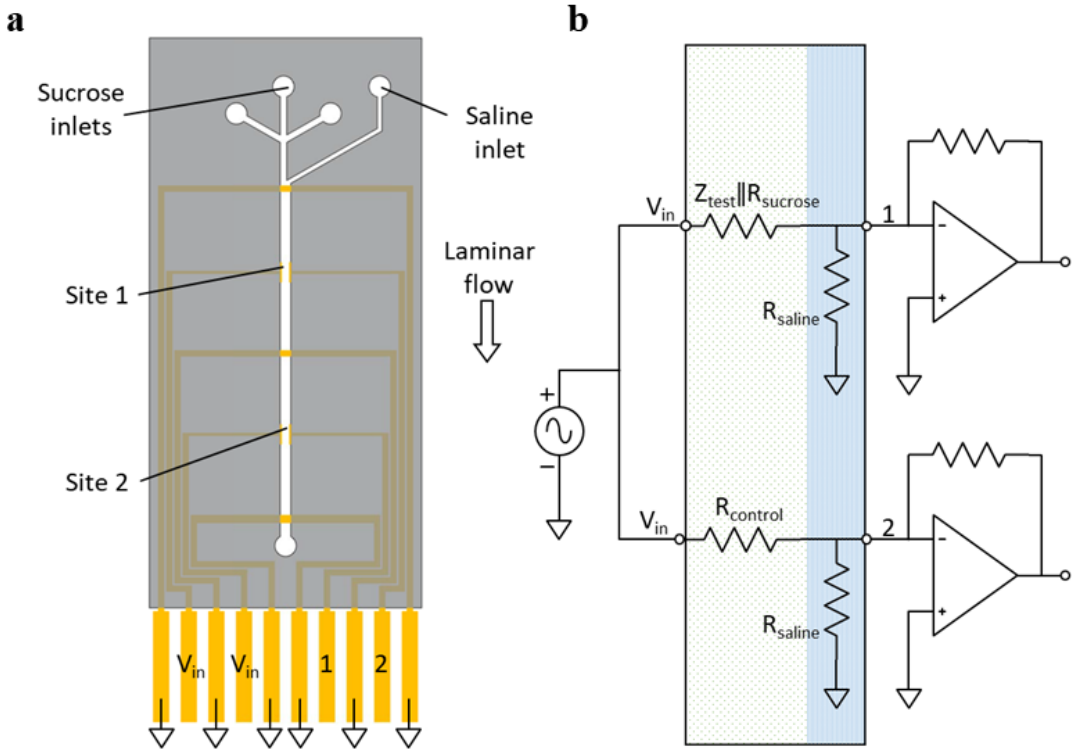

Figure 4.9: Design of a bilaminar flow devices. (**a**) A bilaminar flow device was designed to include two interrogation sites separated by grounding electrode planes. (**b**) The electrical grounding scheme uses operational amplifiers to prevent shunt currents through the saline.

difficult to manage in terms of preventing leakage and bubble formation while maintaining sterility and repeatable flow. Integrated valves might be used in future designs to facilitate selective seeding in a sealed device. The proposed electrode scheme uses a two point measurement rather than a four point electrode configuration. Two point measurement does not screen electrode impedances, so the electrodes would need to be well matched or calibrated out through separate testing. Finally, the flow profile between the two sites is not necessarily perfectly matched. If flow is not sufficiently fast, diffusion will lead to significant spreading of the laminar flow boundary at the downstream site. In addition, the presence of cells, especially if they are clumped or raised, at the test site can locally deflect the flow boundaries. Similarly, debris or bubbles in the channel can cause stream width mismatch between the sites. All of these issues could be addressed through careful design improvements to provide a more accurate extraction of the cell layer impedance. However, the bilaminar design does not address cell health concerns related to extended sucrose exposure, nor does it provide improved intracellular access.

4.5 Conclusions

A trilaminar flow sucrose gap approach to in vitro electrical measurement of gap junction networks has been re-examined. However, the attempts replicate the results of Cedric Bathany et al. (2012) have resulted in marginal results. Potential sources of error in the design have been identified including stream width instability, control solution matching, and cell health concerns under extended sucrose exposure. Despite engineering improvements (namely on-chip perfusion switching and a novel stream width-based calibration approach) to address these potential sources of error, the approach proves unreliable in gap junction blocker assays on NRK-49F cells. Potential issues in the bioelectrical model leading to these results have been identified to be addressed in future systems. A reliable and accessible means of electrical gap junction connectivity examination remains an important goal toward gaining more fundamental understanding of how we develop, grow, and heal.

Chapter 5

ELASTOMERIC VALVE BASED DEVICES TO INTERROGATE GAP JUNCTION CONNECTIVITY

5.1 Introduction

5.1.1 Importance of Gap Junction Measurement

Gap junctions are the cytosolic couplings between adjacent cells that mediate intercellular communication in non-neural cells. Numerous studies have shown that network connectivity though gap junctions is an essential element of growth, regrowth, and development (Mathews and Levin, 2016; Emmons-Bell et al., 2015; Oviedo, Morokuma, et al., 2010). Meanwhile abnormal gap junction expression has been associated with various disease states including cancers (Moore, Walker, and Levin, 2017; Levin, 2019). There is a clear need to develop tools to measure gap junction connectivity in developing cell cultures to study the fundamental processes of how intercellular communication guides growth and development.

5.1.2 Existing Gap Junction Measurement Techniques

The conventional gold standard approach to electrical measurement of gap junction connectivity (and to cell electrophysiology in general) is patch clamping (Rash et al., 2013; Adermark and Lovinger, 2008). The process is both invasive and difficult to perform. There are several techniques for "patching" into a cell, but all of them perturb the cell membrane in some way. A portion of the cell membrane is captured tightly (often punctured) and sealed by vacuum in a glass micropipette. The tight seal allows stable electrical recording from the interior of the cell. The risk of cell damage and the complexity of operation is further increased in the case of measuring intercellular connectivity, as a second patch clamp must be performed on a neighboring cell (Veenstra, 2001). Patch clamping apparatuses are generally bulky and expensive, and they require a highly skilled operator.

Dye diffusion techniques can also be employed to measure membrane potential and gap junction connectivity, though with less precision (Babica, Sovadinová, and Upham, 2016). Membrane impermeable fluorescent dyes can be injected into tissue to monitor diffusion rates through gap junctions. However, the results of these dye tests are difficult to quantify and repeatability is a significant issue as washout of the dye is often difficult. Additionally, dye testing necessitates expensive and bulky optics.

An electrical measurement of gap junction connectivity is desirable to enable real-time monitor-

ing and repeatable assays. As long as induced electrical currents are sufficiently low (typically less than 1 µA), electrical measurement is non-destructive and fundamentally non-invasive and repeatable (Meng, Rouabhia, and Z. Zhang, 2021). Electrical measurement systems can provide near instantaneous quantitative results which are ideal as feedback parameters into a closed loop system. Further, electrical impedance measurements are an ideal starting point for microfluidic devices examining intercellular connectivity as they can be directly compared to trusted benchtop electrophysiological recordings.

One benchtop electrophysiology technique that might be leveraged for electrical gap junction measurement is the "sucrose gap" approach. Figure 5.1a shows a diagram of the sucrose gap technique in which a nerve bundle or other electrically active tissue sample is fixed across three different baths. The two end baths are filled with conductive solutions, usually isotonic KCl and Krebbs or Ringer solutions while the middle bath contains a non-conductive isotonic sucrose solution. The baths are typically isolated from each other by encapsulating the sample in a silicone grease. A stimulus can be applied from the test bath (or in some cases from a separate fourth conductive bath) and its conduction through the sample is forced due to the non-conductive sucrose gap (Mert, 2007). While this approach is typically used to study action potential propagation, a continuous stimulus could also be monitored to yield sample conductivity.

Previous attempts have been made to measure gap junction connectivity using the microfluidic phenomenon of laminar flow to mimic a sucrose gap experiment (Cedric Bathany et al., 2012). Under the regime of laminar flow convergent streams do not mix chaotically, allowing distinct fluid regions to be created over a single cell monolayer. Thus, trilaminar flow devices can be constructed wherein electrical signals from electrodes submersed in saline on either side of the sucrose region are forced through the cell layer and must traverse horizontally though gap junctions. However, in practice maintaining consistent flow boundaries throughout an experiment can be a practically limiting challenge (See Section 4.4).

A microfluidic device that can electrically measure intercellular connectivity has enormous potential to develop closed loop systems. Feedback signals will allow devices to train and tailor gap junction connectivity, unlocking endogenous control over cellular communication.

5.1.3 A Thin Flexible Membrane Approach

The success of a microfluidic platform in measuring electrical connectivity through gap junctions hinges on gaining intracellular electrical access and on limiting parasitic conduction through extracellular media (Figure 5.1b). Patch clamping succeeds in taking high fidelity measurements by puncturing the cell membrane to gain intracellular access. Some techniques are in development to achieve parallelized intracellular access similar to patch clamping, but most approaches are quite

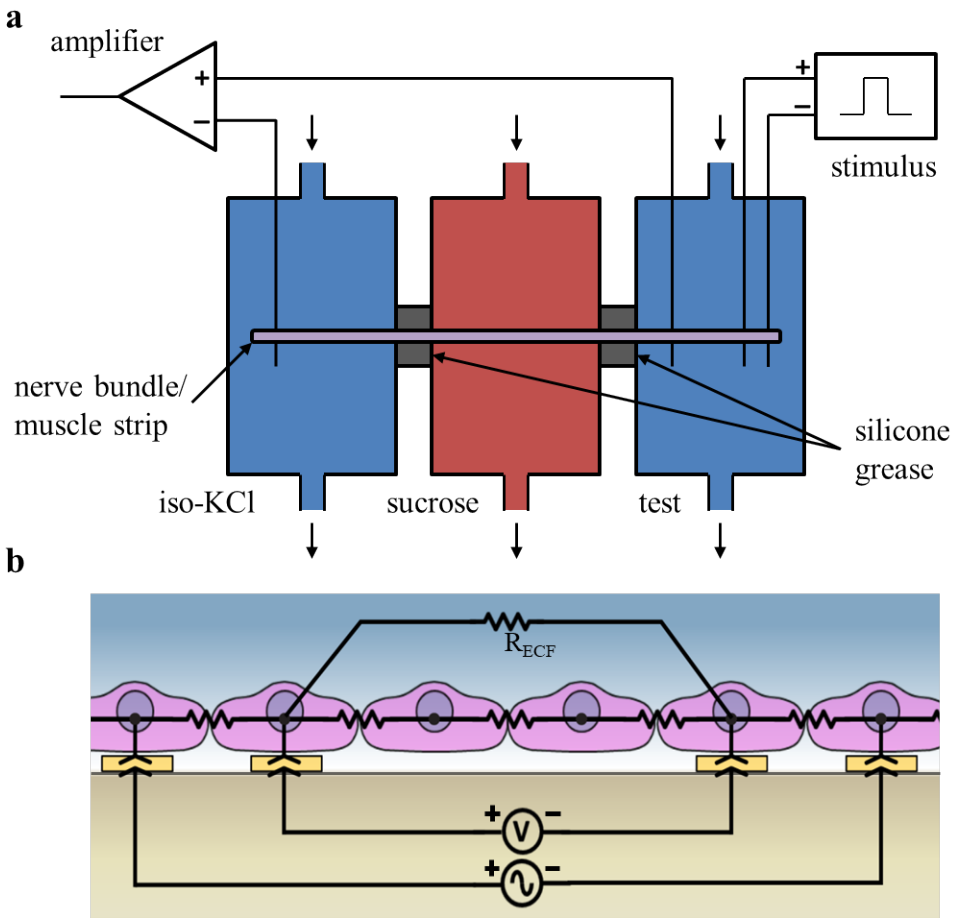

Figure 5.1: Conceptual approaches to gap junction measurement. (**a**) In benchtop sucrose gap, a tissue sample lays across 3 perfused baths that are sealed off using silicone grease. Without a special setup like the sucrose gap experiment, gap junction connectivity is difficult to measure (**b**) in bulk tissue because of barriers to intracellular access and shorting through the extracellular media.

difficult to implement. Nanoneedle probes in combination with electroporation or optoporation (induced temporary breakdown of the cell membrane) require exceptional fabrication expertise and can damage cells (Abbott, Ye, Qin, et al., 2017; Bruno et al., 2020). Other microfluidic approaches attempting to replicate patch clamp-like membrane seals involve micropores or constrictions and are unsuitable for cell monolayer experimentation (C.-Y. Chen et al., 2009; X. Li et al., 2006).

The simplest and most practical solution to gaining intracellular electrical access to a cell monolayer then simply relies on maintaining the electrodes and cells in a highly conductive solution, relying on charge transport through ion channels. This approach to the intracellular access problem, however, shifts the burden of the design challenge wholly onto the task of limiting extracellular conduction. Instead of creating a tight seal to the membrane of a single cell, a seal must be constructed against

the exterior membranes of a complete span of the cell monolayer. At the benchtop level, the sucrose gap technique aims to do just that, using non-conductive sucrose to seal against the cell layer.

Chapter 2 introduced a novel fabrication method to construct normally closed elastomeric valves on glass substrates. These valves operate by pneumatically actuating a thin, conformable PDMS membrane. Because the membrane is highly conformable and can seal tightly to the cell layer under low activation pressures, it is proposed as a solution to the extracellular media shorting issue shown in Figure 5.1b. Elastomeric valves can temporarily expel sufficient extracellular media to create isolation impedances on par with sucrose gap laminar flow techniques and offer advantages in terms of scalability and 2D spatial resolution.

This chapter will investigate two approaches to gap junction isolation using elastomeric valves. First, single valve membranes conforming against a cell layer are examined and characterized to determine whether they can provide sufficient electrical isolation to isolate gap junction measurements. Additionally, a hybrid approach is pursued in which elastomeric valves are used in place of laminar flow to form a sucrose gap over the cell layer.

5.2 Materials and Methods

5.2.1 Device Fabrication

Cr/Au planar electrodes are sputter coated onto glass substrate using a standard liftoff process. In brief, standard soda lime glass microscope slides are first piranha etched in a solution of 3:1 sulfuric acid to hydrogen peroxide. Photolithography is performed to using positive photoresist AZ9260 (AZ Electronic Materials) to a thickness of 6.5 µm to pattern the electrodes. Chromium and gold layers are sputtered to depths of 14 nm and 210 nm, respectively. Liftoff is performed overnight in heated Microposit Remover 1165 (Dow Chemical).

Normally-closed PDMS valves are fabricated, aligned, and selectively bonded to the substrate using an oligomer stamping technique that was previously characterized (Dungan et al., 2023). Briefly, master molds for three layers are fabricated by photolithography using negative photoresist, SU8-3050 (Kayaku Advanced Materials) on silicon wafers. Molds for both the fluid flow layer and the pneumatic layer are patterned to 65 µm depth. A third stamping mold, which defines the valve seat areas which should not be bonded to the substrate, is deposited at roughly 100 µm thickness. A 10:1 by mass base to curing agent mixture of PDMS (Sylgard 184, Dow Chemical) is prepared and cast molded over the pneumatic and stamp masters. PDMS is spin coated onto the flow layer mold at 2000 rpm to form a thin membrane (roughly 50 µm).

The flow and pneumatic layers are aligned and bonded using oxygen plasma treatment (20 W, 30 s, 500 mT), before being released from the mold, diced, and cored to create fluidic and pneumatic ports. To selectively bond the valves to the substrate, both PDMS device and substrate are oxygen

plasma treated (20 W, 30 s, 500 mT). The untreated stamping mold is then aligned and brought into light contact with the PDMS device to locally remove the surface treatment. The device is then aligned over the electrodes and bonding is completed by baking on a hotplate at 80°C for greater than 10 mins. The valves are carefully actuated approximately 5 minutes into this bake cycle.

5.2.2 Cell Culture Protocols

Prior to cell seeding, the microfluidic device is treated with Matrigel (Corning) to form an extracellular matrix that promotes cell adhesion. After thorough flushing with ethanol and deionized water, a 1:20 dilution of Matrigel in Dulbecco's Modified Eagle Medium (Fischer Scientific) is injected into the device while vacuum is maintained on all valves. The device is then incubated at 37°C for 30 min. Prior to seeding, a large media droplet is formed on the top of the device connecting all the fluidic ports to prevent hydrostatic flow.

Normal rat kidney (NRK-49F) epithelial cells are seeded into the valved microfluidic device using a hybrid incubation scheme. Prior to seeding, cells are cultured in polystyrene plates but are not allowed to become fully confluent before dissociation in Accutase (Innovative Cell Technologies). Cells are resuspended in media at a concentration of 15,000 cells/μL, and a volume of roughly 50 μL is carefully injected into the outlet port (fluid port 5 in Figure 5.7a). The input switching valves (associated with pneumatic ports a and b in Figure 5.7a) are closed during seeding to prevent cells from accumulating beneath them.

After seeding the cells are allowed to sediment in an incubator for 1.25 hours. The large surface droplet preventing hydrostatic flow is then split, allowing microflows to deliver additional nutrients. Additionally, excess cell buildup is scraped out of the fluidic ports using a 10 μL pipette tip to prevent obstruction of flow and reduce nutrient depletion. The chip is maintained under static culture in the incubator for greater than 2 hours before transitioning to pressure driven flow. During flow, the device is temperature regulated at 37°C and pH is maintained by HEPES buffer in the media.

5.2.3 Electrical Measurement

Four point electrical impedance measurements are achieved using a lock-in amplification scheme. A four point electrode configuration helps to reduce the impact of lead impedance and the electrode/solution interfacial impedance (Pelc, Marion, and Mario, 2011). Lock-in impedance measurement provide several advantages over direct current measurement. The low magnitude alternating source prevents charge build up and redox reactions from depleting the electrodes. Further, the approach gives insight into frequency dependent impedance effects and phase delays imposed by the sample under test. Finally, the homodyning approach of lock-in amplification serves to reduce the noise bandwidth of the measurement to a narrow band around the reference frequency.

Here, a Keithley 6221 current source (Tektronix) provides a 100 nA stimulus between the outer planar electrodes. An SR830 digital lock-in amplifier (Stanford Research Systems) measures the RMS voltage across the interior electrode pair. The SR830 is set in a floating configuration with a time constant of 300 ms.

5.2.4 Chemicals and Reagents

Sucrose solution is prepared at 300 mM concentration in deionized water and passed through a 0.22 µm filter before use. The saline solution consists of 75 mM NaCl, 15 mM KCl, 2 mM $MgCl_2$, 1 mM $CaCl_2$, 94 mM mannitol, and 10 mM HEPES buffer. The solution is pH corrected to 7.4. 2-APB (Millipore Sigma) stock is prepared 100 mM concentration in DMSO. Aliquots are kept frozen at -80 °C and diluted to 100 µM in sucrose solution. Control sucrose solution is balanced with 0.1% DMSO to match the 2-APB solution content. Cell culture media is prepared using FluoroBrite DMEM (Thermo Fisher Scientific) with 10% by volume fetal bovine serum, 100 U/mL penicillin-streptomycin, and 1X GlutaMAX. Ethidium homodimer-1 (EthD-1, Thermo Fischer Scientific) is prepared at a concentration of 1:2000 (v/v) in cell culture media. Rhodamine B dye (Thermo Fisher Scientific) was added to the sucrose solution at 1.5 µM concentration.

5.3 Single Valve Devices

5.3.1 Design and Theory of Operation

To evaluate the suitability of elastomeric valves for gap junction isolation, a simple test device was designed as shown in Figure 5.2a. The device comprises three functional layers; fluidic, pneumatic, and electric. Two fluid inlets (ports 1 and 2) feed into two large cell culture chambers (3×3 mm), which house the two electrode pairs. The culture chambers are separated by an 850× 500 µm channel with a 400 µm wide elastomeric "interrogation valve" (controlled by pneumatic port c). Inner electrode separation is 1 mm. Additionally, integrated normally-closed valves (controlled by pneumatic valves a and b) are placed on each inlet channel to facilitate rapid on-chip switching between input solutions. During experimentation, cells are seeded and cultured throughout the fluidic layer on the substrate side. However, during measurement the interrogation valve compresses against a network of cells that is approximately ten cells deep. The gap junction measurement then only reflects this smaller network of cells that are mechanically isolated by the interrogation valve.

The devices are fabricated at the maximum reliable depth (75 µm) to reduce shear stress on the cell layer. Shearing forces due to flow are greatest in the device in the critical area under the interrogation valve, where the valve (even in the open state) partially occludes the channel. In operation (and setup especially), special care should be taken to avoid forcing flow while the interrogation valve is closed or partially closed. Additionally, an "H" shaped design was devised where flow would

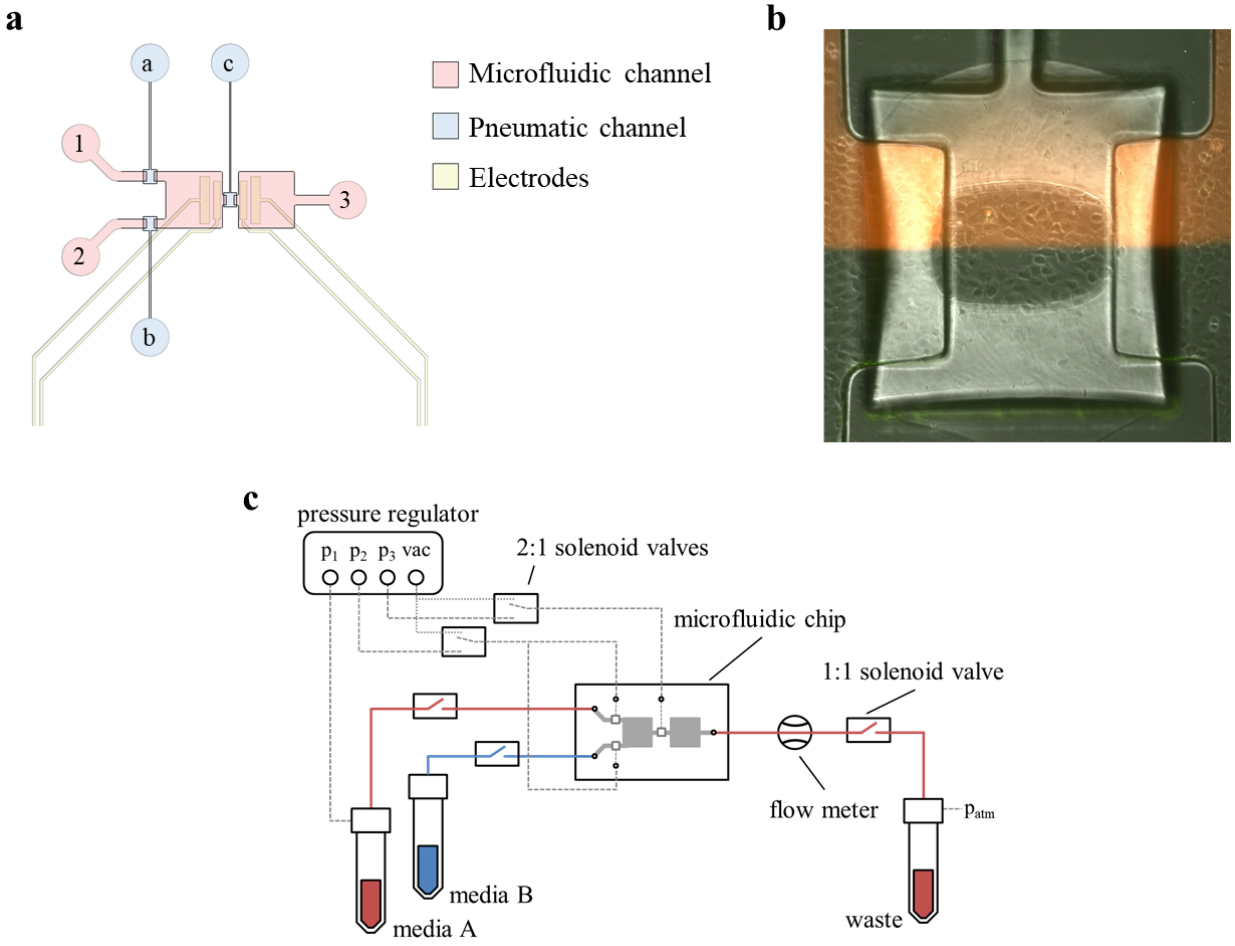

Figure 5.2: Microfluidic chip design using a single elastomeric valve to electrically isolate gap junctions. (**a**) A top-down schematic of the device layers, showing placement of the fluidic ports (1-3) and the pneumatic ports (a-c). (**b**) An image of the interrogation valve between the two cell culture chambers in the completed device (10x, phase contrast/RFP, false color). Dye shows that when both input valves are open, flow is well matched and the laminar boundary is centered under the interrogation valve. (**c**) A block diagram of the experimental setup and peripherals supporting the microfluidic chip during standard operation.

run perpendicular to the interrogation valve to alleviate shear stress concerns. This design was not thoroughly evaluated once it was determined that the NRK cell line could withstand shear forces under the valve in the simpler "I" configuration of Figure 5.2.

During operation, the device is nominally setup as shown in Figure 5.2c with two input solutions gated by external solenoid valves. Additionally, the waste output is controlled by an external 1:1 solenoid valve and monitored by an inline flow meter. All external valves are closed during measurement cycles (when the interrogation valve is lowered onto the cell layer) to ensure that flow is completely arrested in the device. External valves also significantly simplify the setup process

of transitioning the microfluidic chip from incubator culture to pressure driven flow by facilitating the bubble-less coupling of microfluidic tubing. The on-chip elastomeric valves are pneumatically driven in sync with the external solenoid valves to enable near instantaneous perfusion switching between the test solutions with essentially zero dead volume. The input pneumatic valves are connected to an independent pressure source from the interrogation valve, allowing them to be driven at significantly higher pressures (usually 10 mbar for the interrogation valve and 50 mbar for the input valves) to ensure that no leakage current or diffusion of active compounds can occur between the test solutions.

5.3.2 Results and Discussion

5.3.2.1 Elastomeric valve characterization

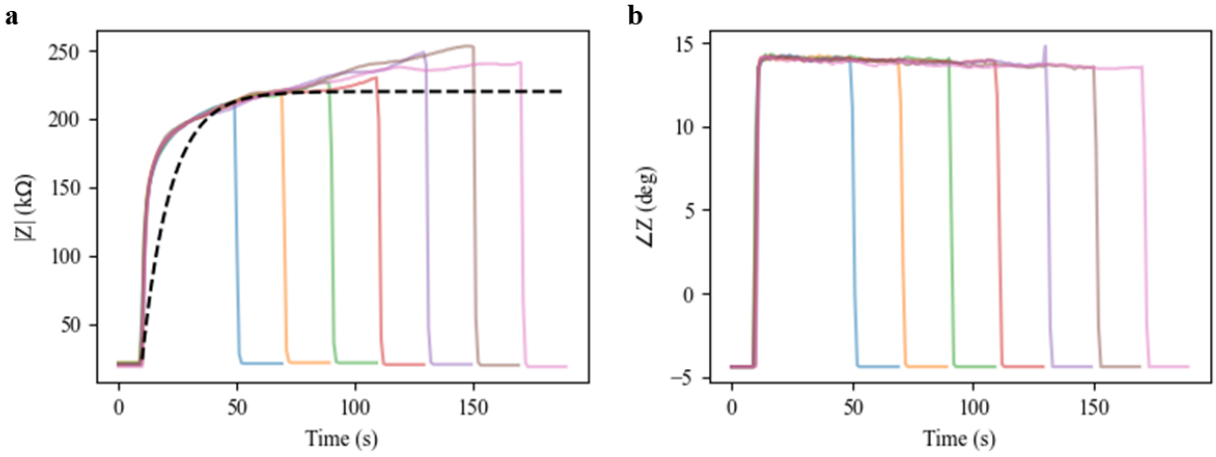

Figure 5.3: Impedance measurements at 100Hz in DPBS show the settling characteristic of the elastomeric valves. The dashed line represents a standard exponential RC step response. Phase decays at a very slow linear rate (0.005 deg/s).

In order to provide an adequate alternative to sucrose gap based approaches, the thin membrane of the elastomeric devices must be capable of sealing tightly enough to the substrate or cell layer to produce an electrical barrier similar to sucrose solution. Figure 5.3 shows representative transient electrical characteristics of a valve sealing in a DPBS solution at 100 Hz source frequency. The curves show that when the valve is compressed downward (in this case under 10 mbar of positive pressure), the impedance rises rapidly above 200 kHz which is similar to the usual values seen in trilaminar flow device sucrose gap experiments (see Figure 4.2d. Impedance in stream width dependent, but nominally operated around 275 kΩ). By slightly increasing the media conductivity (through sucrose dilution) the sealing impedance of a single valve can easily match that of a sucrose stream.

The unusual settling characteristics of Figure 5.3 merit further discussion. In both the magnitude and phase, the measured value rises quickly but does not settle to a constant value even after times longer the maximum practical duration of cell compression. The massive timescale of the drifting component suggests that the effect is not the result of changes in passive components of an electrical model, nor the result of the time constant of the amplifier (200 ms). The curves clearly do match the exponential RC response (displayed in black for the magnitude plot) that would result from an instantaneous state change from one impedance to another, so more complex electromechanical effects must be present. The shunt capacitance in the system should be sufficiently low that any electrical settling should be resolve in the short period in which the phase transition occurs (roughly 3 s). The slower transition of the magnitude, then, is more likely the result of the mechanical settling of the PDMS membrane against the substrate. The long term rise in impedance magnitude may reflect a slow expunging process of any residual trapped media being forced out (or absorbed into the PDMS material). The good repeatability of the early settling characteristic versus the more uneven long term settling supports this theory as the mechanical processes such as the point of first contact, spreading of the contacted surface, and potential media trapping are more chaotic and less well controlled. Practically, because the response is initially repeatable, an impedance can be reliably measured by compressing the valve for a short fixed amount of time (less than 1 min.) and extracting the final or peak values measured. Additionally, these results suggest that phase measurements may prove a more reliable marker, especially where rapid compression cycles (whether for higher throughput or reduced cell stress) are desired.

Additional electrical characterization of valve performance in control settings including hysteresis, actuation time, and frequency response is provided in Section 2.4.3.

5.3.2.2 Control testing in single valve devices

Control testing in the single valve devices give insight into the noise floor of the system. Figure 5.4a shows a simple no-cell control test in which the chip is alternately perfused for 270 s with pure cell culture media or media containing 100 µM 2-APB and rhodamine dye. After each perfusion period, flow is arrested and the interrogation valve is compressed against the substrate under 10 mbar pressure for 30 s. The electrical impedance at 100 Hz is continuously monitored and the device is periodically monitored with fluorescence imaging to confirm complete solution exchange. The extracted impedance values over 13 full cycles fluctuate around 224 kΩ and 14.3° with standard deviations of 4.72 kΩ and 0.061°. The addition of 100 µM 2-APB does not significantly affect the solution conductivity. The inherent noise in the system due to electrical, mechanical, and fluidic sources reflects a 2.1% variation from the baseline measurement, which is an acceptable noise floor.

The cell control in Figure 5.4b shows somewhat larger fluctuation in baseline measurement, as might

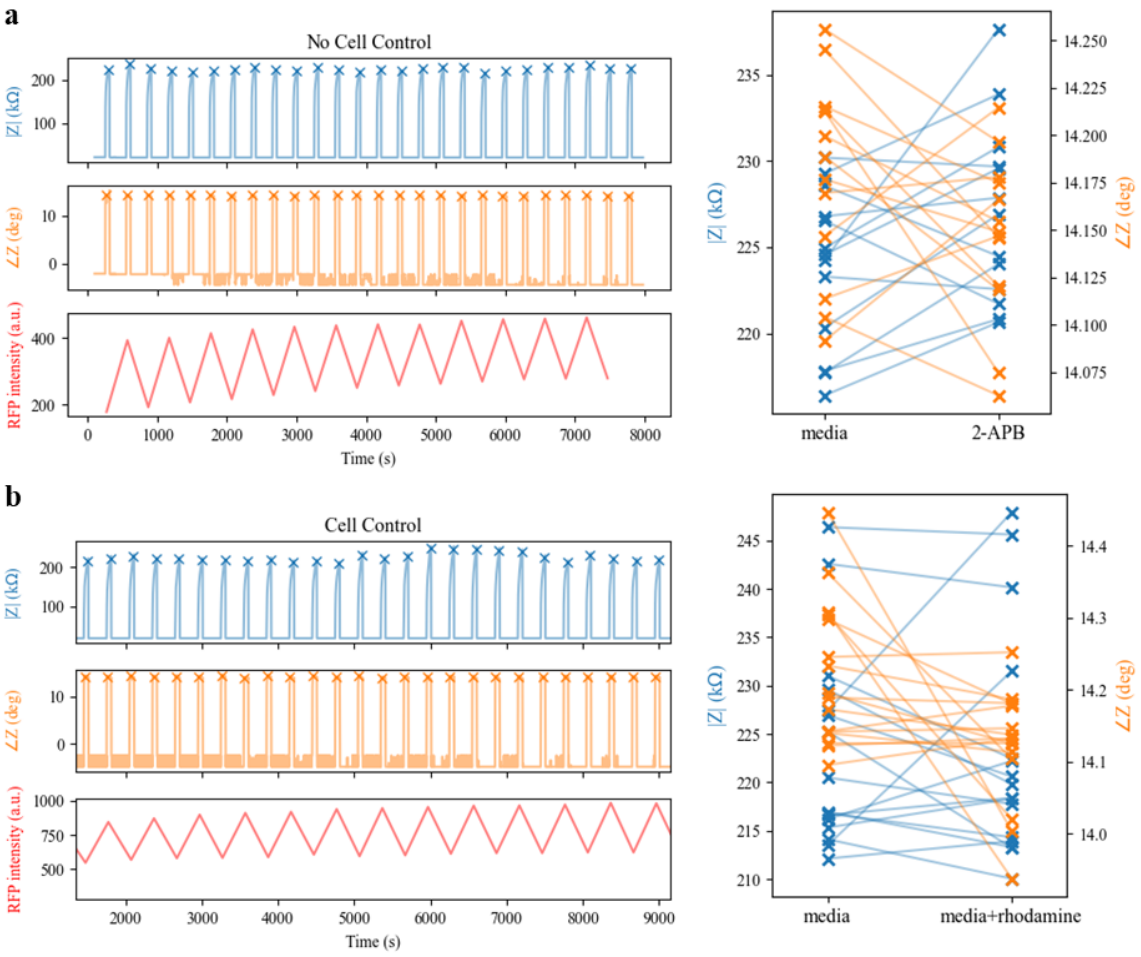

Figure 5.4: Control experiments for the single valve device. (**a**) Time series and extracted transition values for a no-cell control in which pure media and media containing 100 µM 2-APB are alternately perfused. (**b**) Time series and extracted transition values for a cell control in which pure media and media containing 1.5 µM rhodamine dye are alternately perfused over confluent NRK-49F cells.

be expected due to the introduction of biological material. In the experiment, two media solutions (one rhodamine dyed) are alternate perfused every 270 s as in the no-cell control. The impedance at 100 Hz across the cell layer compressed by the interrogation valve is measured continuously and peak values are extracted. Transitions between the two solutions show no clear bias in the resulting impedance as expected. The impedance magnitude holds an average value of 223 kΩ with a much larger standard deviation of 8.66 kΩ. The remarkably similar average value of the cell control measurements suggests that the gap junctional network in the cell layer (or the pathway into the intracellular space) may present a significantly higher electrical impedance.

5.3.2.3 Device verification through gap junction blocker testing

Single valve devices have shown promising results in some tests using the gap junction blocker, 2-APB, to reduce network connectivity. Figure 5.5 shows three independent trials in which NRK-49F cells show increased impedance after treatment with 100 µM 2-APB. In the experiments, the cell monolayer is alternately perfused for 4 min periods with cell culture media and culture media containing 100 µM 2-APB and 1.5 µM rhodamine dye. (The 2-APB solution was dyed to track complete exchange of the test solutions. The elastomeric valve approach is fundamentally less reliant on careful impedance balancing of the control solution. Agents can freely by added to the solution containing the gap junction inhibitor, so long as the volume added causes negligible dilution the test solution.) After each perfusion period, flow in the device was arrested and the interrogation valve was sealed against the cell layer under 10 mbar pressure for 60 s. The extracted impedance magnitudes showed averaged increases due to the presence of 2-APB of 8.71, 5.93, and 6.66 kΩ with respective standard deviations of 1.69, 0.78, and 0.42 kΩ. Across all the trials, measurements in 2-APB represented a 10.28% increase over the impedance measured in pure media at 410 Hz. The phase results are less conclusive. While magnitude measurements always increased in response to 2-APB, the phase consistently increased in trial 1 (0.238°±0.248°), consistently decreased in trial 3 (-0.080°±0.028°), and transitioned in both directions in the second trial (-0.076°±0.533°). Overall, these results appear to show a sensitivity of the elastomeric valve device in the electric impedance magnitude correlated to the gap junction connectivity of the cells compressed by the interrogation valve.

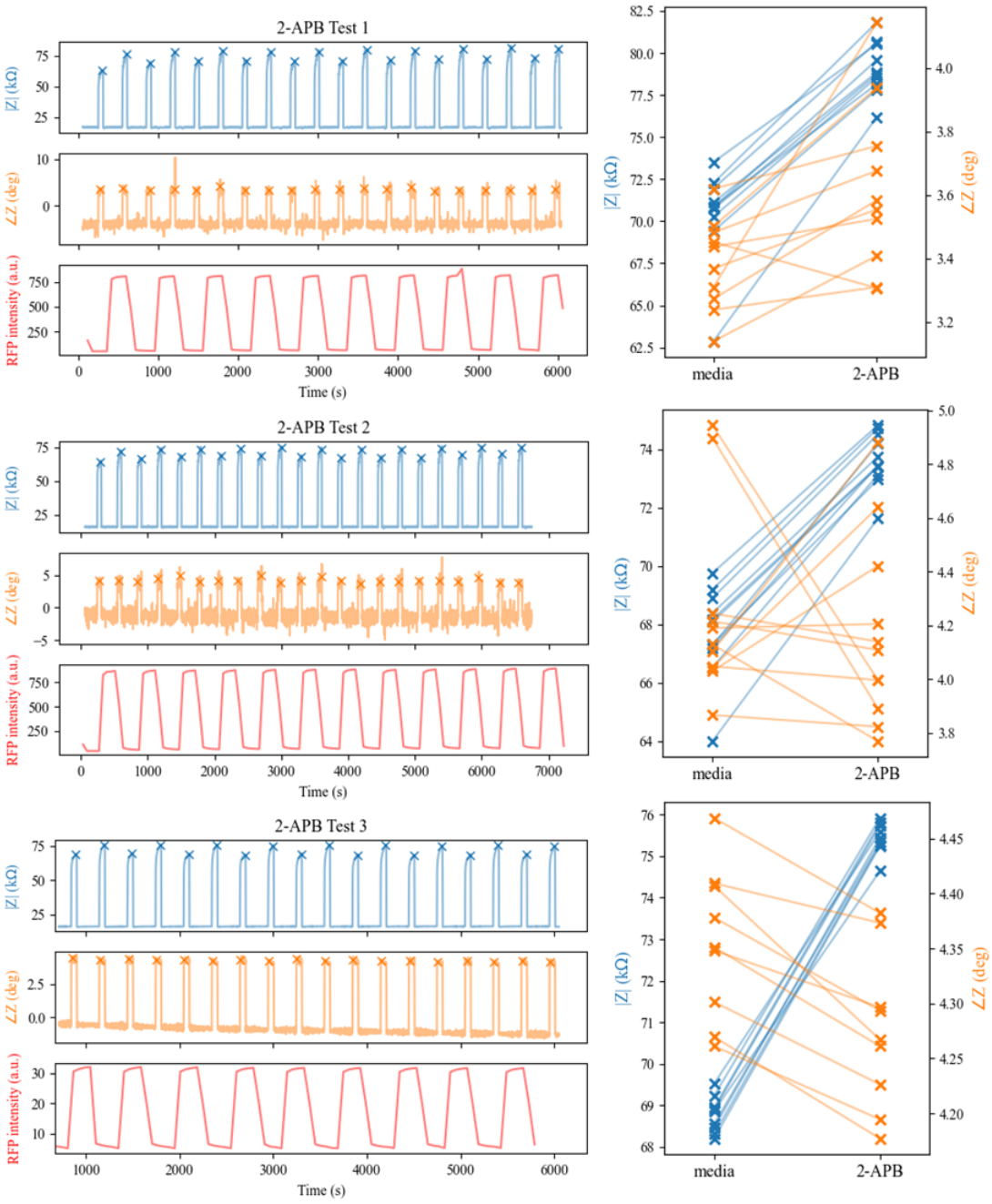

Figure 5.5: Promising results in single valve devices showing increased impedance for NRK cells measured in the presence of 2-APB. Three independent trials are shown with the filtered time series test data displayed at left (electrical impedance measured at 410 Hz). RFP imaging was used to ensure complete perfusion of the rhodamine dyed 100µM 2-APB media solution. "×" markers denote extracted impedance maxima, which are displayed as transition pairs between subsequent media and 2-APB treated values at right. The average observed impedance magnitude increases due to the presence of 2-APB in the three trials are 8.71, 5.93, and 6.66 kΩ, respectively (standard deviations: 1.69, 0.78, and 0.42 kΩ).

5.3.3 Memory Effects

The results of Figure 5.5 are somewhat sullied by the discovery of a flow rate dependent memory effect in these devices. While some control tests such as the those displayed in Figure 5.4 showed good results, it became apparent through continued testing that some unanticipated complicating factor was affecting control results, causing them to be unreliable. Initially, the issue was thought to be an effect of upstream valve heating or solution contamination, but experiments eventually showed that in control tests where a significant differential appeared, swapping input tubing was sufficient to reverse the apparent difference between the matched test solutions. These results pointed to the upstream switching valves as the source of error. The addition of flow rate monitoring, revealed that consistent flow rate differences between the switching valves (resulting from differences in geometry due to fabrication defects or from trapped debris) correlated to the measured impedance differences.

The most unexpected result from this debugging process was that even though flow was completely halted during the measurement phase, the measured impedances were being affected by the previous flow rate through the devices. Figure 5.6 shows that for a ramp of increasing driving pressures, the impedance measured across the closed interrogation valve after the flow is arrested is negatively correlated with the previous flow rate. The effect is highly repeatable and persists in the absence of flow for as long as 10 minutes. The phenomenon has been thoroughly explored and a publication on the subject is included in full in Appendix C.

The memristor effect in simple PDMS devices is a significant discovery in its own right, and it could impact the fields of non-von Neumann and neuromorphic computing. However, it is a significant detriment to the reliability of single valve device results. Further research is needed to uncover the most effective method to combat the memory effect where it serves as a source of error. It has not been confirmed whether the effect is present in devices where the primary flow runs perpendicular to the interrogation valve, such as the "H" shaped device design. One direct method to produce reliable results would be ensure that flow rate of each test solution is perfectly matched in the device, for which a highly sensitive flow rate monitor will be required. In the long term a more reliable solution could be designed at the device level, where input valves could be made much larger than the input channels in the device such that they have an insignificant impact on the total hydraulic resistance of the channel in the open state. Under such a design regime, temperature and viscosity of the test solutions will still need to be closely matched to ensure equal flow rates.

5.3.4 Scalability and experimental improvements

If better intracellular access cannot be achieved through electrode improvements, the media conductivity may be reduced through sucrose dilution in an attempt to increase the extracellular impedance.

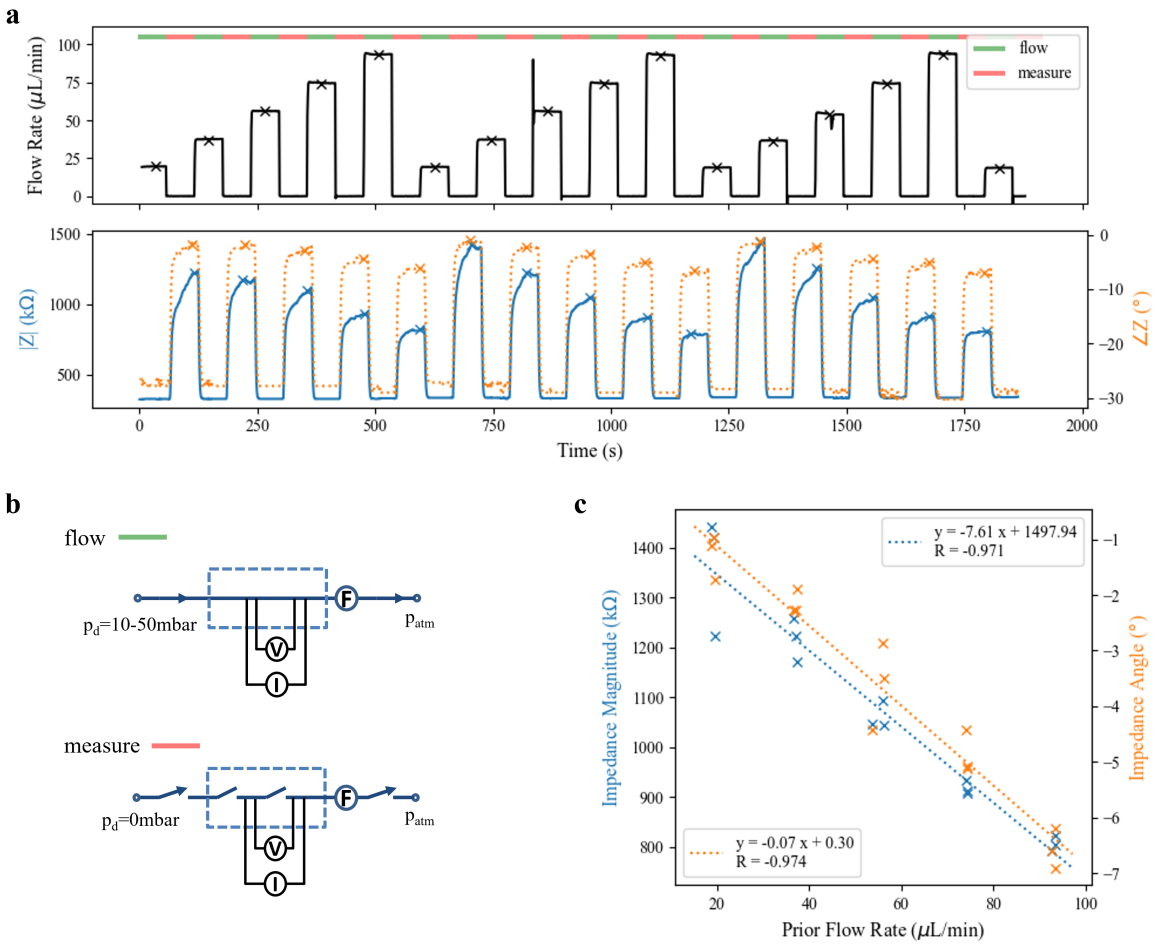

Figure 5.6: A representative experiment showing correlation between the flow rate through PDMS valves and the subsequent impedance measured across them in the closed state. The time course of the experiment (**a**) shows a repeated flow rate ramp as the device is switched between flow and measurement states (**b**). The extracted values for flow rate and impedance in each period are denoted with color coded '×' markers. A strong correlation between these extracted flow rates prior to measurement and the extracted impedance values in the absence of flow is demonstrated (**c**).

However, this compromise would need to be closely balanced to maintain cell health and avoid membrane depolarization.

One of the primary advantages of the elastomeric valve approach over laminar flow techniques is that is easily scaled to two dimensional networks. A proof-of-concept device containing 16 valve-connected wells was demonstrated in Section 3.4.2. Moving to 2-D devices enables new experimental paradigms for exploration of network connectivity, such as measurement over treatment gradients or on co-cultured developing cells.

5.4 Valved Sucrose Gap Devices

5.4.1 Design and Theory of Operation

Single elastomeric valves seal sufficiently tightly against cell monolayers to provide electrical isolation on a similar scale to the values measured in trilaminar flow devices. However, elastomeric valves, in providing a mechanical barrier to conduction through the extracellular fluid, more closely resemble the role silicone oil bridges that isolate the fluid baths (See Figure 5.1a), than the role of the sucrose gap itself. For this reason, a more faithful microfluidic analog of the benchtop sucrose gap setup has been designed in which two saline compartments are connected to a central sucrose filled region via elastomeric valves. Two such designs have been realized and evaluated for suitability in electrically measuring gap junction connectivity.

A microfluidic analog of the benchtop sucrose gap setup has been designed in which two saline compartments are connected to a central sucrose filled region via elastomeric valves. Figure 5.7 shows the design of a valved sucrose gap chip which features an on-chip junction for switching the between two different sucrose solutions. Channel widths in the device (including through all valves) are 500 µm and the channel depth is approximately 75 µm. The main cell culture chambers, which contain Cr/Au electrodes are 1.7 by 3 mm, while the sucrose chamber between the electrodes is roughly 1.5 by 1.5 mm. Relatively wide and deep channels reduce shear stress on cells during operation and increase the nutrient volume available to the cells during culture. The valves themselves are 400 µm across which allows them to seal over a network of roughly 120 NRK cells. Corner features in the flow layer have been intentionally rounded to reduce the chances of trapping gas in the chip during wetting. The pneumatic layer channels are narrow (100 µm) to reduce affecting flow where they cross flow channels.

The diagram in Figure 5.7a shows three layers of the sucrose gap design. In the device, conductive saline solution flows through the top and bottom channels (from ports 1 and 2 to ports 6 and 7, respectively). The sucrose gap is established by flow from one two inlets (port 3 or port 4) that converge and travel between two isolation valves to the sucrose waste outlet (port 5). The two sucrose inlets are individually pneumatically controlled (ports a and b), allowing complete switching of the sucrose perfusion stream within hundreds of microseconds. A single pneumatic input (port c) operates the isolation valves shown in Figure 5.7c simultaneously. These valves serve to isolate the sucrose region in a manner analogous to silicone bridges in a benchtop setup. Figure 5.7d shows that a valve in the closed state seals tightly over a cell monolayer, isolating membrane non-permeable dye in the sucrose chamber from the outer electrode chamber. The isolation valves are connected an independent positive pressure source from the switching valves in order to apply reduced mechanical pressure on the cell layer.

To optimize the performance of the pneumatic valves controlled by pneumatic ports a and b in

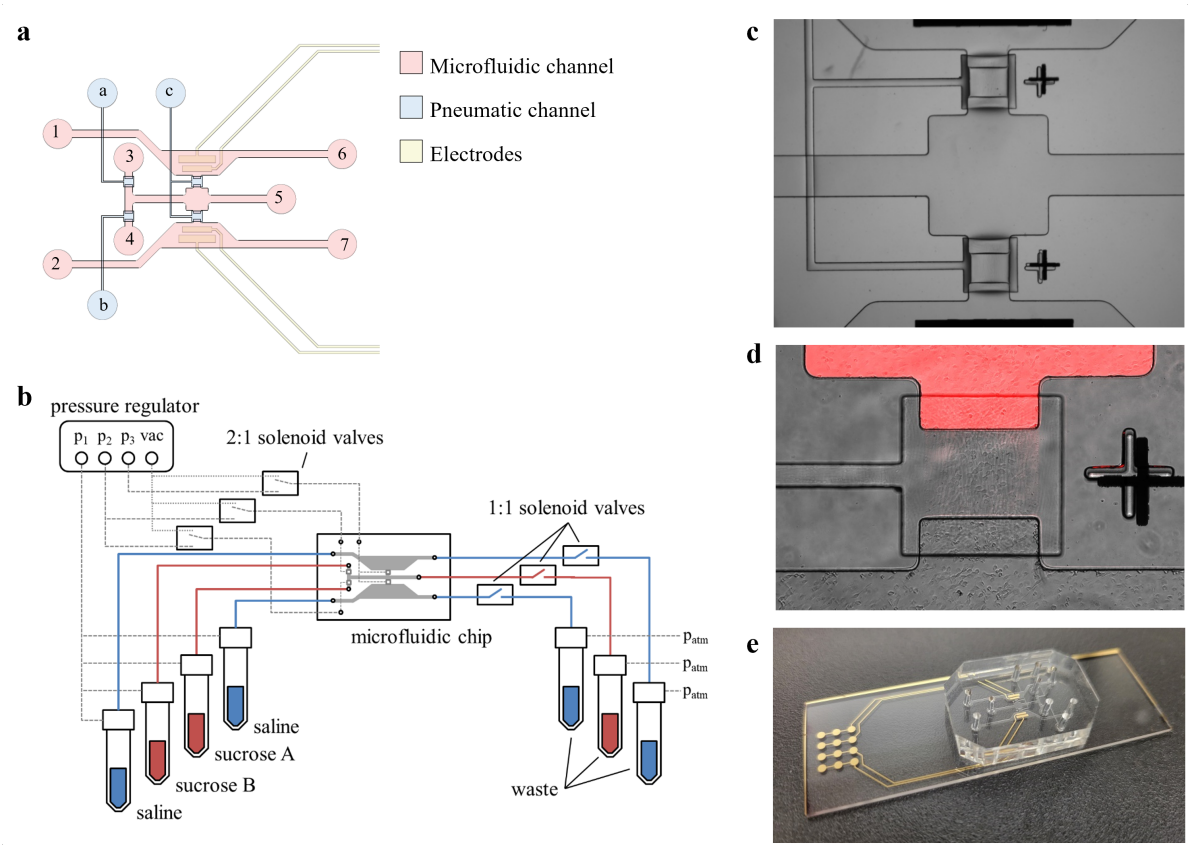

Figure 5.7: Design of a microfluidic sucrose gap device. (**a**) The device is designed with 7 fluid ports (1-7) and 3 pneumatic ports (a-c). Elastomeric valves controlled by pneumatic inputs a and b provide on-chip switching between sucrose streams, while pneumatic port c controls the isolation valves that seal against a cell layer. (**b**) In the intended experimental operation, the device requires 7 fluid reservoirs to electrically isolate solutions, 3 wetted 1:1 valves to arrest flow for measurement, and 3 2:1 valves to control pneumatic pressure on the valves. (**c**) A micrograph shows actuation of the isolation valves in the realized device (bright field, 2×). (**d**) Membrane non-permeable rhodamine dye shows confinement of the sucrose solution using elastomeric valves (phase contrast/RFP false color, 4×).(**e**) The completed device is fabricated onto a standard 1×3 in. glass slide for convenient microscopy mounting.

Figure 5.7a, these two valves can be left in their normally-closed state when cells are seeded into the device. Doing so prevents cells from adhering beneath the valves, effectively eliminating the possibility of leakage currents through these valves. Perfect sealing of these two valves at the sucrose junction is crucial to control a number of experimental variables. Complete seals serve to prevent backflow of ionic solutions (or diffusion of ionic species) during setup or media exchanges, preserving the purity of the sucrose solutions and thereby their impedance matching. Further, faithful operation of these valves ensures unobstructed flow, such that washout timings are reliable and balanced between the two solutions. Finally, preventing leakage is imperative to ensure that

no active compound (i.e. chemical gap junction blockers) from one test sucrose solution can contaminate a control sucrose solution.

One drawback of this design is that it requires a large number of reservoirs and external valves adding to the complexity of setup and operation. The saline side channels must remain independent (i.e. separate input and output reservoirs) as shown in 5.7b. Combining the saline reservoirs by using an off chip junction would provide a high conductance liquid connection between the two saline culture chambers, effectively shorting the electrical measurement. External solenoid valves on each line allow the flow to be completely arrested, eliminating a potential confounding variable during measurement.

Figure 5.8 presents an alternative design in which flow control valves are integrated onto the chip to reduce the setup complexity at the cost of fabrication complexity. This design also reduces the number of required reservoirs, but has the primary drawback that switching between different sucrose test solutions must occur through off-chip solenoid valves. Depending on flow rates and dead volume in the input tubing, complete perfusion change over in the device can take up to ten minutes, significantly lengthening experimental times and exposure to sucrose solution. For this reason, this design was not as thoroughly evaluated and the experiments that follow report results from the on-chip switching device.

A hybrid of the two designs presented in Figures 5.7 and 5.8 is achievable. Such a device could incorporate on-chip switching but would also simplify the burden of required external support systems by incorporating on-chip valves to arrest fluid flow. However, the junction of the saline channels in the design of Figure 5.8 may not be preferable, as these devices showed reduced isolation impedance in control testing (365 kΩ at 100 Hz), possibly due to leakage through the split saline channel.

5.4.2 Results and Discussion

5.4.2.1 Cell health and viability under compression

Tests were carried out to assess the viability of cells cultured under the elastomeric valves and to estimate the stress induced on the monolayer under compression from the PDMS membrane. Figure 5.9 shows these test results. NRK cells were cultured under valves and then subjected to 25 consecutive compressions of one minute duration at a fixed pressure. After each set of 25 compressions, the positive pressure on the valve was escalated, eventually performing a total of 200 compressions at 0, 10, 20, 30, 40, 50, and 100 mbar. Moderate flow of media was applied for one minute between compressions. EthD-1 was used to stain for cell death. EthD-1 is a membrane impermeable dye that binds to DNA becoming fluorescent. Thus, compromised cell membranes can be detected through RFP fluorescent imaging.

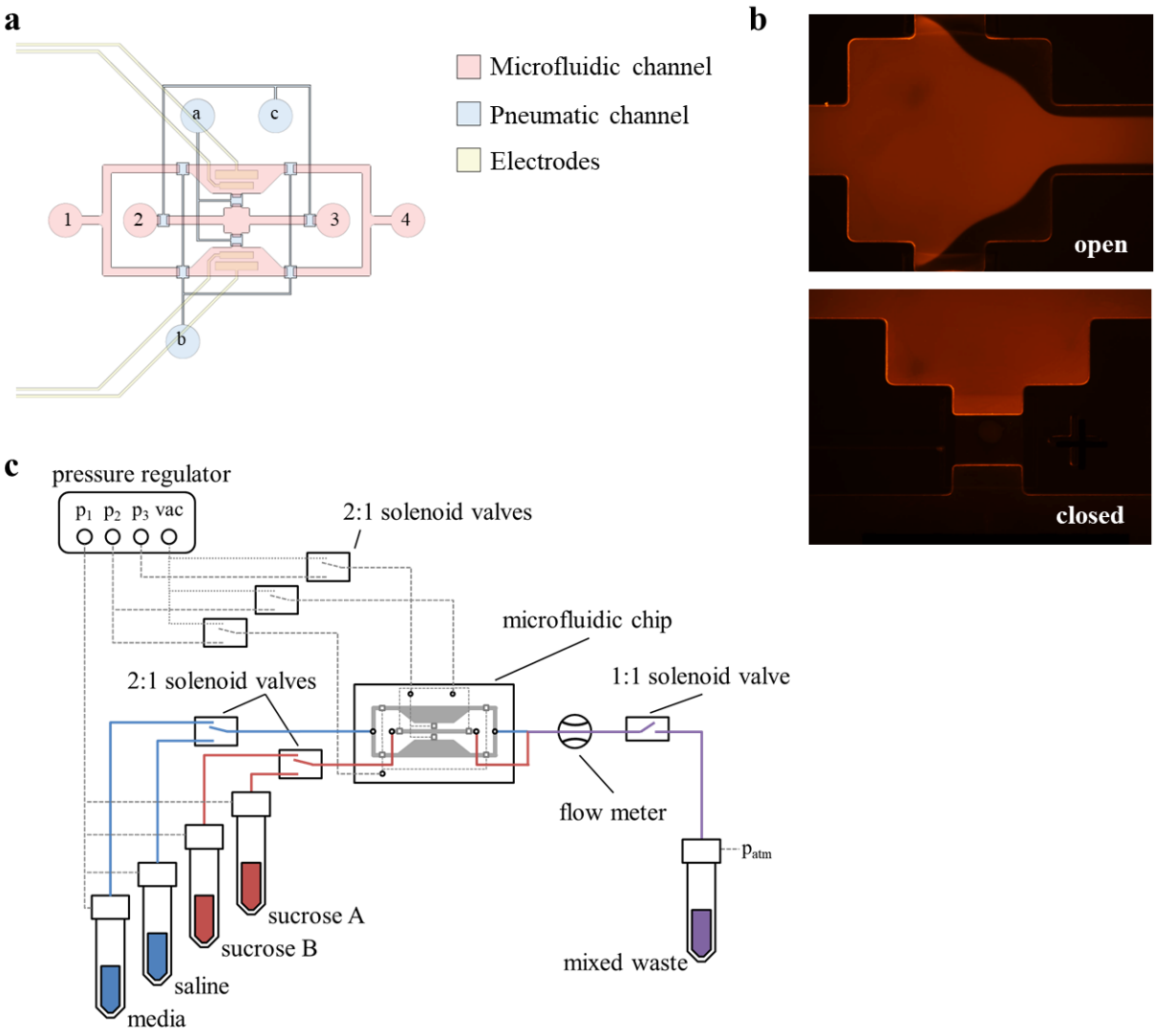

Figure 5.8: (**a**) Microfluidic sucrose gap device designed for external sucrose perfusion switching, (**b**) a micrograph of the device in operation showing laminar flow with the valves open and isolation of dye in the closed position (phase contrast/false color RFP fluorescence, 2x, 4x), and (**c**) the intended experimental setup to operate the sucrose gap device.

The results of viability testing (Figure 5.9c) show that cell death is low (<2%) for compression at 10 mbar or less. In testing of the microfluidic device, 10 mbar compression is always used to seal out as much extracellular fluid as possible without adversely affecting cell health. NRK cells cultured in the device consistently remained healthy for greater than 6 hours.

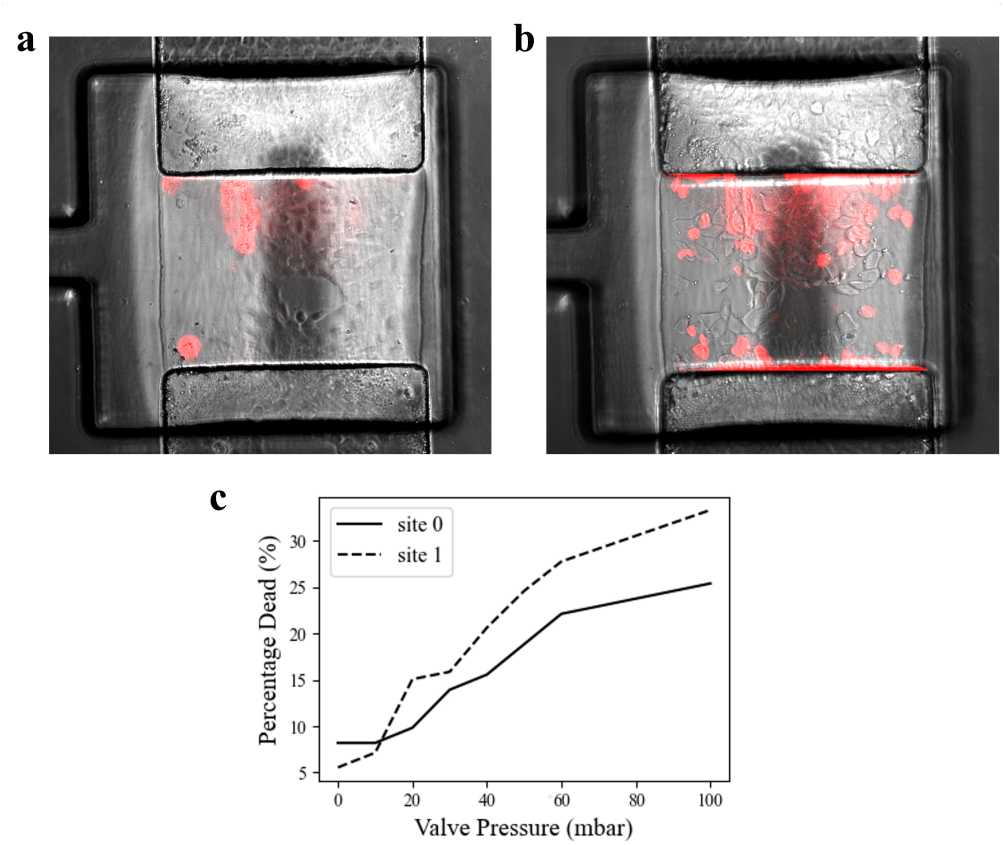

Figure 5.9: Cell viability testing under compressive strain from valves in the microfluidic device. NRK cells at two valve sites were compressed for 1 min. duration 25 times (each) at increasing pressures of 0, 10, 20, 30, 40, 50, 60, and 100 mbar. Dead cells were marked with EthD-1 (**a**) before and (**b**) after all 800 actuations (10x, false color composite phase contrast/RFP). (**c**) The cumulative percentage of cells that died after each sequence of 25 actuations, showing good viability at low compression pressure.

5.4.2.2 Control testing and experimental results

Because the sucrose solution is designed to be as non-conductive as possible, the addition of any drug or reagent into the assay needs to be carefully characterized. Figure 5.10 shows that the polarity of the 2-APB molecule (pK_a=9.6 (Bilmen et al., 2002)) alters the frequency response of the solution dramatically. Fortunately, in this case there exists a point within the biologically relevant spectrum at 410 Hz at which the impedance magnitude of the test and control solutions is well matched. In other cases, especially where an additive is conductive, the solutions would need to be carefully balanced with biologically inert substitutes.

Figure 5.11 shows the results of control experiments carried out using the microfluidic sucrose gap device. During experimentation, each measurement is carried out in two phases. In the flow phase,

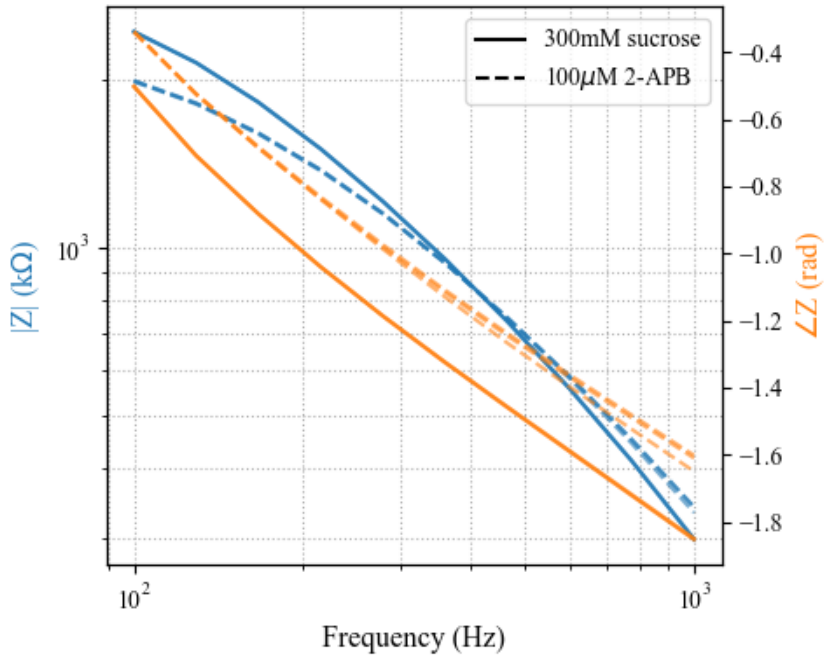

Figure 5.10: The polarity of the 2-APB molecule results in an altered frequency response. However, 100 µM 2-APB in 300 mM sucrose solution has a magnitude crossover point with the control solution (300 mM sucrose, 0.1% DMSO) at 410 Hz. The plot shows three independent measurements for each solution.

the external solenoids are open and one of the on-chip valves is pulled to vacuum to allow continuous perfusion. In order to ensure matching conditions in the measurement phase, the flow is arrested by closing the external valves and the applying positive pressure on the on-chip switching valves (30 mbar). Additionally, the driving pressure on the fluid is reduced to 0 mbar during measurement. Throughout the experiment, the isolation valves separating the sucrose and saline streams remain closed (and sealed against the cell monolayer if present).

Arresting flow results in an increased measured impedance as seen in the no cell control (Figure 5.11a). This small repeatable change of approximately 15 kΩ and 1° can be attributed to the local convection-diffusion mechanics near the electrodes under flow (Ayliffe and Rabbitt, 2003). The time signal is smoothed using a moving average (kernel size of 10) and peak values for each measurement are extracted to clearly show (Figure 5.11b) that switching between the two identical sucrose solutions is well matched.

Figure 5.11c shows the time sequence of the same control experiment with NRK cells cultured in the microfluidic device. With biology in play, a larger amount of baseline drift is present. Additionally, significant leakage through the isolation valves is present under flow. This effect may be attributed to the flow pressure forcing small leakage channels of extracellular fluid under the

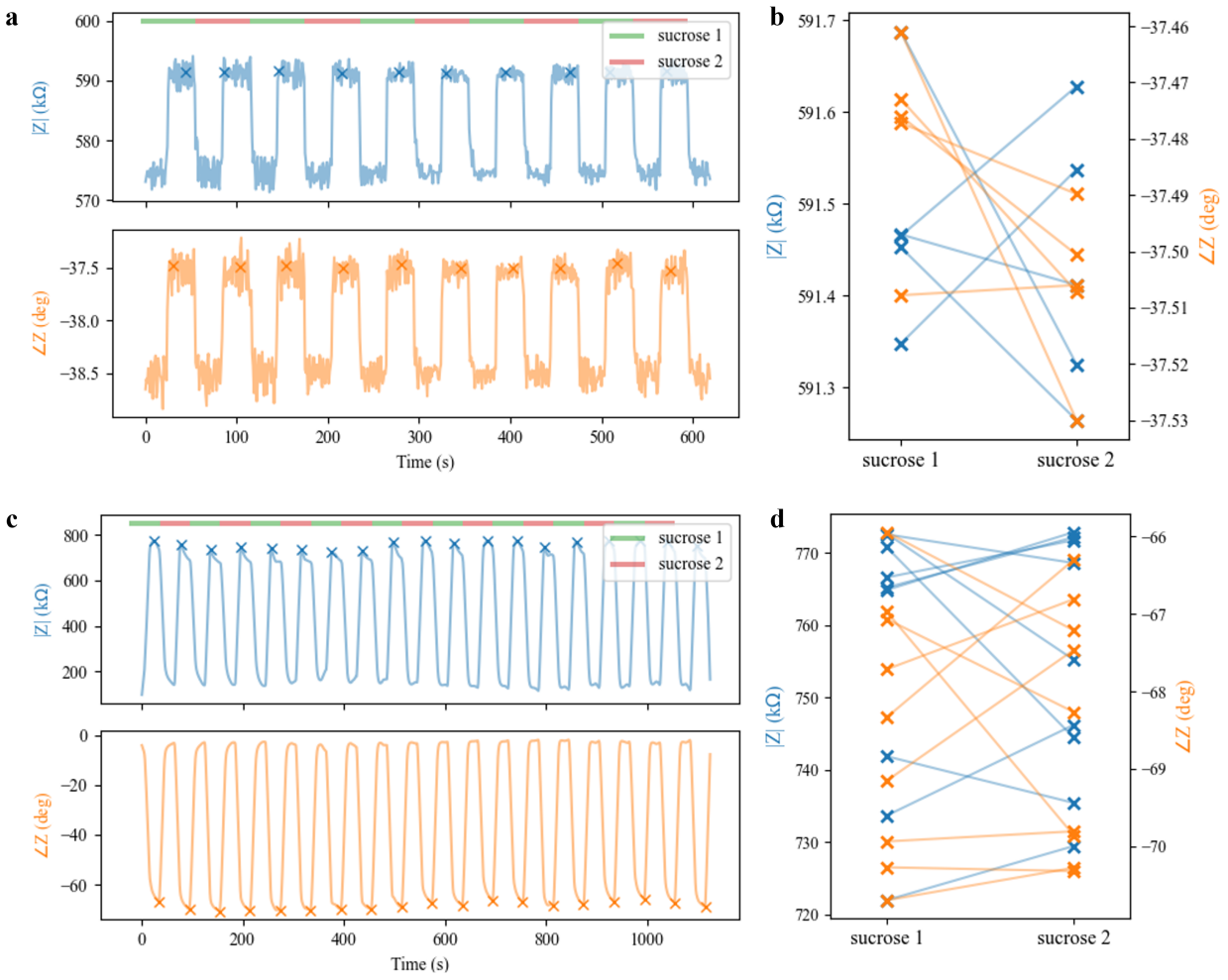

Figure 5.11: Control experiments in the sucrose gap microfluidic device. (a-b) Electrical impedance measurements at 410 Hz in the absence of cells show that the two switching channels on the chip are well matched. (c-d) Similarly, control experiments with NRK cells cultured in the device show no preference between input channels.

valve if the cell culture has gaps in confluency. However, these parasitic leakage channels appear to seal in the absence of driving pressure and the device seals even more tightly than in the no cell control.

The measured impedance through the cell layer near 750 kΩ is of the same order of magnitude as the literature (Table 5.1), though sources vary significantly. The result in this case is not a direct measurement of the gap junction resistance between two cells, rather it is a measure over an interconnected lattice. The measurement reflects an averaged gap junction over the network and the resulting value will depend heavily on the interconnectedness of the culture. Resistive lattice studies show that triangular, square, and hexagonal lattices, the network resistance generally converges to a single digit factor of node to node resistance (Atkinson and Steenwijk, 1999).

Table 5.1: Reported values for resistive coupling between adjacent cells.

Source	Cell Line	Method	Cell-cell R_j Estimate
Beyer et al. (2000)	NRK	Dual whole cell patch clamp	10 GΩ (Cx40)
Harris (2001)	various	Review, patch clamp	13 kΩ – 2 GΩ (25 plaques/cell, 1000 channels/plaque)
Valiunas et al. (2005)	NRK	Dual whole cell patch clamp	100 GΩ (high end estimate)
E. G. A. Harks et al. (2003)	NRK, HEK	Single patch clamp	6.6 MΩ (coupled), 2.4 GΩ (2-APB blocked)
Veenstra (2001)	N2A	Dual whole cell patch clamp	50 MΩ – 50 GΩ
Cedric Bathany et al. (2012)	NRK	Estimation based on connexin studies	91 kΩ – 1.3 MΩ (25 plaques/cell, 1000 channels/plaque
Veenstra (2016)	N2A, HeLa	Dual whole cell patch clamp	50 GΩ (poorly coupled, fewer than 6 channels)
This work	NRK	Microfluidic sucrose gap	730 kΩ – 930 kΩ (coupled), 930 kΩ – 940 kΩ (2-APB blocked)[1]

Thus, the recorded value should fall within an order of magnitude of the average cell-cell coupling impedance depending on the cell density and number of channels formed.

5.4.2.3 Verification using chemical gap junction blocker

To verify gap junction measurement in the device, the gap junction blocker, 2-APB (E. G. A. Harks et al., 2003; Ma et al., 2011), was alternately perfused into one of the sucrose input channels. Figure 5.12 shows that treatment with 100 µM 2-APB results in a consistent increase in measured impedance magnitude at 410 Hz. The average increase of 6.51 kΩ suggests that gap junction blockage due to 2-APB increases network resistance and that this instrumentation is sufficiently sensitive to detect this physiological change.

Additionally, the phase measurement shows a significant average increase of 0.464 °, suggesting that electrical measurement of phase delay may be a significant indicator of changes in intercellular connectivity. This result is not unexpected as cells isolated from their neighbors would trap charge in place, creating dielectric moments and behaving similarly to capacitors at low frequencies. Some patch clamp data supports this analysis that capacitance may be a promising model to study cells isolated by blocked gap junctions (Roos, Zoelen, and Theuvenet, 1996). It should be noted, however, that the constant phase offset in the 2-APB solution impedance (Figure 5.10) somewhat

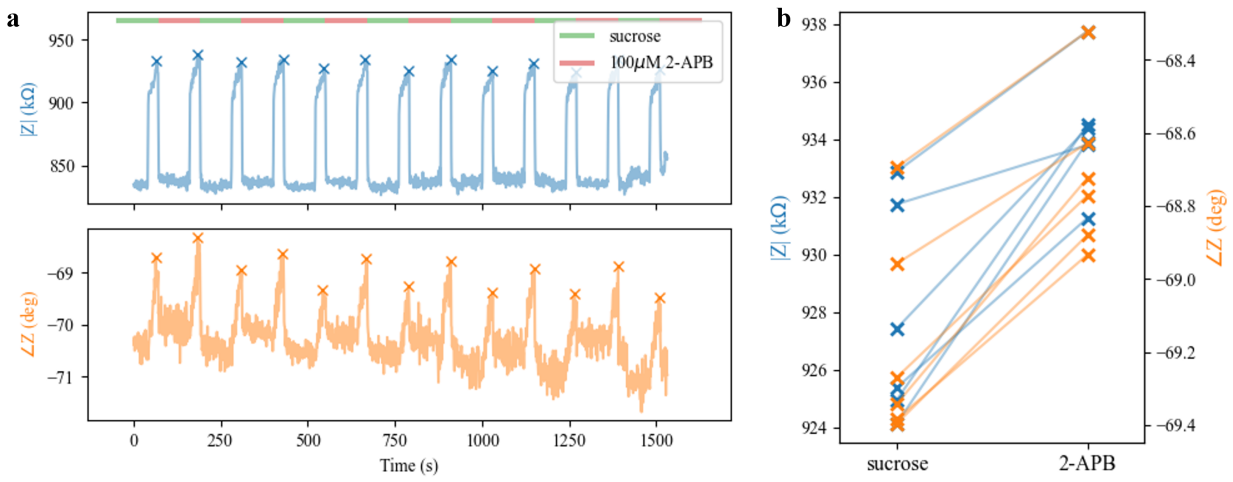

Figure 5.12: Gap junction blocker verification of device operation. (**a**) Time course of the experiment in which central sucrose chamber was alternately perfused with a control sucrose solution and a 100 µM 2-APB solution. "X" markers represent the extracted maxima for each measurement cycle. (**b**) Adjacent pairs of extracted maxima are plotted together, showing that after treatment with 2-APB the measured impedance through the cell layer increases by 6.51 kΩ and 0.46 degrees on average despite baseline drift.

confounds the magnitude of these phase data results.

Though these results are significant (Figure 5.13), the impedance increase due to gap junction blocker is closer than ideal to the noise floor demonstrated in the cell control. A number of improvements could be made in future investigations to improve this signal quality. The crucial sealing impedance is directly affected by the uniformity of the cell culture. Continued improvements should be made on this front to improve device design and culture protocols to increase cell viability. Additional control valves to facilitate media exchange between measurements and more specifically define cell seeding areas may prove important. Additional testing should explore the parameter space in terms of treatment and measurement timings, alternate gap junction blocker agents, and alternate interrogation frequencies. In particular, the electrical phase response of gap junction connected cells across a broader frequency range merits further exploration.

5.5 Conclusions

Elastomeric valves show promise as a novel approach to isolation of gap junction measurement. Single valves showed control testing sealing as high as 250 kΩ at 100 Hz and offer distinct advantages in terms of scalability and 2-D network examination.

A microfluidic device has been designed and fabricated to realize the sucrose gap technique at microscale. The device uses elastomeric valves to seal tightly against a cell monolayer, forcing a

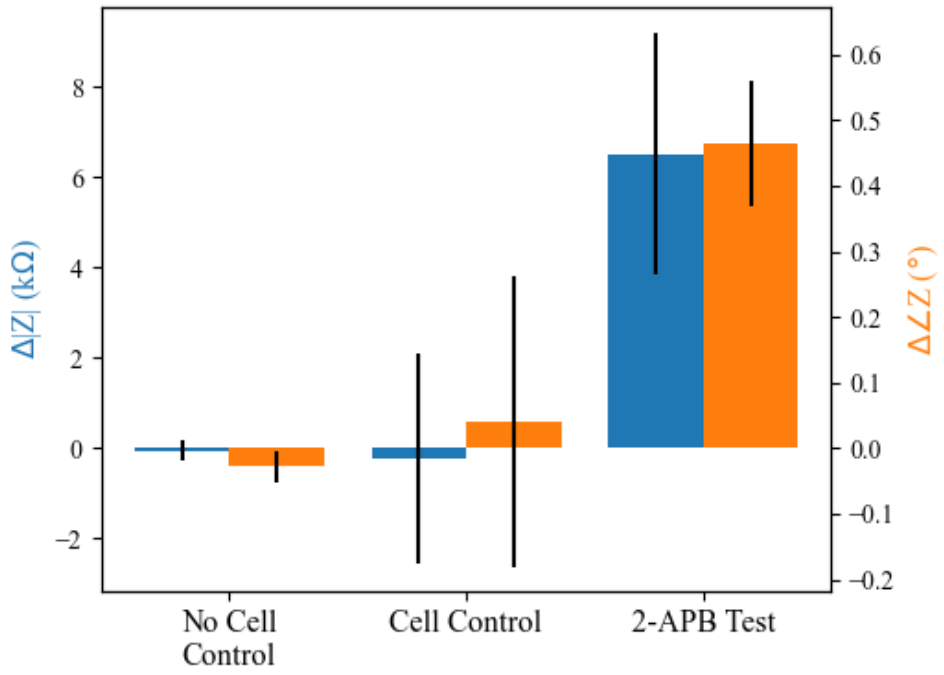

Figure 5.13: Test results for the proof-of-concept microfluidic gap junction device. Experiments with the gap junction blocker, 2-APB, show a significantly increased change in impedance in the presence of the blocker as compared to control experiments.

detectable portion of stimulated electrical current through the gap junctions in the cellular network. The proof-of-concept system was able to detect a 6.5 kΩ increase in cell network impedance at 410 Hz in response to treatment with the chemical gap junction blocker, 2-APB. Microfluidic devices capable of reliable electrical measurement of gap junction connectivity could enable advances in developmental and regenerative biology that shed light on how we grow, develop, and heal.

Chapter 6

CONCLUSIONS: TOWARD MICROFLUIDIC GAP JUNCTION MEASUREMENT

6.1 Comparison of Microfluidic Designs for Gap Junction Interrogation

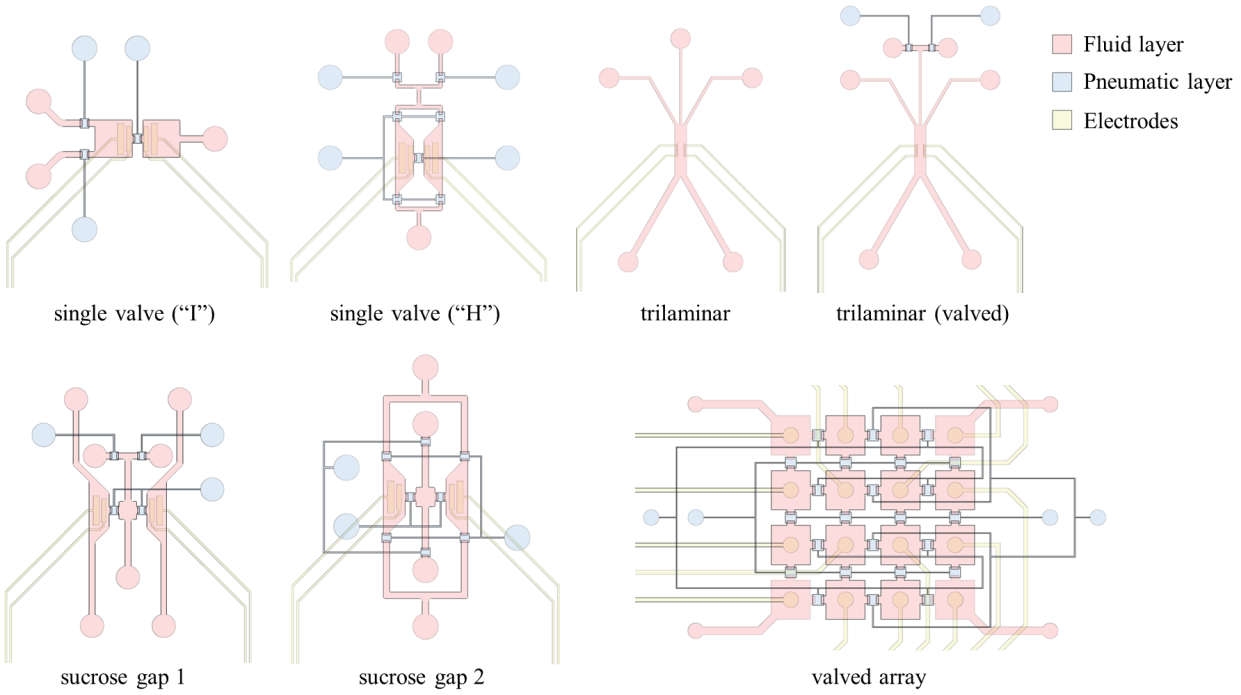

Figure 6.1: A pictorial summary of all microfluidic device designs intended for gap junction connectivity measurement on the Lab-on-Scope system. Scale is not matched between diagrams.

A number of microfluidic device designs have been implemented to attempt to electrically assess gap junction connectivity in cell monolayers. Figure 6.1 shows seven designs which were evaluated on the Lab-on-Scope system. The measurement scheme for the *trilaminar* and *trilaminar (valved)* designs relies on laminar flow of sucrose, while the other five designs are based on the principle of mechanically induced electrical isolation by elastomeric valves. (The *sucrose gap 1* design could be operated in a trilaminar flow mode as well. A bilaminar flow design with multiple electrode sites was also examined, but is not included in Figure 6.1 as its fabrication and electrode scheme are not directly comparable to presented designs.) The two single valve schemes are differentiated by the direction of fluid flow relative the to electrical interrogation site, with the "I" design channeling all flow under the interrogation valve and flow running perpendicular to electrical measurement in the

	Single Valve ("I")	Single Valve ("H")	Trilaminar	Trilaminar (valved)	Sucrose Gap 1	Sucrose Gap 2	Valved Array
Isolation approach	valve	valve	sucrose gap	sucrose gap	valve, sucrose gap	valve, sucrose gap	valve
Measurement conditions	static media	static media	trilaminar flow	trilaminar flow	static sucrose	static sucrose	static media
On-chip perfusion switching	Yes	Yes	No	Yes	Yes	No	No
Total ports	6	7	5	7	10	7	8
Total valves	3	6	0	2	4	8	24
Measured cell area (µm)	400× 500	400× 500	300× 5000*	300× 5000*	2350× 500	2350× 500	400× 500 (×24)
Average sealing impedance (kΩ@100Hz)	250	250	275*	275*	575 (400Hz)	365	–

Table 6.1: A comparison of the microfluidic device designs for electrical measurement of gap junction connectivity. Device names correspond to the designs shown in Figure 6.1. *value represents a stream width comprising 50% of the inter-electrode space.

"H" design. The two trilaminar devices are differentiated only by the presence of on-chip perfusion switching in *trilaminar (valved)*. *Sucrose gap 1* features on-chip perfusion switching, but does not have any internal valves to arrest flow in the saline channels. In contrast, *sucrose gap 2* requires external switches to change perfusion but internal switches can be used to halt flow and electrically isolate the saline chambers. Table 6.1 provides a summary comparison of the important metrics between the sucrose gap measurement designs.

The primary design decisions for each device center on balancing the trade offs and benefits of the isolation approach, measurement conditions, and perfusion style. Devices using the valve isolation approach solely have the primary advantage of measuring the cells in biologically relevant media

conditions. Trilaminar flow based approaches may offer slightly greater electrical isolation, so the sucrose gap devices attempt to incorporate both schemes. The addition of on-chip perfusion switching through integrated valves significantly reduces the experimental run times by eliminating dead volumes. However, this increased throughput comes at the cost of increased fabrication and operational complexity. Both the valved and laminar flow approaches must combat cell health concerns in terms of managing shear stress and nutrient delivery. However, some cell types may be more susceptible to the additional stressors of mechanical compression from elastomeric valves or continuous sucrose exposure in laminar flow devices.

The total number of ports (both fluid and pneumatic) in each device design serves as a proxy measure for the setup complexity. Each port must be connected to a fluid/pneumatic line (maintaining sterility) after incubation and must be carefully managed to avoid the introduction of air bubbles. Additionally, the number of ports corresponds directly to approximate volume of the chip, since the volume of the microfluidic channels is negligible compared to the macroscale ports (approx. 15 mm^3/per port). Generally, a design like *sucrose gap 1* will require significantly more setup, external components (such as tubing, valves, and reservoirs), and operator experience to assemble for experimentation than *sucrose gap 2*. Likewise, the *trilaminar (valved)* and *single valve "H"* designs add moderate setup complexity compared to their counterparts.

The total number of valves serves as an approximate measure of the fabrication complexity, as each valve has a small chance of misalignment or incomplete oligomer stamping. Further, larger designs, which tend to encompass more valves, become more difficult to manage in terms of drooping, stretch, and thermal contraction in the PDMS. (For standard lithography using rigid layers, poor alignment would generally effect yield uniformly across the whole wafer. However, the elasticity of PDMS and the small scale nature of the prototyping process with makeshift alignment tools, means that defect probability becomes more independent for each valve even with proper alignment.) To a lesser extent, the valve count also reflects the operational complexity of managing fluid flows in the chip. However, a well automated support system like the Lab-on-Scope mitigates operational load. The *sucrose gap 2* design trades off the setup complexity in *sucrose gap 1* for fabrication and operational complexity. The *valved array* design has by far the highest fabrication complexity and only one device was ever successfully produced as a proof-of-concept.

To compare the electrical performance of each design, a rough average of the typical no-cell control baseline impedance is provided in Table 6.1. This "sealing" impedance is a measure of the resistance seen in parallel with the gap junction network during measurement. Ideally, it should be as large as possible to avoid signal loss through conduction sharing. However, it is important to note that, as previously discussed, the measurement conditions are not equivalent across all the devices. The single valve devices report the lowest isolation impedance, but also measure across a narrow active

area (400 µm) and crucially immerse the cells in ion-rich media rather than sucrose. Single valve devices have the potential to increase their sealing impedance through dilution of the extracellular media. For the trilaminar flow devices, the control impedance is a function of the sucrose stream width. At 100 Hz, it can be increased as high as 500 kΩ, but operating stability becomes precarious. The sucrose gap devices show the highest isolation impedance, using both sucrose solution and two elastomeric valves to prevent extracellular ion currents. The *sucrose gap 1* device, especially, exhibited control experiment impedances large enough that they became difficult to capture with current instrumentation at low frequencies. The devices showed an average sealing impedance of 575 kΩ at 400 Hz, however, the sucrose perfused cell culture area across which the measurement is taken is nearly 8 times the length of the single valve device. The *sucrose gap 2* design showed appreciable sealing impedance at 365 kΩ, but may be degraded due to current leakage through the branching saline input channel. Overall, while single elastomeric valves offer slightly less isolation impedance, their qualities in terms of scalability and measurement in media conditions make them worth pursuing. However, for the greatest possible isolating effect, a combined approach using valves to create a sucrose gap appears to be the most effective solution.

6.2 Future Work

6.2.1 Intracellular Access

The primary advancement that would greatly enhance the viability of both the laminar flow and elastomeric membrane isolation schemes is improved intracellular electrode access. As discussed at length in Section 4.4, the cell membrane provides a significant electrical barrier on par with (or exceeding) the electrical isolation provided by sucrose solutions or mechanical barriers. Biological systems inherently introduce significant noise and test-to-test variation, and a device measuring gap junction connectivity is likely to need intracellullar electrical access in order to attain an acceptable signal to noise ratio. Bringing the electrodes into the intracellular space causes the membrane impedance to work in favor of the measurement rather than against it, confining the induced ion currents to the cell network and forcing them through the gap junction couplings.

Accessing the intracellular space generally requires complicated fabrication of nanostructures small enough to be enveloped by cell growth. Nanostructures that have been used to gain intracellular access include gold mushroom caps (Ojovan et al., 2015), platinum nanoneedles (Abbott, Ye, Ham, et al., 2018), and platinum black clusters (Abbott, Ye, Krenek, et al., 2020). While these structures coupled with temporary electroporation can offer high fidelity intracellular recordings, their reliability and reusability is still an area of active research. Other attempts to emulate patch clamp-like access in planar electrodes have used vacuum to seat cells tightly into micropores (X. Li et al., 2006; C.-Y. Chen et al., 2009; Y. Lau et al., 2006). The feasibility of such systems for use on static confluent cultures will need to be accessed. Further, true intracellular access would require

operating such a planar patch clamp system in a whole-cell configuration, while most research has been conducted thus far in the cell-attached mode.

Even moderate advances in lowering the barrier to intracellular access (lowering the total membrane resistance to hundreds of kiloOhms) would significantly increase the viability of these microfluidic approaches. The sealing impedance control measurements of Table 6.1 set a rough upper bound for the minimum target membrane impedance that should be encountered by the system. However, in the case that electrode advances succeed entirely in gaining intracellular access, such that electrodes are positioned interior to the cell membranes, a microfluidic setup may no longer be strictly necessary. Rather, an array of intracellular electrodes could spatially measure gap junction connectivity either through local capacitive transients (see Roos, Zoelen, and Theuvenet (1996)) or through impedance measurement between electrode pairs.

6.2.2 System Improvements

The parameter space in which the gap junction measurement systems can operate is enormous. Though we have attempted to identify and explore the more relevant points in the parameter space, much is still left uncharted. Nowhere is this more true than in the frequency domain. Stimulus frequencies have been selected to avoid interference and to match control solution impedances, but other frequencies in the biological spectrum may offer additional information. There may be a frequency on the higher end of the relevant range which more optimally bypasses the cell membrane capacitance and still drives ionic moments through the gap junction network. One study has even suggested that gap junction blocker effects are best observed at exceptionally low frequencies (sub 1 Hz), though the findings of this report are tenuous (Asfour et al., 2010). The current electrical instrumentation is capable of performing electrical impedance spectroscopy, but broad frequency sweeps can take more than a minute to allow for sufficient settling time and sampling at each step. Future iterations of the platform may instead invest in frequency domain multiplexing to allow continuous impedance monitoring at several fixed frequencies. A well engineered system would solve the timing problems of periodic sweeps with little trade-off, and it would multiply the amount of information gathered in any given experiment.

Continued optimization of culture conditions for cell health and monolayer uniformity is one of the key areas for improvement of the devices for all devices, but especially for those using the elastomeric valve isolation scheme. A tight and consistent monolayer will provide the most uniform surface for the valve membrane to seal against, resulting in the greatest sealing resistance. While the protocols developed here work reliably, alternate timings, extracellular matrix treatments, or seeding densities could result in more resilient and better connected cultures. Lowered seeding densities with more time allowed for growth and replication may also result in tighter more connected tissues.

On the device design side, tighter sealing of valves to the cell layer could be achieved through improved conformabilty of the elastomer membrane. Membrane shape, thickness, and material properties could all be re-examined to optimize for maximum sealing resistance versus fabrication reliability. Anecdotally, PDMS devices tend to stiffen with use and aging, so improving the fabrication yields to allow a regime of single-use disposable devices could also lead to better elastomeric membrane sealing.

Trilaminar flow devices would be significantly improved by the development of a real time stream width monitoring system. Mavrogiannis et al. (2017) showed that high frequency impedance monitoring of a flow boundary across interdigitated electrodes can measure stream position with high sensitivity. Continuous stream width monitoring could be used along with calibration sweeps to correct impedance measurements or could be treated as input for closed loop control of stream width. Reducing the system dependence on imaging would additionally help facilitate parallelization of the experiments as optics are often the bottleneck in terms of both throughput and cost.

6.2.3 Parallelization and Throughput

The valve fabrication process necessitates that devices be closed and sealed to the substrate. While elastomeric valves present new opportunities to reduce extracellular media and eliminate flush out times in perfusion, the single most significant drawback is that cells must be seeded into the devices and cultured prior to experimentation. Effective protocols for cell culture have been developed (Appendix B), however, the time-cost associated with cultivating healthy confluent cell monolayers in the devices is unavoidable. A 6-8 hour culture protocol significantly reduces the throughput of biological experimentation, especially in a prototyping environment where few duplicates of a design can be manufactured at once.

To combat the time-cost of cell culture, parallelization should be pursued both at the device and test fixture level. The number of parallel devices (or interrogation sites) that can be fabricated in the microfluidic chip is limited more by the number of input/output connections (fluidic, pneumatic, and electrical) rather than by the size of the microfluidic channels and features. That is, the majority of the footprint of the device is consumed by the ports to connect macroscale tubing. Reworking the microfluidic designs to feature multiple devices operating synchronously off of shared pneumatic controls would greatly increase the number of replicates that can be produced. If the number of input/output ports allows, placing fully independent test chambers on the same device would be ideal to support simultaneous control and experimental conditions in the same device under test.

To facilitate additional ports on parallelized chips, the lab-on-scope system could be expanded to accommodate a larger valve array and to accept multiple devices. Alternately, because of its low-cost and small form factor, multiple lab-on-scope systems could be run simultaneous through

centralized software.

Development of a wafer-level fabrication flow for PDMS bonding and alignment would significant increase the number of available devices and allow parametric optimization of device parameters such as valve sizes and membrane thicknesses. Overcoming issues of PDMS thermal expansion and alignment of non-rigid layers would likely require development of dedicated equipment (see Section 2.5). However, a reliable automated process for multilayer PDMS alignment, stamping, and bonding would be a fundamental advancement that could enable integration of valves into microfluidic devices across a wide variety of applications.

6.2.4 Alternate Approaches to Gap Junction Measurement

The microfluidic device development pursued in this work enabled several notable additional research opportunities that could not be specifically pursued.

At a stable laminar flow boundary between saline and sucrose, a sharp transition in membrane potential is induced by the sucrose-side depolarization. Theoretically, the slope of this transition should this transition should be a function of the gap junction connectivity, so imaging using genetic voltage indicators could be used to extract a measure correlated with the average gap junction resistance in the network. However, this approach incurs some of the issues that the trilaminar technique encounters, namely a critical dependence on laminar flow boundary stability and issues with cell health in a sucrose environment. It will need to be determined if the stochastic average membrane potential at the flow boundary is a reliable indicator, as the transition region may span a single cell or less in some networks.

Laminar flow devices may benefit from studying the electric and fluid dynamics of the establishment of laminar flow boundaries, rather than the flow in dynamic equilibrium. The fluid dynamics of pulsing in a trilaminar bolus are significantly more difficult to capture and anaylze, but the this tranisition situation may be the best window to capture the effects of gap junction connectivity before voltage gating at the flow boundaries becomes significant. This opportunity for exploration is enabled by the presence of automated on-chip valves that can pulse well defined boluses into the electrode channel.

Additionally, the laminar flow devices are well suited to performing dye diffusion assays using membrane permeable fluorescent dyes. While this approach lacks the real-time readout and repeatability of an electrical measurement of gap junction connectivity, for applications that can tolerate long washout cycles, this approach should be considered a viable option.

Finally, the microvalve fabrication technology explored in this work enables a number of related microfluidic cell culture studies that could be pursued in these devices or close variants. Valves can be used to isolation other forms of long range molecular signaling between cells, such as hormonal

or paracrine signaling. Generally, co-culture studies are enabled where the extracellular exchange between symbiotic or antagonistic cell lines can be selectively permitted or removed. Valves can be used to create localized stress patterns or to completely rupture cells to study regrowth and regeneration.

6.3 Contributions to the State of the Art

This work has made meaningful advances in both science and engineering with accomplishments spanning a wide variety of fields. A brief summary of important contributions is provided here.

A novel microfabrication method of oligomer stamping has been characterized and optimized for selective bonding of PDMS onto glass surfaces. The process enables reliable fabrication of normally closed elastomeric valves on rigid substrates, which is ideal for integrating electrodes into valved microfluidic devices.

A lab-on-scope system to densely integrate the peripheral systems necessary for a microfluidics lab into a unified platform has been developed. Magnetically latched switches, temperature regulation, flow sensing, fluorescent imaging, and electrical impedance spectroscopy are all enabled in a compact, cost-effective, and automated system. This platform fills a gap between scientists looking to leverage microfluidic technologies and the large and costly array of peripheral lab systems needed to operate microfluidic devices.

Protocols were developed for seeding and culture of NRK cell monolayers in closed microfluidic devices. Outside of scaffolded organ-on-chip devices, static cell culture in microfluidic devices is rare, and we contribute the first protocol for the NRK cell line. Further, we believe that the general procedures developed for seeding, maintaining sterility, avoiding bubble formation, and interfacing with with electronics and macrofluidic lines are widely applicable to many microfluidic projects.

A memory mechanism was inadvertently discovered in PDMS. Flow rate of ionic solution through valved PDMS microfluidic devices was correlated with the electrical impedance measured across the valves up to 10 minutes after flow was arrested. This analog material memory could be a consequential discovery for microfluidic and neuromorphic computing.

Significant improvements were made to the laminar flow sucrose gap approach to gap junction measurement, including on-chip switching and stream width based impedance calibration approach, for which a theoretical model was developed from fundamental fluid dynamics principles. Weaknesses in the electrical modeling for this approach have been identified that explain insignificant test results and suggest improvements for future microfluidic gap junction measurement devices.

Finally, a new microfluidic method for gap junction isolation through mechanical reduction of the extracellular media using elastomeric valves was proposed, prototyped, and evaluated. As a gap

junction blocker assay, the elastomeric valve approach allows measurement in media environments, can accommodate inhibitors with slower mechanisms, and allows two dimensional network examination. This new micromechanical approach shows promise as a method to isolation gap junction currents for real time electrical measurement.

6.4 Final Thoughts

This project was an ambitious attempt to provide an alternative to a Nobel prize winning technology (namely patch clamping). In the attempt to use microfluidic means to provide test conditions suitable for electrical measurement of gap junction connectivity, expertise in many areas of science and engineering were developed. Knowledge of microfabrication, material science, fluid dynamics, electrical instrumentation, cell biology, and bioelectric modeling are all necessary to produce effective devices. In order to drive continued progress, significant interdisciplinary collaboration will be needed to find a reliable solution to this significant, but ultimately important and meaningful challenge.

BIBLIOGRAPHY

Aasen, Trond et al. (Dec. 2016). "Gap junctions and cancer: communicating for 50 years". en. In: *Nature Reviews Cancer* 16.12. Publisher: Nature Publishing Group, pp. 775–788. ISSN: 1474-1768. DOI: 10.1038/nrc.2016.105. URL: https://www.nature.com/articles/nrc.2016.105 (visited on 12/19/2024).

Abbaci, Muriel et al. (July 2008). "Advantages and limitations of commonly used methods to assay the molecular permeability of gap junctional intercellular communication". eng. In: *BioTechniques* 45.1, pp. 33–52, 56–62. ISSN: 0736-6205. DOI: 10.2144/000112810.

Abbott, Jeffrey, Tianyang Ye, Donhee Ham, et al. (Mar. 2018). "Optimizing Nanoelectrode Arrays for Scalable Intracellular Electrophysiology". en. In: *Accounts of Chemical Research* 51.3, pp. 600–608. ISSN: 0001-4842, 1520-4898. DOI: 10.1021/acs.accounts.7b00519. URL: https://pubs.acs.org/doi/10.1021/acs.accounts.7b00519 (visited on 06/16/2022).

Abbott, Jeffrey, Tianyang Ye, Keith Krenek, et al. (Feb. 2020). "A nanoelectrode array for obtaining intracellular recordings from thousands of connected neurons". en. In: *Nature Biomedical Engineering* 4.2. Publisher: Nature Publishing Group, pp. 232–241. ISSN: 2157-846X. DOI: 10.1038/s41551-019-0455-7. URL: https://www.nature.com/articles/s41551-019-0455-7 (visited on 09/25/2024).

Abbott, Jeffrey, Tianyang Ye, Ling Qin, et al. (Feb. 2017). "CMOS nanoelectrode array for all-electrical intracellular electrophysiological imaging". In: *Nature Nanotechnology* 12, pp. 460–466.

Abu-Nimeh, Faisal T. and M. Salem Fathi (Nov. 2010). "Integrated magnetic array for bio-object sensing and manipulation". In: IEEE, pp. 62–65. URL: http://ieeexplore.ieee.org/document/5709571/.

Adermark, Louise and David M. Lovinger (June 2008). "Electrophysiological properties and gap junction coupling of striatal astrocytes". eng. In: *Neurochemistry International* 52.7, pp. 1365–1372. ISSN: 0197-0186. DOI: 10.1016/j.neuint.2008.02.006.

Allen, Francesca, Cheryll Tickle, and Anne Warner (Apr. 1990). "The role of gap junctions in patterning of the chick limb bud". en. In: *Development* 108.4, pp. 623–634. ISSN: 0950-1991, 1477-9129. DOI: 10.1242/dev.108.4.623. URL: https://journals.biologists.com/dev/article/108/4/623/36620/The-role-of-gap-junctions-in-patterning-of-the (visited on 06/15/2024).

Asfour, H. et al. (Apr. 2010). "Low frequency impedance spectroscopy of cell monolayers using the four-electrode method". en. In: *Journal of Physics: Conference Series* 224.1, p. 012085. ISSN: 1742-6596. DOI: 10.1088/1742-6596/224/1/012085. URL: https://dx.doi.org/10.1088/1742-6596/224/1/012085 (visited on 05/17/2024).

Atkinson, D. and F. J. van Steenwijk (June 1999). "Infinite resistive lattices". en. In: *American Journal of Physics* 67.6, pp. 486–492. ISSN: 0002-9505, 1943-2909. DOI: 10.1119/1.19311. URL: http://aapt.scitation.org/doi/10.1119/1.19311 (visited on 04/13/2021).

Au, Anthony K. et al. (June 2011). "Microvalves and Micropumps for BioMEMS". en. In: *Micromachines* 2.2. Number: 2 Publisher: Molecular Diversity Preservation International, pp. 179–220. ISSN: 2072-666X. DOI: 10.3390/mi2020179. URL: https://www.mdpi.com/2072-666X/2/2/179 (visited on 04/06/2023).

Ayliffe, H Edward and RD Rabbitt (Aug. 2003). "An electric impedance based microelectromechanical system flow sensor for ionic solutions". In: *Measurement science & technology* 14.8, pp. 1321–1327. ISSN: 0957-0233. DOI: 10.1088/0957-0233/14/8/318. URL: https://www.ncbi.nlm.nih.gov/pmc/articles/PMC2723957/ (visited on 06/07/2024).

Babica, Pavel, Iva Sovadinová, and Brad L. Upham (2016). "Scrape Loading/Dye Transfer Assay". en. In: *Gap Junction Protocols*. Ed. by Mathieu Vinken and Scott R. Johnstone. Methods in Molecular Biology. New York, NY: Springer New York, pp. 133–144. ISBN: 978-1-4939-3664-9. DOI: 10.1007/978-1-4939-3664-9_9. URL: https://doi.org/10.1007/978-1-4939-3664-9_9 (visited on 12/03/2018).

Babikian, Sarkis (2016). "Heterogeneous Integration of Microfluidics on Printed Circuit Boards for Lab-on-Chip Applications". en. PhD thesis. UC Irvine. URL: https://escholarship.org/uc/item/78p3292v (visited on 06/05/2022).

Baek, Ju Yeoul et al. (Mar. 2005). "A pneumatically controllable flexible and polymeric microfluidic valve fabricated via in situ development". en. In: *Journal of Micromechanics and Microengineering* 15.5, p. 1015. ISSN: 0960-1317. DOI: 10.1088/0960-1317/15/5/017. URL: https://dx.doi.org/10.1088/0960-1317/15/5/017 (visited on 04/06/2023).

Bai, Donglin et al. (Dec. 2006). "Block of specific gap junction channel subtypes by 2-aminoethoxydiphenyl borate (2-APB)". eng. In: *The Journal of Pharmacology and Experimental Therapeutics* 319.3, pp. 1452–1458. ISSN: 0022-3565. DOI: 10.1124/jpet.106.112045.

Bakkum, Douglas J., Zenas C. Chao, and Steve M. Potter (Sept. 2008). "Spatio-temporal electrical stimuli shape behavior of an embodied cortical network in a goal-directed learning task". eng. In: *Journal of Neural Engineering* 5.3, pp. 310–323. ISSN: 1741-2560. DOI: 10.1088/1741-2560/5/3/004.

Bani-Yaghoub, Mahmud et al. (Mar. 1999). "The Effects of Gap Junction Blockage on Neuronal Differentiation of Human NTera2/Clone D1 Cells". In: *Experimental Neurology* 156.1, pp. 16–32. ISSN: 0014-4886. DOI: 10.1006/exnr.1998.6950. URL: https://www.sciencedirect.com/science/article/pii/S0014488698969503 (visited on 09/10/2024).

Bates, Emily (2015). "Ion channels in development and cancer". eng. In: *Annual Review of Cell and Developmental Biology* 31, pp. 231–247. ISSN: 1530-8995. DOI: 10.1146/annurev-cellbio-100814-125338.

Bathany, Cedric et al. (Sept. 2012). "A microfluidic platform for measuring electrical activity across cells". In: *Biomicrofluidics* 6.3.

Bathany, Cédric et al. (Feb. 2011). "High Throughput Assay of Diffusion through Cx43 Gap Junction Channels with a Microfluidic Chip". en. In: *Analytical Chemistry* 83.3, pp. 933–939. ISSN: 0003-2700, 1520-6882. DOI: 10.1021/ac102658h. URL: https://pubs.acs.org/doi/10.1021/ac102658h (visited on 04/13/2021).

Beyer, E C et al. (2000). "Modulation of intercellular communication by differential regulation and heteromeric mixing of co-expressed connexins". en. In: *Braz J Med Biol Res*, p. 7.

Bhattacharya, S. et al. (June 2005). "Studies on surface wettability of poly(dimethyl) siloxane (PDMS) and glass under oxygen-plasma treatment and correlation with bond strength". In: *Journal of Microelectromechanical Systems* 14.3. Conference Name: Journal of Microelectromechanical Systems, pp. 590–597. ISSN: 1941-0158. DOI: 10.1109/JMEMS.2005.844746.

Bilmen, Jonathan G. et al. (Aug. 2002). "Inhibition of SERCA Ca2+ pumps by 2-aminoethoxydiphenyl borate (2-APB). 2-APB reduces both Ca2+ binding and phosphoryl transfer from ATP, by interfering with the pathway leading to the Ca2+-binding sites". eng. In: *European Journal of Biochemistry* 269.15, pp. 3678–3687. ISSN: 0014-2956. DOI: 10.1046/j.1432-1033.2002.03060.x.

Borek, C., S. Higashino, and W. R. Loewenstein (Dec. 1969). "Intercellular communication and tissue growth : IV. Conductance of membrane junctions of normal and cancerous cells in culture". eng. In: *The Journal of Membrane Biology* 1.1, pp. 274–293. ISSN: 0022-2631. DOI: 10.1007/BF01869786.

Borók, Alexandra, Kristóf Laboda, and Attila Bonyár (Aug. 2021). "PDMS Bonding Technologies for Microfluidic Applications: A Review". In: *Biosensors* 11.8, p. 292. ISSN: 2079-6374. DOI: 10.3390/bios11080292. URL: https://www.ncbi.nlm.nih.gov/pmc/articles/PMC8394141/ (visited on 10/06/2022).

Bruno, Giulia et al. (June 2020). "Microfluidic Multielectrode Arrays for Spatially Localized Drug Delivery and Electrical Recordings of Primary Neuronal Cultures". In: *Frontiers in Bioengineering and Biotechnology* 8, p. 626. ISSN: 2296-4185. DOI: 10.3389/fbioe.2020.00626. URL: https://www.ncbi.nlm.nih.gov/pmc/articles/PMC7325920/ (visited on 07/23/2024).

Bruus, Henrik (2008). *Theoretical Microfluidics*. Vol. 18. Oxford Master Series in Physics. OUP Oxford.

Bukauskas, Feliksas F. and Vytas K. Verselis (Mar. 2004). "Gap junction channel gating". In: *Biochimica et biophysica acta* 1662.1-2, p. 42. ISSN: 0006-3002. DOI: 10.1016/j.bbamem.2004.01.008. URL: https://www.ncbi.nlm.nih.gov/pmc/articles/PMC2813678/ (visited on 12/20/2024).

Cabrera-López, J. J. et al. (Feb. 2016). "Bioimpedance measurement using mixed-signal embedded system". In: *2016 IEEE 7th Latin American Symposium on Circuits Systems (LASCAS)*, pp. 335–338. DOI: 10.1109/LASCAS.2016.7451078.

Chen, Chang-Yu et al. (Aug. 2009). "Patch clamping on plane glass—fabrication of hourglass aperture and high-yield ion channel recording". en. In: *Lab on a Chip* 9.16. Publisher: The Royal Society of Chemistry, pp. 2370–2380. ISSN: 1473-0189. DOI: 10.1039/B901025D. URL: https://pubs.rsc.org/en/content/articlelanding/2009/lc/b901025d (visited on 06/07/2022).

Chen, Hao et al. (Aug. 2008). "Electromechanical properties of pressure-actuated PDMS microfluidic push-down valves". In: *Analytical chemistry* 80.15, pp. 6110–6113. ISSN: 0003-2700. DOI: 10.1021/ac800506n. URL: https://www.ncbi.nlm.nih.gov/pmc/articles/PMC2587325/ (visited on 10/06/2022).

Chen, Sisi and Luke P. Lee (Mar. 2010). "Non-invasive microfluidic gap junction assay". en. In: *Integrative Biology* 2.2-3, pp. 130–138. DOI: 10.1039/b919392h. URL: https://academic.oup.com/ib/article/2/2-3/130/5210997 (visited on 08/28/2019).

Coluccio, Maria Laura et al. (Mar. 2019). "Microfluidic platforms for cell cultures and investigations". en. In: *Microelectronic Engineering* 208, pp. 14–28. ISSN: 0167-9317. DOI: 10.1016/j.mee.2019.01.004. URL: https://www.sciencedirect.com/science/article/pii/S016793171930019X (visited on 04/25/2022).

De Blasio, Birgitte Freiesleben et al. (Apr. 2004). "Combining optical and electrical impedance techniques for quantitative measurement of confluence in MDCK-I cell cultures". In: *BioTechniques* 36.4. Publisher: Taylor & Francis _eprint: https://doi.org/10.2144/04364RR01, pp. 650–662. ISSN: 0736-6205. DOI: 10.2144/04364RR01. URL: https://doi.org/10.2144/04364RR01 (visited on 10/11/2024).

Dungan, Joel et al. (Sept. 2023). "Optimization of Oligomer Stamping Technique for Normally Closed Elastomeric Valves on Glass Substrate". en. In: *Micromachines* 14.9. Number: 9 Publisher: Multidisciplinary Digital Publishing Institute, p. 1659. ISSN: 2072-666X. DOI: 10.3390/mi14091659. URL: https://www.mdpi.com/2072-666X/14/9/1659 (visited on 08/28/2023).

Eddings, Mark A., Michael A. Johnson, and Bruce K. Gale (Apr. 2008). "Determining the optimal PDMS–PDMS bonding technique for microfluidic devices". en. In: *Journal of Micromechanics and Microengineering* 18.6, p. 067001. ISSN: 0960-1317. DOI: 10.1088/0960-1317/18/6/067001. URL: https://dx.doi.org/10.1088/0960-1317/18/6/067001 (visited on 06/29/2023).

Ellappan, Premkumar and Raji Sundararajan (Mar. 2005). "A simulation study of the electrical model of a biological cell". en. In: *Journal of Electrostatics* 63.3-4, pp. 297–307. ISSN: 03043886. DOI: 10.1016/j.elstat.2004.11.007. URL: http://linkinghub.elsevier.com/retrieve/pii/S0304388604002141 (visited on 11/18/2018).

Emmons-Bell, M et al. (Nov. 2015). "Gap Junctional Blockade Stochastically Induces Different Species-Specific Head Anatomies in Genetically Wild-Type Girardia dorotocephala Flatworms". In: *International Journal of Molecular Sciences* 16.11, pp. 27865–27896.

Estlack, Zachary and Jungkyu Kim (July 2022). "Microvalve array fabrication using selective PDMS (polydimethylsiloxane) bonding through Perfluorooctyl-trichlorosilane passivation for long-term space exploration". en. In: *Scientific Reports* 12.1. Number: 1 Publisher: Nature Publishing Group, p. 12398. ISSN: 2045-2322. DOI: 10.1038/s41598-022-16574-9. URL: https://www.nature.com/articles/s41598-022-16574-9 (visited on 10/06/2022).

F. Henry, Olivier Y. et al. (2017). "Organs-on-chips with integrated electrodes for trans-epithelial electrical resistance (TEER) measurements of human epithelial barrier function". en. In: *Lab on a Chip* 17.13, pp. 2264–2271. DOI: 10.1039/C7LC00155J. URL: http://pubs.rsc.org/en/content/articlelanding/2017/lc/c7lc00155j (visited on 11/28/2018).

Fernandes, João et al. (Apr. 2022). "Real-time monitoring of epithelial barrier function by impedance spectroscopy in a microfluidic platform". en. In: *Lab on a Chip*. Publisher: The Royal Society of Chemistry. ISSN: 1473-0189. DOI: 10.1039/D1LC01046H. URL: https://pubs.rsc.org/en/content/articlelanding/2022/lc/d1lc01046h (visited on 04/30/2022).

Ferreira, Germán et al. (July 2021). "Hydrodynamic Entrance Length for Laminar Flow in Microchannels with Rectangular Cross Section". en. In: *Fluids* 6.7. Number: 7 Publisher: Multidisciplinary Digital Publishing Institute, p. 240. ISSN: 2311-5521. DOI: 10.3390/fluids6070240. URL: https://www.mdpi.com/2311-5521/6/7/240 (visited on 02/29/2024).

Franks, Wendy et al. (July 2005). "Impedance characterization and modeling of electrodes for biomedical applications". In: *IEEE Transactions on Biomedical Engineering* 52.7, pp. 1295–1302. ISSN: 1558-2531. DOI: 10.1109/TBME.2005.847523.

Fütterer, C. et al. (2004). "Injection and flow control system for microchannels". en. In: *Lab on a Chip* 4.4. Publisher: Royal Society of Chemistry, pp. 351–356. DOI: 10.1039/B316729A. URL: https://pubs.rsc.org/en/content/articlelanding/2004/lc/b316729a (visited on 12/17/2024).

Gajasinghe, R. W. R. L. et al. (Oct. 2016). "Label-free tumor cell detection and differentiation based on electrical impedance spectroscopy". In: *2016 IEEE SENSORS*, pp. 1–3. DOI: 10.1109/ICSENS.2016.7808466.

Gerasimenko, Tatiana et al. (Jan. 2020). "Impedance Spectroscopy as a Tool for Monitoring Performance in 3D Models of Epithelial Tissues". In: *Frontiers in Bioengineering and Biotechnology* 7, p. 474. ISSN: 2296-4185. DOI: 10.3389/fbioe.2019.00474. URL: https://www.ncbi.nlm.nih.gov/pmc/articles/PMC6992543/ (visited on 10/11/2024).

Giouroudi, Ioanna and Georgios Kokkinis (July 2017). "Recent Advances in Magnetic Microfluidic Biosensors". In: *Nanomaterials* 7.7, p. 171. ISSN: 2079-4991. DOI: 10.3390/nano7070171. URL: https://www.ncbi.nlm.nih.gov/pmc/articles/PMC5535237/ (visited on 06/15/2022).

Gnyawali, Vaskar et al. (May 2017). "Stable microfluidic flow focusing using hydrostatics". In: *Biomicrofluidics* 11.3, p. 034104. ISSN: 1932-1058. DOI: 10.1063/1.4983147. URL: https://www.ncbi.nlm.nih.gov/pmc/articles/PMC5418130/ (visited on 07/18/2024).

Gorcum, Mathijs van (2023). *Drop analysis*. URL: https://drop-analysis.com/ (visited on 04/03/2023).

Gu, Sumin et al. (May 2003). "Stimulation of Lens Cell Differentiation by Gap Junction Protein Connexin 45.6". en. In: *Investigative Ophthalmology & Visual Science* 44.5, pp. 2103–2111. ISSN: 1552-5783. DOI: 10.1167/iovs.02-1045. URL: https://iovs.arvojournals.org/article.aspx?articleid=2163598 (visited on 11/19/2018).

Hamdallah, Sherif I. et al. (June 2020). "Microfluidics for pharmaceutical nanoparticle fabrication: The truth and the myth". In: *International Journal of Pharmaceutics* 584, p. 119408. ISSN: 0378-5173. DOI: 10.1016/j.ijpharm.2020.119408. URL: https://www.sciencedirect.com/science/article/pii/S0378517320303926 (visited on 07/18/2024).

Harks, E.g.a. et al. (2003). "Ionic basis for excitability of normal rat kidney (NRK) fibroblasts". en. In: *Journal of Cellular Physiology* 196.3, pp. 493–503. ISSN: 1097-4652. DOI: 10.1002/jcp.10346. URL: https://onlinelibrary.wiley.com/doi/abs/10.1002/jcp.10346 (visited on 09/07/2024).

Harks, Erik G. A. et al. (2003). “Besides affecting intracellular calcium signaling, 2-APB reversibly blocks gap junctional coupling in confluent monolayers, thereby allowing the measurement of single-cell membrane currents in undissociated cells”. en. In: *The FASEB Journal* 17.8, pp. 1–21. ISSN: 1530-6860. DOI: https://doi.org/10.1096/fj.02-0786fje. URL: https://faseb.onlinelibrary.wiley.com/doi/abs/10.1096/fj.02-0786fje (visited on 04/13/2021).

Harris, Andrew L. (Aug. 2001). “Emerging issues of connexin channels: biophysics fills the gap”. en. In: *Quarterly Reviews of Biophysics* 34.3. Publisher: Cambridge University Press, pp. 325–472. ISSN: 1469-8994, 0033-5835. DOI: 10.1017/S0033583501003705. URL: https://www.cambridge.org/core/journals/quarterly-reviews-of-biophysics/article/emerging-issues-of-connexin-channels-biophysics-fills-the-gap/4EA5604638068A784FE93A48C2468059 (visited on 04/13/2021).

Herr, Amy E. et al. (2007). “Integrated Microfluidic Platform for Oral Diagnostics”. en. In: *Annals of the New York Academy of Sciences* 1098.1, pp. 362–374. ISSN: 1749-6632. DOI: 10.1196/annals.1384.004. URL: https://onlinelibrary.wiley.com/doi/abs/10.1196/annals.1384.004 (visited on 08/23/2023).

Hodgkin, A. L. and A. F. Huxley (Aug. 1952). “A quantitative description of membrane current and its application to conduction and excitation in nerve”. In: *The Journal of Physiology* 117.4, pp. 500–544. ISSN: 0022-3751. URL: https://www.ncbi.nlm.nih.gov/pmc/articles/PMC1392413/ (visited on 11/18/2018).

Huang, X. et al. (Oct. 2003). “Impedance based biosensor array for monitoring mammalian cell behavior”. In: Toronto, Ont., Canada: IEEE, pp. 304–309. ISBN: 0-7803-8133-5. DOI: 10.1109/ICSENS.2003.1278947. (Visited on 01/24/2108).

Hung, Paul J. et al. (2005). “Continuous perfusion microfluidic cell culture array for high-throughput cell-based assays”. en. In: *Biotechnology and Bioengineering* 89.1, pp. 1–8. ISSN: 1097-0290. DOI: 10.1002/bit.20289. URL: https://onlinelibrary.wiley.com/doi/abs/10.1002/bit.20289 (visited on 06/13/2022).

Irimia, Daniel and Mehmet Toner (Mar. 2006). “Cell handling using microstructured membranes”. eng. In: *Lab on a Chip* 6.3, pp. 345–352. ISSN: 1473-0197. DOI: 10.1039/b515983k.

Jin, Lei et al. (Sept. 2012). “Single Action Potentials and Subthreshold Electrical Events Imaged in Neurons with a Fluorescent Protein Voltage Probe”. In: *Neuron* 75.5, pp. 779–785. ISSN: 0896-6273. DOI: 10.1016/j.neuron.2012.06.040. URL: https://www.sciencedirect.com/science/article/pii/S0896627312007040 (visited on 12/23/2024).

Kim, Ji Woon et al. (Mar. 2022). “Microfluidic electrode array chip for electrical stimulation-mediated axonal regeneration”. en. In: *Lab on a Chip*. Publisher: The Royal Society of Chemistry. ISSN: 1473-0189. DOI: 10.1039/D1LC01158H. URL: https://pubs.rsc.org/en/content/articlelanding/2022/lc/d1lc01158h (visited on 04/30/2022).

Kim, Jongsoo, Manoj K. Chaudhury, and Michael J. Owen (June 2000). “Hydrophobic Recovery of Polydimethylsiloxane Elastomer Exposed to Partial Electrical Discharge”. en. In: *Journal of Colloid and Interface Science* 226.2, pp. 231–236. ISSN: 0021-9797. DOI: 10.1006/jc

is.2000.6817. URL: https://www.sciencedirect.com/science/article/pii/S0021979700968176 (visited on 06/29/2023).

Kim, Lily et al. (2007). "A practical guide to microfluidic perfusion culture of adherent mammalian cells". en. In: *Lab on a Chip* 7.6, p. 681. ISSN: 1473-0197, 1473-0189. DOI: 10.1039/b704602b. URL: http://xlink.rsc.org/?DOI=b704602b (visited on 05/04/2021).

Kodirov, Sodikdjon A. (Apr. 2023). "Whole-cell patch-clamp recording and parameters". In: *Biophysical Reviews* 15.2, pp. 257–288. ISSN: 1867-2450. DOI: 10.1007/s12551-023-01055-8. URL: https://www.ncbi.nlm.nih.gov/pmc/articles/PMC10133435/ (visited on 09/10/2024).

Koklu, Anil, Ahmet C. Sabuncu, and Ali Beskok (July 2016). "Rough Gold Electrodes for Decreasing Impedance at the Electrolyte/Electrode Interface". In: *Electrochimica Acta* 205, pp. 215–225.

Kwok, D. Y. and A. W. Neumann (Sept. 1999). "Contact angle measurement and contact angle interpretation". en. In: *Advances in Colloid and Interface Science* 81.3, pp. 167–249. ISSN: 0001-8686. DOI: 10.1016/S0001-8686(98)00087-6. URL: https://www.sciencedirect.com/science/article/pii/S0001868698000876 (visited on 01/04/2023).

Lenshof, Andreas, Cecilia Magnusson, and Thomas Laurell (Mar. 2012). "Acoustofluidics 8: Applications of acoustophoresis in continuous flow microsystems". en. In: *Lab on a Chip* 12.7. Publisher: The Royal Society of Chemistry, pp. 1210–1223. ISSN: 1473-0189. DOI: 10.1039/C2LC21256K. URL: https://pubs.rsc.org/en/content/articlelanding/2012/lc/c2lc21256k (visited on 06/15/2022).

Levin, Michael (Dec. 2019). "The Computational Boundary of a "Self": Developmental Bioelectricity Drives Multicellularity and Scale-Free Cognition". English. In: *Frontiers in Psychology* 10. Publisher: Frontiers. ISSN: 1664-1078. DOI: 10.3389/fpsyg.2019.02688. URL: https://www.frontiersin.org/journals/psychology/articles/10.3389/fpsyg.2019.02688/full (visited on 06/15/2024).

– (Apr. 2021a). "Bioelectric signaling: Reprogrammable circuits underlying embryogenesis, regeneration, and cancer". eng. In: *Cell* 184.8, pp. 1971–1989. ISSN: 1097-4172. DOI: 10.1016/j.cell.2021.02.034.

– (Oct. 2021b). "Bioelectrical approaches to cancer as a problem of the scaling of the cellular self". eng. In: *Progress in Biophysics and Molecular Biology* 165, pp. 102–113. ISSN: 1873-1732. DOI: 10.1016/j.pbiomolbio.2021.04.007.

Li, Nianzhen, Chia-Hsien Hsu, and Albert Folch (Oct. 2005). "Parallel mixing of photolithographically defined nanoliter volumes using elastomeric microvalve arrays". In: *Electrophoresis* 26.19, 10.1002/elps.200500171. ISSN: 0173-0835. DOI: 10.1002/elps.200500171. URL: https://www.ncbi.nlm.nih.gov/pmc/articles/PMC3848874/ (visited on 04/06/2023).

Li, Shiting et al. (Oct. 2015). "Connexin43-containing gap junctions potentiate extracellular Ca2+-induced odontoblastic differentiation of human dental pulp stem cells via Erk1/2". In: *Experimental Cell Research* 338.1, pp. 1–9. ISSN: 0014-4827. DOI: 10.1016/j.yexcr.2015.09.008. URL: http://www.sciencedirect.com/science/article/pii/S0014482715300914 (visited on 11/19/2018).

Li, Xiaohui et al. (Apr. 2006). "Microfluidic System for Planar Patch Clamp Electrode Arrays". In: *Nano Letters* 6.4. Publisher: American Chemical Society, pp. 815–819. ISSN: 1530-6984. DOI: 10.1021/nl060165r. URL: https://doi.org/10.1021/nl060165r (visited on 06/07/2022).

Lin, Shang-Jyun et al. (Mar. 2022). "An antibiotic concentration gradient microfluidic device integrating surface-enhanced Raman spectroscopy for multiplex antimicrobial susceptibility testing". en. In: *Lab on a Chip*. Publisher: The Royal Society of Chemistry. ISSN: 1473-0189. DOI: 10.1039/D2LC00012A. URL: https://pubs.rsc.org/en/content/articlelanding/2022/lc/d2lc00012a (visited on 04/30/2022).

Lorraine, Claire, Catherine S. Wright, and Patricia E. Martin (June 2015). "Connexin43 plays diverse roles in co-ordinating cell migration and wound closure events". In: *Biochemical Society Transactions* 43.3, pp. 482–488. ISSN: 0300-5127. DOI: 10.1042/BST20150034. URL: https://doi.org/10.1042/BST20150034 (visited on 12/19/2024).

Lu, Yen-Wen, Po-Ting Lin, and Chien-Shing Pai (June 2007). "Polydimethylsiloxane (PDMS) Bonding Strength Characterization by a Line Force Model in Blister Tests". In: *TRANSDUCERS 2007 - 2007 International Solid-State Sensors, Actuators and Microsystems Conference*. ISSN: 2164-1641, pp. 2095–2098. DOI: 10.1109/SENSOR.2007.4300578.

Ma, Ke-Tao et al. (Jan. 2011). "2-Aminoethoxydiphenyl borate blocks electrical coupling and inhibits voltage-gated K+ channels in guinea pig arteriole cells". In: *American Journal of Physiology - Heart and Circulatory Physiology* 300.1, H335–H346. ISSN: 0363-6135. DOI: 10.1152/ajpheart.00737.2010. URL: https://www.ncbi.nlm.nih.gov/pmc/articles/PMC3023242/ (visited on 06/15/2024).

Madsen, Morten Hannibal et al. (Oct. 2014). "Accounting for PDMS shrinkage when replicating structures". en. In: *Journal of Micromechanics and Microengineering* 24.12. Publisher: IOP Publishing, p. 127002. ISSN: 0960-1317. DOI: 10.1088/0960-1317/24/12/127002. URL: https://dx.doi.org/10.1088/0960-1317/24/12/127002 (visited on 04/07/2023).

Mahnam, Amin, Hassan Yazdanian, and Mohsen Mosayebi Samani (Mar. 2016). "Comprehensive study of Howland circuit with non-ideal components to design high performance current pumps". en. In: *Measurement* 82, pp. 94–104. ISSN: 0263-2241. DOI: 10.1016/j.measurement.2015.12.044. URL: https://www.sciencedirect.com/science/article/pii/S0263224115007046 (visited on 02/21/2021).

Marh, Joel et al. (Nov. 2012). "Hyperactive self-inactivating piggyBac for transposase-enhanced pronuclear microinjection transgenesis". In: *Proceedings of the National Academy of Sciences* 109.47. Publisher: Proceedings of the National Academy of Sciences, pp. 19184–19189. DOI: 10.1073/pnas.1216473109. URL: https://www.pnas.org/doi/10.1073/pnas.1216473109 (visited on 12/23/2024).

Măriuţa, Daniel et al. (Aug. 2020). "Miniaturization of fluorescence sensing in optofluidic devices". en. In: *Microfluidics and Nanofluidics* 24.9, p. 65. ISSN: 1613-4990. DOI: 10.1007/s10404-020-02371-1. URL: https://doi.org/10.1007/s10404-020-02371-1 (visited on 06/15/2022).

Mathews, Juanita and Michael Levin (June 2016). "Gap junctional signaling in pattern regulation: Physiological network connectivity instructs growth and form". In: *Developmental Neurobiology*.

Mavrogiannis, Nicholas et al. (Feb. 2017). "Monitoring microfluidic interfacial flows using impedance spectroscopy". In: *Sensors and Actuators B: Chemical* 239, pp. 218–225. ISSN: 0925-4005. DOI: 10.1016/j.snb.2016.07.123. URL: https://www.sciencedirect.com/science/article/pii/S0925400516311674 (visited on 04/10/2024).

Mazzeo, Brian A. (May 2009). "Parasitic capacitance influence of potential-sensing electrodes on four-electrode liquid impedance measurements". In: *Journal of Applied Physics* 105.9, p. 094106.

Mazzeo, Brian A. and Andrew J. Flewitt (Nov. 2007). "Two- and four-electrode, wide-bandwidth, dielectric spectrometer for conductive liquids: Theory limitations, and experiment". In: *Journal of Applied Physics* 102, p. 104106.

McEvoy, Eoin et al. (Dec. 2020). "Gap junctions amplify spatial variations in cell volume in proliferating tumor spheroids". en. In: *Nature Communications* 11.1. Publisher: Nature Publishing Group, p. 6148. ISSN: 2041-1723. DOI: 10.1038/s41467-020-19904-5. URL: https://www.nature.com/articles/s41467-020-19904-5 (visited on 12/19/2024).

Meda, Paolo (Feb. 2000). "Probing the Function of Connexin Channels in Primary Tissues". In: *Methods* 20.2, pp. 232–244. ISSN: 1046-2023. DOI: 10.1006/meth.1999.0940. URL: https://www.sciencedirect.com/science/article/pii/S1046202399909404 (visited on 07/08/2024).

Meer, B. J. van et al. (Jan. 2017). "Small molecule absorption by PDMS in the context of drug response bioassays". In: *Biochemical and Biophysical Research Communications* 482.2, pp. 323–328. ISSN: 0006-291X. DOI: 10.1016/j.bbrc.2016.11.062. URL: https://www.sciencedirect.com/science/article/pii/S0006291X16319179 (visited on 06/10/2024).

Meng, Shiyun, Mahmoud Rouabhia, and Ze Zhang (Dec. 2021). "Electrical Stimulation and Cellular Behaviors in Electric Field in Biomedical Research". eng. In: *Materials (Basel, Switzerland)* 15.1, p. 165. ISSN: 1996-1944. DOI: 10.3390/ma15010165.

Mert, T (May 2007). "Sucrose-gap technique: Advantages and limitations". In: *Neurophysiology* 39.3, pp. 270–274.

Mohan, Ritika et al. (Dec. 2011). "Design considerations for elastomeric normally closed microfluidic valves". en. In: *Sensors and Actuators B: Chemical* 160.1, pp. 1216–1223. ISSN: 0925-4005. DOI: 10.1016/j.snb.2011.09.051. URL: http://www.sciencedirect.com/science/article/pii/S0925400511008537 (visited on 11/26/2019).

Moore, Douglas, Sara I. Walker, and Michael Levin (Sept. 2017). "Cancer as a disorder of patterning information: computational and biophysical perspectives on the cancer problem". en. In: *Convergent Science Physical Oncology* 3.4. Publisher: IOP Publishing, p. 043001. ISSN: 2057-1739. DOI: 10.1088/2057-1739/aa8548. URL: https://dx.doi.org/10.1088/2057-1739/aa8548 (visited on 06/15/2024).

Mosadegh, Bobak et al. (Jan. 2011). "High-density fabrication of normally closed microfluidic valves by patterned deactivation of oxidized polydimethylsiloxane". en. In: *Lab on a Chip* 11.4. Publisher: The Royal Society of Chemistry, pp. 738–742. ISSN: 1473-0189. DOI: 10.1039/C0LC00112K. URL: https://pubs.rsc.org/en/content/articlelanding/2011/lc/c0lc00112k (visited on 04/26/2022).

Natu, Rucha et al. (June 2023). "A Systematic Analysis of Recent Technology Trends of Microfluidic Medical Devices in the United States". In: *Micromachines* 14.7, p. 1293. ISSN: 2072-666X. DOI: 10.3390/mi14071293. URL: https://www.ncbi.nlm.nih.gov/pmc/articles/PMC10384103/ (visited on 07/17/2024).

Niculescu, Adelina-Gabriela et al. (Feb. 2021). "Fabrication and Applications of Microfluidic Devices: A Review". In: *International Journal of Molecular Sciences* 22.4, p. 2011. ISSN: 1422-0067. DOI: 10.3390/ijms22042011. URL: https://www.ncbi.nlm.nih.gov/pmc/articles/PMC7921936/ (visited on 07/19/2024).

Nunes, J. K. and H. A. Stone (Apr. 2022). "Introduction: Microfluidics". en. In: *Chemical Reviews*. Publisher: American Chemical Society. DOI: 10.1021/acs.chemrev.2c00052. URL: https://pubs.acs.org/doi/full/10.1021/acs.chemrev.2c00052 (visited on 07/19/2024).

Ojovan, Silviya M. et al. (Sept. 2015). "A feasibility study of multi-site,intracellular recordings from mammalian neurons by extracellular gold mushroom-shaped microelectrodes". en. In: *Scientific Reports* 5.1. Publisher: Nature Publishing Group, p. 14100. ISSN: 2045-2322. DOI: 10.1038/srep14100. URL: https://www.nature.com/articles/srep14100 (visited on 09/13/2024).

Oviedo, Néstor J. and Michael Levin (May 2007). "Gap junctions provide new links in left-right patterning". eng. In: *Cell* 129.4, pp. 645–647. ISSN: 0092-8674. DOI: 10.1016/j.cell.2007.05.005.

Oviedo, Néstor J., Junji Morokuma, et al. (Mar. 2010). "Long-range neural and gap junction protein-mediated cues control polarity during planarian regeneration". eng. In: *Developmental Biology* 339.1, pp. 188–199. ISSN: 1095-564X. DOI: 10.1016/j.ydbio.2009.12.012.

Owen, Michael J. and Patrick J. Smith (Jan. 1994). "Plasma treatment of polydimethylsiloxane". In: *Journal of Adhesion Science and Technology* 8.10. Publisher: Taylor & Francis _eprint: https://doi.org/10.1163/156856194X00942, pp. 1063–1075. ISSN: 0169-4243. DOI: 10.1163/156856194X00942. URL: https://doi.org/10.1163/156856194X00942 (visited on 06/29/2023).

Owens, Jesse B. et al. (Dec. 2013). "Effective Targeted Gene Knockdown in Mammalian Cells Using the piggyBac Transposase-based Delivery System". eng. In: *Molecular Therapy. Nucleic Acids* 2.12, e137. ISSN: 2162-2531. DOI: 10.1038/mtna.2013.61.

Palacios-Prado, Nicolas and Feliksas F. Bukauskas (Sept. 2009). "Heterotypic gap junction channels as voltage-sensitive valves for intercellular signaling". In: *Proceedings of the National Academy of Sciences of the United States of America* 106.35, pp. 14855–14860. ISSN: 0027-8424. DOI: 10.1073/pnas.0901923106. URL: https://www.ncbi.nlm.nih.gov/pmc/articles/PMC2736430/ (visited on 06/15/2024).

Palacios-Prado, Nicolás, Wolf Huetteroth, and Alberto E. Pereda (2014). "Hemichannel composition and electrical synaptic transmission: molecular diversity and its implications for electrical rectification". English. In: *Frontiers in Cellular Neuroscience* 8. ISSN: 1662-5102. DOI: 10.3389/fncel.2014.00324. URL: https://www.frontiersin.org/articles/10.3389/fncel.2014.00324/full (visited on 10/22/2018).

Pasirayi, G. et al. (2022). "Microfluidic Bioreactors for Cell Culturing: A Review". en. In: *Micro and Nanosystems* 3.2 (), pp. 137–160. URL: https://www.eurekaselect.com/article/40827 (visited on 06/12/2022).

Pelc, Damjan, Sanjin Marion, and Basletic Mario (July 2011). "Four-contact impedance spectroscopy of conductive liquid samples". In: *Review of Scientific Instruments* 82, p. 073907.

Pliquett, Uwe et al. (July 2011). "Front end with offset-free symmetrical current source optimized for time domain impedance spectroscopy". en. In: *Physiological Measurement* 32.7, pp. 927–944. ISSN: 0967-3334, 1361-6579. DOI: 10.1088/0967-3334/32/7/S15. URL: https://iopscience.iop.org/article/10.1088/0967-3334/32/7/S15 (visited on 07/30/2020).

Pradhan, Rangadhar, Analava Mitra, and Soumen Das (Nov. 2012). "Characterization of Electrode/Electrolyte Interface of ECIS Devices". In: *Electroanalysis* 24.12, pp. 2405–2414.

Rash, John E. et al. (Sept. 2013). "Molecular and functional asymmetry at a vertebrate electrical synapse". eng. In: *Neuron* 79.5, pp. 957–969. ISSN: 1097-4199. DOI: 10.1016/j.neuron.2013.06.037.

Rivet, Catherine et al. (Apr. 2011). "Microfluidics for medical diagnostics and biosensors". In: *Chemical Engineering Science*. Microfluidic Engineering 66.7, pp. 1490–1507. ISSN: 0009-2509. DOI: 10.1016/j.ces.2010.08.015. URL: https://www.sciencedirect.com/science/article/pii/S0009250910004823 (visited on 07/18/2024).

Roos, Albert D. G. de, Everardus J. J. van Zoelen, and Alexander P. R. Theuvenet (Feb. 1996). "Determination of gap junctional intercellular communication by capacitance measurements". en. In: *Pflügers Archiv* 431.4, pp. 556–563. ISSN: 1432-2013. DOI: 10.1007/BF02191903. URL: https://doi.org/10.1007/BF02191903 (visited on 12/20/2024).

Rubin, H. (July 1985). "Cancer as a dynamic developmental disorder". eng. In: *Cancer Research* 45.7, pp. 2935–2942. ISSN: 0008-5472.

Schwan, H. P. (May 1966). "Alternating Current Electrode Polarization". In: *Biophysik* 3, pp. 181–201.

Selberg, John et al. (2020). "Machine Learning-Driven Bioelectronics for Closed-Loop Control of Cells". en. In: *Advanced Intelligent Systems* 2.12, p. 2000140. ISSN: 2640-4567. DOI: 10.1002/aisy.202000140. URL: https://onlinelibrary.wiley.com/doi/abs/10.1002/aisy.202000140 (visited on 06/15/2022).

Shaffer, Tyler A. et al. (July 2023). "A Cost-Effective Microfluidic Device to Teach the Principles of Electrophoresis and Electroosmosis". In: *Journal of Chemical Education* 100.7. Publisher: American Chemical Society, pp. 2782–2788. ISSN: 0021-9584. DOI: 10.1021/acs.jchemed.2c01028. URL: https://doi.org/10.1021/acs.jchemed.2c01028 (visited on 07/23/2024).

Shahaf, Goded and Shimon Marom (Nov. 2001). "Learning in Networks of Cortical Neurons". In: *Journal of Neuroscience* 21.22, pp. 8782–8788.

Shao, Qing et al. (Apr. 2005). "Down-regulation of Cx43 by Retroviral Delivery of Small Interfering RNA Promotes an Aggressive Breast Cancer Cell Phenotype". In: *Cancer Research* 65.7, pp. 2705–2711. ISSN: 0008-5472. DOI: 10.1158/0008-5472.CAN-04-2367. URL: https://doi.org/10.1158/0008-5472.CAN-04-2367 (visited on 12/16/2024).

Simon, Daniel T. et al. (Nov. 2016). "Organic Bioelectronics: Bridging the Signaling Gap between Biology and Technology". en. In: *Chemical Reviews* 116.21, pp. 13009–13041. ISSN: 0009-2665, 1520-6890. DOI: 10.1021/acs.chemrev.6b00146. URL: http://pubs.acs.org/doi/10.1021/acs.chemrev.6b00146 (visited on 10/14/2018).

Steinberg, T H et al. (Feb. 1994). "Connexin43 and connexin45 form gap junctions with different molecular permeabilities in osteoblastic cells." In: *The EMBO Journal* 13.4, pp. 744–750. ISSN: 0261-4189. URL: https://www.ncbi.nlm.nih.gov/pmc/articles/PMC394870/ (visited on 12/20/2024).

Stojek, Zbigniew (2002). "The Electric Double Layer and Its Structure". In: *Electroanalytical Methods: Guide to Experiments and Applications*. 1st ed. Springer-Verlag Berlin Heidelberg. ISBN: 978-3-662-04757-6. URL: http://www.springer.com/us/book/9783662047576.

Takayama, Shuichi et al. (May 1999). "Patterning cells and their environments using multiple laminar fluid flows in capillary networks". In: *Proceedings of the National Academy of Sciences* 96.10. Publisher: Proceedings of the National Academy of Sciences, pp. 5545–5548. DOI: 10.1073/pnas.96.10.5545. URL: https://www.pnas.org/doi/10.1073/pnas.96.10.5545 (visited on 06/15/2022).

Tarn, Mark D., Maria J. Lopez-Martinez, and Nicole Pamme (Jan. 2014). "On-chip processing of particles and cells via multilaminar flow streams". en. In: *Analytical and Bioanalytical Chemistry* 406.1, pp. 139–161. ISSN: 1618-2650. DOI: 10.1007/s00216-013-7363-6. URL: https://doi.org/10.1007/s00216-013-7363-6 (visited on 06/13/2022).

Tjong, Jonathan, Alyne Teixeira, and John Frampton (June 2020). *Solvent Extraction of 3D Printed Molds for Soft Lithography*. en-US. URL: https://blogs.rsc.org/chipsandtips/2020/06/12/solvent-extraction-of-3d-printed-molds-for-soft-lithography/ (visited on 07/16/2024).

Traub, O. et al. (June 1994). "Immunochemical and electrophysiological characterization of murine connexin40 and -43 in mouse tissues and transfected human cells". eng. In: *European Journal of Cell Biology* 64.1, pp. 101–112. ISSN: 0171-9335.

Unger, Marc A. et al. (Apr. 2000). "Monolithic Microfabricated Valves and Pumps by Multilayer Soft Lithography". In: *Science* 288.5463. Publisher: American Association for the Advancement of Science, pp. 113–116. DOI: 10.1126/science.288.5463.113. URL: https://www.science.org/doi/10.1126/science.288.5463.113 (visited on 04/05/2023).

Valiunas, V et al. (Oct. 2005). "Connexin-specific cell-to-cell transfer of short interfering RNA by gap junctions". In: *The Journal of Physiology* 568.Pt 2, pp. 459–468. ISSN: 0022-3751. DOI: 10.1113/jphysiol.2005.090985. URL: https://www.ncbi.nlm.nih.gov/pmc/articles/PMC1474730/ (visited on 04/13/2021).

Veenstra, Richard D. (May 2001). "Voltage clamp limitations of dual whole-cell gap junction current and voltage recordings. I. Conductance Measurements". In: *Biophysical Journal* 80.5, pp. 2231–2247.

– (2016). "Establishment of the Dual Whole Cell Recording Patch Clamp Configuration for the Measurement of Gap Junction Conductance". en. In: *Gap Junction Protocols*. Ed. by Mathieu Vinken and Scott R. Johnstone. Methods in Molecular Biology. New York, NY: Springer, pp. 213–231. ISBN: 978-1-4939-3664-9. DOI: 10.1007/978-1-4939-3664-9_16. URL: https://doi.org/10.1007/978-1-4939-3664-9_16 (visited on 04/13/2021).

Vollertsen, A. R. et al. (Nov. 2020). "Modular operation of microfluidic chips for highly parallelized cell culture and liquid dosing via a fluidic circuit board". en. In: *Microsystems & Nanoengineering* 6.1. Number: 1 Publisher: Nature Publishing Group, pp. 1–16. ISSN: 2055-7434. DOI: 10.1038/s41378-020-00216-z. URL: https://www.nature.com/articles/s41378-020-00216-z (visited on 06/12/2022).

Wade, Margaret H., James E. Trosko, and Melvin Schindler (Apr. 1986). "A Fluorescence Photobleaching Assay of Gap Junction-mediated Communication Between Human Cells". In: *Science* 232.4749. Publisher: American Association for the Advancement of Science, pp. 525–528. DOI: 10.1126/science.3961495. URL: https://www.science.org/doi/10.1126/science.3961495 (visited on 12/20/2024).

Wang, Renjie et al. (Mar. 2022). "A Standalone and Portable Microfluidic Imaging Detection System With Embedded Computing for Point-of-Care Diagnostics". In: *IEEE Sensors Journal* 22.6. Conference Name: IEEE Sensors Journal, pp. 6116–6123. ISSN: 1558-1748. DOI: 10.1109/JSEN.2022.3148768.

Wang, Ting, Cecilia Yu, and Xing Xie (2022). "Microfluidics for Environmental Applications". en. In: *Microfluidics in Biotechnology*. Ed. by Janina Bahnemann and Alexander Grünberger. Cham: Springer International Publishing, pp. 267–290. ISBN: 978-3-031-04188-4. DOI: 10.1007/10_2020_128. URL: https://doi.org/10.1007/10_2020_128 (visited on 07/19/2024).

Warawdekar, Ujjwala M. (Apr. 2019). "An Assay to Assess Gap Junction Communication in Cell Lines". In: *Journal of Biomolecular Techniques : JBT* 30.1, pp. 1–6. ISSN: 1524-0215. DOI: 10.7171/jbt.19-3001-001. URL: https://www.ncbi.nlm.nih.gov/pmc/articles/PMC6352750/ (visited on 07/07/2024).

Whitesides, George M. (July 2006). "The origins and the future of microfluidics". en. In: *Nature* 442.7101, pp. 368–373. ISSN: 0028-0836, 1476-4687. DOI: 10.1038/nature05058. URL: http://www.nature.com/articles/nature05058 (visited on 10/04/2018).

Wu, Amy et al. (Feb. 2010). "Modular integration of electronics and microfluidic systems using flexible printed circuit boards". en. In: *Lab on a Chip* 10.4. Publisher: The Royal Society of Chemistry, pp. 519–521. ISSN: 1473-0189. DOI: 10.1039/B922830F. URL: https://pubs.rsc.org/en/content/articlelanding/2010/lc/b922830f (visited on 06/05/2022).

Wu, Jiandong et al. (Aug. 2014). "A compact microfluidic system for cell migration studies". en. In: *Biomedical Microdevices* 16.4, pp. 521–528. ISSN: 1572-8781. DOI: 10.1007/s10544-014-9854-4. URL: https://doi.org/10.1007/s10544-014-9854-4 (visited on 08/23/2023).

Xu, Yan et al. (Jan. 2021). "Connexin43 is differentially distributed within renal vasculature and mediates profibrotic differentiation in medullary fibroblasts". In: *American Journal of Physiology-Renal Physiology* 320.1. Publisher: American Physiological Society, F17–F30. ISSN: 1931-857X. DOI: 10.1152/ajprenal.00453.2020. URL: https://journals.physiology.org/doi/full/10.1152/ajprenal.00453.2020 (visited on 12/16/2024).

Xu, Youchun et al. (Mar. 2016). "A review of impedance measurements of whole cells". In: *Biosensors and Bioelectronics* 77, pp. 824–836. ISSN: 0956-5663. DOI: 10.1016/j.bios.2015.10.027. URL: https://www.sciencedirect.com/science/article/pii/S0956566315304917 (visited on 09/10/2024).

Y. Lau, Adrian et al. (2006). "Open-access microfluidic patch-clamp array with raised lateral cell trapping sites". en. In: *Lab on a Chip* 6.12, pp. 1510–1515. DOI: 10.1039/B608439G. URL: https://pubs.rsc.org/en/content/articlelanding/2006/lc/b608439g (visited on 11/27/2018).

Yang, Ming and William J. Brackenbury (July 2013). "Membrane potential and cancer progression". In: *Frontiers in Physiology* 4.185, pp. 1–10. DOI: 10.3389/fphys.2013.00185.

Yousuff, Caffiyar Mohamed et al. (Aug. 2017). "Study on the Optimum Cutting Parameters of an Aluminum Mold for Effective Bonding Strength of a PDMS Microfluidic Device". en. In: *Micromachines* 8.8. Number: 8 Publisher: Multidisciplinary Digital Publishing Institute, p. 258. ISSN: 2072-666X. DOI: 10.3390/mi8080258. URL: https://www.mdpi.com/2072-666X/8/8/258 (visited on 06/29/2023).

Yuan, Yuehua and T. Randall Lee (2013). "Contact Angle and Wetting Properties". en. In: *Surface Science Techniques*. Ed. by Gianangelo Bracco and Bodil Holst. Springer Series in Surface Sciences. Berlin, Heidelberg: Springer, pp. 3–34. ISBN: 978-3-642-34243-1. DOI: 10.1007/978-3-642-34243-1_1. URL: https://doi.org/10.1007/978-3-642-34243-1_1 (visited on 11/22/2022).

Yufera, Alberto et al. (Aug. 2011). "Cell Biometrics Based on Bio-Impedance Measurements". In: *Advanced Biometric Technologies*, pp. 343–366.

Zhang, Haoqing, Honglong Chang, and Pavel Neuzil (June 2019). "DEP-on-a-Chip: Dielectrophoresis Applied to Microfluidic Platforms". In: *Micromachines* 10.6, p. 423. ISSN: 2072-666X. DOI: 10.3390/mi10060423. URL: https://www.ncbi.nlm.nih.gov/pmc/articles/PMC6630590/ (visited on 07/23/2024).

Zhang, Weitao et al. (Sept. 2020). "Experimental and Modeling of Conductivity for Electrolyte Solution Systems". In: *ACS Omega* 5.35. Publisher: American Chemical Society, pp. 22465–22474. DOI: 10.1021/acsomega.0c03013. URL: https://doi.org/10.1021/acsomega.0c03013 (visited on 03/13/2024).

Zhang, Yushen, Tsun-Ming Tseng, and Ulf Schlichtmann (Sept. 2021). "Portable all-in-one automated microfluidic system (PAMICON) with 3D-printed chip using novel fluid control mechanism". en. In: *Scientific Reports* 11.1. Number: 1 Publisher: Nature Publishing Group, p. 19189. ISSN: 2045-2322. DOI: 10.1038/s41598-021-98655-9. URL: https://www.nature.com/articles/s41598-021-98655-9 (visited on 08/23/2023).

Appendix A

DETAILED FABRICATION RECIPES

This appendix contains detailed recipes and techniques for fabricated PDMS microfluidic devices with integrated planar electrodes and elastomeric microvalves. While the approaches and protocols are generally applicable, some directions reference equipment specific to the Tufts Microfab.

A.1 Electrode Fabrication

A.1.1 General Approach

Electrodes are fabricated on glass microscope slides using a standard liftoff technique. Glass substrates are prepared for processing through plasma treatment. An oxygen plasma clean is performed for 90 seconds at 300 W. Electrode patterning is achieved through photolithography using the positive photoresist, AZ9260. An additional oxygen plasma treatment (200 W for 30 s) is performed as a "descum" to prepare substrates for sputtering. Chromium and gold are sputtered to a depth of 30 nm and 210 nm, respectively. Finally, liftoff is performed for 12+ hours in Microposit Remover 1165 heated to 55°C.

A.1.2 Detailed Protocol

1. Substrate clean

    a) Select clean microscope slides to be used as substrates. Generally, 8 samples per run is advisable as the working capacity of the sputter tool is approximately 8 standard 1 by 3 inch microscope slides.

    b) (optional) Piranha clean the slides. The plasma clean in 1.d) may be sufficient to prepare the substrates without piranha etch. Alternately, premium glass slides may be purchased that have already been more aggressively cleaned than standard slides. To perform the Piranha etch, follow the detailed SOP provided by Tufts Micro/nanofab.

    c) In a fume hood and wearing proper PPE, place substrates in a glass container and fill with sulfuric acid to ¾ of expected total volume.

        i. Carefully add the remaining ¼ volume of hydrogen peroxide. The reaction is exothermic and will bubble and produce steam. Allow samples to etch for approximately 10 mins.

        ii. Remove samples and perform a two stage rinse in deionized water for 5 mins per stage.

iii. Properly dispose of the etching fluid waste in vented glass containment.

d) Perform a plasma clean using the March Reactive Ion Etcher (RIE). Use 300 W power, 180 s duration, and 70 mT base pressure. The automatic RF tuning should be sufficient.

2. AZ9260 photolithography (~6 μm target)

a) Allow AZ9260 photoresist to warm to room temperature. Additionally, prepare transfer pipettes to handle viscous photoresist by cutting about one inch of the tip, or until the opening is roughly one centimeter in diameter.

b) Spin MCC Primer. Place the slide adapter on the spinner wafer chuck and position a slide into the adapter. Activate vacuum to secure the slide in place. If the vacuum pressure does not exceed 16 units, reposition the slide or the adapter gasket. Spincoat (10 s at 500 rpm – acc. 2, 30 s at 5000 rpm – acc. 5).

c) Spin AZ9260. Use a transfer pipette to apply roughly 2.5 mL of photoresist (one squeeze) to the slide. Spread the photoresist across the slide without introducing bubbles (See Figure A.1a) to ensure that the entire slide is coated during spin. Spincoat (10 s at 500 rpm – acc 1, 20 s at 2000 rpm – acc 5, 40 s at 5000 rpm – acc 15, 10 s at 0 rpm acc 10).

d) Softbake. On a level hotplate, bake for 3 min at 115°C.

e) Expose. To use the OAI mask aligner with glass slide substrates, use the custom acrylic chuck adapter laser cut for this purpose. The adapter has small metal pins to guide positioning of a 1 by 3 inch slide (see Figure A.1b).

f) Insert the chuck adapter into the mask aligner. Position a background slide with a diffusive (tape) surface into the adapter. Apply chuck vacuum.

i. Align mask with the background slide and bring into contact to level. Lock the ball-and-socket chuck coupling and lower the stage.

ii. Insert and align sample to the background slide. Bring into light contact by lowering the “Chuck Z Adjust” knob to reduce the z-axis micrometer sensitivity.

iii. Execute UV exposure for 40 s.

g) Develop sample for 2.5 mins in a thoroughly mixed 4:1 dilution of AZ400k developer (with agitation). The 3 inch Teflon wafer holders can be used to secure microscope slides vertically.

h) Rinse. Perform a 2 stage rinse, allowing samples to soak for greater than 1 min in 2 1000 mL beakers of deionized water. Dry with CDA.

3. O2 Plasma Descum - Immediately prior to sputtering, perform an oxygen plasma etch to remove contaminants and the MCC Primer. Using automatic RF tuning on the RIE etch at 200 W for 30 s duration at 70 mT base pressure.

4. Sputter

    a) Load all samples into the NSC 3000 sputter tool. Center samples a much as possible.

    b) Pump down the vacuum chamber for an excess of 1 hour. Lower base pressures will result in better film purity and adhesion.

    c) Sputter chromium adhesion layer at 180 W to 30 nm thickness (earlier devices used 15 nm). Immediately sputter gold at 140 W to 210 nm thickness (earlier devices used 105 nm). Deposition rates should be close to 5.5 Å/s and 15 Å/s, respectively.

5. Liftoff

    a) Place samples in an appropriate flat bottomed glass container on a hotplate in a chemical fume hood.

    b) Pour Remover 1165 to cover the samples to a depth of approximately 1 inch.

    c) Set the hotplate to 55°C, cover with aluminum foil, and let sit for greater than 12 hours.

    d) Spray with deionized water to rinse off particulates. Additional time in clean Remover 1165 may be necessary if liftoff is incomplete. Soak in 1 L for 5min in deionized water and dry with CDA.

A.1.3 Considerations for working with glass slides

Glass substrates represent a compromise, trading fabrication purity for ease of use and accessibility of materials. Slides are durable and have the added advantage of fitting conveniently on most microscopy systems. With additional attention the downsides of working with microscope slides as substrates can be for the most part mitigated.

For the best processing results, borosilicate glass offers a more ideal transparent substrate. Borosilicate has a lower coefficient of thermal expansion than the soda lime glass comprising standard microscope slides. Reduced thermal expansion more closely matches silicon substrates, for which most photoresists are designed, and is preferable for uniformity of photoresist deposition in general.

Photolithography tools are designed with circular wafers in mind and many tools need adapters to accommodate slides. The adapter of Figure A.1b is specially designed to allow repeatable alignment of the mask and substrate. This alignment is essential to facilitate reliable electrical coupling into the chip. For chemical processing, slides can be clamped into Teflon 3 inch wafer holders for easier manipulation.

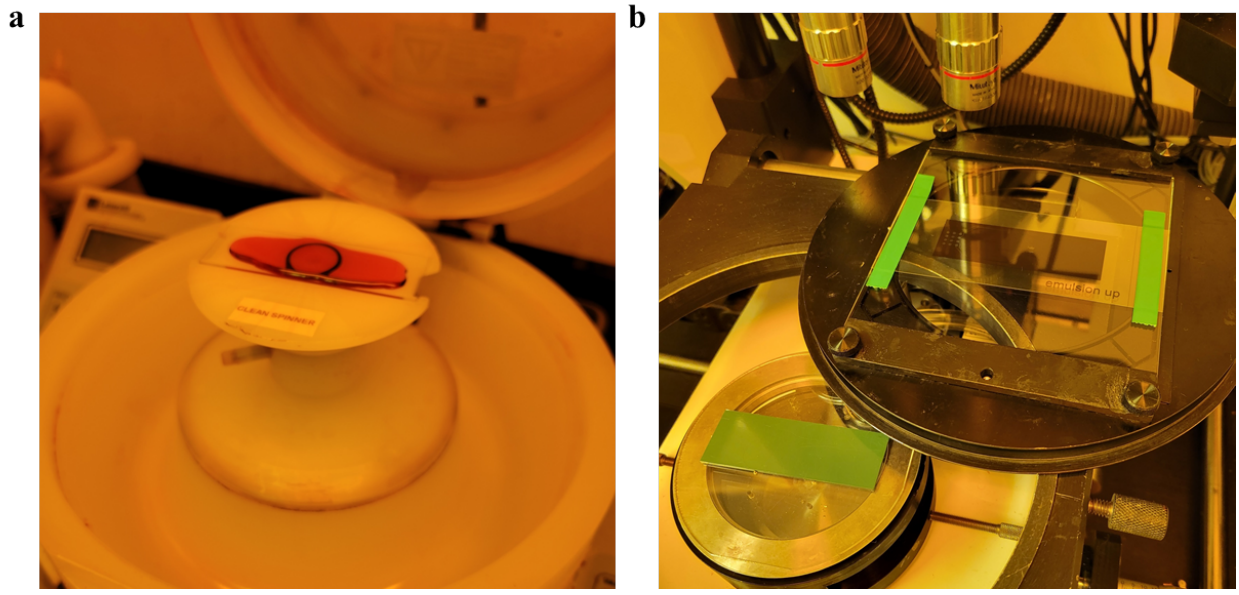

Figure A.1: Electrode fabrication details. (**a**) Photoresist should be carefully spread by pipette to ensure complete coating of the slide. (**b**) A custom laser cut acrylic chuck adapter allows repeatable processing on glass slides.

A.2 SU8 Master Mold Fabrication

A.2.1 General Approach

PDMS master molds are fabricated using the negative photoresist SU-8. SU-8 adhesion is optimized on silicon substrates, but glass can be used. The recipe below intended for use with SU8-3050 on silicon wafers with a target thickness of 75 µm. Refer to manufacturer datasheets for adjusted spin and bake times when working with other SU8 formulations or different substrates. After lithography, molds are silianized using , tridecafluoro-1,1,2,2-tetrahydrooctyl trichlorosilane.

A.2.2 Detailed Protocol

1. Lithography - It may be prudent to cover SU-8 films during baking cycles to avoid contamination. In addition for especially thick films (>100µm) and when working with glass substrates, take special care to cool samples slowly proceeding.

    a) Allow SU-8 photoresist to warm to room temperature.

    b) Substrate clean. Perform a plasma clean using the March Reactive Ion Etcher (RIE). Use 300 W power, 180 s duration, and 70 mT base pressure. The automatic RF tuning should be sufficient.

    c) Spin SU-8. Carefully pour a half-dollar sized portion of SU-8 onto the center of the (dirty materials) spinner. Spincoat (15 s at 500 rpm – acc 1, 30 s at 2000 rpm – acc 5,

10s at 0 rpm – acc 8).

d) Softbake. The manufacturer recommends a two-step baking process. For best results, replace with a ramped bake.

   i. Starting at 45°C increase hotplate temperature by 5°C every 30 s until reaching 105°C.

   ii. Bake at 105°C for 9 minutes.

   iii. Check that the bake is complete by touching an edge with tweezers. It should extrude with the removal of the tweezers and crystallize immediately.

   iv. Cool the sample to room temperature.

e) Exposure. Perform UV exposure for 16 s at 15 mW/cm^2 (using either the OAI 204AI or Karl Suss MA6 mask aligner). Ensure soft contact to avoid wrinkling the SU-8 film. Extend exposure time by 50% for transparent substrates and ensure a diffuse background.

f) Post-exposure bake. Again, ramp the hotplate temperature from 45°C to 105 °C. Ramp rate may be increased to 10°C per 30 s for thinner films. Bake at 105°C for 7 minutes. Allow to cool before developing. (This step may require a second hotplate or rapid cooling of the hotplate following the softbake.)

g) Develop in SU-8 developer.

   i. Agitate the sample continuously for 7 minutes in a bath of enough SU-8 developer to cover the wafer.

   ii. Rinse the sample in isopropyl alcohol. If murky white films appear on the surface, continue developing in a fresh bath of SU-8 developer for 1 minute. Repeat until sample is fully developed. Over developing SU-8 is quite difficult, so development can be extended significantly without issue.

   iii. Rinse in deionized water and dry with CDA.

2. Mold assembly – For cast molding (e.g. pneumatic and stamp molds), an assembly should be used to ensure molded PDMS layers have uniform thickness (and to a lesser extent to reduce PDMS waste). Mold walls can be laser cut out of 5 mm acrylic and secured onto the substrates using vacuum tape.

3. Silanization – Silanization greatly reduces the force required to release PDMS from the molds. The treatment should be effective for many mold cycles but should be repeated if the master's surface is handled or encounters solvents.

a) Arrange the fully assembled mold and cover glass into a desiccator labeled for use with silanizing agents. Elevate all components above the desiccator floor.

b) Cut a thin strip of fab wipe and dip it into the silanizing agent, tridecafluoro-1,1,2,2-tetrahydrooctyl trichlorosilane. Try to absorb as little silanizing agent into the strip as possible.

c) Place the soaked paper strip in the desiccator below the level of the molds. Close the desiccator and apply vacuum for at least 1 hour.

A.3 PDMS Molding

A.3.1 General Approach

A standard PDMS (Sylgard 184) preparation is used for all device layers. The molding process can be deceptively detail oriented (and time consuming). The main concerns stem from avoiding air in the mold features and from careful disassembly of cast mold assemblies. However, molding can be repeated many times to create reliable replicas with a consistent method.

A.3.2 Detailed Protocol

1. PDMS preparation

    a) Mix PDMS elastomer base with curing agent at a ratio of 10:1 by weight. Stir thoroughly until the mixture is translucent due to bubbles (approximately 2 minutes). A 1 by 3 inch mold with 6 mm thickness requires approximately 15 g of PDMS, while spin coating a 3 inch wafer requires about 2 g.

    b) Degas the PDMS in a desiccator for roughly 45 minutes or until all the bubbles have been removed. Compressed nitrogen gas may be applied to remove bubbles resting on the surface.

2. Molding

    a) Pour PDMS as slowly as possible into the mold to avoid trapping air. Slightly overfill any mold assembly so that the PDMS forms a convex dome help in place by surface tension.

    b) Cover cast molds with a silanized lid. Lower the lid very slowly starting at one end. Allow surface tension to spread the contact wave front to prevent trapping air. Secure the lid with vacuum tape.

    c) Cure the PDMS completely. Place PDMS molds into secondary containment and allow to rest in a leveled oven at 60°C for 1.5 hours.

3. Spinning (~50 μm target)

    a) In a (dirty materials) spinner, pour a quarter-sized amount of PDMS onto mold. Spincoat (15 s at 250 rpm – acc 1, 60 s at 500 rpm – acc 3).

    b) Cure the PDMS completely. Place the wafer in secondary containment and allow to rest in a leveled oven at 60°C for 45 minutes.

4. Mold release and preparation

a) Release samples from their mold fixtures. Most importantly, be very careful not to apply pressure on the master mold! Silicon wafers shatter very easily. Keeping the wafer side firmly against a benchtop surface at all times is recommended.

   i. Remove the lid first. The lid may be quite difficult to remove. Gentle lateral twisting and leverage with razor blades is recommended.

   ii. Remove any vacuum tape that secured the side walls of the mold fixture. Remove the side walls. Doing so may require cutting along the walls with a razor.

   iii. Gently peal the PDMS layer off of the master mold.

b) Dice the sample with a clean razor blade if necessary. Cut away edges with thin film defects from the molding process.

c) Clean the mold for reuse.

A.4 PDMS-PDMS Bonding

A.4.1 General Approach

PDMS layers can be reliably bonded by oxygen plasma treatment. Experimentation has shown that the optimal bonding parameters occur at high base pressures for plasma generation, which requires manual operation of the Tufts Microfab's RIE. Both PDMS layers to be bonded should be treated with oxygen plasma at 20 W for 30 s and then quickly brought into gentle contact. The alignment rig of Figure 2.3a has been designed to facilitate alignment in close proximity to the RIE.

A.4.2 Detailed Protocol

1. Plasma treatment – RF matching for the March CS-1701F RIE is unstable at low RF power settings. To achieve a stable plasma, the tool should be operated in manual mode to allow the pressure gas pressure during treatment to stabilize using the Independent Pressure Control protocol. Additionally, PDMS samples should be centered on the vacuum chamber plate and a dummy run manually calibrate RF matching parameters may be necessary.

2. (optional) Dummy treatment – manual operation

    a) Configure the tool with etch pressure (PRESS): 500 mT, power (POWER): 20 W, end-point (ENDPT): 100, time (TIME): 0 s, base pressure (BP/RP): 500 mT, O_2 gas flow (gas 3): 100%

    b) Center a dummy PDMS slab of similar dimensions to the pneumatic layer in the vacuum chamber.

    c) Pump down the vacuum chamber until the turbo pump reaches approximately 23,000 rpm (around 80 mT).

    d) Enable the oxygen gas pressure (at 100%) and allow the feedback system to stabilize the gas pressure to 500 mT (the process will take around 5 minutes).

    e) Enable the RF source at 20 W and manually adjust the RF tuning parameters until zero reflected power is achieved.

    f) Bleed the chamber vacuum and remove the dummy device.

3. Device plasma treatment – manual operation

    a) Inspect the pneumatic layer for dust or particles (including the backside). Remove using vacuum or Scotch tape if necessary.

    b) Configure the tool with etch pressure (PRESS): 500,mT, power (POWER): 20 W, end-point (ENDPT): 100, time (TIME): 30 s, base pressure (BP/RP): 500 mT, O_2 gas flow (gas 3): 100%

c) Center the pneumatic layer in the vacuum chamber and place the fluid layer PDMS coated wafer adjacent.

d) Pump down the vacuum chamber until the turbo pump reaches approximately 23,000 rpm (around 80 mT).

e) Enable the oxygen gas pressure (at 100%) and allow the feedback system to stabilize the gas pressure to 500 mT (the process will take around 5 minutes).

f) Enable the RF source at 20 W for 30 seconds.

g) Bleed the chamber vacuum.

4. Alignment – While a pre-alignment step similar to the PDMS-glass bonding is possible, contact between the layers should be avoided as it can pull the fluid layer off of the wafer.

a) Carefully affix the pneumatic layer to the glass backing. Do not touch or bend the bonding surface of the device.

b) Insert the glass backing into the alignment rig armature so that the fiducials are centered in the field of view. Adjust the microscope lighting and focus as necessary.

c) Place the fluid layer wafer on the alignment stage.

d) Align the layers according to their fiducial markers, adjusting the wafer rotation angle first before the x-y micrometers.

e) Slowly bring the layers into gentle contact. Alignment cannot be adjusted after the initial contact.

f) Carefully release the glass backing from the alignment rig using the pull tabs.

5. Bake and release – Devices should be heated and cooled gradually to prevent thermal contraction of the PDMS from damaging the bond.

a) Place the wafer, device, and glass backing on the hotplate.

b) Set hotplate to 85°C.

c) If necessary, apply firm steady pressure to the glass backing for 30 seconds for complete contact between the device and substrate.

d) After 5 minutes, remove the glass backing. Use tweezers to release one edge and then lever the glass off slowly.

e) After more than 10 minutes, remove from hotplate and allow to cool.

f) Once cooled, use a razor to cut back the PDMS film on the wafer. Pull on the film to release the bonded device.

g) Transfer the device to a cutting mat and trim the edges of the device to remove any extra film from the fluidic layer.

h) Use a 1.5 mm biopsy punch to core all inlet and outlet ports on the device.

A.5 PDMS-Glass Bonding (Oligomer Stamping Method)

A.5.1 General Approach

Selective bonding of PDMS devices to glass is performed using an oligomer stamping method. Microcontact with an untreated PDMS surface locally reduces the effect of plasma treatment. The alignment rig of Figure 2.3a has been designed to facilitate the stamping and alignment process in close proximity to the RIE. Some operator skill/experience is needed to ensure reliable bonding (or lack thereof), especially in regards to performing accurate and gentle contact (see Figure 2.12) under tight time constraints. Manual release of the slide holder on the alignment rig also requires special care and consistency.

A.5.2 Detailed Protocol

1. Pre-alignment – A pre-alignment step is recommended to increase the efficiency of the stamping process after plasma treatment (since the surface modification due to plasma treatment is transient). An equally important goal of this step is to level the stamp and the device to be bonding to avoid applying unequal stamping force on different valves across the device.

    a) Fix the PDMS stamp to the dummy wafer and center below microscope.

    b) Fix the valved device on the glass backing ensuring that when inserted into the alignment rig, the fiducial markers will appear in the microscope field of view.

    c) Align the layers and bring the device into contact with the stamp.

    d) If contact is not simultaneous between all stamping areas, adjust the alignment rig arm accordingly to level the two surfaces.

2. Plasma treatment – RF matching for the March CS-1701F RIE is unstable at low RF power settings. To achieve a stable plasma, the tool should be operated in manual mode to allow the pressure gas pressure during treatment to stabilize using the Independent Pressure Control protocol. Additionally, PDMS samples should be centered on the vacuum chamber plate and a dummy run to manually calibrate RF matching parameters may be necessary.

    a) (optional) Dummy treatment – manual operation

        i. Configure the tool with etch pressure (PRESS): 500 mT, power (POWER): 20 W, endpoint (ENDPT): 100, time (TIME): 0 s, base pressure (BP/RP): 500 mT, O_2 gas flow (gas 3): 100%

        ii. Center a dummy PDMS slab of similar dimensions to the device to bond in the vacuum chamber.

        iii. Pump down the vacuum chamber until the turbo pump reaches approximately 23,000 rpm (around 80 mT).

iv. Enable the oxygen gas pressure (at 100%) and allow the feedback system to stabilize the gas pressure to 500 mT (the process will take around 5 minutes).

v. Enable the RF source at 20 W and manually adjust the RF tuning parameters until zero reflected power is achieved.

vi. Bleed the chamber vacuum and remove the dummy device.

b) Device plasma treatment – manual operation

i. Inspect the device to be bonded for dust or particles (including the backside). Remove using vacuum or Scotch tape if necessary.

ii. Configure the tool with etch pressure (PRESS): 500 mT, power (POWER): 20 W, endpoint (ENDPT): 100, time (TIME): 30 s, base pressure (BP/RP): 500 mT, O_2 gas flow (gas 3): 100%

iii. Center the device in the vacuum chamber.

iv. Pump down the vacuum chamber until the turbo pump reaches approximately 23,000 rpm (around 80 mT).

v. Enable the oxygen gas pressure (at 100%) and allow the feedback system to stabilize the gas pressure to 500 mT (the process will take around 5 minutes).

vi. Enable the RF source at 20 W for 30 seconds.

vii. Bleed the chamber vacuum and carefully affix to the glass backing in the same orientation at the pre-alignment. Do not touch or bend the bonding surface of the device.

c) Substrate plasma treatment – automated operation

i. Center the glass substrate in the RIE vacuum chamber.

ii. Configure the tool with etch pressure (PRESS): 0 mT, power (POWER): 100 W, endpoint (ENDPT): 100, time (TIME): 30 s, base pressure (BP/RP): 80 mT, O_2 gas flow (gas 3): 100%

iii. Run an automated treatment.

3. Oligomer stamping – Alignment and stamping can be performed while the automated substrate treatment is running.

a) Insert the PDMS device on its glass backing into the alignment rig. Position in the microscope's field of view.

b) Align the layers according to their fiducial markers, adjusting the stamp rotation first before the x-y micrometers.

c) Slowly bring the layers into gentle contact. Repeat contact three times.

d) After raising the alignment rig arm, remove the stamp from the dummy wafer.

4. Substrate alignment

   a) Place the treated substrate on the dummy wafer.

   b) Align the substrate to the device and bring into gentle contact. Alignment cannot be adjusted after the initial contact.

   c) Carefully release the glass backing from the alignment rig using the pull tabs.

5. Final bake and vacuum valve release – Devices should be heated and cooled gradually to prevent thermal contraction of the PDMS from damaging the bond.

   a) Place the substrate, device, and backing on the hotplate.

   b) Set hotplate to 85°C.

   c) If necessary, apply firm steady pressure to the glass backing for 30 seconds for complete contact between the device and substrate.

   d) After 5 minutes, remove the glass backing. Use tweezers to release one edge and then lever the glass off slowly.

   e) Pull vacuum on the pneumatic outlets using tubing and a 10 mL syringe.

   f) After more than 10 minutes, remove from hotplate and allow to cool.

Appendix B

CELL CULTURE AND SEEDING PROTOCOLS

B.1 General Approach

NRK cells are seeded into microfluidic devices at very high density (1.5M/100µL) such that only have to form cell-cell connections to become confluent. A Matrigel treatment creates an ECM to promote good cell adhesion. Throughout seeding and culture, hydrostatic flow must be managed by forming droplets on the chip surface. Additionally, care is needed to avoid injecting bubbles into the system at any point in the process.

B.2 Detailed Protocol

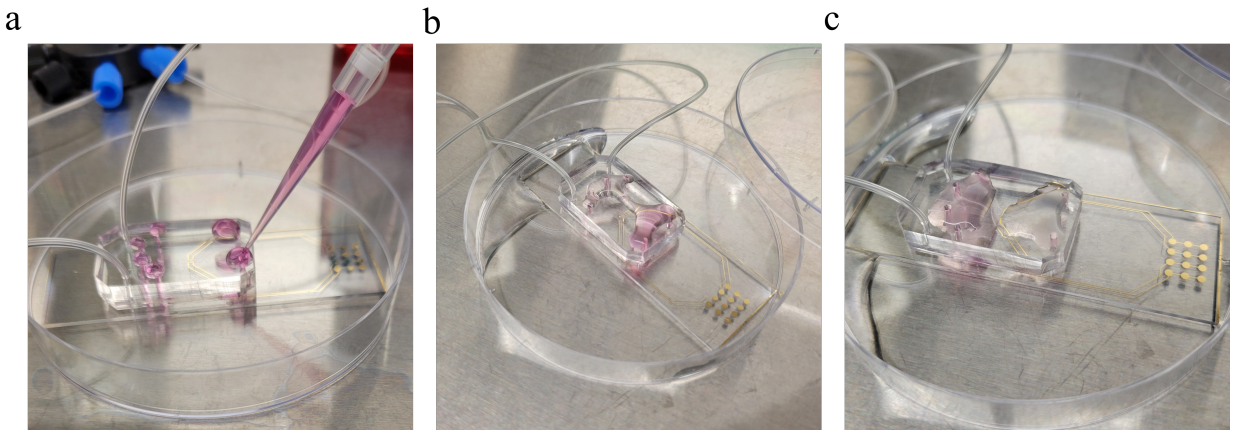

Figure B.1: (**a**) Throughout the seeding process, it is important to maintain liquid droplets on all ports and to always make liquid to liquid contact when pipetting. (**b**) Connecting the droplets on all microfluidic ports over the top surface of the chip eliminates hydrostatic flow. (**c**) Breaking the droplet connection using a laboratory wipe allows microflow and nutrient delivery.

1. Materials and Preparation

    a) Materials – 20 mL cell culture media (warmed to 37°C), 2 mL Accutase, 2 mL DPBS, 5 μL Matrigel, 100 μL DMEM, 70% ethanol solution, deionized water, Tergazyme solution (10 mg/mL)

    b) Equipment – cell counter, biosafety hood, CO2 controlled incubator at 37°C, pipettors, (optional) inspection microscope located in the biosafety hood

c) Microfluidic peripherals – actuating valves during the seeding process requires a vacuum line of appropriate pressure (roughly -200 mbar) that can be maintained between the biosafety hood and the cell culture incubator.

2. Adhesion Promoter Coating

   a) Wet the microfluidic device

      i. Connect all pneumatic ports on the device to vacuum in order to actuate valves and prevent liquid entering the pneumatic lines.

      ii. Flush the device with 70% ethanol. Choose a port and inject roughly 200 μL of ethanol into the device using a 200 μL or 1 mL pipetting syringe.

      iii. As a surfactant, ethanol should more easily wet the chip without forming bubbles. However, full and bubble-free wetting should be checked under the microscope before proceeding. If bubbles are present, continue flushing the device with ethanol.

      iv. Flush the device with at least 1 mL of deionized water. Use a laboratory wipe to absorb the droplets on the chip as they expand. Be sure to remove all of the ethanol as it is flushed out.

   b) Apply adhesion coating

      i. Prepare a 20:1 dilution of Matrigel in DMEM media. For most devices, 100 μL should be a sufficient volume to fill the chip. Ensure that Matrigel stock and media are as cold as possible to avoid premature gelling of the Matrigel. Return the Matrigel stock to refrigeration as quickly as possible after use.

      ii. Flush the device with the Matrigel solution. Use a wipe to absorb the water droplets while continuing to flush the Matrigel.

      iii. Add approximately 1mL of DI water to a polystyrene dish housing the microfluidic device to limit evaporation of the Matrigel surface droplets. Replace the dish lid and incubate the device at 37°C for greater than 30 minutes.

3. Cell Suspension Preparation

   a) Cleave cells from culture dish

   b) Estimate plated cell confluence. For the NRK cell line, a fully confluent monolayer in a 100mm culture dish contains roughly 2 million cells. The target seeding density is 1.5 million cells per 100 μL, so 75% confluence across the culture dish is ideal. The plate should not be allowed to reach full confluence as this can trigger morphological changes.

i. Completely aspirate media off of the culture.

ii. Pipette 2 mL of DPBS onto the culture dish. Rock the dish to ensure a complete wash.

iii. Aspirate off the DPBS.

c) Add 2 mL of Accutase into the culture dish and incubate at 37°C for 6 minutes.

i. Using a 1000 μL pipetting tip, break up the cleaved cell clumps by pipetting them gently onto the culture dish. Incline the dish slightly to facilitate easier pipetting.

ii. Pipette 2 μL the cell suspension out of the culture dish and into a 10 mL centrifuge tube. (Media can be added to the empty dish to repopulate it from the small fraction of cells remaining.)

d) Count cells

i. Thoroughly triturate the cell suspension to create a homogeneous mixture. Then remove two 10 uL samples for cell counting.

ii. Count the suspension sample using a hemacytometer or automated cell counter. If using the Countess cell counter, ensure that the settings are not accounting for a dilution in Typan blue.

iii. Determine the resuspension volume. Multiply the counted cell concentration by 2 mL to get the total cell count. The target concentration should be 1.5 million cells per 100 μL. 100 μL should be more than sufficient volume to seed most microfluidic chips, but as little as 20-30 μL may be sufficient for some designs.

e) Resuspend to desired concentration

i. Neutralize the Accutase by adding 4 mL of cell culture media to the cell suspension in the centrifuge tube. Cap the tube securely.

ii. Centrifuge the cell suspension for 3 minutes at 0.2 RCF.

iii. Aspirate off the supernatant.

iv. Resuspend the pellet in the calculated volume of media. To improve seeding density accuracy and account for the pellet volume, perform the initial resuspension in slightly less media volume (roughly 25 μL less). Measure the total solution volume using the pipettor and add additional media as necessary.

4. Microfluidic Seeding

a) Use cell culture media to connect all the droplets over the microfluidic chip inlet/outlet ports, forming a single continuous liquid bead. Connecting all fluid ports prevents hydrostatic flow within the chip after seeding.

b) Triturate the cell suspension immediately prior to seeding. Slowly inject the cell suspension into one of the microfluidic ports, taking care not to introduce any air into the system.

c) Incubate the chip for 1 hour at 37°C. Add approximately 1 mL to the dish housing the microfluidic device to prevent evaporation of the media.

d) Using a 10 μL elongated pipette tip, gently scrape the bottom the inlet ports to remove excess cell build up in the ports. Depress the pipettor before inserting into the port and slowly pull media while scraping the device substrate. Repeat 2-3 times for all inlet/output ports.

e) Fold a laboratory wipe multiple times and draw it quickly across the PDMS surface to break the merged droplet (see Figure B.1c.). Decoupling the inlet and outlet droplets will allow a small amount of hydrostatic flow to refresh nutrient supply.

f) After 1.5 hours, performs a media exchange. Partially insert a 200 μL pipette tip into a fluid port but do not seal it completely against the port edge. Gently and slowly inject media. Caution – small macroscale pressures can translate into significant flow rates at the microscale. Perform media exchanges roughly every 1.5 hours until experimentation.

g) After 3 hours in the incubator, the cells should be sufficiently adhered to accept microfluidic perfusion. Static culture longer than 5-6 hours prior to microfluidic flow is not recommended.

5. Microfluidic Perfusion Coupling

a) Pre-fill all the perfusion system tubing lines to ensure expedient coupling to the microfluidic chip.

b) Ensure that the fluid droplets on the top surface of the microfluidic chip are a safe distance away from the pneumatic ports before turning off the vacuum line and removing the tubing connections.

c) Carefully transport the chip to the perfusion system for experimentation. Keep the device level so that droplets do not leak into the pneumatic ports.

d) Connect the pneumatic ports to the perfusion system first to apply vacuum and actuate all valves. Elastomeric valves should be in the open state during perfusion setup because any accidental flow forced through a closed or neutral valve will cause catastrophic shear stresses on any cells adhered under it.

e) Connect all input perfusion lines to the corresponding inlets on the chip. Perfusion lines should be very slowly expelling fluid during coupling to avoid trapping air and causing bubbles in the microfluidic device. Ensure liquid to liquid contact during coupling.

f) Connect all waste lines. Again, ensure liquid to liquid contact during coupling. Use a syringe to pull liquid into the line and elevate the waste reservoir to create a slow hydrostatic flow. Return the waste reservoir to the same elevation as the input reservoirs.

g) Enable heating in the perfusion system.

6. Clean up and Maintenance

a) Detach the microfluidic chip from the perfusion system, transport to biosafety hood, and connect vacuum line to all pneumatic ports.

b) Flush the chip with 200 μL Tergazyme solution.

c) Incubate at 37°C for 5 minutes.

d) Repeat Tergazyme flush as necessary. Inspect the device under the microscope to ensure that all cell debris has been cleaved.

e) Flush the chip with 200 μL ethanol, ensuring complete exchange of the Tergazyme solution.

f) Use a 1000 μL pipettor to force air through the microfluidic device. Repeat at least once for each microfluidic port to expel as much ethanol from the chip as possible.

g) Store in a clean environment at room temperature. Periodic (roughly weekly) actuation of the elastomeric valves is recommended.

Appendix C

ELECTRICAL IMPEDANCE CORRELATED TO FLOW RATE IN ELASTOMERIC VALVES: AN ANALOG MATERIAL MEMORY

C.1 Introduction

Data storage as much as computation has powered the information era. However, the slowing of Moore's law has lead to increasing interest in novel computing models outside of the von-Neumann paradigm. In turn, advances in new memory systems and approaches are of increasing importance (Kaushik, 2022).

Materials exhibiting memory are remarkable but not unprecedented. At some level, any disordered material stores a memory of the forces that acted on it (Galloway et al., 2022). Non-volatile memory fundamentally requires changing the state of a material in response to a stimulus. Examples include strain annealing in glassy materials (Keim and Medina, 2022), resistive switching in colloids (Kheirabadi et al., 2023), and thermal hysteresis in shape memory alloys (Cho et al., 2022). Many natural bio-materials even show promise as resistive switching memory devices (Rahman, Bhattacharjee, and Hussain, 2023).

We investigate the potential of polydimethylsiloxane (PDMS) as a metamaterial with dielectric memory properties. PDMS is a transparent elastomer that is pervasive in laboratory settings for its optical transparency, low temperature processing, and high fidelity in replica molding processes. PDMS finds a wide array of uses including as a flexible substrate (Khan, Lorenzelli, and Dahiya, 2015), in strain sensors (Verma et al., 2023; R. Wang, X. Li, and Chen, 2024), and in a wide variety of microfluidic applications. Additionally, PDMS can bond covalently with glass or silicon substrates via surface activation with plasma, UV, or chemical treatment (Borók, Laboda, and Bonyár, 2021).

PDMS's high electronegativity also makes it a promising material for use in triboelectric energy harvesters (Zhou, Takita, and Ikuno, 2023; Lee et al., 2022), harvesting charge differences generated by flowing droplets over an engineered surface. PDMS has additionally seen some investigation as a shape memory polymer (Sha et al., 2023; Xiang Li et al., 2020), returning to its original shape state after mechanical or thermal perturbation. PDMS is microscopically porous and is moderately gas permeable and capable of small molecule absorption (Toepke and Beebe, 2006; Meer et al., 2017).

Here we report a phenomenon in which a device comprised primarily of PDMS appears to exhibit

a capacity to store analog information. This discovery suggests a range of possible applications in computing outside the von-Neumann paradigm. In particular, new forms of analog memory are ideal for advances in neuromorphic computing and artificial synapses (Lv et al., 2018; Di Ventra and Pershin, 2011).

C.2 Methods

C.2.1 Device Fabrication

Devices integrating normally closed PDMS microvalves onto a glass substrate are fabricated using an oligomer stamping process previously described (Dungan et al., 2023). In brief, positive photoresist, AZ9260, is used as a sacrificial layer to pattern electrodes on to glass substrates. Cr/Au electrodes are deposited by sputter coating and exposed through lift-off in heated Microposit Remover 1165. Three PDMS layers (flow, pneumatic, and stamp) are produced through the"soft lithography" replica molding process. Master molds are fabricated in negative photoresist SU8-3050 using standard lithography techniques. PDMS (Sylgard 184, Dow Chemical) is prepared in the standard 10:1 base to curing agent mass ratio. The flow layer is spin coated at 2000 rpm for 30s resulting in a membrane thickness of roughly 50 µm in the valve areas. The pneumatic and stamp layers are cast molded to 6 mm depth. The pneumatic layer is aligned and bonded to the flow layer via oxygen plasma treatment at 200W for 30s before the devices are diced and fluidic ports are cored. In order to form normally open valves, an oligomer stamping technique is used to selectively bond the PDMS devices to the glass substrates. The PDMS device and substrate are first oxygen plasma treated (200W, 30s), then the untreated stamping layer is carefully contacted to the device only in the valve active areas. This microcontact serves to locally remove the effect of the plasma treatment, restoring the PDMS's hydrophobicity. Finally, after stamping the device is aligned over the electrodes and bonded to the substrate.

Figure C.1c illustrates the device design used in these experiments. The device includes two input valves intended to switch between input media sources in for a different application. However, for this work, both valves are operated in parallel and are fed from the same source reservoir, effectively functioning as a single valve. Planar electrodes are placed in large wells at either side of the test valve. Dimensions of the valve seat are 400 µm by 500 µm. Minimum spacing between the sensing electrodes is 1 cm.

C.2.2 Experimental Setup

Gas pressure for both liquid flow (p_d) and pneumatic valve operation is controlled by an OB1 Mk3+ pressure regulator (Elveflow). Additional flow control is provided by external solenoid valves (MPV2/2NC, Elveflow), while pneumatic pressure control is directed by magnetic latching valves (LHLA1231111H, Lee Co). Redundant external valves aid in setup of the device and ensure

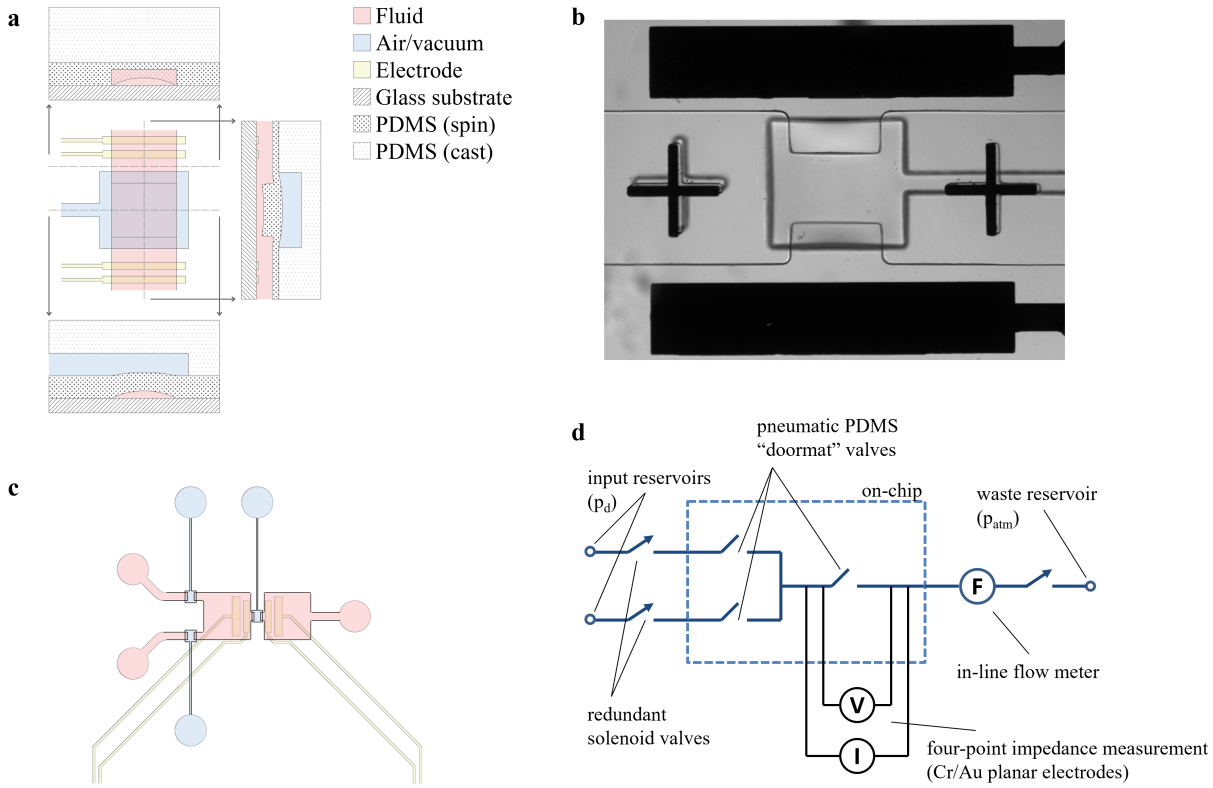

Figure C.1: Device design for evaluation of normally closed elastomeric valves. (**a**) Valves are fabricated using a multilayer process and (**b**) are pneumatically actuated by vacuum (4x, bright-field). (**c**) The schematic of the complete device includes three such valves, though the two input valves are always operated in parallel in these experiments. Impedance measurements are taken by four planar electrodes separated by the "test" valve. (**d**) The microfluidic device is externally connected to three solenoid valves, an inline flow meter, and apparatuses for electrical measurement.

that flow is completely arrested during measurement. Vacuum is provided by a portable laboratory vacuum pump (N810FTP, Ideal Vacuum Products) and is regulated by the OB1 controller to -200 mbar, unless otherwise specified. Flow rates in the device are monitored using an SLF3S-0600F liquid flow sensor (Sensirion). The microthermal sensor is not electrically isolated from the flowing medium, but operates at a different frequency from the impedance sensing. An EVOS FL Auto 2 (Thermo Fisher) captures fluorescent microscopy images. Electrical measurement is captured through a four point measurement scheme with planar Cr/Au electrodes integrated into the microfluidic device. A Keithley 6221 current source (Tektronix Inc.) provides alternating current electrical stimulation at 100 nA and 100Hz, unless otherwise noted. The signal is captured by a SR830 digital lock-in amplifier (Stanford Research Systems). The amplifier performs quadrature detection, multiplying by a reference signal from the current source, yielding the complex impedance at the source frequency. Coordination of all of the instruments is accomplished through

a combination of custom Python scripting and LabVIEW drivers.

Figure C.1d shows the experimental setup. Prior to experimentation, the input and output reservoir heights are balanced to prevent hydrostatic flow at zero driving pressure. Large diameter reservoirs prevent the accumulation of significant hydrostatic flow throughout the experiment. Devices are reused after flushing thoroughly with Tergazyme detergent, 70% ethanol solution, and deionized water.

C.2.3 Chemicals and Materials

Dulbecco's phosphate-buffered saline without calcium chloride or magnesium chloride (DPBS, Thermofisher) solution is used as the primary ionic test solution throughout these tests. Nitrogen gas (AirGas) provides positive pressure drive flow and seal the pneumatic valves. Tergazyme (Alconox Inc.) is an enzymatic detergent that was prepared at 10 mg/mL to flush devices before reuse. (tridecafluoro-1,1,2,2-tetrahydrooctyl)dimethylchlorosilane (PFDCS, Gelest Inc.) is used as a silanizing agent in a 99.8% anhydrous acetonitrile solvent (Sigma-Aldrich). Cell culture media is composed of FluoroBrite DMEM (Thermo Fisher Scientific) with 10% by volume fetal bovine serum, 100 U/mL penicilin-streptomycin, and 1X GlutaMAX.

C.2.4 Data Processing

A moving average filter (kernel size of 10) is used to smooth impedance data prior to peak extraction. Peaks are extracted based on prominence and peak-peak spacing. Extracted flow rate values are based on the average value while the device is in the flow state. Fitting is performed by least squares linear regression. Reported R values refer to the Pearson correlation coefficient.

C.3 Results

C.3.1 Flow Rate Dependent Impedance

Elastomeric PDMS valves appear to exhibit a persistent flow rate dependent impedance. Figure C.2 shows experimental results demonstrating this effect. Electrical impedance across the valve is measured continuously while the system alternates between flow and measurement states (each 60 s in duration). In the flow state, DPBS is driven through the microfluidic chip with the valve in the active open state (vacuum). The driving pressure is ramped at 10 mbar per step resulting in the linear flow rate ramp in Figure C.2a. In the alternating measurement phases, the flow is arrested by closing the external solenoid valves as well as all on-chip pneumatically actuated valves. A positive pressure of 30 mbar for the upstream valves and 10 mbar for the valve under test is applied to ensure a close seal to the substrate. As expected, closing the test valve results in a sharp rise in the impedance corresponding to the voiding of conductive solution between the electrodes. However, the peak impedance values reached during this measurement phase (where flow is arrested) show

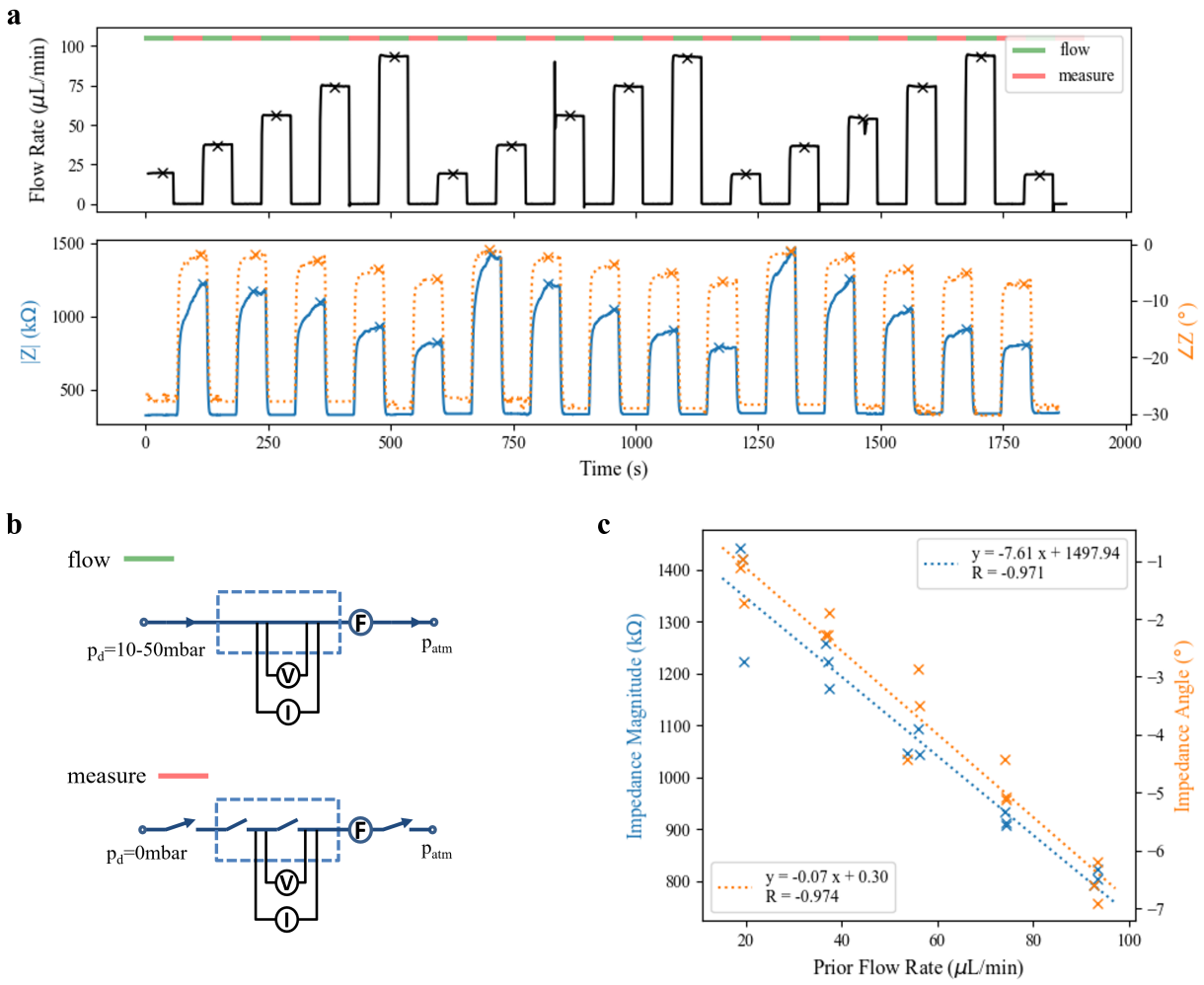

Figure C.2: A representative experiment showing correlation between the flow rate through PDMS valves and the subsequent impedance measured across them in the closed state. The time course of the experiment (**a**) shows a repeated flow rate ramp as the device is switched between flow and measurement states (b). The extracted values for flow rate and impedance in each period are denoted with color coded '×' markers. A strong correlation between these extracted flow rates prior to measurement and the extracted impedance values in the absence of flow is demonstrated (c).

strong linear correlation with the flow rate in the *previous* phase (Figure C.2b). This impedance is inversely proportional to flow rate in both magnitude and phase, exhibiting proportionality constants of -7.6 kΩ min/μL and -0.071 ° min/μL. In this sense, the device acts as an analog memory element, storing the information about the previously applied flow rate in its electrical properties. Notably from the time course data, lower flow rate stimuli are able to "overwrite" higher flows when the pressure ramp resets.

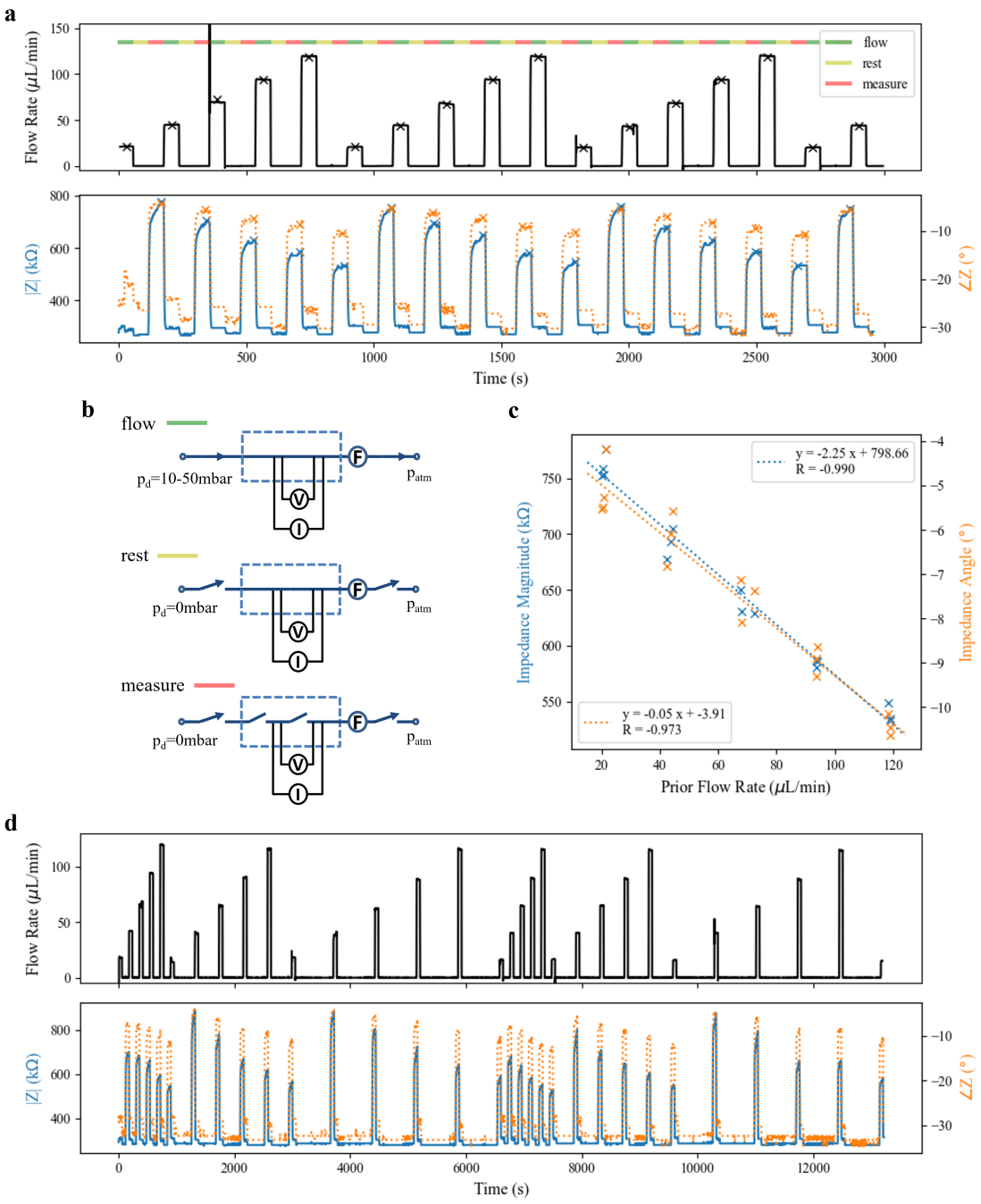

Figure C.3: Demonstration of the longevity of the memory effect. (**a**) The time course of the experiment shows the flow and electrical impedance during the (**b**) three experimental phases. During the rest phase flow is arrested externally but the test valve remains open to allow inertial effects to settle. (**c**) The material's memory is maintained after 1 minute rest cycles with good linearity and (**d**) has been demonstrated to be relatively non-volatile for up to 10 min.

C.3.2 Longevity and Inertial Effects

The memory effect is relatively non-volatile in the absence of fluid flow through the device. Figure C.3 shows the results of three phase experiments, where operation in the flow and measurement phases remain the same as the basic pressure ramp in Section C.3.1. However, after the flow phase, a rest phase is introduced in which the driving pressure is removed and the external solenoid valves are closed to arrest the flow (including hydrostatic flow). During the rest phase the on-chip valves remain open and fluid is allowed to settle. In this settling period, any residual flow or inertial effects of rapidly arresting flow in the chip are expected to resolve themselves. Figure C.3c shows that a 1 minute rest period has little effect on the memory phenomenon. With a high degree of linearity (R^2=.98) the impedance measured through across the closed valve corresponds with the flow rate through the valve 1 minute prior. The fitted slope is reduced to -2.25 kΩ min/μL which is accompanied by a reduction in the measured impedance magnitudes of roughly 50 percent.

The rest period can be extended, seemingly without loss in magnitude or linearity. Figure C.3d shows pressure ramps with 5 and 10 minute rest periods. The flow rate information is held in the material memory for greater than 10 min in the absence of flow. The data show no signs that 10 minutes nears the fundamental limit of memory state's longevity.

C.3.3 Dosage Response

The measured valve impedance corresponds to the previous flow magnitude rather than the total flow exposure or the flux of ionic solution through the valve. As shown in Figure C.4a, when flow rate is set constant to a driving pressure of 30 mbar while the flow exposure time is varied at 30, 60, 90, and 120 seconds, the measured impedance remains relatively constant. The impedance is not well correlated to the total flux of ionic liquid to which the valve has been exposed. Figure C.4b shows this lack of dosage response in the device.

C.3.4 Mechanical Resilience

Additionally, the memory is resilient to mechanical perturbation during the rest phase. Figure C.5 shows the linearity between prior flow rate and measured impedance is preserved after toggling the sensing valve three times during the rest phase (zero flow rate).

C.3.5 Vacuum Effects

Because PDMS is moderately gas permeable, gas exchange with the test fluid is a potential complicating factor in the experimental conditions. The effect of vacuum pressure on the valves is further compounded because the vacuum mechanically affects the valve cross-section and thereby the flow rate through the device. Figure C.6 shows experimental results in which the vacuum pressure on the valves in the flow phase is varied between -100, -150, and -200 mbar. The driving pressure is held constant at 30 mbar, but the change in valve cross-section results in increased flow rate at higher

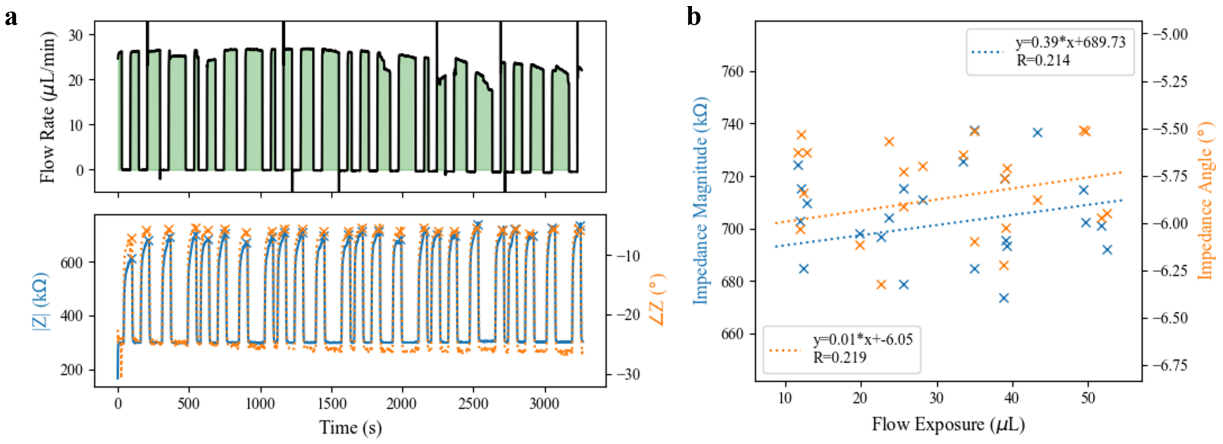

Figure C.4: Impedance response to different flow interval duration. (**a**) The green shaded area in the time course data is integrated to yield a total flow exposure over the interval. (**b**) Electrical impedance is reasonably constant relative to the prior flow exposure and shows poor correlation in both magnitude and phase.

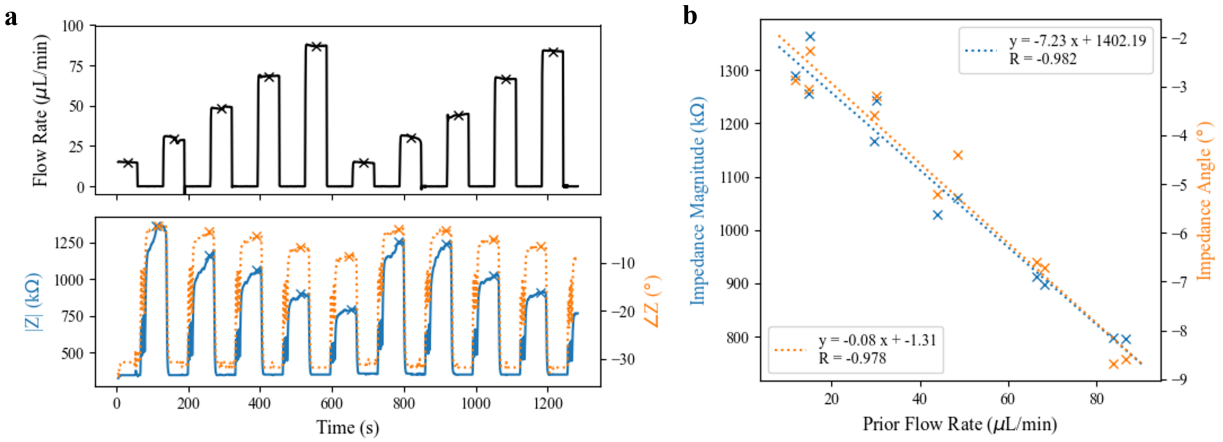

Figure C.5: A demonstration of the mechanical stability of the memory effect. The test valve was rapidly toggled between the open and closed states 3 times (at 1s intervals) while the system is otherwise at rest. (**a**) The toggles appear in the time data as fluctuations in the impedance data prior to peaks in the closed measurement state. (**b**) Despite mechanical perturbation, the memory effect is preserved with good linearity.

vacuum pressures. The impedance in the flow phase additionally reflects the vacuum dependent geometry change. Nevertheless, the memory effect can still be observed with a magnitude fitting function of $-3.56\,\mathrm{k\Omega\,min/\mu L}$ x + $1223\,\mathrm{k\Omega}$ (R^2=0.823).

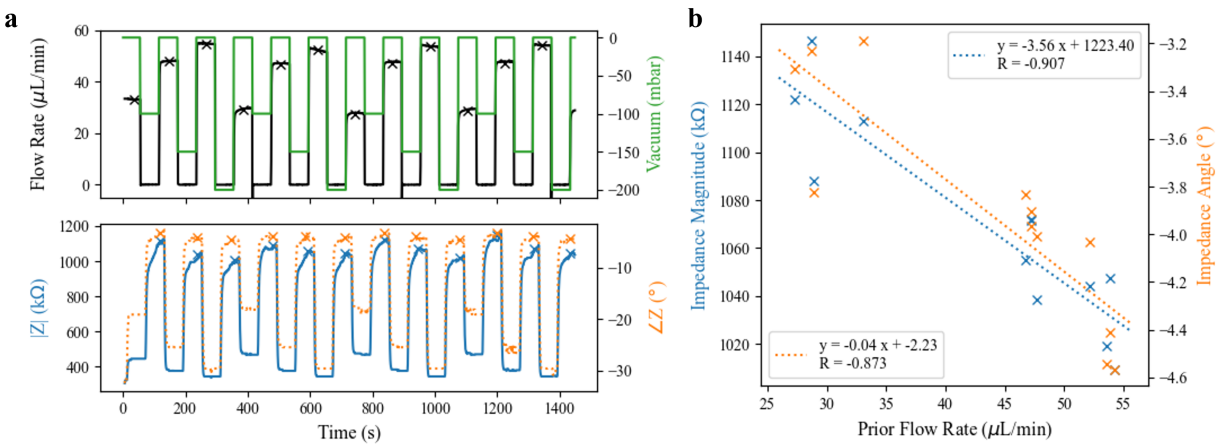

Figure C.6: Impedance response to different vacuum levels on the elastomeric valves during the flow phase. (**a**) The vacuum pressure is stepped at -100, -150, and -200 mbar at a constant p_d of 30 mbar. The vacuum pressure affects flow rate through the valves, so (**b**) the correlation between extracted impedance and prior flow rate is still present.

C.3.6 Overwrite and Anesthesia

The results of the standard pressure ramp (Section C.3.1) showed that lower flow rates are capable of over overwriting greater flow rates for 60 second flow phases. Further investigation into the overwrite behavior and timing is displayed in Figure C.7. The typical test ramp is performed but prior to measurement, the flow is set by a 30 mbar driving pressure for a fixed period of time in an attempt to overwrite previous flow. Overwrite times of 5, 10, 20, 30, 40, and 50 s were tested for 3 ramps cycles each and a linear fit was performed on the resulting impedance measurements. Figure C.7b shows that the resulting slope for the impedance magnitudes is still significant for overwrite times less than 30 s but starts to approach 0 around 40 s, signifying a complete overwrite of the ramped flow. The trend in the phase slopes is less clear. Values are already significantly lower and near 0 after only 5 s of overwrite stimulus, suggesting that the phase information can be re-written much more quickly than the impedance magnitude. As a memory element, this device may be more efficient as a memcapacitor than a memristor.

Further testing is required to determine if the overwrite time depends on the strength of the overwriting flow. However, one experiment (Figure C.8) shows that a significant backflow can effectively anaesthetize the device to a previously flow ramp. To create reverse flow in this experiment, reservoirs are positioned for significant hydrostatic flow at zero driving pressure. The experimental results show that 10 s of backflow causes an impedance fitting slope near zero.

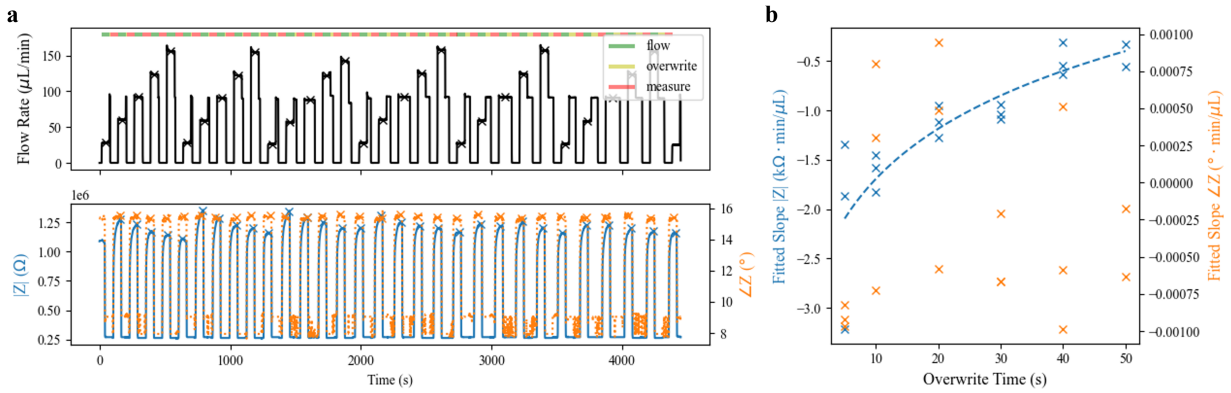

Figure C.7: Test of overwrite time for a fixed flow rate. (**a**) A pressure ramp is performed, but prior to measurement flow is driven at 30 mbar for 5, 10, 20, 30, 40, and 50 s. Time course for one of three replicates is shown.(**b**) For each overwrite time, the impedance data is linearly fitted and the slope is extracted. A logarithmic fit of the magnitude data slopes approaches 0 near 40 s suggesting a minimum overwrite time near 40 s for this flow rate.

C.3.7 Additional Characterization

In order to investigate the contribution of the upstream elastomeric valves in this phenomenon, the standard pressure ramp was conducted by driving flow in the opposite direction through the device. As shown in Table C.1, flow rate dependence of the valve impedance was still detected in the absence of upstream PDMS valves with linear relationship of -0.47 kΩ min / µL. The correlation in phase is significantly reduced in this data set. The extracted impedance peaks reach only 275 kΩ, which is significantly reduced compared to previous measurements.

The sealing impedance of the microfluidic valves generally degrades with time and usage. Devices are cleaned and reused many times. Table C.1 shows the extracted results for the same device used in Section C.2 after it has been reused approximately 25 times over the course of 3 months, representing approximately 100 hours of testing. This testing included static cell culture in the device and extracellular matrix coatings.

Table C.1 additionally presents results indicating that the memory is preserved across multiple frequencies of the electrical stimulus. At 1 kHz, the effect is arguably enhanced, showing a slope of -3.22 kΩ min/µL and very strong linearity (R^2=0.941). At 10 kHz, the correlation between the measured impedance and prior flow rate is still strong, however the fitted magnitude slope is significantly reduced (-0.05 kΩ min/µL). The proportionality reduction, at least in part, reflects the fact that the absolute impedance measured at higher frequencies is significantly reduced. This high-pass filtering effect is expected for a model in which the closed valve acts as a dielectric material between the electrodes forming a capacitor. Notably at both 1 kHz and 10 kHz, the correlation with the phase shifts to a positive slope while maintaining a strong linear fit.

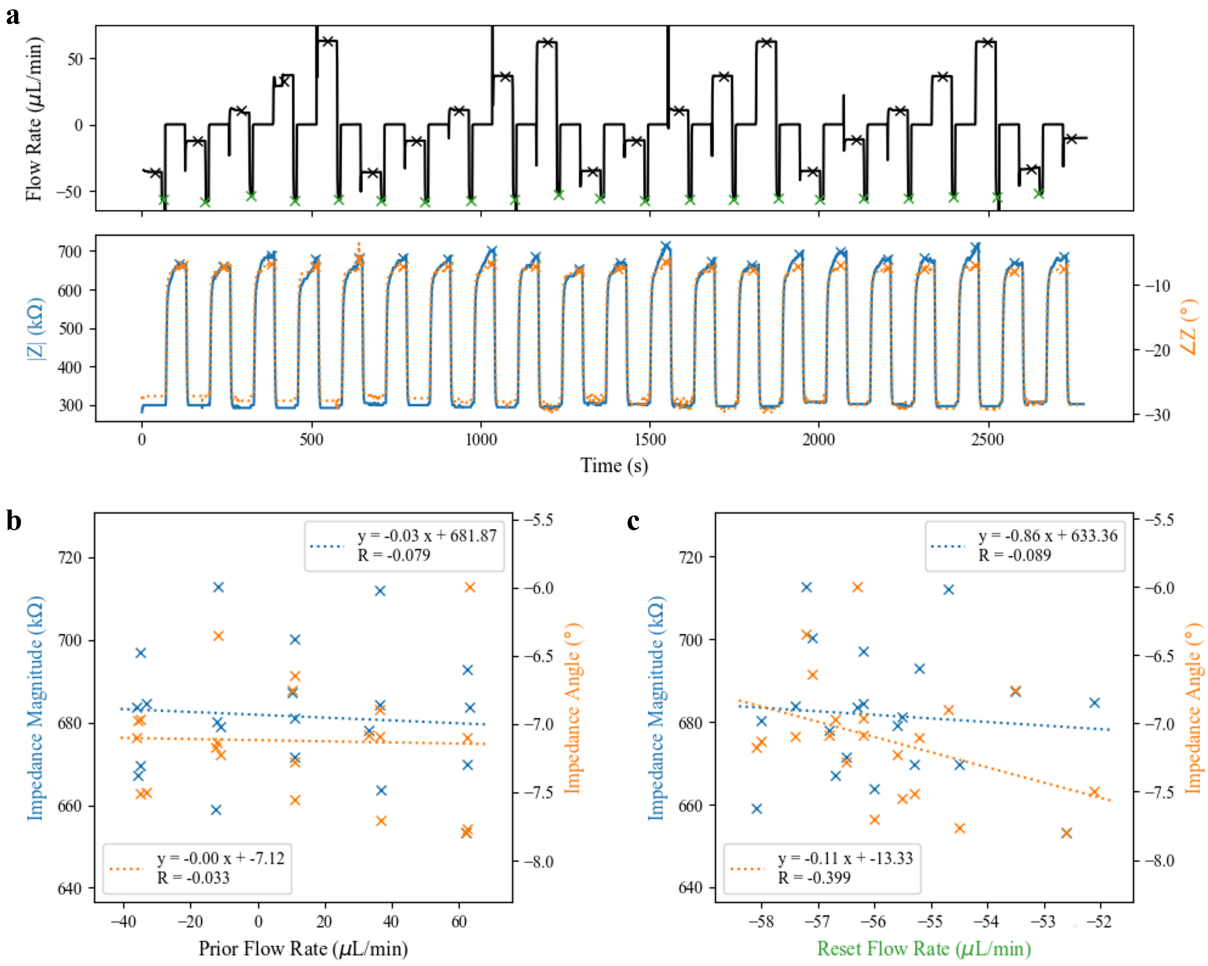

Figure C.8: Investigation of an anesthesia technique. (**a**) Reservoir are positioned for strong hydrostatic backflow which is permitted for 10 seconds prior to impedance measurement. Linear fitting of the extracted impedances results in slopes near near zero for both the (**b**) prior flow rate and (**c**) backflow peak value.

A hydrophobic coating was applied to the device following a previously published protocol (X. Wang et al., 2019). The devices were treated overnight in a 2% by volume solution of PFDCS in acetonitrile, and then flushed with acetonitrile, ethanol, and deionized water. The results in Table C.1 show that this process had little to no effect on the correlation between flow rate and the measured impedance. However, the treatment also did not significantly increase the quality of valve sealing as reported previously (X. Wang et al., 2019), so it is unclear whether the coating was simply unsuccessfully applied or not impactful on the memory phenomenon. Notably, Wang et al. X. Wang et al. (2019) applied this coating scheme only to the glass valve seat prior to fabrication rather than to the entire device including the PDMS components.

The memory effect has been observed in all of our valved PDMS devices with this design. Table

Test	Linear Fit	R
reverse flow	$\|Z\| = -0.47\,k\Omega\,min/\mu L\ x + 285\,k\Omega$	−0.963
	$\angle Z = +0.001\,^\circ\,min/\mu L\ x + 14.66\,^\circ$	+0.630
device degradation	$\|Z\| = -2.55\,k\Omega\,min/\mu L\ x + 1099\,k\Omega$	−0.916
	$\angle Z = -0.012\,^\circ\,min/\mu L\ x + 14.29\,^\circ$	−0.886
frequency response		
100 Hz	$\|Z\| = -2.93\,k\Omega\,min/\mu L\ x + 1169\,k\Omega$	−0.969
	$\angle Z = -0.015\,^\circ\,min/\mu L\ x + 14.81\,^\circ$	−0.929
1 kHz	$\|Z\| = -3.22\,k\Omega\,min/\mu L\ x + 1178\,k\Omega$	−0.970
	$\angle Z = +0.038\,^\circ\,min/\mu L\ x - 11.28\,^\circ$	−0.903
10 kHz	$\|Z\| = -0.05\,k\Omega\,min/\mu L\ x + 312\,k\Omega$	−0.943
	$\angle Z = +0.100\,^\circ\,min/\mu L\ x - 61.98\,^\circ$	−0.987
device-device variation		
#1	$\|Z\| = -2.55\,k\Omega\,min/\mu L\ x + 1099\,k\Omega$	−0.916
	$\angle Z = -0.012\,^\circ\,min/\mu L\ x + 14.29\,^\circ$	−0.886
#2	$\|Z\| = -0.93\,k\Omega\,min/\mu L\ x + 532\,k\Omega$	−0.877
	$\angle Z = -0.024\,^\circ\,min/\mu L\ x + 9.69\,^\circ$	−0.903
#3	$\|Z\| = -0.97\,k\Omega\,min/\mu L\ x + 542\,k\Omega$	−0.980
	$\angle Z = -0.007\,^\circ\,min/\mu L\ x + 15.49\,^\circ$	−0.892
hydrophobic coating	$\|Z\| = -2.74\,k\Omega\,min/\mu L\ x + 929\,k\Omega$	−0.990
	$\angle Z = -0.012\,^\circ\,min/\mu L\ x + 14.68\,^\circ$	−0.970
dilution	$\|Z\| = -4.89\,k\Omega\,min/\mu L\ x + 2782\,k\Omega$	−0.792
	$\angle Z = -0.004\,^\circ\,min/\mu L\ x + 13.02\,^\circ$	+0.486
media*	$\|Z\| = -0.08\,k\Omega\,min/\mu L\ x + 84\,k\Omega$	−0.937
	$\angle Z = -0.01\,^\circ\,min/\mu L\ x + 12.43\,^\circ$	−0.649

Table C.1: *All tests were performed using identical test parameters to the basic pressure ramp experiment in Section C.3.1 with the exception of the media experiment, which used a reduced pressure ramp of 5, 8, 11, 14, 17, and 20 mbar.

C.1 shows the results of identical tests on three representative devices. While the effect is clearly present across all devices, the variation in sensitivity (i.e. the fitted slope) is quite significant - as much as 275%. These devices vary significantly in terms of bond quality.

Finally, the phenomenon has been investigated in a variety of different solutions. Tests using a 1:3 dilution of DPBS in deionized water result in significantly increased impedance magnitude measurement (approximately 3x). The fitting function shows increased slope (-4.89 kΩ min/μL) and reduced linearity (R=-0.792). However, the lowered Pearson coefficient results largely from degraded values for the lowest pressure setting in the ramp. The lowered impedances for the first ramp point may be the result of incomplete overwriting if the write time is increased by lowered solution conductivity and dependent on flow rate. Tests in cell culture media (which is

more conductive that the DPBS test solution) demonstrate the opposite effect of dilution. Peak magnitudes and the sensitivity (evidenced by the fitting intercept and slope, respectively) are both reduced.

C.4 Discussion

The nature of memory is of high interest not only to behavioral science and biology, but also to engineering and information technology. Here, we have demonstrated a new property of an important and widely-used material: PDMS. A closer examination of the electrodynamics is merited as a means to narrow the field of potential mechanisms at play in these devices. We examine a non-exhaustive list of the possible explanations for the observed phenomenon including fluid leakage/trapping, gas permeability, PDMS gap permeability, PDMS sorption, the triboelectric effect, and instrumentation error.

Fluid leakage/trapping. The measured impedance valves may suggest some amount of leakage or trapping of the test solution under the closed valves. Impedance magnitudes do not match a simple first order model of the valve as a dielectric material between planar electrodes, having voided all of the test solution beneath it. Rough estimates place this model at 2.07 fF ($\epsilon_{\text{PDMS}} \approx 2.5$), resulting in an expected impedance magnitude of 767 GΩ at 100 Hz. Clearly, the test solution plays an important role either through conduction at the valve/substrate surface and/or through direct modification of the PDMS permittivity. This observation is further supported by the results of dilution and media testing (Table C.1) which showed direct scaling of the measured impedance peaks (reflected as well in the fit line intercepts) with the solution resistivity.

It seems clear that significant electrical conduction occurs at the interface of the PDMS valve and the glass valve seat. If the valve does not seal closely to the substrate and instead permits some fluid leakage, a rectangular channel spanning the full valve seat would need to be roughly 500 nm in depth ($\sigma_{\text{DPBS}} \approx 15$ mS/cm) to approach the measured values. More likely, such a leakage channel (or channels) would be significantly narrower and might have nearer to a semicircular cross section, requiring a significantly greater maximum depth. This geometry of leakage channel would likely be optically detectable. Hydrophobic surface modification of device would in theory lower any leakage by more closely matching the surface energy of the valve and valve seat as observed by Wang et al. (X. Wang et al., 2019), but a similar treatment was ineffective at reducing the memory sensitivity in these devices.

Increased electrophoretic mobility and conductivity have been observed in shallow channels where the electric double layer at the top and bottom walls overlap (Dukhin and Reisel, 2022; Carrique et al., 2003). In our case, the Debye length in DPBS at 298 K is approximately is approximately 0.115 nm, according to $\kappa^{-1} = 0.304\sqrt{[\mathbf{M}]}$ nm (Israelachvili, 2011). Enhanced conduction in an

exceptionally thin layer of trapped fluid may help explain the magnitudes of the measured impedance values in the absence of optically detectable leakage currents.

While it seems clear that some amount of fluid dependent conduction is present at the valve/surface interface, it is less clear how the volume of liquid trapped under the valve would be flow rate dependent. Fluid leakage seems unlikely to fully explain the memory phenomenon demonstrated, especially in light of the longevity tests (Figure C.3) where flow is fully arrested well in advance of valve closure and the mechanics of valve sealing should be identical.

PDMS gas permeability. The gas permeability of PDMS might offer another explanation of the mechanism, especially since vacuum is applied across thin (approx. 50 µm) PDMS membranes when valves are in the open state (Firpo et al., 2015). Permeation of oxygen, carbon dioxide, or other gases out of the solution could result in local pH changes and alter electrical measurement. The vacuum experiment results of Figure C.6 are somewhat difficult to interpret because the vacuum level directly modifies flow rate. However, the longevity tests (Figure C.3) are evidence against significant gas exchange. Extended vacuum exposure during the rest phases would lead to diminished sensitivity to gas exchange during the previous flow phase, which is not the case.

PDMS sorption. Since PDMS has been shown to absorb small molecules, one possible explanation of the phenomenon might be that the valve material is absorbing charged ions or molecules from the solution. This absorption would likely be proportional to the flow rate and the cross-sectional area of the valve that obstructs the channel during flow. However, a theory of ionic bombardment and absorption does not harmonize well with the overwrite data in Section C.3.6. Previous reports of small molecule absorption in PDMS have shown very slow release rates of the trapped molecules, up to 100 times slower than the absorption process, on the scale of days (Iyer and Eddington, 2019; Toepke and Beebe, 2006). The overwrite data, especially by smaller flow rates, does not seem to comport with this explanation. However, absorption in the PDMS over time may help explain the decreased sensitivity of the devices to the memory effect after reuse and aging.

The results of the anesthesia test (Figure C.8), where backflow is used to annul the forward flow ramp, suggest that the vertical surfaces of the valve that oppose flow are not where the efficacious interaction occurs. Rather, flow across the bottom surface of the valve seems to affect charge or ionic build up on that surface. While bulk absorption seems an unlikely cause, temporary adsorption of ions from solution near the valve seat interface could help provide the thin conduction layer previously posited. While studies of flow rate dependent surface adsorption in PDMS are not known to the authors, the porous nature of the material suggests that some level of ion capture due to flow may be possible.

Triboelectric effect. The triboelectric effect is a complex process, wherein bodies that come into

contact or slide against each other cause significant charge transfer and the development of surface charge on either body. The exact mechanism of triboelectrification is not well understood (Z. L. Wang and A. C. Wang, 2019). Triboelectrification of droplets in PDMS devices is the focus of many triboelectric energy harvesting devices, but the effect has not been characterized for bulk flow. Development of a surface charge on the PDMS valve proportional to the flow rate through triboelectrification would align well with the experimental data.

Instrumentation error. In the absence of a clear physical explanation of the mechanism responsible for the phenomenon, it is natural to suspect an artifact of instrumentation or an experimental inconsistency as the root cause. Though the experimenters have searched meticulously, no such explanation has materialized. To the contrary, no device fabricated in this manner has ever failed to exhibit the memory effect to some extent. Roughly a dozen devices from two different fabrication runs have been tested and the automated systems for impedance measurement, pressure control, and fluid control have been vetted in other applications.

Further investigation into this phenomenon is warranted to identify the mechanism and to optimize for future applications. The effect of device scaling on memory sensitivity and linearity will be important to evaluate and may lend further insight into the mechanism responsible for the effect. Additional surface treatments and investigations into construction in other polymers could help construct optimized devices to capitalize on this phenomenon and build novel analog memory elements.

C.5 Conclusion

A memory effect has been observed in PDMS microfluidic devices implementing normally closed elastomeric valves on glass substrates. Across multiple devices, stimulus frequencies, and test solutions, it has been shown that impedance measured across the closed valve correlates inversely with the flow rate over the valve at some time prior. The observed phenomenon presents an important consideration for electrical sensing in PDMS microfluidics with integrated microvalves. Dependencies as high as 7.61 kΩ per µL/min have been observed which are sufficient to be a significant source of measurement error if flow rates are not closely repeatable.

These findings suggest the use of PDMS in microfluidic devices as a tunable dielectric metamaterial. Flow rate over the valves alter both the resistance and capacitance of the device in a relatively non-volatile manner. However, where write speed is of most importance, the device appears to function more effectively as a memcapacitor than a memristor. These non-linear elements function as low power analog memory and could be ideal for applications in microfluidic computation (Gopinathan et al., 2023). Further, this capacity for analog memory could enable novel, massively parallel computing architectures that are biologically inspired. Artificial synapses and neuromorphic

computing enabled by analog material memories have the potential to unlock new avenues of computation and problem solving.

References

Borók, Alexandra, Kristóf Laboda, and Attila Bonyár (Aug. 2021). "PDMS Bonding Technologies for Microfluidic Applications: A Review". In: *Biosensors* 11.8, p. 292. ISSN: 2079-6374. DOI: 10.3390/bios11080292. URL: https://www.ncbi.nlm.nih.gov/pmc/articles/PMC8394141/ (visited on 10/06/2022).

Carrique, Félix et al. (Apr. 2003). "Influence of Double-Layer Overlap on the Electrophoretic Mobility and DC Conductivity of a Concentrated Suspension of Spherical Particles". In: *The Journal of Physical Chemistry B* 107.14. Publisher: American Chemical Society, pp. 3199–3206. ISSN: 1520-6106. DOI: 10.1021/jp027148k. URL: https://doi.org/10.1021/jp027148k (visited on 02/20/2024).

Cho, W. et al. (May 2022). "Engineering thermal hysteresis of ferromagnetic shape memory alloy sensory particles". In: *Scripta Materialia* 213, p. 114619. ISSN: 1359-6462. DOI: 10.1016/j.scriptamat.2022.114619. URL: https://www.sciencedirect.com/science/article/pii/S1359646222001191 (visited on 06/13/2024).

Di Ventra, Massimiliano and Yuriy V. Pershin (Dec. 2011). "Memory materials: a unifying description". In: *Materials Today* 14.12, pp. 584–591. ISSN: 1369-7021. DOI: 10.1016/S1369-7021(11)70299-1. URL: https://www.sciencedirect.com/science/article/pii/S1369702111702991 (visited on 06/11/2024).

Dukhin, Andrei S. and Alexander Reisel (Mar. 2022). "Overlapping double layers in electrokinetics of concentrated dispersions". In: *Journal of Colloid and Interface Science* 609, pp. 764–774. ISSN: 0021-9797. DOI: 10.1016/j.jcis.2021.11.092. URL: https://www.sciencedirect.com/science/article/pii/S0021979721020002 (visited on 02/20/2024).

Dungan, Joel et al. (Sept. 2023). "Optimization of Oligomer Stamping Technique for Normally Closed Elastomeric Valves on Glass Substrate". en. In: *Micromachines* 14.9. Number: 9 Publisher: Multidisciplinary Digital Publishing Institute, p. 1659. ISSN: 2072-666X. DOI: 10.3390/mi14091659. URL: https://www.mdpi.com/2072-666X/14/9/1659 (visited on 08/28/2023).

Firpo, G. et al. (May 2015). "Permeability thickness dependence of polydimethylsiloxane (PDMS) membranes". In: *Journal of Membrane Science* 481, pp. 1–8. ISSN: 0376-7388. DOI: 10.1016/j.memsci.2014.12.043. URL: https://www.sciencedirect.com/science/article/pii/S0376738814009466 (visited on 06/30/2024).

Galloway, K. L. et al. (May 2022). "Relationships between structure, memory and flow in sheared disordered materials". en. In: *Nature Physics* 18.5. Publisher: Nature Publishing Group, pp. 565–570. ISSN: 1745-2481. DOI: 10.1038/s41567-022-01536-9. URL: https://www.nature.com/articles/s41567-022-01536-9 (visited on 05/28/2024).

Gopinathan, Kaustav A. et al. (Oct. 2023). "A microfluidic transistor for automatic control of liquids". en. In: *Nature* 622.7984. Publisher: Nature Publishing Group, pp. 735–741. ISSN: 1476-

4687. DOI: 10.1038/s41586-023-06517-3. URL: https://www.nature.com/articles/s41586-023-06517-3 (visited on 05/07/2024).

Israelachvili, Jacob N (2011). *Intermolecular and Surface Forces*. en. 3rd. Waltham, MA: Academic Press. ISBN: 978-0-12-391927-4.

Iyer, M. Adiraj and D. T. Eddington (Feb. 2019). "Storing and releasing rhodamine as a model hydrophobic compound in polydimethylsiloxane microfluidic devices". en. In: *Lab on a Chip* 19.4. Publisher: The Royal Society of Chemistry, pp. 574–579. ISSN: 1473-0189. DOI: 10.1039/C9LC00039A. URL: https://pubs.rsc.org/en/content/articlelanding/2019/lc/c9lc00039a (visited on 06/28/2024).

Kaushik, Brajesh Kumar (July 2022). "Memories-materials, devices, circuits and systems". In: *Memories - Materials, Devices, Circuits and Systems* 1, p. 100005. ISSN: 2773-0646. DOI: 10.1016/j.memori.2022.100005. URL: https://www.sciencedirect.com/science/article/pii/S2773064622000032 (visited on 06/13/2024).

Keim, Nathan C. and Dani Medina (Oct. 2022). "Mechanical annealing and memories in a disordered solid". In: *Science Advances* 8.40. Publisher: American Association for the Advancement of Science, eabo1614. DOI: 10.1126/sciadv.abo1614. URL: https://www.science.org/doi/10.1126/sciadv.abo1614 (visited on 05/08/2024).

Khan, Saleem, Leandro Lorenzelli, and Ravinder S. Dahiya (June 2015). "Technologies for Printing Sensors and Electronics Over Large Flexible Substrates: A Review". In: *IEEE Sensors Journal* 15.6. Conference Name: IEEE Sensors Journal, pp. 3164–3185. ISSN: 1558-1748. DOI: 10.1109/JSEN.2014.2375203. URL: https://ieeexplore.ieee.org/document/6974982 (visited on 06/12/2024).

Kheirabadi, Noushin Raeisi et al. (Nov. 2023). "Learning in colloids: Synapse-like ZnO + DMSO colloid". In: *Neurocomputing* 557, p. 126710. ISSN: 0925-2312. DOI: 10.1016/j.neucom.2023.126710. URL: https://www.sciencedirect.com/science/article/pii/S0925231223008330 (visited on 05/06/2024).

Lee, Kangpyo et al. (Jan. 2022). "A high-performance PDMS-based triboelectric nanogenerator fabricated using surface-modified carbon nanotubes via pulsed laser ablation". en. In: *Journal of Materials Chemistry A* 10.3. Publisher: The Royal Society of Chemistry, pp. 1299–1308. ISSN: 2050-7496. DOI: 10.1039/D1TA08414C. URL: https://pubs.rsc.org/en/content/articlelanding/2022/ta/d1ta08414c (visited on 05/07/2024).

Li, Xiang et al. (2020). "A broadband and tunable microwave absorption technology enabled by VGCFs/PDMS-EP shape memory composites". In: *Composite Structures* 238. Publisher: Elsevier Ltd. ISSN: 02638223. DOI: 10.1016/j.compstruct.2020.111954.

Lv, Ziyu et al. (June 2018). "From biomaterial-based data storage to bio-inspired artificial synapse". In: *Materials Today* 21.5, pp. 537–552. ISSN: 1369-7021. DOI: 10.1016/j.mattod.2017.12.001. URL: https://www.sciencedirect.com/science/article/pii/S1369702117305977 (visited on 06/11/2024).

Meer, B. J. van et al. (Jan. 2017). "Small molecule absorption by PDMS in the context of drug response bioassays". In: *Biochemical and Biophysical Research Communications* 482.2, pp. 323–328. ISSN: 0006-291X. DOI: 10.1016/j.bbrc.2016.11.062. URL: https://www.sciencedirect.com/science/article/pii/S0006291X16319179 (visited on 06/10/2024).

Rahman, Farhana Yasmin, Debajyoti Bhattacharjee, and Syed Arshad Hussain (Sept. 2023). "An Account of Natural Material-Based Nonvolatile Memory Device". en. In: *Proceedings of the National Academy of Sciences, India Section A: Physical Sciences* 93.3, pp. 497–510. ISSN: 2250-1762. DOI: 10.1007/s40010-023-00830-2. URL: https://doi.org/10.1007/s40010-023-00830-2 (visited on 05/29/2024).

Sha, Wenjing et al. (Apr. 2023). "Water-actuated reversible shape-memory polydimethylsiloxane for potential biomedical applications". en. In: *Journal of Materials Chemistry B* 11.16. Publisher: The Royal Society of Chemistry, pp. 3579–3586. ISSN: 2050-7518. DOI: 10.1039/D2TB02503E. URL: https://pubs.rsc.org/en/content/articlelanding/2023/tb/d2tb02503e (visited on 05/29/2024).

Toepke, Michael W. and David J. Beebe (Nov. 2006). "PDMS absorption of small molecules and consequences in microfluidic applications". en. In: *Lab on a Chip* 6.12. Publisher: The Royal Society of Chemistry, pp. 1484–1486. ISSN: 1473-0189. DOI: 10.1039/B612140C. URL: https://pubs.rsc.org/en/content/articlelanding/2006/lc/b612140c (visited on 06/10/2024).

Verma, L. et al. (2023). "Design and Fabrication of Flexible Carbon Fabric PDMS-Based Strain Sensor for Human Motion Monitoring". In: *IEEE Sensors Journal*. IEEE Sens. J. (USA). Place: USA Publisher: IEEE, pp. 16729–35. ISSN: 1558-1748. DOI: 10.1109/JSEN.2023.3290218.

Wang, R., X. Li, and T. Chen (2024). "Resistive flexible strain sensor based on AgNWs-Gr-PDMS for wearable electronics". In: *AIP Advances*. AIP Adv. (USA) 14.5. Place: USA Publisher: AIP Publishing, 055028 (7 pp.) ISSN: 2158-3226. DOI: 10.1063/5.0211831.

Wang, Xuemin et al. (Sept. 2019). "Surface Modification of Glass/PDMS Microfluidic Valve Assemblies Enhances Valve Electrical Resistance". In: *ACS Applied Materials & Interfaces* 11.37. Publisher: American Chemical Society, pp. 34463–34470. ISSN: 1944-8244. DOI: 10.1021/acsami.9b12342. URL: https://doi.org/10.1021/acsami.9b12342 (visited on 04/30/2024).

Wang, Zhong Lin and Aurelia Chi Wang (Nov. 2019). "On the origin of contact-electrification". In: *Materials Today* 30, pp. 34–51. ISSN: 1369-7021. DOI: 10.1016/j.mattod.2019.05.016. URL: https://www.sciencedirect.com/science/article/pii/S1369702119303700 (visited on 06/13/2024).

Zhou, Qingyang, Ryuto Takita, and Takashi Ikuno (Feb. 2023). "Improving the Performance of a Triboelectric Nanogenerator by Using an Asymmetric TiO2/PDMS Composite Layer". In: *Nanomaterials* 13.5, p. 832. ISSN: 2079-4991. DOI: 10.3390/nano13050832. URL: https://www.ncbi.nlm.nih.gov/pmc/articles/PMC10005343/ (visited on 05/07/2024).

Appendix D

TRILAMINAR FLOW THEORY

For Poiseuille flow, the width of streams in the trilaminar flow is proportional to their incident flow rates (after the entrance region(Ferreira et al., 2021)). That is, for our trilaminar case where Q_{mid} and Q_{side} represent the incident flow rates of the middle and side channels, respectively, the fractional stream width of the middle stream under laminar flow can be given as

$$W_{mid}/W = \frac{Q_{mid}}{Q_{mid} + 2Q_{side}}. \tag{D.1}$$

The incident flow rates are proportional to the driving pressure (P_d) with the (inverse) constant of proportionality termed the hydrodynamic resistance, R_{hyd}. For rectangular channels of length, L, the formulation is

$$Q = \frac{P_d}{R_{hyd}} \approx P_d \left(\frac{12\mu L}{wh^3(1 - 0.63h/w)} \right)^{-1}, \tag{D.2}$$

where $w \times h$ is the cross-sectional area and μ is the fluid viscosity (Bruus, 2008). Additionally, resistance in the input tubing and interconnects may be significant if the on-chip resistance is relatively low.

To calculate the electrical resistance associated with trilaminar flow of saline-sheathed sucrose, consider the simplified trilaminar flow model of Figure D.1a, letting d_0 denote the horizontal position of the laminar flow boundary. To first order, the total resistance through the idealized sample then is given by:

$$\begin{aligned} R &= \int_0^W \frac{\rho(x)}{A}\, dx \\ &= \frac{2}{A} \int_0^{W/2} \rho(x)\, dx \\ &= \frac{2}{A} \int_0^{d_0} \rho_{sucrose}\, dx + \frac{2}{A} \int_{d_0}^{W/2} \rho_{saline}\, dx \\ &= \frac{2}{A}\rho_{sucrose} d_0 + \frac{2}{A}\rho_{saline}(W/2 - d_0) \end{aligned} \tag{D.3}$$

While laminar flow prevents chaotic mixing, transverse diffusion at the fluid boundary still affects the concentration of charge carriers at the boundary. For each ion species, the concentration due to diffusion at the laminar flow boundary is governed by the diffusion equation:

$$\frac{\partial c}{\partial t} = D \frac{\partial^2 c}{\partial x^2}, \tag{D.4}$$

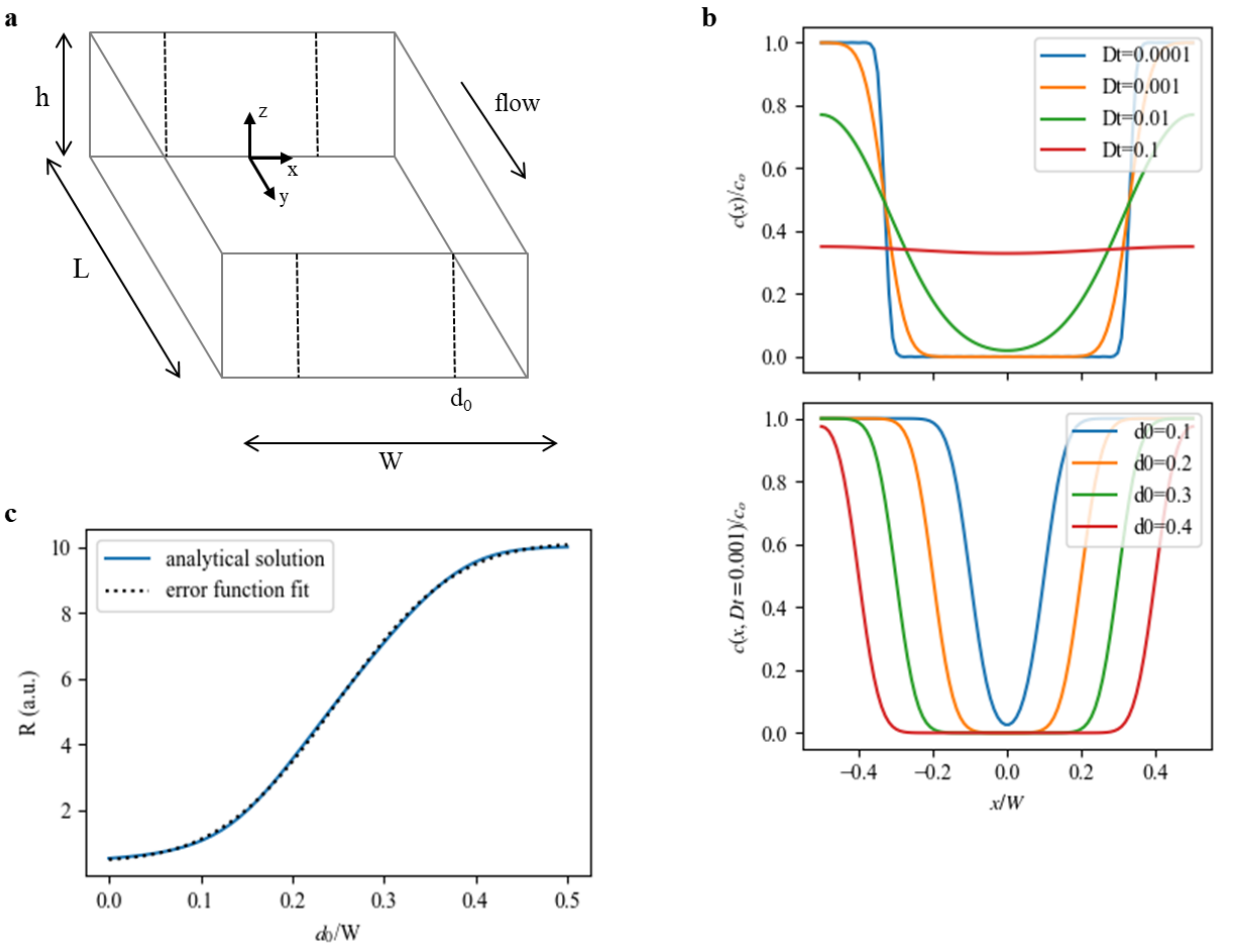

Figure D.1: Model of electrical resistance resulting from trilaminar flow. (**a**) coordinate system and dimensions for the trilaminar flow model, (**b**) ion concentration in the channel cross section for different values of time/diffusivity and middle stream width (Eq. D.7), and (**c**) the analytical model for measured electrical resistance as a function of sucrose stream width, which is closely approximated by the error function.

where $c(x,t)$ is the ion concentration, D is the diffusion constant, and t is the simulation time. Alternately, the simulation time can be considered a measure of distance along the direction of flow (i.e. $t = y/Q$).

Using symmetry, the initial conditions that $c(x, t = 0) = c_0$ for $x \leq d_0$, and the boundary condition of no flux at the channel wall (i.e. $\frac{\partial c}{\partial x}\big|_{x=0,W/2} = 0$), the differential equation can be solved through separation of variables.

$$\begin{aligned} c(x,t) &= X(x)T(t) \\ T(t) &= Ae^{-\lambda^2 Dt} \\ X(x) &= B\cos\lambda x + C\sin\lambda x \end{aligned} \tag{D.5}$$

Applying the boundary condition, we find that $C = 0$ and $0 = \sin(\lambda W/2)$ or $\lambda_n = \frac{2\pi n}{W}$. Then,

$$c(x,t) = \sum_{n=0}^{\infty} D_n \cos\left(\frac{2\pi n}{W}x\right) e^{-Dt(\frac{2\pi n}{W})^2} \tag{D.6}$$

Applying the initial conditions, we eventually arrive at:

$$c(x,t) = c_0\left(1 - \frac{2d_0}{W}\right) - c_0 \sum_{n=1}^{\infty} \frac{2}{n\pi} \sin\left(\frac{2\pi n}{W}d_0\right) \cos\left(\frac{2\pi n}{W}x\right) e^{-Dt(\frac{2\pi n}{W})^2}. \tag{D.7}$$

Figure D.1b shows this solution for different values of d_0 and Dt.

Generally, the relationship between ionic concentration and solution resistivity is a non-linear function of the mobility of the ion species present (W. Zhang et al., 2020) However, the relationship is roughly linear at low concentrations when mobility is high, so resistivity can be considered inversely proportional to the ion concentration ($\rho(x) \propto^{-1} c(x)$). Additionally assuming for simplicity that Dt is a constant (i.e. flow is fast enough that diffusion is constant relative to the length of the laminar flow region), we can arrive at the analytical solution shown in Figure D.1c using the formulation:

$$R(d_0) = \frac{2}{A} \int_0^{d_e} \frac{1}{\lambda_{saline} c(x) + \lambda_{sucrose}(1 - c(x))}\, dx, \tag{D.8}$$

where d_e is the position of a sensing electrode at a distance $0 < d_e < W/2$. λ_{saline} and $\lambda_{sucrose}$ are constants of proportionality such that $\lambda_{saline} >> \lambda_{sucrose}$. The analytical solution can be closely fit with an error function.